Faculdade de Engenharia da Universidade do Porto

Departamento de Engenharia Mecânica

Torque Loss in a planetary multiplier gearbox: Influence of operating conditions and gear oil formulation

Diogo Costa Todo-Bom Pereira

Master's Degree Dissertation presented to the

Faculdade de Engenharia da Universidade do Porto

Dissertation supervised by

Doutor Jorge H. O. Seabra

Full Professor of FEUP

Doutor Ramiro C. Martins

Auxiliary researcher of INEGI

Porto, July 2013

Acknowledgments

I would like to acknowledge and express my deepest appreciation to a few people without whom this dissertation couldn't have been accomplished.

I would like to thank my family and girlfriend for all the help and support given throughout my academic life.

I would also like to thank my supervisors, Prof Jorge H. O. Seabra, Dr. Ramiro C. Martins and Eng. Pedro M. T. Marques for their constant support, availability, readiness, transmitted knowledge and especially for all their patience.

I would like to express my gratitude to CETRIB (Unidade de Tribologia, Vibrações e Manutenção Industrial) for allowing me to do this work in a laboratory of such high standards and my fellow colleagues there: Armando Campos, Beatriz Graça, Carlos Fernandes, David Gonçalves, Jorge Castro, José Brandão, Luís Magalhães, Tiago Cousseau, Ricardo Machado, Rui Marques and César Ferreira not only for their constant help and support but also for being able to interact and learn from these experienced and knowledgeable professionals and especially for the great moments we spent together.

I would also like to acknowledge the Fundação para a Ciência e Tecnologia for the financial support given through the project High efficiency lubricants and gears for windmill planetary gearboxes, with research contract PTDC/EME-PME/100808/2008.

Finally I would like to give my sincere thanks to the Instituto Superior de Engenharia do Porto and to the Faculdade de Engenharia da Universidade do Porto and their staff, for the time and resources spent on my graduation in Mechanical Engineering.

Keywords

Wind Turbine gear oils

Power loss

Efficiency

Planetary gearbox

Multiplier gearbox

Coefficient of Friction

Gears friction loss

Rolling bearings power loss

Wear

Palavras chave

Lubrificantes para engrenagens de turbinas eólicas

Perdas de Potência

Eficiência

Engrenagens planetárias

Caixa de engrenagens multiplicadora

Coeficiente de fricção

Perdas de potência por atrito nos engrenamentos

Perdas de potência nos rolamentos

Desgaste

Abstract

The importance of renewable energy sources has been increasing recently caused by the growing number of world population and an increasing demand for electricity, providing 19% of electricity generation worldwide.

Wind power, a renewable energy source, is growing at the rate of 30% annually, with a worldwide installed capacity going from 18 GW at the end of the year 2000, up to 282.4 GW at the end of 2012. It is generated using the kinetic energy of the wind through a wind turbine.

A wind turbine has several components, among these are the tower, blades, nacelle, hub, gearbox and the generator. Despite its growth, the wind energy industry has experienced high failure rates since the beginning. A majority of these failures occur in the gears and bearings, which are under variable speed and loading conditions for the greater part of their life. Even nowadays wind turbine gearboxes still haven't achieved their design life goal of twenty years, being that most systems require significant overhaul or repair well before the intended life is reached. An increase in efficiency of a wind turbine can be obtained through an optimization of the gearbox design.

The main objective of this work was to analyse the influence of the operating conditions (low speed and high torque) and lubricant formulation (different ISO VG 320 wind turbine gear oils) in the power loss of a multiplier planetary gearbox.

Four fully formulated wind turbine gear oils, two mineral (MINR and MINE), a polyalkylene Glycol (PAGD) and a Poly-α-olefin (PAOR) were tested in a back-to-back gearbox test rig with recirculating power in order to evaluate the power loss performance of each oil. Input speeds ranging from 100 to 300 rpm and torques ranging from 500 to 1000 Nm were tested. Low speeds and high torques were chosen in order to have conditions similar to the ones found in a real wind turbine gearbox. Wear performance was evaluated through oil analysis using Direct Reading Ferrography (*DRIII*), particles concentration (*CPUC*) and wear particles severity (*ISUC*).

A power loss model was implemented aiming to understand the influence of each power loss component in the multiplier planetary gearbox.

Resumo

A importância das fontes de energia renovavéis têm aumentado recentemente devido ao crescente número da população mundial e ao consequente aumento das necessidades enegéticas, representando actualmente 19% da geração de electricidade mundial.

A energia eólica, uma das fontes de energia renovável, tem vindo a crescer a uma taxa anual de 30% , tendo aumentado de uma capacidade instalada mundial de 18 GW no final do ano 2000 até 282,4 GW no final de 2012. Esta é gerada, utilizando uma turbina eólica, através da energia cinética do vento.

As turbinas eólicas são constituidas por diversos components dos quais se destacam a torre, as pás, a nacelle, a caixa de engrenagens e o gerador. Apesar do seu desenvolvimento, a indústria da energia eólica tem se deparado, desde a sua origem, com ínumeras falhas. A maioria delas ocorrem ao nível das engrenagens e dos rolamentos, por estarem sujeitos a velocidades e cargas variáveis durante a sua vida útil. Actualmente, as turbinas eólicas ainda não conseguiram atingir a sua esperança de vida prevista de vinte anos, sem necessitarem que ocorra uma reparação ou inspecção significaficativa muito antes da esperança de vida prevista ser atingida. O aumento da eficiência numa turbina éolica pode ser obtida através da optimização da caixa de engrenagens.

O principal objectivo deste trabalho consistiu no teste de várias formulações de óleos para turbinas eólicas com diferentes condições de teste, de forma a medir a perda de binário numa caixa de engrenagens planetária multiplicadora.

Num banco de ensaio com recirculação de potência foram ensaiados quatro óleos certificados para turbinas eólicas, dois minerais (MINR e MINE), um polialquilenoglicol (PAGD) e uma polilalfaolefina (PAOR). Cada óleo foi testado a num intervalo de velocidades entre 100 e 300 rpm e num intervalo de binários entre 500 a 100 Nm. Baixas velocidades e elvados binários foram utilizados de forma a simular as condições reais de operação de uma turbina eólica. As partículas de desgaste resultantes dos testes foram analisadas usando Ferrometria

de Leitura Directa (*DRIII*) e Ferrometria analítica (*FRIII*). Os indíces de concentração (*CPUC*) e de severidade das partículas (*ISUC*) também foram avaliados.

Um modelo numérico de perda de potência foi implementado com base nos dados experimentais obtidos nos testes de forma a tornar possível a análise da perda de potência de cada componente de uma caixa de engrenagens planetária multiplicadora.

Nomenclature

Symbol	Units	Description
a	m	Centre distance
$a_{0,1,2,3,4}$	-	Coefficient that depends on the tip contact ratio
A	m^2	External area of the gearbox
b	m	Gear width
B	mm	Width of the bearing
$c_{A,B}$	N/m	Spring constant of a bearing
$CPUC$	-	Index of wear particle concentration
C_w	-	Variable used for the calculation of the frictional moment of drag losses
d	mm	Bearing bore diameter
D	mm	Bearing outside diameter
D_L	-	Number of large particles
d_m	m	Mean diameter of a bearing
D_S	-	Number of small particles
d_{sh}	mm	Shaft diameter
$d_{sun,planet,ring}$	m	Reference diameter of the sun, planet or ring gear
E^*	Pa	Equivalent Young modulus
F	N	Force
f_A	-	Variable used for the calculation of the frictional moment of drag losses
F_r	N	Radial force
F_n	N	Normal force
F_N^{max}	N	Maximum normal force
f_t	-	Variable used for the calculation of the frictional moment of drag losses
F_t	N	Tangential force

F_Z	N	Force projection over the z axis
f_0	-	Coefficient that depends on the bearing design and lubrication method
F_0	N	Preload force
$f_{1,2}$	-	Coefficient that takes into account the direction of load application
G_{rr}	N·m	Variable used to calculate the rolling frictional moment
G_{sl}	N·m	Variable used to calculate the sliding frictional moment
H	mm	Oil level
h_0	m	Film thickness
h_{0T}	m	Corrected film thickness
H_v	-	Gear loss factor
$ISUC$	-	Index of wear severity
K	W/m·K	Thermal conductivity
K_a	N	Constant that depends on the gearbox manufacturer specifications
$K_{ball,roll}$	-	Rolling element related constant
K_{rs}	-	Replenishment/starvation constant
K_Z	-	Bearing type related geometric constant
i_{rw}	-	Number of rows of the bearing
ℓ	m	Average sum of contacting lines length
L	-	Thermal parameter of the lubricant
l_D	-	Variable used for the calculation of the frictional moment of drag losses
l_g	-	Parameter for the calculation of $a_{0,1,2,3,4}$
m	m	Module

m_g	-	Parameter for the calculation of $a_{0,1,2,3,4}$
M	N·m	Total frictional moment of a bearing
$M_{A,D,ext,Mot}$	N.m	Moment or torque (the index is related to the application point)
M_{drag}	N·m	Frictional moment of drag losses
M_{rr}	N·m	Rolling frictional moment
M_{seal}	N·m	Frictional moment of the bearing seal
M_{sl}	N·m	Sliding frictional moment
n	rpm	Rotational speed
n_{sh}	Rad/s	Rotational speed of the shaft
N	-	Number of planets
n_g	-	Parameter for the calculation of $a_{0,1,2,3,4}$
p	Pa	Pressure
P_a	W	Transmitted power
p_H	N/mm^2	Contact pressure
p_R	N/mm^2	Reference value for contact pressure
P_V	W	Global power loss
P_{VD}	W	Seals power losses
P_{VL0}	W	Bearings no-load power losses
P_{VLP}	W	Bearings load power losses
P_{VZ0}	W	Gears no-load power losses
P_{VZP}	W	Gears load power losses
$\dot{Q}_{cd}$	W	Heat flow rate due to conduction
$\dot{Q}_{cv}$	W	Heat flow rate due to radiation
$\dot{Q}_{rad}$	W	Heat flow rate due to radiation
$\dot{Q}_{total}$	W	Total heat flow rate
R_a	m	Arithmetic mean roughness

r_b	m	Radius at the base
R_s	-	Variable used for the calculation of the frictional moment of drag losses
R_X	m	Equivalent radius
$R_{1,2}$	-	Geometric constants for rolling frictional moment
t	-	Variable used for the calculation of the frictional moment of drag losses
T	K	Temperature
T_{oil}	$°C$	Oil temperature
T_{room}	$°C$	Ambient room temperature
T_{VL}	N·m	Total frictional moment of a needle bearing
T_{VL0}	N·m	No-load component frictional moment of a needle bearing
$T_{VLP1,2}$	N·m	Load component frictional moment of a needle bearing
u	-	Gear ratio
U	-	Speed parameter
$U_{1,2}$	m/s	Velocity of each surface
v	m/s	Tangential speed
V_e	-	Sliding ratio
$V.I.$	-	Viscosity index
V_M	-	Drag loss factor
$v_{R,EHD}$	m/s	Reference value of speed for fluid friction from a test
v_Σ	m/s	Sum velocity at pitch point
W	-	Load parameter
Y	-	Axial load factor for single row bearings
Z	-	Number of teeth
α	Pa^{-1}	Coefficient of piezoviscosity

α_{EHD}	-	Pressure exponent for fluid friction from a test
α_t	Rad	Transverse pressure angle
α_F	-	Pressure exponent for solid friction from a test
α_{FSKF}	°	Variable used to calculate G_{rr}
α_{heat}	W/m·K	Heat transfer coefficient
β	K^{-1}	Thermoviscous coefficient
β_b	Rad	Base helix angle
β_{EHD}	-	Speed exponent for fluid friction from a test
β_F	-	Speed exponent for solid friction from a test
γ_{EHD}	-	Viscosity exponent for fluid friction from a test
ΔT	$°C$	Stabilized operating temperature
ϵ_α	-	Transverse contact ratio
$\epsilon_{1,2}$	-	Tip contact ratio, pinion and gear
η	Pa.s	Dynamic viscosity
η_0	Pa·s	Dynamic viscosity at the oil bath temperature
η_R	Pa·s	Dynamic viscosity reference value from a test
θ	$°C$	Temperature
Λ	-	Specific film thickness
μ_{bl}	-	Coefficient that depends on the additive package of the lubricant
μ_{EHD}	-	Fluid friction coefficient
$\mu_{EHD,R}$	-	Reference value of the fluid friction coefficient
μ_F	-	Solid friction coefficient
$\mu_{F,R}$	-	Reference value of a solid friction coefficient
$\mu_{ISO,mich,M}$	-	Coefficient of friction
μ_{sl}	-	Sliding friction coefficient
ν	cSt	Kinematic viscosity
ξ	-	Portion of fluid film
ϕ_{bl}	-	Weighting factor for the sliding coefficient

ϕ_{ish}	-	Inlet shear heating reduction factor
ϕ_{rs}	-	Kinematic replenishment/starvation reduction factor
ϕ_T	-	Inlet heating influence
ω	Rad/s	Rotational speed

Contents

List of Figures

List of tables

1. Wind turbines

The growing number of world population and an increasing demand for electricity emphasize the importance of renewable energy sources like wind, hydropower, solar, geothermal and wave energy.

Renewable energy provides 19% of electricity generation worldwide. Wind power is growing at the rate of 30% annually, with a worldwide installed capacity going from 18 GW at the end of the year 2000, up to 282.4 GW at the end of 2012 (as shown in Figure 1) [1].

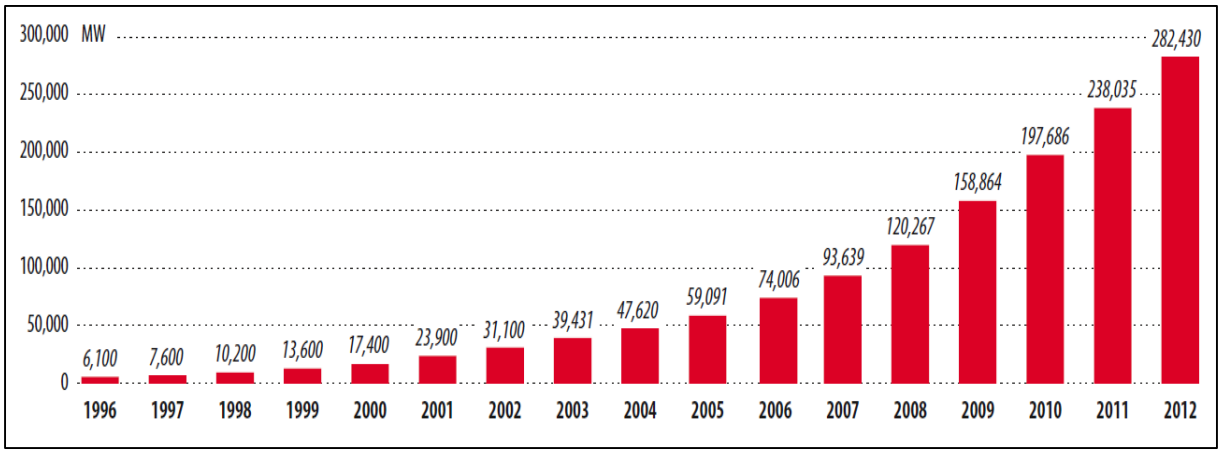

Figure 1. Global cumulative installed wind capacity 1996-2012 [1].

Wind power is obtained using wind turbines. Wind turbines work by turning the kinetic energy of the wind into torque (mechanical energy) that causes the turbine to turn. The generator uses this turning motion to spin a magnetic rotor inside the generator housing that is surrounded by loops of copper wire. As the rotor spins around the inside of the core it excites "electromagnetic induction" through the wire that generates an electrical current.

Wind turbines can be divided into two main types: the horizontal-axis wind turbine (HAWT) and the vertical-axis wind turbine (VAWT).

The key components of horizontal-axis wind turbines are: the tower, blades, nacelle, hub, gearbox and the generator (as shown in Figure 2). The blades capture the kinetic energy of the wind. The number of blades in HAWT can vary being defined by the need to seize the

maximum amount of wind passing through the turbine, the size of the turbine itself and the cost. While increasing the number of blades may result in a gain in power and energy it will not justify the additional cost. Blades are typically manufactured from composite materials. The blades are connected to a hub which is the connection point between the blades and the rotor. The generator in a large scale HAWT usually is a 3-phase AC generator. Typically generators operate at high rotational speeds and therefore it is necessary to have a gearbox to increase the rotational speed from the rotor to match the requirements of the generator. The gearbox, generator and rotor are all housed in the nacelle. The tower usually has a slightly conical shape and is hollow inside. Turbine towers normally are higher than 40m since there is a correlation between the wind speed and the height. Therefore to capture the maximum amount of wind the blades and nacelle are hoisted on the tower.

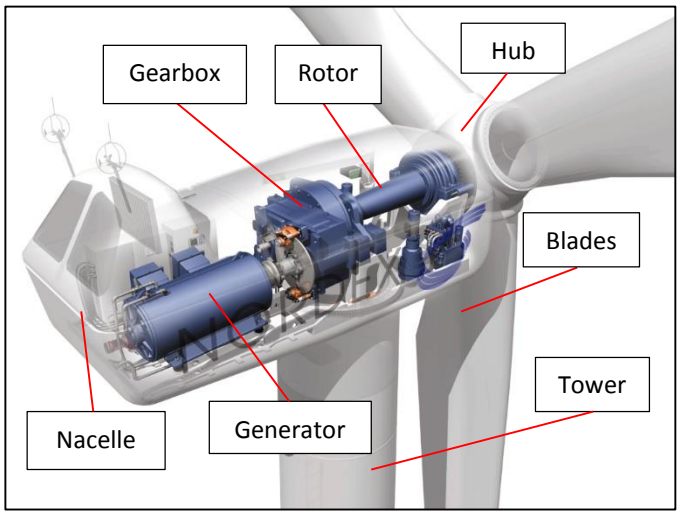

Figure 2. Main components of a horizontal-axis wind turbine [2].

Despite its growth the wind energy industry has experienced high failure rates since the beginning. A majority of these failures occur in the gears and bearings, which are under variable speed and loading conditions for the greater part of their life. Because of this reason under-estimation of the operating loads and gearbox design errors were abundant on the early wind turbine designs. But through a joint effort of wind turbine manufacturers, gear designers, bearing manufacturers, consultants, and lubrication engineers to improve load prediction, design, manufacturing, and operation there was a significant improvement in the

wind turbine design. This collaboration resulted in internationally recognized gearbox wind turbine design standards [3] [4].

Regardless of the adherence to these accepted design practices, wind turbine gearboxes still haven't achieved their design life goal of twenty years, being that most systems require significant overhaul or repair well before the intended life is attained.

Fixing a gearbox may include removing it from the tower. As such, multiple cranes must be used in order to remove the nacelle and rotor making it possible to hoist the gearbox to the ground. To compensate the cost of bringing a crane in to remove the gearbox, owner-operators of wind farms frequently wait until there are a substantial number of turbines with a failure. In the meanwhile the turbines are no longer generating electricity meaning that production capacity is being lost [3] [5].

2. Overview of lubricants

A lubricant is any substance that is used to reduce friction and wear to provide smooth running and a satisfactory life for machine elements. The main purpose of a lubricant is to provide the fluid layer to separate moving surfaces. It also removes heat and wear particles whilst minimizing friction. Most lubricants are liquids (like mineral oils, the synthetic esters and silicone fluids), but they may be solids (such as polytetrafluoroethylene) for use in dry bearings or gases (such as air) for use in gas bearings. An understanding of the physical and chemical interactions between the lubricant and the tribological surfaces is necessary if the machine elements are to be provided with satisfactory life. This chapter is mostly based on the information presented on [6].

There's a wide range of lubricants available on the market nowadays. The main types of lubricants are: liquid lubricants, lubricant greases, solid lubricants and gaseous lubricants.

2.1. Liquid lubricants

Liquid lubricants are the most used kind of lubricant and they can be classified according to their origin as: vegetable, animal, mineral and synthetic.

2.1.1. Vegetable and animal oils

Vegetable and animal oils were the first lubricants to be used by mankind. Yet because these lubricants failed to meet certain requisites imposed by an increase in demand of the operating conditions and because of their chemical inertia these were gradually replaced by petroleum, and more recently by, synthetic based oils. Low resistance to high temperatures and rapid oxidation are examples of other disadvantages found in this type of liquid lubricant.

In spite of their abandonment these lubricants, compared to mineral oils, actually present some advantages worth of noting like their high viscosity index, low evaporation rate and, probably their most important characteristic, a fast biodegradability. This property, biodegradability, is as a matter of fact the one that stands out the most since due to increasing

environmental worries and demands there has been an increase in the use of this kind of oil especially in Nordic countries where it's used, for example, to lubricate forestry equipment.

2.1.2. Mineral based oils

Crude oil results from physical and chemical processes acting over many million years on the buried remains of plants and animals (e.g. zooplankton and algae). Each oilfield, a region with an abundance of oil wells extracting crude oil, produces a different crude oil which varies in chemical composition and physical properties [7].

Hydrocarbons are organic compounds composed exclusively of carbon and hydrogen that can be found in all crude oils and can be further subdivided into the following:

- Alkanes, known as paraffins, with saturated linear or branched-chain structures;
- Alkenes, known as olefins, unsaturated molecules, but comparatively rare in crude oils;
- Alicyclics, known as naphthenes, are saturated cyclic structures based on five- and six-membered rings;
- Aromatics, cyclic structures with conjugated double bonds, mainly based on the six-membered benzene ring.

2.1.2.1. Paraffin basis

Paraffinic base oils are produced from crude oils of relatively high alkane content. Paraffinic base oils are characterised by good viscosity/temperature characteristics, i.e. high viscosity index, low freeze point and by a great oxidation resistance and a low specific weight.

Paraffin based oils are also elastomer friendly which is a favourable characteristic.

2.1.2.2. Naphthenic basis

Naphthenic base oils are made from a more limited range of crude oils than paraffinic base oils, and in smaller quantities, at a restricted number of refineries. Important characteristics of naphthenic base oils are their naturally low pour points, because they are wax-free, and excellent solvency powers. They have a low/medium viscosity index, but they

are used in a wide range of applications where this is not a problem. They also have a high specific weight, high freezing point and a low resistance to oxidation. Unlike paraffin based oils they are relatively aggressive to the elastomers used on seals.

2.1.2.3. Other mineral oils

Paraffins and naphthenes can also be mixed to obtain different mineral based oils. These are largely used as lubricants because it allows for a combination of the following properties:

- Availability on a wide range of viscosities;
- Low volatility;
- Good/high degradation resistance;
- Creation of a good corrosion protection;
- Low price.

2.1.3. Synthetic based oils

Synthetic based oils are lubricants synthetized from hydrocarbons or from its constitutive elements, having at its basis petroleum derived products, vegetable oils, and others. Synthetic lubricants were not commercially significant until after the Second World War. Since, in general, the improved properties of lubricants achieved with early synthetic base stocks could be obtained more cost effectively by improved formulations based on mineral oils.

The development of synthetic lubricant technology was stimulated by the requirement for lubricants to perform over increasing temperature ranges, led by military and aero-engine performance. Nowadays synthetic lubricants can be found in all areas of lubrication like automobiles, trucks, marine diesels, transmissions and industrial lubricants, as well as aviation and aerospace lubricants.

Generally synthetic based oils perform better than the mineral based ones specially when referring to oxidation resistance, viscosity index and the coefficient of friction. The

significance of its usage is greater at higher and lower temperatures. However its cost is significantly higher than the mineral oil based. There is a huge array of synthetic oils. Some of these are: Synthetic hydrocarbons, polyglycols, esters and silicons.

2.1.3.1. Synthetic hydrocarbons

The most common types among synthetic hydrocarbons are polyalphaolefins (PAO) and benzenes.

Their chemical structure is similar to that of mineral hydrocarbons. They also show good compatibility with elastomers that are usually used on seals, a good miscibility with mineral oils as well as an excellent behaviour at low temperatures. They possess an excellent thermal stability but anti-oxidation additives are needed.

Synthetic hydrocarbons can be used to obtain lubricants that fulfil the requirements needed by the food and pharmaceutical industry.

2.1.3.2. Polyglycols

Polyglycols are characterized by a low coefficient of friction making them particularly interesting for high sliding applications, e.g. worm gears. Generally these have a limited miscibility with mineral oils.

A careful assessment of the compatibility with seals and other polymers must be made in cases where the operating temperature is above 100 $°C$.

2.1.3.3. Esters

Ester based oils are the product of a reaction between acids and alcohols followed by water separation. A wide range of esters are available and each one has its own characteristics that will influence the final lubricant properties.

Esters have high thermal resistance and an excellent behaviour at low temperatures.

These oils are also biodegradable but beyond that they are also rapidly degraded. This characteristic is highly relevant when choosing a lubricant since nowadays environmental

issues are of major importance. A coefficient of friction similar to those of polyglycols can also be attained with an adequate choice of the ester basis.

A disadvantage of some esters is its low hydrolytic stability. This depends not only on the ester type but also on the additive package used on the final lubricant.

2.1.3.4. Silicones

Silicones are chemically inert, fire resistant and non-toxic. They also have a high resistance to oxidation at high temperatures, good thermal stability and are not mixable with water.

2.1.4. Lubricant Greases

Grease lubrication is a complex mixture of science and engineering, requires an interdisciplinary approach, and is applied to the majority of bearings worldwide.

Lubricant greases result from the dispersion of a thickening agent on a lubricant oil. It is a viscoelastic plastic solid, therefore, a liquid or solid, depending on the applied physical conditions of stress and/or temperature. The characteristics of these lubricants are dependent upon the properties of the thickener, base oil and additives.

A thickening agent or thickener, generally, can be either a soap, like aluminium, barium, calcium, lithium, sodium and strontium, or a non-soap, like organiphilic clays, polyureas and inorganic compounds. A grease can be more than a lubricant since it is often expected to perform as a seal, corrosion inhibitor, shock absorber and as a noise suppressant.

Lubricant greases are used when continuous oil lubrication is not technically or economically viable and when the protection against outside contaminants or against outside contamination is needed (e.g. pharmaceutical and food industries).

2.2. Solid lubricants

A solid lubricant is any solid material constituted by organic or inorganic compound used to reduce friction and wear between two moving surfaces. Solid lubricants are used in many cases, for example when bearings are used under vacuum, at very high temperatures or under very high radiation and therefore cannot be lubricated by liquid lubricants or greases. In general, the solid material is interposed as a film between sliding and/or rolling surfaces.

2.2.1. Inorganic solid lubricants

There are three different types of compounds used as inorganic solid lubricants: gelatinous solids, soft solids mixtures and surface coating protection by chemical reaction with the surface.

Gelatinous solids use materials like graphite and molybdenum disulphide laid in layers. Easy sliding between the layers occur since inter atomic forces inside a layer are high while inter atomic force of the interface between layers is quite weak.

Soft solid mixtures like lead calcium oxide, talc, silver iodide and lead monoxide that are among a huge variety of inorganic solids, are used as lubricants

There are countless compounds that can chemically react with the surface creating a surface coating that protects the said surface. Well known surface coatings among these compounds are chlorides, oxides, phosphates and sulphides.

2.2.2. Organic solid lubricants

There are two categories of organic solid lubricants. The first are soaps, waxes and fats while the other are polymeric films.

In the soaps, waxes and fats are included metallic soaps like calcium, sodium and lithium as well as beeswax and fatty acids. Polytetrafluoroethylene (PTFE or Teflon®) and polychlorotrifluoroethylene (PCTFE) are synthetic substances that belong to the polymeric films category which are known for having a great resistance to environmental aggression.

2.3. Gaseous lubricants

Both gaseous and liquid lubrication are based on the principles of hydrodynamic lubrication however gaseous lubricants have lower viscosity and higher compressibility thus resulting in lower film thicknesses and load carrying capacities.

Air, water vapour and industrial gases are examples of gaseous lubricants.

2.4. Additives

Additives, firstly used during the 1920s, are chemical compounds that are added to lubricating oils in order to impart specific properties to them. Some additives add new and useful properties to the lubricant while others enhance properties already present and/or act to reduce the rate at which undesirable changes take place in the product during its service life.

Additives and the performance benefits they provide allowed a much faster development of modern passenger car engines, automatic transmissions, hypoid gears, railroad and marine diesel engines, high speed gas and steam turbines, and industrial processing machinery, as well as many other types of equipment.

Actually, today, practically all types of lubricating oil contain at least one additive, and some oils contain additives of several different types. The amount of additive used in a lubricant can vary, going from a few hundredths of a percent to 30% or more.

2.4.1.1. Viscosity index improvers

The most important property of a lubricating oil is probably its viscosity. Viscosity index improvers are used to increase the viscosity index of the oil base, in other words, it diminishes its viscosity at low temperatures and/or increases it at high temperatures.

So, high viscosity index (VI) indicates a relatively low rate of change of viscosity with temperature while a low VI indicates a relatively high rate of change of viscosity with temperature. For example, considering a high VI oil and a low VI oil with the same viscosity at

room temperature, with an increased temperature, the high VI oil will thin out less and, therefore, will have a higher viscosity than the low VI oil.

This improvement occurs by adding high molecular weight polymers like polyisobutylenes and polymethacrylates and fatty alcohol esters.

These additives are used in engine oils, automatic transmission fluids, multipurpose tractor fluids, hydraulic fluids and in automotive gear lubricants.

2.4.1.2. Anti-wear and extreme-pressure additives

Anti-wear (AW) and extreme-pressure (EP) additives reduce or eliminate friction and wear at extreme lubrication conditions. They can be separated into three categories: lubricity agents, anti-wear additives and extreme-pressure additives.

Lubricity agents are added to the base oils in order to diminish the coefficient of friction on limit film lubrication conditions. The kind and quantity used should be selected accordingly with the application requirements. Lubricity agents are used to fight “quawk” and “schatter” phenomena and to avoid phenomena like “stick-slip”.

Anti-wear additives increase the anti-wear properties of the base oil by forming a protective film from a reaction with the metallic surfaces on contact. Zinc dialkyldithiophosphates (ZDDP), phosphorous compounds, zinc compounds and other alkaline compounds are commonly used as anti-wear additives.

Extreme pressure additives form extremely durable protective films by thermo-chemically reacting with the metal surfaces. When rupture of the lubricant film occurs, due to high sliding speeds and/or high contact pressures, the film created by the EP additives that can withstand extreme temperatures and mechanical pressures will minimize the adhesion of the surfaces, thereby protecting them from scoring and seizing.

EP additives are usually added to gear lubricants when the contact pressure between teeth is higher than 700 MPa. When formulating lubricants with this additives, thermal and chemical stability must be ensured since EP additives are prone to induce lubricant instability.

2.4.1.3. Antioxidants

Exposure of hydrocarbons to oxygen and heat will accelerate the oxidation process. Antioxidants additives are used to avoid, delay or modify this reaction.

Oxidation generally results in formation of the following compounds: resins, lacquers, insoluble asphaltic compounds, acidic compounds and hydroperoxides. The addition of antioxidant additives to lubricating oils prevents the formation of all these compounds.

The antioxidant additive can work by directly affecting the lubricant oil, or by affecting the metallic surfaces.

The internal combustion engine is an excellent chemical reactor for catalysing the process of oxidation. Also, the engine's metal parts, such as copper and iron, act as effective oxidation catalysts. Thus, engine oils are probably more susceptible to oxidation than any other lubricant application.

The base lubricant oil should be meticulously refined and its anti-corrosion additives should be carefully selected in order to have the desired stability and corrosion resistance.

2.4.1.4. Other additives

There are other types of additives added to lubricants like:

- Detergents – Used to avoid the formation of deposits of extremely viscous compounds on the lubricant;
- Corrosion inhibitors – These are usually the same additives as antioxidants, since oxidation can result on the formation of acid components that can deteriorate the surfaces;
- Surface oxidation inhibitors – By interacting physically or chemically with certain metals, these can form a continuous and extremely strong layer over the metallic surfaces that doesn’t allow contact between water and those surfaces;

- Foam inhibitors – The most used foam inhibitor is silicon. Usually foam inhibitors are extremely effective because only a few parts per million are enough to attain the desired effect. These avoid foam formation caused by intense lubricant agitation during operation. It can be used on any type of liquid lubricant.

2.5. Physical properties of the lubricant oils

The physical properties of lubricants are mostly defined by the base oil [6] [8] [9] [10] [11].

2.5.1. Viscosity

In hydrodynamic and elastohydrodynamic lubrication the most important physical property of a lubricant is its viscosity. The viscosity of a fluid may be associated with its resistance to flow, that is, with the resistance arising from intermolecular forces and internal friction as the molecules move past each other. So, Fluids with a high viscosity don't flow easily while fluids with a lower viscosity flow very easily. The afore mentioned resistance can be calculated using Newton's formula relative to the laminar flow between a mobile surface with a velocity *V* and a fixed surface (see Figure 3).

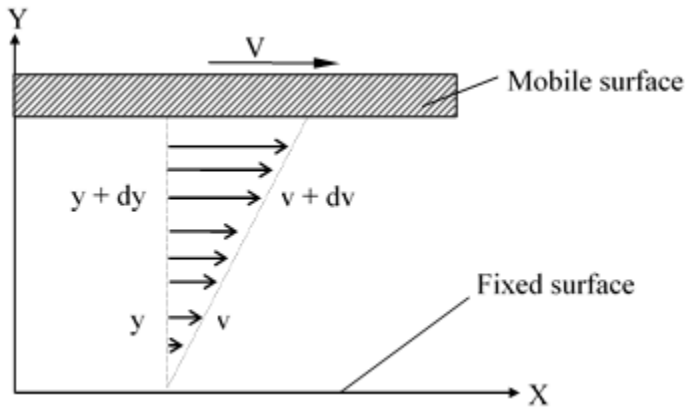

Figure 3. Laminar flow between two planar surfaces.

Since there is relative movement between both surfaces and the no slip boundary condition needs to be verified, it is obvious understanding that there will be different "layers" of fluid moving at different speeds ranging from 0 to *V*.

At any given distance, *y,* from the fixed surface the speed of the fluid will be *v*, so at a *y+dy* distance the speed will be *v+dv*. Hence, the shear stress, *τ*, can be given by:

$$\tau = \sigma_{zy} = \eta \frac{dv}{dy} \qquad \text{Equation 2.1}$$

Where *η* is the dynamic viscosity, a characteristic coefficient of the fluid.

This mathematical hypothesis proposed by Newton in 1687 can be experimentally verified for many fluids. These fluids are accordingly called as Newtonian fluids. Among Newtonian fluids are water and several lubricating oils.

If the stated linear relationship isn't valid then the fluid can be classified as non-Newtonian.

The rheological behaviour of a lubricant is the law that defines and describes the relationship between the deformation speed and the applied shear stress. The rheological model used for Newtonian fluids is stated in Equation 2.1.

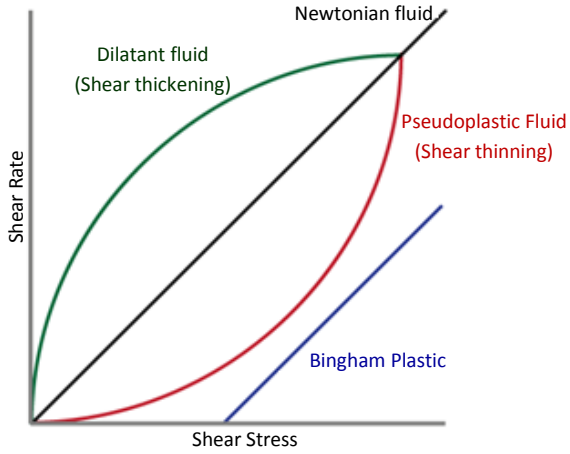

Figure 4. Shear stress vs. Shear rate for different types of fluids, including common non-Newtonian fluids.

The dimensional equation of the dynamic viscosity can be found by doing a dimensional analysis of Equation 2.1.

$$\eta = ML^{-1}T^{-1} \qquad \text{Equation 2.2}$$

So by dividing the dynamic viscosity by the bulk density of the fluid the kinematic viscosity is obtained, Equation 2.3.

$$\nu = \frac{\eta}{\rho} \qquad \text{Equation 2.3}$$

The dimensional equation of kinematic viscosity is presented in Equation 2.4.

$$\nu = L^2 T^{-1} \qquad \text{Equation 2.4}$$

Kinematic viscosity is commonly used in lubrication.

The units of both dynamic and kinematic viscosity are summed up in Table 1:

Table 1. Viscosity units.

Viscosity	Dimension	C.G.S.	S.I.	Correspondence
Dynamic	$ML^{-1}T^{-1}$	Poise = [Po]	Pascal second = [Pa·s]	1 [cPo] = 1 [mPa·s]
Kinematic	L^2T^{-1}	Stokes = [cm^2/s]	[m^2/s];	1 [cSt] = 1 [mm^2/s]

2.5.1.1. Viscometry

A viscometer is an instrument used to measure the viscosity of a fluid. These can be divided into two main categories: absolute viscometers and empirical viscometers.

There are several types of absolute viscometers: capillary viscometers, Couette's viscometers and disc and cone viscometers.

Capillary viscometer measure the viscosity of a liquid by measuring the how long it takes the liquid to flow through a small-diameter tube, or capillary. These can measure with a precision higher than 0.3 %.

Couette's viscometer, also known as rotational viscometer, measures the resistant torque of the fluid that is filling the space between two vertical coaxial cylinders. The inner cylinder is rotated at a constant rate while the outer cylinder remains motionless.

The disc and cone viscometers works by using the same principle as the Couette viscometer, using a conic surface and a fixed plane instead of two cylinders.

There are specific mathematical equations used to determine the viscosity for each absolute viscometer that are a function of several physical parameters.

Empirical viscometers are used for industrial measurements. The most common empirical viscometers are: Saybolt (USA), Redwood (UK) and Engler (Continental Europe). The measurement in these devices is done by the means of a comparison between the time it takes for a certain volume of fluid to completely flow off a recipient and the corresponding time a reference fluid. The viscosities are determined at a constant temperature and each viscometer has its own viscosity unit.

Since the flow on empirical viscometers does not occur at steady state, the law used to determine the viscosity will have to be an empirical law.

2.5.2. Viscosity variation with temperature

The viscosity of most fluids is greatly depending on the temperature. Water, for example, has a variation of around 2.5%, when near 20 $°C$, while mineral oils can have variations of 10% up to 15%. This variation displays itself as a decrease of viscosity with an increase of temperature.

2.5.3. Viscosity Index

The viscosity index was created out of a need to differentiate the reaction of different oil grades to similar temperature variations. Dan and Davis, in 1929, classified every known oil according to their kinematic viscosity value (SUS) at 210 $°F$ (98.8 $°C$). They chose, between all the oils with the same viscosity at 210$°F$, the oil with the highest, a naphthenic oil, and the lowest, a paraffinic oil, viscosity at 100$°F$ (37.8$°C$). They gave an index number of 100 to the first and 0 to the second.

So the viscosity index of an oil can be calculated according to Equation 2.5:

$$V.I. = \frac{L - U}{L - H} \times 100 \qquad \text{Equation 2.5}$$

Where *L* and *H* are the viscosities of the reference oil at 100°F and *U* is the viscosity, at the same temperature, of the required oil. As shown in Figure 5:

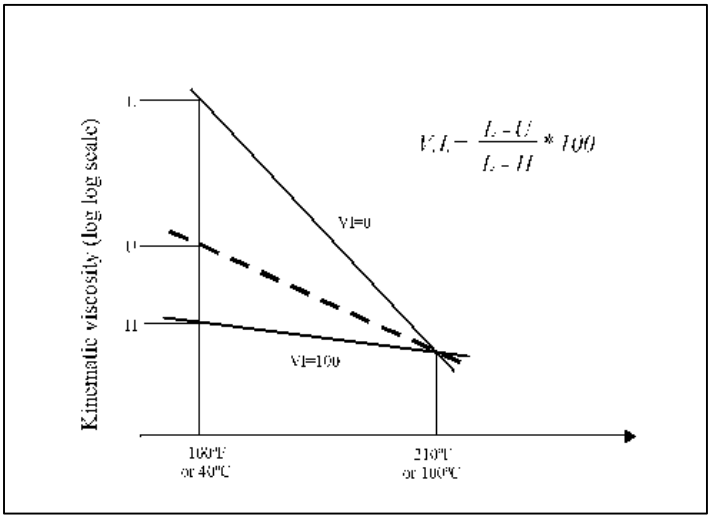

Figure 5. Viscosity index definition.

Temperatures of 40°C and 100°C are used for the calculation of the viscosity index instead of 210°F and 100°F in Europe and the U.S.A. since 1975.

Also worthy of mentioning is the fact that the viscosity index, by itself, is not enough to fully characterize an oil since, generally, two oils with the same viscosity index do not exhibit the same viscosity variation with temperature.

2.5.4. Thermoviscosity

Thermoviscosity represents how viscosity changes with temperature variations. There are several mathematical expressions that try to represent this relationship. The simplest was proposed by Cameron (Equation 2.6):

$$\nu_1 = \nu_0 e^{-\beta \Delta \theta} \qquad \text{Equation 2.6}$$

Where:

- ν_1 is the lubricant's kinematic viscosity at θ_1 temperature;
- ν_0 is the lubricant's kinematic viscosity at θ_0 temperature;

- β is the thermoviscous coefficient;
- $\Delta\theta = \theta_1 - \theta_0$ is the lubricant's temperature variation.

The Equation 2.6 is only valid for small temperature variations and it can be mathematically manipulated in order to obtain the value of β (Equation 2.7):

$$\beta = -\frac{\ln\left(\frac{\nu_1}{\nu_0}\right)}{\theta_1 - \theta_0} \qquad \text{Equation 2.7}$$

ASTM D341 also proposes an equation (Equation 2.8) to calculate the viscosity-temperature behaviour of a lubricant. This equation is widely used.

$$LogLog(\nu + a) = n - mLog(T) \qquad \text{Equation 2.8}$$

Where:

- v is the kinematic viscosity [cSt];
- T is the temperature [K];
- m, n and *a* are experimentally determined lubricant dependent constants.

For oils with v > 0.2 [mm^2/s] the value of *a* will be *a* = 0.7 [12].

The values of n and m can be calculated using Equation 2.9.

$$m = \frac{log\left[\frac{\log(\nu_0 + a)}{\log(\nu_1 + a)}\right]}{\log\left(\frac{\theta_1 + 273}{\theta_0 + 273}\right)} \qquad \text{Equation 2.9}$$

And Equation 2.10.

$$n = LogLog(\nu_0 + a) + mLog(T_0)$$
$$\text{or,} \qquad \text{Equation 2.10}$$
$$n = LogLog(\nu_1 + a) + mLog(T_1)$$

The values of temperature should be in K when the variable is stated as $T_{0,1}$ or in $°C$ when the variable is stated as $\theta_{0,1}$.

The value of β can now be obtained with more accuracy according to Equation 2.11 using Equation 2.8 for a given temperature:

$$\beta = -\frac{1}{\nu}\frac{d\nu}{d\theta} \qquad \text{Equation 2.11}$$

There is yet another equation that can be used to determine the thermoviscosity. It is the Vogel's equation (Equation 2.12).

$$\nu = Ke^{\frac{b}{\theta+c}} \qquad \text{Equation 2.12}$$

Where:

- ν is the kinematic viscosity, [cSt], of the lubricant at θ temperature;
- K, b, c are experimentally determined lubricant dependant constants;
- θ is the temperature [$°C$].

The value of β can also be determined using Vogel's equation (Equation 2.13).

$$\beta = \frac{b}{(\theta + c)^2} \qquad \text{Equation 2.13}$$

A comparison between the results given by the mentioned laws and experimental values are represented in Figure 6.

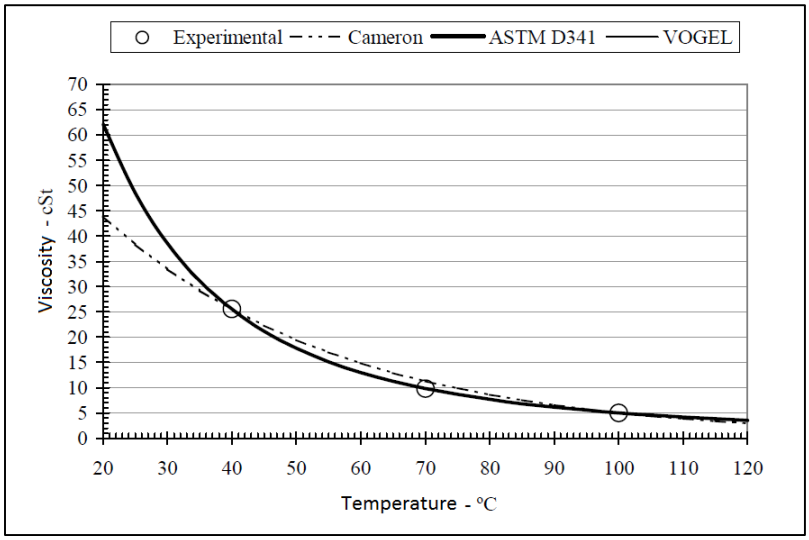

Figure 6. Kinematic viscosity variation with temperature for MOBIL Jet oil II, according to Cameron, ASTM D341 and Vogel laws [6].

2.5.5. Viscosity variation with pressure

Generally, most lubricants have an increase of viscosity with pressure. This phenomenon is of great importance in practical applications since the lubricant can be submitted to pressures of about 10^9 Pa during operation in rolling bearings and gears.

This variation of viscosity with pressure is of an exponential type. This behaviour depends on the lubricant's nature and is more relevant for naphthenic than paraffinic oils.

2.5.6. Piezoviscosity

The way lubricants behave under extreme pressures, (0.5 to 4 GPa), found in elastohydrodynamic (EHD) lubrication is of extreme importance since piezoviscous properties are extremely relevant on the film thickness generation.

If the lubricant is tested on a viscometer at high pressure and with a constant ambient temperature, Baru's law can define the relationship between pressure and viscosity, as shown in Equation 2.14.

$$\eta_s = \eta_0 e^{\alpha p} \qquad \text{Equation 2.14}$$

Where:

- η_s is the dynamic viscosity at a p pressure;
- η_0 is the dynamic viscosity at a pressure p=0;
- α is the coefficient of piezoviscosity, [Pa^{-1}].

In Equation 2.14 it's considered that the coefficient of piezoviscosity, α, is independent of pressure and that it is defined at the temperature of the oil in the contact inlet. Equation 2.14 is also inadequate for pressures above 0.5 GPa and for high ambient temperatures.

2.5.7. Viscosity variation with shear strain rate

For Newtonian fluids, the shear strain rate imposed on the lubricant film has no influence on the dynamic viscosity. If the shear strain rate affects the lubricant viscosity then the lubricant will be a non-Newtonian fluid. This can be observed in Figure 7.

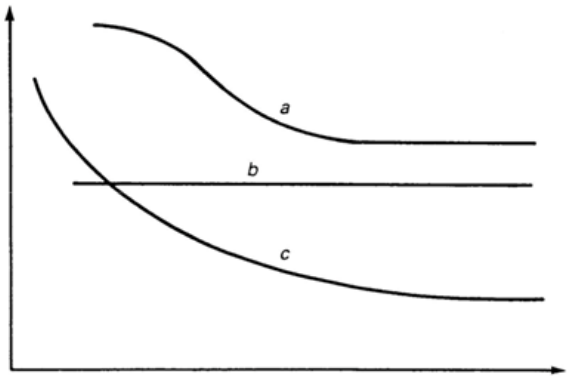

Figure 7. Viscosity variation with shear strain rate for a) Grease; b) Newtonian Fluid; c) non-Newtonian Fluid.

Sometimes lubricants may operate under extremely high shear strain rate conditions which causes a decrease in viscosity. So a rheological model that takes into account the effects of pressure, temperature and shear strain rate needs to be established, since, under these conditions, Newton's model is no longer valid.

2.5.8. Amorphous state of the lubricant

If a lubricant is cooled down, at constant pressure, its viscosity will progressively increase until it reaches a viscosity value of 10^{13} Pa·s. Furthermore, when the temperature surpasses a certain value, vitreous transition temperature, the lubricant will display a behaviour similar to that of an amorphous solid.

The same transformation occurs if the temperature is kept constant and the temperature is progressively risen.

The pressures and temperatures inside EHD contact are enough for such a transformation to take place or, at least, for extremely high viscosities to be observed.

2.5.9. Bulk density and specific gravity

Bulk density is defined as the ratio between the mass of a body and its volume kg/m^3. The bulk density of a lubricating oil varies with temperature although this variation is insignificant when calculating the specific film thickness on a contact.

But the variation of bulk density with pressure is of high importance and very relevant for the calculation of the lubricant film thickness in a contact.

Specific gravity is defined as the ratio between a given material and water's bulk density.

2.5.10. Thermal conductivity

Thermal conductivity is the heat flow transferred due to a unitary temperature gradient per unit of time in a normal direction to a surface of unitary area. Heat transfer occurs at a higher rate across materials of high thermal conductivity than across materials of low thermal conductivity. This property has a linear variation with temperature and its unit is W/m·K.

2.5.11. Specific Heat

Specific heat specifies the amount of energy needed to have a temperature variation of a single degree for a unitary mass. Like the thermal conductivity, specific heat varies linearly with temperature. Its unit is J/kg·K.

2.5.12. Thermal diffusivity

Thermal diffusivity is the property that describes the propagation of temperature on bodies. Being defined as the ratio between thermal conductivity and the product of the bulk density by its specific heat. Its unit is m^2/s.

2.5.13. Lubricant oil specifications

There are two types of specifications available for lubricant oils: viscosity specifications and service specifications.

Viscosity specifications can be established according to two main purposes:

- Identification: there are refining or manufacturing specifications that take into account tolerances for certain ranges of viscosity;
- Usage: these are imposed by consumers and they take into account the use given to the lubricant oils. There are certain ranges of maximum and minimum viscosity at certain temperatures.

The above mentioned classifications are based solely on the lubricant oil viscosity.

There are several professional organizations that classify lubricants according to their viscosity range. The most important ones are the: Society of Automotive Engineers (SAE), International Standards Organization (ISO), American Gear Manufacturers Association (AGMA) and American Society for Testing and Materials (ASTM).

The SAE viscosity classification is the most adopted for pure or additivated mineral oils used for engines, gearboxes and differentials. This classification is exclusively based on the oil viscosity. The only information given by this classification is an estimate for the viscosity at a certain temperature. A different classification is given to each oil according to its application, e.g. SAE J306 is the classification given to lubricant oils for automotive gearboxes and differentials while the SAE J300 is for engines.

The ISO viscosity classification is extremely simple. Each oil grade is defined by a round number that corresponds to the kinematic viscosity, [cSt], of the said lubricant at 40 $^{\circ}C$. The limits for each class correspond to 10% of the average value.

2.5.13.1. Service classification

The most usual service classifications for lubricants are the American Petroleum Institute (API) and Association des Constructeurs Européens d' Automobiles (ACEA). The service classification specifies the desired properties of a lubricant oils for a given application.

Table 2. API classification for gasoline engine lubricant oil [13].

API Category	Status	Service
SN	CURRENT	Introduced in October 2010 for 2011 and older vehicles, designed to provide improved high temperature deposit protection for pistons, more stringent sludge control, and seal compatibility. API SN with Resource Conserving matches ILSAC GF-5 by combining APISN performance with improved fuel economy, turbocharger protection, emission control system compatibility, and protection of engines operating on ethanol-containing fuels up to E85.
SM	CURRENT	For 2010 and older automotive engines
SL	CURRENT	For 2004 and older automotive engines
SJ	CURRENT	For 2001 and older automotive engines
SH	OBSOLETE	
SG	OBSOLETE	
SF	OBSOLETE	
SE	OBSOLETE	CAUTION: Not suitable for use in gasoline-powered automotive engines built after 1979.
SD	OBSOLETE	CAUTION: Not suitable for use in gasoline-powered automotive engines built after 1971
SC	OBSOLETE	CAUTION: Not suitable for use in gasoline-powered automotive engines built after 1967
SB	OBSOLETE	CAUTION: Not suitable for use in gasoline-powered automotive engines built after 1951
SA	OBSOLETE	CAUTION: Contains no additives. Not suitable for use in gasoline-powered automotive engines built after 1930

ACEA also developed several service classifications for engine oils. It proposed three distinct groups: gasoline engines, light diesel engines and heavy diesel engines.

2.5.13.2. Green certification

Millions of tons of lubricants are dumped into the environment through leakage, exhaust gas and careless disposal. Some of these wastes are resistant to biodegradation and are threats to the environment. On the last few years a growing concern about these matters have led to the development of environmentally friendly lubricants.

In order to diminish their impact on the environment they must fulfil certain requirements, like:

- Reduce and, if possible, eliminate sulphur, phosphorous and aromatic components;
- Reduce volatility to reduce its impact on the surrounding atmosphere and on the user;
- To be partially or totally recyclable;
- Diminish toxicity and increase its biodegradability;
- Improve its thermal stability and its oxidation resistance (in order to satisfy the need of a higher operating temperature and in order to have less frequent oil changes);
- Reduce the friction power loss.

Represented in Figure 8 are several common green certifications.

Figure 8. Green certifications: Blauer Engel [14], EU Eco-Label [15], White Swan [16] and Green Seal [17].

3. Wind Turbine Gear oils

Four fully formulated ISO VG 320 grade wind turbine gear oils were selected. Two mineral based oils, MINR and MINE, a Polyalkylene Glycol, PAGD, and a Poly-α-olefin, PAOR, were used. MINR, MINE, PAOR and PAGD is the terminology that was used in this work to make reference to each one the mentioned oils.

The physical properties of these oils were available from previous works [18]. Table 3 shows the properties of the selected gear oils.

Table 3. Physical properties of the wind turbine gear oils [18].

Parameter	Unit	MINR	MINE	PAOR	PAGD
Base oil	-	Mineral	Mineral+PAMA	Poly-α-olefin	Polyalkylene Glycol
-- Chemical composition --					
Zinc (Zn)	[ppm]	0.9	3.5	<1	1.0
Magnesium (Mg)	[ppm]	0.9	0.5	<1	1.4
Phosphorus (P)	[ppm]	354.3	415.9	460	1100
Calcium (Ca)	[ppm]	2.5	0.5	2	0.8
Boron (B)	[ppm]	22.3	38.4	36	1.0
Sulfur (S)	[ppm]	11200	5020	6750	362
-- Physical properties --					
Density @ 15°C	[g/cm^3]	0.902	0.893	0.859	1.059
Thermal expansion coefficient (α_t)	x10^{-4} [K^{-1}]	-5.8	-6.7	-5,6	-7.1
Viscosity @ 40°C	[cSt]	319.25	324.38	324.38	290.26
Viscosity @ 70°C	[cSt]	65.87	92.72	87.92	102.33
Viscosity @ 100°C	[cSt]	22.41	37.88	35.27	51.06
Viscosity Index	-	85	166	155	241

3.1. Techniques and devices used

3.1.1. Engler viscometer

The Engler viscometer has a container inside of another container. The oil is placed inside the first container. There, a wood pointer is either inserted or removed in order to stop or allow the oil to flow through a small hole at the bottom of that recipient.

To keep the oil at a desired temperature a fluid (oil or water) is placed inside the second container, being therefore in contact with the first container. This fluid is heated by a resistance and since there are two thermometers, one on each fluid, the temperature can therefore be controlled.

This set of containers is held by a three legged support that can be adjusted in order to level the set of containers.

The measurement procedure followed the IP 212/92 standard [18]. Figure 9 shows the Engler viscometer used to perform these measurements.

Figure 9. Engler viscometer.

3.1.2. Rheometer

A rheometer tests the character of a fluid. Testing if it's a Newtonian or Non-Newtonian fluid at atmospheric pressure.

The rheometer shown in Figure 10 is a coaxial measurement system.

Figure 10. Rotational viscometer *Contraves Rheomat 115*.

In this rheometer the measuring shaft, which is powered by an electrical motor, is rotating at a set speed inside the test substance. Then the opposing torque is measured and shown on the control instrument display. By performing tests at various shear strain rates the fluid behaviour, Newtonian or Non-Newtonian, can be tested.

3.1.3. Density meter

The variation of the density with temperature at atmospheric pressure for the wind turbine gear oils used on this work were tested using a density meter (shown in Figure 11).

Figure 11. *Anton Paar DM A35N* density meter used to test the density measurements.

A density meter like the one used to make the tests takes a 2 mL oil sample from a recipient that contains the sample in question at a temperature that ranges from 0 to 40°C or the sample can be directly injected into the density meter using a specific syringe.

Three values of the density, each at different temperatures, were recorded in order to calculate the thermal expansion coefficient thus allowing to calculate the density at any given temperature.

3.2. Physical properties

3.2.1. Viscosity and density variation with temperature

The variation of viscosity with temperature is shown in Figure 12.

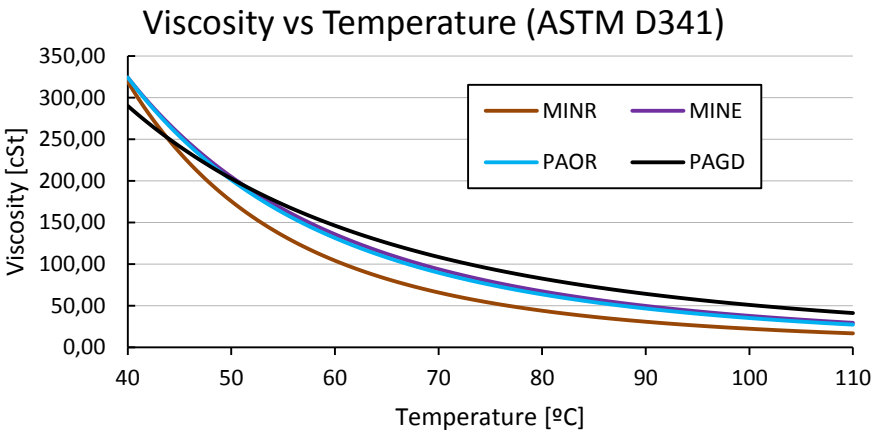

Figure 12. Variation of the tested oils viscosity with temperature (ASTM D341).

By observing Figure 12 it's possible to conclude that the MINR gear oil shows the highest viscosity variation with temperature of all the tested oils. PAGD gear oil shows the highest viscosity at high temperatures having, at 100°C, approximately 51 cSt while MINR oil only has a viscosity of 22.41 cSt at the same temperature. The MINE and PAOR gear oils show a similar behaviour regarding the viscosity and have, at high temperatures, a viscosity that ranges between the middle of the MINR and PAGD gear oils.

As for the density (shown in Figure 13) it's important to underline that the density of the PAGD is higher than the density of water at 40 °C.

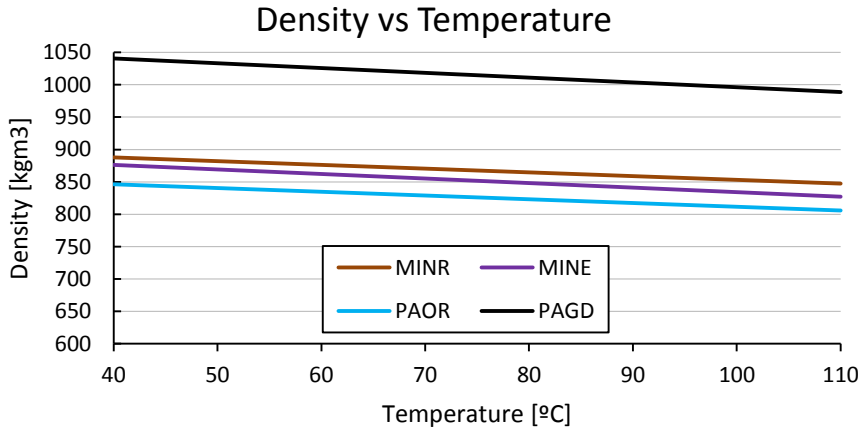

Figure 13. Variation of the tested oils density with temperature.

3.2.2. Dynamic viscosity variation with the shear strain rate

In order to evaluate the dynamic viscosity and the behaviour of the gear oils (Newtonian or Non-Newtonian at atmospheric pressure), tests at different shear strain rates and temperatures were performed on a concentric cylinder rheometer (*Contraves Rheomat 115*). The dynamic viscosity was dependant on the shear rate for the measurements performed at 40 $°C$, mainly due to thermal effects and non-Newtonian behaviour. For higher temperatures (70 and 100 $°C$), this behaviour was no longer observed (see Figure 14). The dynamic viscosity measurements were in accordance with the kinematic viscosity measurements.

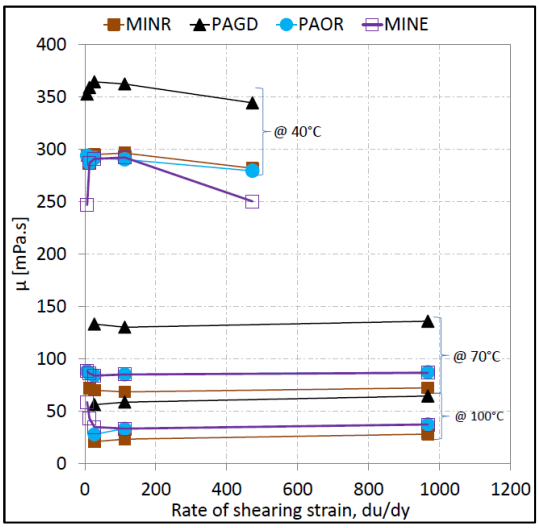

Figure 14. Variation of the dynamic viscosity with the shear strain rate [18].

4. Test rig

4.1. Gearbox components

An attempt to open the planetary gearbox, in order to ascertain its components, was made but there were some difficulties encountered that prevented it. So an estimate of the gearbox rolling bearings was made based on the size and dimension of the gearbox, on the shaft diameter, on the visible components and on the scheme displayed in Wittenstein's catalogue (see Figure 15).

The main components, excluding the gears, shafts and housing, of the gearbox are listed in Table 4:

The geometrical characteristics of the gears of the planetary gearbox are listed in Table 5.

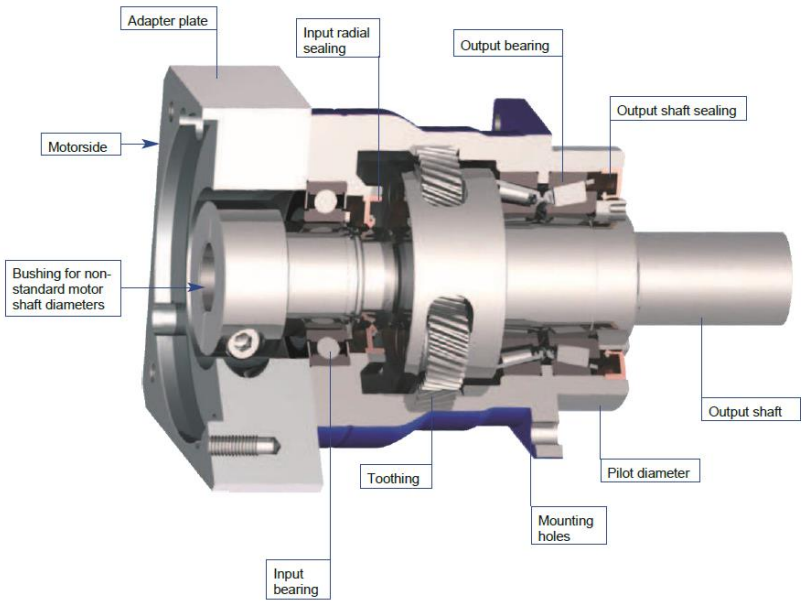

Figure 15. Representative picture of the planetary gearbox [19].

Table 4. Rolling bearings and lip seals in the planetary gearbox.

Component	Quantity	Designation
Tapered roller bearings	2	32022 X/Q
Deep groove ball bearing	1	6217-2Z
Input/Output seal	2	BAUM6 SLX7 140-170-13/12 CFW A1
Needle roller bearing	6	K 40x48x4

Table 5. Geometrical characteristics of the gears of the planetary gearbox

	Sun	Planet	Internal ring
Number of teeth [/]	36	36	-108
Width [mm]	42		
Pressure angle [°]	20		
Working transverse pressure angle [°]	22,071		
Helix angle [°]	10		
Normal module [mm]	2		
Transverse module [mm]	2.031	2.031	2.031
Profile shift coefficient [/]	0.2318	0.2318	-0.6955
Transverse module [mm]	2.031	2.031	2.031
Reference diameter [mm]	73.111	73.111	-219.332
Base diameter [mm]	68.577	68.577	-205.731
Tip diameter [mm]	77.962	77.962	-218.114
Centre distance [mm]	74.000		
Working centre distance [mm]	74.899		74.899

4.2. Test rig

The gearbox test rig works on a back-to-back configuration with recirculating power. Recirculating power is obtained, in this case, by having two gearboxes (number 2 and 7 in Figure 16), which are lubricated by oil injection, at each end of the test rig.

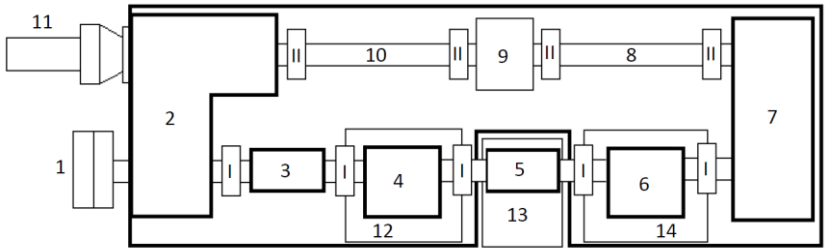

1 – Power input
2, 7 – Test rig gear sets
3, 5 – Torque transducers
4 – Test gearbox
6 – Slave gearbox
8, 10 – Back shafts
9 – Back shafts support
11 – Loading torque cylinder
12, 14 – Adjustable platforms
13 – Mobile platform
15 – Fixed platform
I – Elastic couplings
II – Rigid couplings

Figure 16. Scheme of the test rig.

A photograph of the test rig is shown in Figure 17.

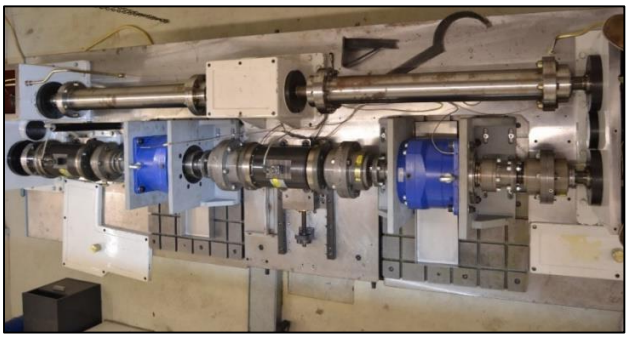

Figure 17. Photograph of the test rig.

This test rig allows the testing of different gearboxes since it has positional adjustment capabilities. Planar adjustment of the test and slave gearboxes can be made by using the platforms (number 12 and 14 in Figure 16). Furthermore, by using the mobile platform (number 13 in Figure 16), the torque sensor (number 5 in Figure 16) can have its height and depth adjusted.

The torque loading mechanism consist of a hydraulic cylinder that introduces an axial displacement on one of the helical gears on the gear set number 2 in Figure 16. This axial movement makes the gear slightly rotate around its axis thus creating a torsional rotation and therefore loading the test rig with a static torque.

The back shaft is divided into two smaller shafts with a support in-between them in order to avoid critical speeds related problems.

The test and slave gearboxes work on a back-to-back configuration in order to match the input speed of the test gearbox with the output speed of the slave gearbox. Therefore only reversible gearboxes can be tested.

Figure 18 shows the central control of the gearbox test rig.

Figure 18. Central control of the test rig.

Through the central control it's possible to set the speed of the electric motor, and the torque on the torque transducer (number 3 in Figure 16).

In order to measure the operating conditions several sensors apart from the already mentioned torque transducers, were installed. These sensors measure:

- The speed before and after the test gearbox (Omron E2EL);
- The oil temperature in two different zones (industrial grade PT100 RTD's);
- The ambient temperature;
- The wall temperature on two different zones on the test gearbox (K type thermocouple and industrial grade PT100 RTD);
- The wall temperature on the slave gearbox (K type thermocouple).

On its current configuration the gearbox test rig allows tests in between the following:

- Input speed: 100-1900 rpm;
- Input torque: 100-1300 Nm.

Two pictures of the test gearbox are shown in Figure 19, where the oil temperature sensors and the wall temperature sensor are highlighted.

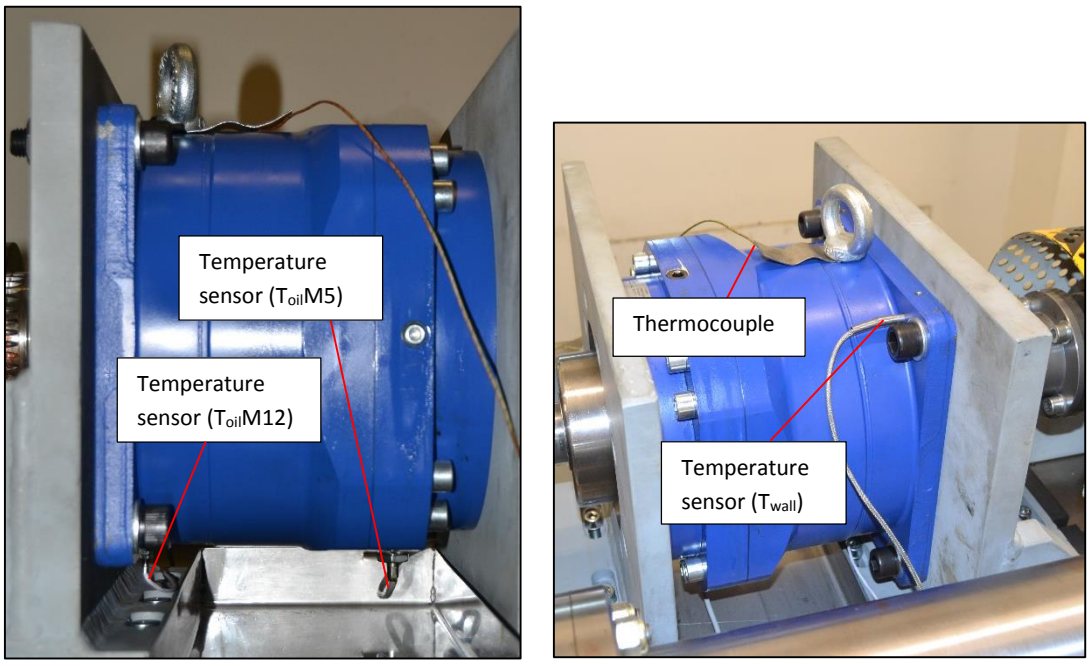

Figure 19. Pictures of the test gearbox.

5. Experimental procedure and oil analysis techniques

5.1. Tests planning

Four fully formulated wind turbine gear oils were tested under different working conditions. The planning of tests is shown in Table 6:

Table 6. Experimental test plan.

Oil	Speed [rpm]	Torque [Nm]	Power [W]	Test time [h]
MINE/PAOR/PAGD/MINR	100	500	5235.99	2+2
		750	7853.98	2+2
		1000	10471.98	2+2
	200	500	10471.98	2+2
		750	15707.96	2+2
		1000	20943.95	2+2
	300	500	15707.96	2+2
		750	23561.94	2+2
		1000	31415.93	2+2

The speeds mentioned in Table 6 are the ones measured between the transducer (number 3 in Figure 16) and the test gearbox. The torques mentioned in Table 6 are the ones measured by the torque transducer referenced as number 3 in Figure 16.

The test gearbox was submitted to running-in before the beginning of the tests.

The first tested oil was MINE, the second was PAOR, the third was PAGD and the last one was MINR.

The followed plan of tests was not the one that was initially set. In the first plan the MINR oil was supposed to be tested first and there were indeed tests made but since the gearbox was still in its running-in period there was a great amount of large particles found in the oil samples. So there was a possibility that these results could've been influenced not only by the operating conditions but also by the running-in. The tests with the MINR gear oil were, therefore, repeated.

5.2. Experimental procedure

The duration of each test was of four hours. This time was set in order to achieve stabilized operating (load, speed and temperature) conditions not only in the test gearbox and gearbox test rig but also in the surrounding environment.

It was found that the calibration values after a warm up period were different from the ideal ones, so two hours after the beginning of each test a calibration of the torque transducers was made, ensuring that the measured values would be close to the actual values of torque.

After each test a 15 minutes no-load test was performed. The loading cylinder control was disabled which assured that no load was applied on the system. This assures that there is no torque imposed in the system making the torque sensors readings a function of the no-load torque loss in the gearbox. The main purpose of these tests was to measure the no-load toque loss of the tested gearbox. These tests were performed right after the "normal" tests in order to capture the no-load behaviour of the test gearbox at the "loaded" operating conditions.

The values read by the sensors were automatically recorded by the central control with a frequency of 0.5 Hz. The software in the central control also calculated, in real time, the power at both sides of the test gearbox and in turn also calculated the instantaneous power loss.

The behaviour over time of various metrics (temperature, torque and power) was also displayed to facilitate the detection of any abnormal variation on the behaviour of the test rig.

An oil sample (Figure 20 (b)) was collected from the test gearbox, through the hole of a plug placed on the upper part of it, using a vacuum pump (Figure 20 (a)). These samples were collected after each set of speeds for each oil, in other words, after the 100 rpm / 1000 Nm, 200 rpm /1000 Nm and 300 rpm /1000 Nm test for each oil. In order to avoid particle deposition at the bottom of the gearbox the samples were collected immediately after the end of a given test and always from the same place.

Changing the oil of the gearbox started with draining the oil through a plug in the bottom and filling it with a solvent, which is chosen according to the oil, and then the shaft between the test gearbox and the torque transducer, number 5 in Figure 16, is rotated during several minutes in order to “clean” the internal parts of the gearbox (removal of remaining oil residue and wear particles). After the completion of this process the gearbox was filled with 1 litre (at ambient temperature) of fresh lubricant.

(a) Vacuum pump

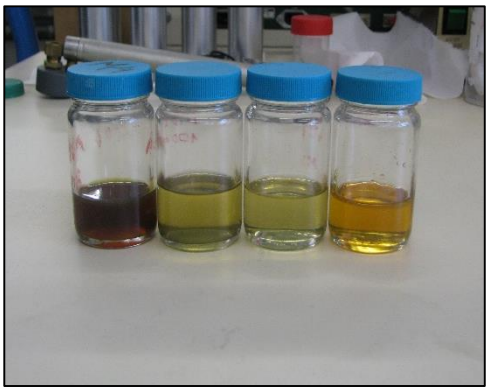

(b) Oil samples

Figure 20. (a) vacuum pump; (b) oil samples (from left to right: MINR, MINE, PAOR, PAGD).

5.3. Ferrography

The oil samples were analysed using a set of techniques called ferrography which are normally used to monitor the wear evolution over time and diagnose the causes of certain failures in mechanical components lubricated by oil or grease. Using this technic the quantity and the morphology of the wear particles suspended in the oil sample can be analysed allowing an evaluation of the wear performance of a lubricant. It can also be used to perform preventive maintenance and to predict the failure of a component in a mechanism.

There were two methods used: direct reading ferrography (DRIII) and analytic ferrography (FMIII).

5.3.1. Direct Reading Ferrography (DRIII)

A direct reading ferrograph allows a rapid and objective relative quantification of large and small particles in an oil sample.

A small volume of oil, 1 ml, circulates through a capillary tube which has a section that is submitted to a strong magnetic field and two beams of light. The particles will lodge along the tube thanks to the magnetic field or simply by sedimentation. The larger particles will deposit first followed by those of smaller dimension.

The beams of light are located in different zones, one at the beginning and the other at the end since, as it has been said, the particles distribute themselves according to their size, and the amount of light that crosses the tube will be limited by the amount of particles so the light will be proportionally inverse to the amount of deposited particles.

There are two values that are obtained through this method: which are the relative quantification of the amount of large, D_L, and small, D_S, particles in the oil sample.

Using these values it's possible to calculate two wear indexes: the Wear Particles Concentration, CPUC (Equation 5.1), and the Wear Severity, ISUC (Equation 5.2).

$$CPUC = \frac{D_L + D_S}{d} \qquad \text{Equation 5.1}$$

$$ISUC = \frac{D_L^2 - D_S^2}{d^2} \qquad \text{Equation 5.2}$$

Where *d* is the factor of dilution which is used in cases of excessive particles which causes saturation of the sensors.

Figure 21. Direct Reading Ferrograph by Predict Technologies.

The model of the used ferrograph was a DR-III-Direct Reading Ferrograph by Predict Technologies (shown in Figure 21).

5.3.2. Analytic ferrography

Analytic ferrography is used to obtain detailed information about the particles. In this method the particles deposit in a thin glass slide which is called a ferrogram.

In this method the oil is forced to flow at a very slow speed between the two edges of the ferrogram. A magnet is located bellow the ferrogram and attracts the magnetic particles causing them to deposit along the ferrogram. The particles will position themselves along the ferrogram according to their size and magnetic properties. So the larger particles will stay at the begging of the ferrogram and their size will decrease along the ferrogram.

Ferromagnetic particles will be perpendicularly arranged relatively to the direction of the oil sample flow.

Even though this method is more efficient on detecting ferrous particle, other types of particles like aluminium and copper alloys can also be deposited due to acquired magnetism from the contact with ferrous particles or trapped between ferrous filaments or simply due to sedimentation. The remaining types of particles like contaminants, products resulting from oxidation and fibbers will randomly deposit along the ferrogram.

Ferrograms are made of a heat resistant glass. This is important because the particles may be submitted to a heat treatment in order to evaluate their composition.

An analytic ferrographer, model FM-III-Ferrograph by Predict Technologies (shown in Figure 22), was used to prepare the ferrogram for observation.

Figure 22. Analytic ferrograph (FMIII) by Predict technologies.

Figure 23. Ferroscope – IV by Predict Technologies

The ferrograms were observed using a Ferroscope which is an optical microscope. The used Ferroscope was a Ferroscope-IV by Predict Technologies (shown in Figure 23).

With this technique the type of particles existing in the sample can be evaluated and by comparing these with reference particles it's possible to have an idea of the type and severity of the wear conditions.

5.4. Fourier transform infrared spectroscopy (FTIR)

Fourier transform infrared spectroscopy (FTIR) is a technique used to obtain an infrared spectrum of absorption, emission, photoconductivity or Raman scattering of a solid, liquid or gas.

The goal of any absorption spectroscopy (FTIR, ultraviolet-visible ("UV-Vis") spectroscopy, etc.) is to measure how well a sample (e.g. an oil sample) absorbs light at each wavelength.

Simplistically the FTIR consists of shining a beam that contains many frequencies of light at once, then it measures the “amount” of the beam that is absorbed by the sample. Afterwards, the beam is modified in order to contain a different combination of frequencies, providing a second data point. This process is done repeatedly. Finally, a computer takes all these data and works backwards to infer what the absorption is at each wavelength [20].

The beam described above is the radiation from a broadband source. This beam shines into a Michelson interferometer (two schemes of a Michelson interferometer adapted for FTIR are shown in Figure 24).

In the Michelson interferometer the beam of light strikes the beamspliter where some of the light is transmitted to a movable mirror and some of the light is reflected to a stationary mirror. The moving mirror, which is moved by a motor, modulates each frequency of light with a different modulation frequency. In general, the paths of the light returning from the stationary mirror and the moving mirror are not in phase. They interfere constructively and destructively to produce a pattern called an interferogram. The interferogram contains all the frequencies which make up the IR spectrum. Computer processing is required to turn the raw data (light absorption for each mirror position) into the desired result (light absorption for each wavelength). The processing required is a common algorithm called the Fourier transform (hence the name, "Fourier transform spectroscopy") [20].

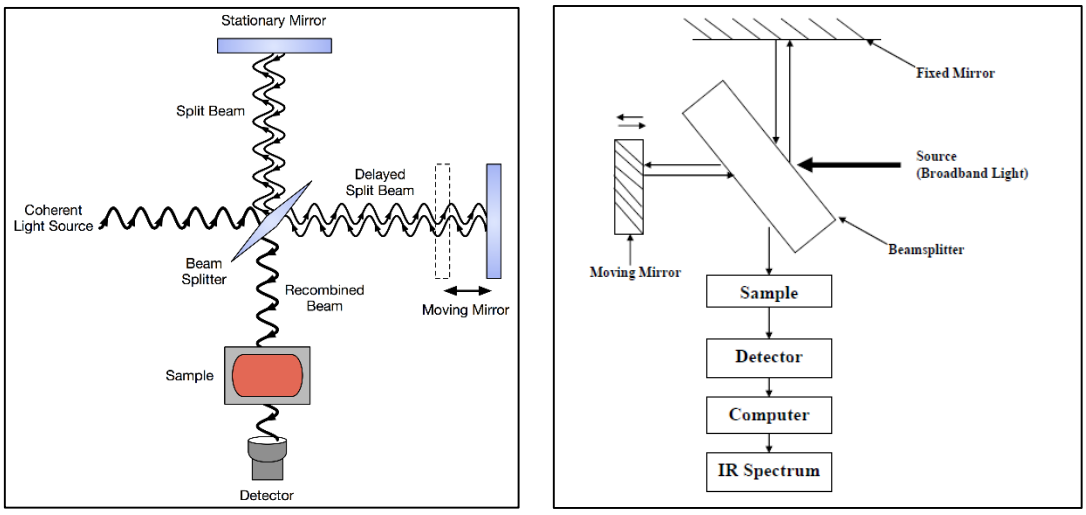

Figure 24. Schematic diagrams of the Michelson Interferometer [20].

An FTIR spectrometer simultaneously collects spectral data in a wide spectral range. This confers a significant advantage over a dispersive spectrometer which measures intensity over a narrow range of wavelengths at a time.

The spectra were obtained on an Agilent® Cary 630 FTIR device, using an ATR (attenuated total reflectance) accessory (shown in Figure 25). The samples were analysed through direct comparison of height and area peaks between the spectra of the samples. All the spectra shown in this work are taken directly from the device's software without any smoothing or peak normalizing treatment.

Figure 25. Agilent® Cary 630 FTIR with an ATR accessory.

6. Power Loss, Loads and Kinematic in a Planetary Gearbox

A detailed analysis, done with the KISSsoft software, of the planetary gearbox load, kinematics and performance is presented in Appendix D.

6.1. Load analysis

The calculation of the load dependant power loss requires the calculation of the loads acting on the contacting components. Thus the analysis of such calculation procedure for a planetary gearbox is presented on the following paragraphs.

The following simplifications were made: forces of inertia, moments of inertia and gravity forces were neglected.

A planetary gear train with a single degree of freedom is schematically represented in Figure 26.

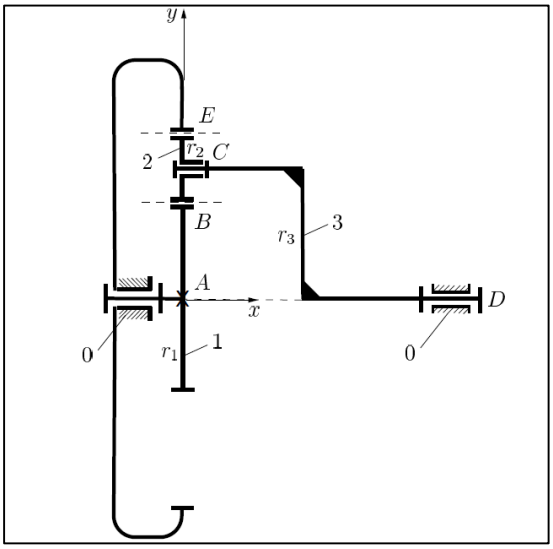

Figure 26. Planetary gear train (single degree of freedom).

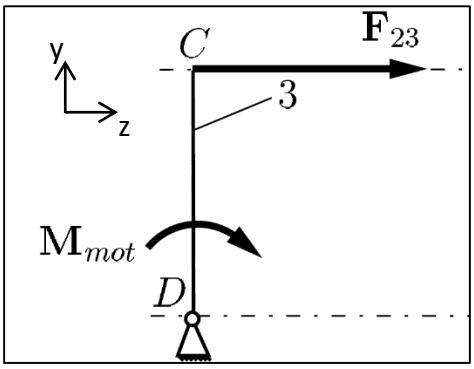

Figure 27. Free body diagram of the planet carrier.

The free body diagram of the planet carrier is shown in Figure 27 (With the torque input being through the planet carrier).

The load F_{23} is therefore calculated according to Equation 6.2.

$$\Sigma M_D = 0 \Leftrightarrow \qquad \text{Equation 6.1}$$

$$\Leftrightarrow F_{23} = \frac{\left(\frac{M_{mot}}{N}\right)}{a} \qquad \text{Equation 6.2}$$

Where *N* is the number of planets of the gearbox and *a* is the centre distance. In a planetary gearbox the working centre distance, *a*, is the same for the sun/planet gears and planet/ring gears.

The free body diagram of the planets is represented in Figure 28.

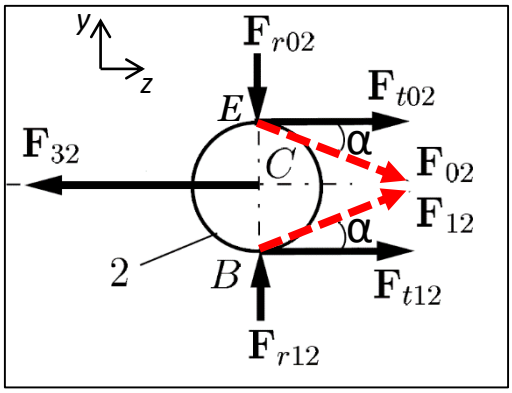

Figure 28. Free body diagram of a planet.

So, on the planet gear one can write the following force equation (Equation 6.3).

$$\Sigma\vec{F} = \overrightarrow{F_{32}} + \overrightarrow{F_{12}} + \overrightarrow{F_{02}} \qquad \text{Equation 6.3}$$

Where:

$$\overrightarrow{F_{12}} = \overrightarrow{F_{t12}} + \overrightarrow{F_{r12}} \qquad \text{Equation 6.4}$$

$$\overrightarrow{F_{12}} = \overrightarrow{F_{t02}} + \overrightarrow{F_{r02}} \qquad \text{Equation 6.5}$$

On the *Cy* axis one can write that:

$$\Sigma F_y = 0 \iff \qquad \text{Equation 6.6}$$

$$\iff F_{r02} = F_{r12} \qquad \text{Equation 6.7}$$

And on the *Cz* axis:

$$\Sigma F_z = 0 \iff \qquad \text{Equation 6.8}$$

$$\iff F_{32} = F_{t02} + F_{t12} \qquad \text{Equation 6.9}$$

So:

$$F_{t02} = F_{t12} = -\frac{F_{32}}{2} \qquad \text{Equation 6.10}$$

And:

$$|F_{r02}| = |F_{r12}| = |F_{t12} \cdot \tan(\alpha_t)| \qquad \text{Equation 6.11}$$

The free body diagram of the sun is represented in Figure 29.

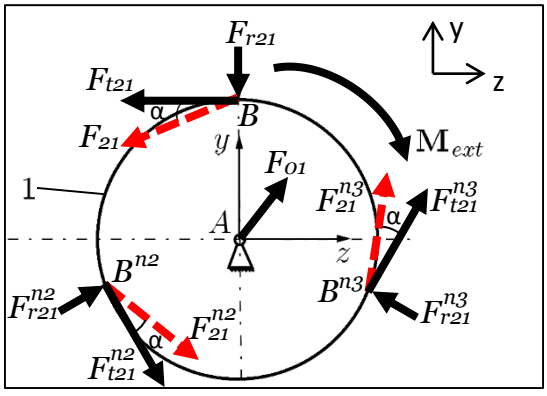

Figure 29. Free body diagram of the sun.

So the moment equation regarding *A* is:

$$\Sigma\overrightarrow{M_A} = \overline{AB^{n2}} \cdot \overrightarrow{F_{21}^{n2}} + \overline{AB^{n3}} \cdot \overrightarrow{F_{21}^{n3}} + \overline{AB} \cdot \overrightarrow{F_{21}} + \overrightarrow{M_{ext}} = \vec{0} \quad \text{Equation 6.12}$$

So,

Since: $$|F_{t21}| = |F_{t21}^{n2}| = |F_{t21}^{n3}| \quad \text{Equation 6.13}$$

And: $$\overline{AB} = \overline{AB^{n2}} = \overline{AB^{n3}} \quad \text{Equation 6.14}$$

Then: $$M_{ext} = 3 \cdot F_{t21} \cdot \left(\frac{d_{sun}}{2}\right) \quad \text{Equation 6.15}$$

The radial forces are equal (Equation 6.16) and due to their spatial position they will cancel each other out.

$$|F_{r21}| = |F_{r21}^{n2}| = |F_{r21}^{n3}| \quad \text{Equation 6.16}$$

The reaction force can be obtained using the force equation of the sun:

$$\Sigma\vec{F} = \overrightarrow{F_{21}} + \overrightarrow{F_{21}^{n2}} + \overrightarrow{F_{21}^{n3}} + \overrightarrow{F_{01}} = \vec{0} \quad \text{Equation 6.17}$$

On the *0z* axis $$F_{01z} - F_{t21} + \overrightarrow{F_{t21}^{n2}} \cdot \sin(30) + \overrightarrow{F_{t21}^{n3}} \cdot \sin(30) = 0 \quad \text{Equation 6.18}$$

$$F_{01z} = 0 \quad \text{Equation 6.19}$$

On the *0y* axis $$F_{01y} - \overrightarrow{F_{t21}^{n2}} \cdot \cos(30) + \overrightarrow{F_{t21}^{n3}} \cdot \cos(30) = 0 \quad \text{Equation 6.20}$$

$$F_{01y} = 0 \quad \text{Equation 6.21}$$

The axial forces can be obtained using the following equations:

$$F_{a02} = F_{t02} \cdot \tan(\beta) \quad \text{Equation 6.22}$$

$$F_{a12} = F_{t12} \cdot \tan(\beta) \quad \text{Equation 6.23}$$

An example of results for the forces is given in Table 7 considering a 10 rad/s ($\approx 100rpm$) speed input and 1000 Nm torque input. The input is considered to be in the planet carrier.

Table 7. Example for 10 rad/s and 1000 Nm (Forces).

	Variables	Results
Tangential force [N]	$F_{t21}, F_{t21}^{n2}, F_{t21}^{n3}, F_{t02}$	2279.648
Axial force [N]	F_{a02}, F_{a12}	402.000
Radial force [N]	$F_{r21}, F_{r21}^{n2}, F_{r21}^{n3}, F_{r02}$	842.524

6.2. Kinematic analysis

The calculation of the rolling bearings, seals and gears power loss requires the calculation of the speeds of each component of the gearbox. In the following paragraphs a method for the calculation of these speeds is proposed.

The angular speed of tooth engagement is the gear speed that would be obtained if the carrier was stationary. In this configuration the sun/planet speed was the sun gear absolute speed less the carrier speed. The planet/ring mesh speed was found by setting the ring speed equal to the negative of the carrier speed [21].

The kinematic diagrams of the planet carrier, planet and internal ring gear set and of the sun, planet and internal ring gear set are shown in Figure 30 and to help understand the kinematic relationship inside the planetary gearbox.

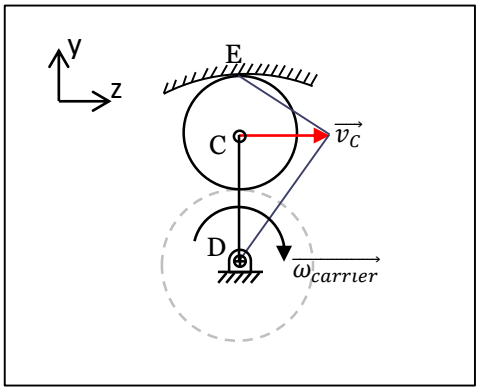

Figure 30. Kinematic diagram of the planet carrier, planet and internal ring gear set.

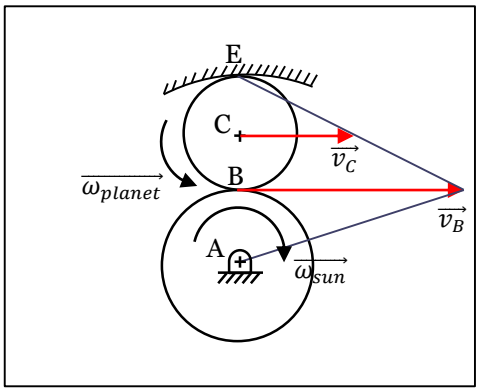

Figure 31. Kinematic diagram of the sun, planet and internal ring gear set.

To calculate the gear ratio Equation 6.24 through Equation 6.35 were used.

$$\overrightarrow{v_C} = \overrightarrow{\omega_{carrier}} \cdot \overline{DC} = \begin{Bmatrix} \omega_{carrier} \\ 0 \\ 0 \end{Bmatrix} \cdot \begin{Bmatrix} 0 \\ a \\ 0 \end{Bmatrix} = \begin{Bmatrix} 0 \\ 0 \\ \omega_{carrier} \cdot a \end{Bmatrix} \qquad \text{Equation 6.24}$$

Since the sliding speed between the planet and the ring is equal to zero the tangential speed $\overrightarrow{v_C}$ can also be calculated using Equation 6.25.

$$\overrightarrow{v_C} = \overrightarrow{\omega_{planet}} \cdot \overline{EC} = \begin{Bmatrix} \omega_{planet} \\ 0 \\ 0 \end{Bmatrix} \cdot \begin{Bmatrix} 0 \\ -\frac{d_{planet}}{2} \\ 0 \end{Bmatrix} = \begin{Bmatrix} 0 \\ 0 \\ -\omega_{planet} \cdot \frac{d_{planet}}{2} \end{Bmatrix} \qquad \text{Equation 6.25}$$

The tangential speed in B, $\overrightarrow{v_B}$, can be calculated using Equation 6.26.

$$\overrightarrow{v_B} = \overrightarrow{\omega_{planet}} \cdot \overline{EB} = \begin{Bmatrix} \omega_{planet} \\ 0 \\ 0 \end{Bmatrix} \cdot \begin{Bmatrix} 0 \\ -d_{planet} \\ 0 \end{Bmatrix} = \begin{Bmatrix} -\omega_{planet} \cdot d_{planet} \\ 0 \\ 0 \end{Bmatrix} \qquad \text{Equation 6.26}$$

And it can also be calculated by using Equation 6.27.

$$\overrightarrow{v_B} = \overrightarrow{\omega_{sun}} \cdot \overline{AB} = \begin{Bmatrix} \omega_{sun} \\ 0 \\ 0 \end{Bmatrix} \cdot \begin{Bmatrix} 0 \\ \frac{d_{sun}}{2} \\ 0 \end{Bmatrix} = \begin{Bmatrix} \omega_{sun} \cdot \frac{d_{sun}}{2} \\ 0 \\ 0 \end{Bmatrix} \qquad \text{Equation 6.27}$$

So, by matching Equation 6.24 with Equation 6.25, Equation 6.28 is obtained.

$$-\omega_{planet} \cdot \frac{d_{planet}}{2} = \omega_{carrier} \cdot a \qquad \text{Equation 6.28}$$

And by matching Equation 6.26 with Equation 6.27, Equation 6.29 is obtained.

$$-\omega_{planet} \cdot d_{planet} = \omega_{sun} \cdot \frac{d_{sun}}{2} \qquad \text{Equation 6.29}$$

Finally by matching Equation 6.28 with Equation 6.29 it's possible to relate the rotational speed of the planet carrier with the rotational speed of the sun thus finding the gear ratio (Equation 6.30 to Equation 6.35).

$$\omega_{carrier} \cdot a \cdot 2 = \omega_{sun} \cdot \frac{d_{sun}}{2} \qquad \text{Equation 6.30}$$

The diameter of the sun and of the planet and the centre distance have the relationship shown in Equation 6.31 and Equation 6.32.

$$d_{sun} = \frac{Z_{sun} \cdot m}{2} \qquad \text{Equation 6.31}$$

$$a = \frac{\left(Z_{planet} + Z_{sun}\right) \cdot m}{2} \qquad \text{Equation 6.32}$$

It's also known that the number of teeth between the sun, planet and ring are related as shown in Equation 6.33.

$$d_{planet} + \frac{d_{sun}}{2} = \frac{d_{ring}}{2} \Leftrightarrow$$

$$\Leftrightarrow Z_{planet} \cdot m + \frac{Z_{sun} \cdot m}{2} = \frac{Z_{ring} \cdot m}{2}$$

$$\Leftrightarrow Z_{planet} = \frac{Z_{ring}}{2} - \frac{Z_{sun}}{2} \qquad \text{Equation 6.33}$$

It's possible to transform Equation 6.30 using Equation 6.31 and Equation 6.32 so that the gear ratio only becomes dependent upon the number of teeth of the inner ring (the number of teeth of the inner ring is considered to be positive in these calculations) and the sun (Equation 6.34).

$$\omega_{sun} = \omega_{carrier} \cdot \frac{\left(Z_{planet} + Z_{sun}\right) \cdot m}{2} \cdot 2 \cdot \left(\frac{2}{Z_{sun} \cdot m}\right) \Leftrightarrow$$

$$\Leftrightarrow \omega_{sun} = \omega_{carrier} \cdot 2 \cdot \left(1 + \frac{Z_{planet}}{Z_{sun}}\right)$$

$$\Leftrightarrow \omega_{sun} = \omega_{carrier} \cdot \left(1 + \frac{Z_{ring}}{Z_{sun}}\right) \qquad \text{Equation 6.34}$$

So the gear ratio, *u*, is calculated according to Equation 6.35.

$$u = 1 + \frac{Z_{ring}}{Z_{sun}}$$ Equation 6.35

The gear ratio can also be written as a function of the number of teeth of planet and the sun according to Equation 6.36.

$$u = 2 + \frac{2 \cdot Z_{planet}}{Z_{sun}}$$ Equation 6.36

An example of results for the forces is given in Table 8 considering a 10 rad/s ($\approx 100rpm$) speed input and 1000 Nm torque input. The input is considered to be in the planet carrier.

Table 8. Example for 100rpm and 1000 Nm (Gear ratio).

	Variables	Results
Gear ratio [/]	u	4
Angular speed of the carrier [rpm]	$\omega_{carrier}$	100
Angular speed of the planet [rpm]	ω_{planet}	-200
Angular speed of the sun [rpm]	ω_{sun}	400

6.3. Introduction to the power loss in a gearbox

The total sum of power loss in a gearbox is the sum of the power loss generated by each component, so it essentially consists of power loss of the gears, bearings, seals and auxiliary losses. Gear and bearing losses have two components: load dependent losses that occur in the contact of the power transmitting components and no-load losses which are independent of torque transmission [22].

No-load losses, excluding operating conditions and internal housing design of the gearbox, are mostly related to lubricant viscosity and density as well as the immersion depth of the components of a sump lubricated gearbox [22].

Load losses are dependent upon transmitted torque, coefficient of friction and sliding velocity in the contact areas of the components [22].

Generally, for nominal power transmission, the load losses of the gear mesh are dominant. For high speeds and low or moderate loads, no-load losses can be the most important power loss source. No-load rolling bearing losses depend on the bearing type, size and arrangement, lubricant viscosity and immersion depth. Load dependent rolling bearing losses are dependent upon bearing type and size, rolling and sliding conditions in the bearing and upon lubricant type. The power loss in a gearbox can be calculated according to Equation 6.37.

$$P_V = P_{V\,Z0} + P_{V\,ZP} + P_{V\,L0} + P_{V\,LP} + P_{V\,D} \qquad \text{Equation 6.37}$$

The *Z*, *L* and *D* indexes refer to gears, bearings and seals, respectively. While the *0* and *P* indexes refer to no-load and load losses, respectively. In Equation 6.37 each variable (e.g. $P_{V\,D}$) takes into account the losses of its respective components.

6.4. Friction and film thickness between gear teeth

The coefficient of friction between the teeth of a gear is extremely important in the determination of the gear mesh power loss since it has a direct influence on the contact temperature, failure probability and efficiency, or in other words, the power loss of the gear [23].

The specific film thickness has a direct correlation with the coefficient of friction. This correlation is exemplified by the Stribeck curve which can be seen in Figure 32.

Knowing the specific film thickness is of major importance since it allows for a better assessment of the coefficient of friction.

According to Dowson and Higginson [24] the film thickness in a linear elastohydrodynamic contact, which is identical to the contact between gear teeth, can be represented as shown in Figure 33.

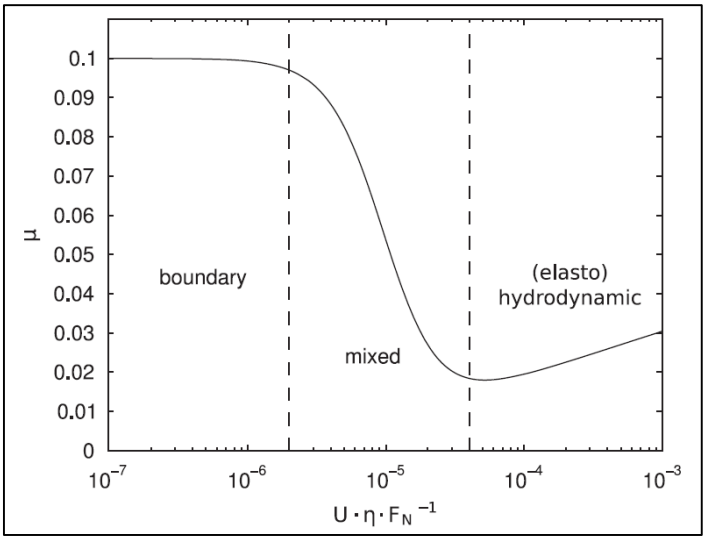

Figure 32. Example of a Stribeck curve [25].

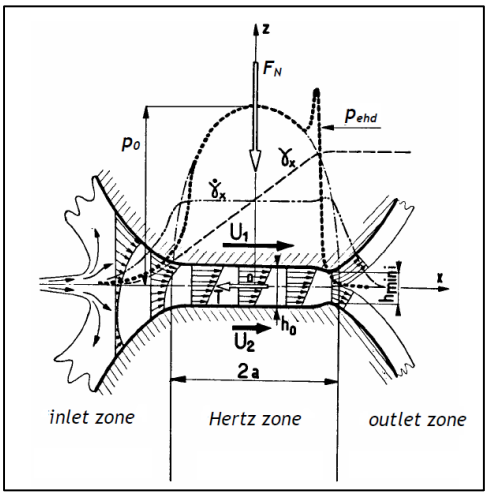

Figure 33. Linear elastohydrodynamic contact [26].

The film thickness depends on:

- Viscosity of the lubricant which in turn depends on the temperature;
- Rolling speed;
- Piezoviscosity coefficient;
- Equivalent radius;
- Normal load;
- Width of the gear.

Classic EHD theory was derived on the assumption that the lubricant flow inside the EHD contact is isothermal, in other words the lubricant temperature is constant. So, accordingly, the viscosity of the lubricant should only be affected by pressure because of its piezoviscous nature.

However, this hypothesis isn't valid for gears as a result of the existing high sliding along the contact line. In the inlet zone, the lubricating film suffers a high shear strain due to the pressure gradient and rolling and sliding velocity. The aforementioned shear strain causes inlet shear heating, which, in turn, causes a temperature rise in the lubricant, a decrease in viscosity and, consequently, a decrease in the lubricating film thickness.

In order to take this into account the previously determined film thickness is multiplied by a heating correction factor, ϕ_T, which depends on the lubricant's coefficient of thermoviscosity and thermal conductivity and on the surface's speed.

However, the EHD film thickness is not used directly, because, in reality, surfaces are not perfectly smooth. Instead, the specific film thickness, Λ, defined as the ratio between the EHD film thickness and the composite surface roughness of the rolling contacts, is used.

Three, typical, lubrication regimes which are dependent upon film thickness can be defined (as shown in Table 9).

Table 9. EHD lubrication regimes [27].

<table>
<tr><td colspan="3">EHD lubrication regimes</td></tr>
<tr><td></td><td>Regime</td><td>Observation</td></tr>
<tr><td>$\Lambda \geq 2.0$</td><td>Full film</td><td>The surfaces are completely separated by the lubricant film.</td></tr>
<tr><td colspan="3"> 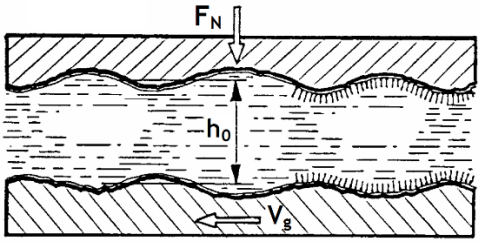
</td></tr>
<tr><td>$0.7 < \Lambda < 2.0$</td><td>Mixed film</td><td>The surfaces are partially separated by the lubricant film, there are some points where there is asperity contact.</td></tr>
<tr><td colspan="3"> 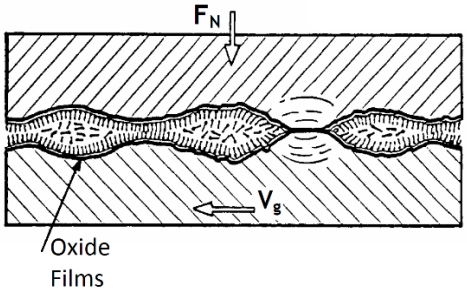
</td></tr>
<tr><td>$\Lambda \leq 0.7$</td><td>Boundary film</td><td>There is no lubricant film separating the surfaces, asperity contact dominates.</td></tr>
<tr><td colspan="3"> 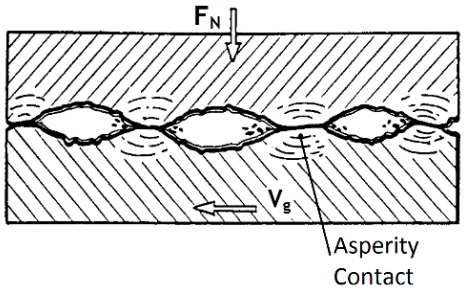
</td></tr>
</table>

The specific film thickness varies along the contact line in a gear mesh. So, several lubrication regimes can be observed along the contact line making the determination of the coefficient of friction a complex matter.

Film thickness:

The main parameters used in the calculation of the film thickness are calculated according to Equation 6.38 to Equation 6.45.

The speed parameter was calculated using Equation 6.38.

$$U = \frac{\eta_0 \cdot (U_1 + U_2)}{2 \cdot R_X \cdot E^*} \qquad \text{Equation 6.38}$$

Where:

- η_0 is the dynamic viscosity;
- $U_{1,2}$ is the velocity of each surface;
- R_X is the equivalent radius;
- E^* is the equivalent Young modulus.

The material parameter was calculated using Equation 6.39.

$$G = 2 \cdot \alpha \cdot E^* \qquad \text{Equation 6.39}$$

Where α is the piezoviscosity coefficient, and it was calculated according to Gold et al. [28]. Yet Gold et al.[28] did not test mineral and pama mixtures (MINE gear oil) but according to tests done by Marques et al. [18] and Fernandes et al. [29] these oils behave similarly to the PAOR gear oil. So the same piezoviscosity coefficients were used for both MINE and PAOR gear oils.

The load parameter was calculated using Equation 6.40.

$$W = \frac{F_n}{R_X \cdot \ell \cdot E^*} \qquad \text{Equation 6.40}$$

Where F_n is the normal force and ℓ is the average sum of contacting lines length on a helical gear, which was calculated according to Equation 6.41.

$$\ell = \frac{b \cdot \epsilon_\alpha}{\cos(\beta_b)} \qquad \text{Equation 6.41}$$

The thermal parameter of the lubricant was calculated using Equation 6.42.

$$L = \frac{\beta \cdot \eta_0 \cdot (U_1 + U_2)^2}{K} \qquad \text{Equation 6.42}$$

Where β is the thermoviscosity coefficient (*ASTM D341*) and *K* is the thermal conductivity.

The inlet shear heating influence was calculated using Equation 6.43.

$$\phi_T = (1 + 0.1 \cdot (1 + 14.8 \cdot V_e^{0.83}) \cdot L^{0.64})^{-1} \qquad \text{Equation 6.43}$$

The centre film thickness in the contact centre was calculated using Equation 6.44.

$$h_0 = 0.975 \cdot R_X \cdot U^{0.727} \cdot G^{0.727} \cdot W^{-0.091} \qquad \text{Equation 6.44}$$

Lastly the corrected film thickness was calculated using Equation 6.45.

$$h_{0T} = h_0 \cdot \phi_T \qquad \text{Equation 6.45}$$

There are several methods to calculate the coefficient of friction ($COF = \mu$) between gear teeth. The ones contemplated in this work are mentioned in the following paragraphs.

Coefficient of friction:

The ISO 6336 part 4 calculates the coefficient of friction using Equation 6.46 [30].

$$\mu_{ISO} = 0.0254 \cdot \left(\frac{F_n \cdot R_a}{\eta_0 \cdot l \cdot R_X \cdot (U_1 + U_2)}\right)^{0.25} \qquad \text{Equation 6.46}$$

Michaelis et al. [31] calculates the coefficient of friction using Equation 6.47.

$$\mu_{mich} = 0.0778 \cdot \left(\frac{F_n}{l \cdot R_X \cdot (U_1 + U_2)}\right)^{0.20} \cdot \left(\frac{1}{\eta_0}\right)^{0.05} \cdot R_a^{0.25} \qquad \text{Equation 6.47}$$

In Equation 6.46 and Equation 6.47 it's possible to observe that the formulation suggested by ISO 6336 part 4 is more sensitive to the dynamic viscosity than the formulation suggested by Michaelis et al..

The average sum of the contacting lines length, ℓ, in Equation 6.46 and Equation 6.47 was calculated according to Equation 6.41.

According to Höhn et al.[22] the coefficient of friction, μ_M, in a gear mesh consists of a portion of solid body friction, μ_F, and a portion of fluid film friction, μ_{EHD}:

$$\mu_M = (1 - \xi) \cdot \mu_F + \xi \cdot \mu_{EHD} \qquad \text{Equation 6.48}$$

Where:

- ξ is the portion of fluid film.

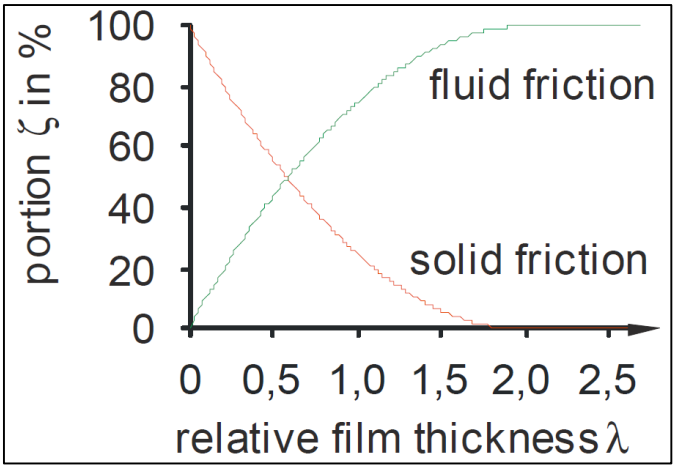

Figure 34. Fluid and solid friction in an EHD contact [22].

The portion ξ of fluid and solid friction depends on the specific film thickness in the contact (as shown in Figure 34).

And it can be determined using:

When $\Lambda < 2$ $$\xi = \Lambda - 0.25 \cdot \Lambda^2$$ Equation 6.49

When $\Lambda \geq 2$ $$\xi = 1$$ Equation 6.50

In order to determine the solid friction coefficient Equation 6.51 is used [22].

$$\mu_F = \mu_{F.R} \cdot \left(\frac{p_H}{P_R}\right)^{\alpha_F} \cdot \left(\frac{v_\Sigma}{v_{R,F}}\right)^{\beta_F}$$ Equation 6.51

Where:

- $\mu_{F,R}$ is a solid friction coefficient;
- p_H is the contact pressure [N/mm^2];
- p_R is a reference value of contact pressure;
- v_Σ is the sum velocity [m/s];
- $v_{R,F}$ is a reference value of speed for solid friction;
- α_F is a pressure exponent for solid friction from a test;
- β_F is a speed exponent for solid friction from a test.

The fluid friction coefficient can be calculated using Equation 6.52 [22].

$$\mu_{EHD} = \mu_{EHD,R} \cdot \left(\frac{p_H}{p_R}\right)^{\alpha_{EHD}} \cdot \left(\frac{v_\Sigma}{v_{R,EHD}}\right)^{\beta_{EHD}} \cdot \left(\frac{\eta_0}{\eta_R}\right)^{\gamma_{EHD}} \quad \text{Equation 6.52}$$

Where:

- μ_{EHD} is the fluid friction coefficient;
- $\mu_{EHD,R}$ is a reference value of the fluid friction coefficient;
- p_H is the contact pressure [N/mm^2];
- p_R is a reference value of contact pressure;
- v_Σ is the sum velocity [m/s];
- $v_{R,EHD}$ is a reference value of speed for fluid friction from a test;
- α_{EHD} is a pressure exponent for fluid friction from a test;
- β_{EHD} is a speed exponent for fluid friction from a test;
- γ_{EHD} is a viscosity exponent for fluid friction from a test.

6.5. Gear friction power loss

Höhn et al. [22] obtained the reference and exponent values for Mineral, polyalphaolefins and for polyglycol oils with the same viscosity grade, ISO VG320, with typical additive packages for wind turbine applications using the FZG-FVA efficiency test.

In order to ascertain the mesh power loss a gear loss factor, H_v (Equation 6.53), must be determined. This factor only depends on gear geometry and was obtained on the assumption that the coefficient of friction was constant along the line of action. Originally this factor was determined for gear pairs with transverse contact ratios up to 2. A more generalist version of the loss factor for various transverse contact ratios is available [32].

$$H_v = \frac{\pi \cdot (u+1)}{z_1 \cdot u \cdot \cos(\beta_b)} \cdot (a_0 + a_1 \cdot |\varepsilon_1| + a_2 \cdot |\varepsilon_2| + a_3 \cdot |\varepsilon_1| \cdot \varepsilon_1 + a_4 \cdot |\varepsilon_2| \cdot \varepsilon_2) \quad \text{Equation 6.53}$$

Where:

- H_v is the gear loss factor;
- u is the gear ratio;
- Z_1 is the number of teeth of the pinion;
- β_b is the helix angle at the base;
- ε_α is the profile contact ratio;
- $\varepsilon_{1,2}$ is the tip contact ratio, pinion and gear;
- $a_{0,1,2,3,4}$ is a coefficient that depends on the tip contact ratio.

The coefficients $a_{0,1,2,3,4}$ can be calculated using Table 10.

Table 10. General formulation of coefficients $a_{0,1,2,3,4}$ [32].

	Case 1: $\epsilon_\alpha < 1$	Case 2: $\epsilon_\alpha > 1$ $\epsilon_1 < 0$ V $\epsilon_2 < 0$	Case 3: $\epsilon_\alpha > 1$ $\epsilon_1, \epsilon_2 > 0$ $l_g + m_g = n_g$	Case 4: $\epsilon_\alpha > 1$ $\epsilon_1, \epsilon_2 > 0$ $l_g + m_g = n_g + 1$
a_0	0	0	$\frac{2 \cdot l_g \cdot m_g}{n_g}$	$\frac{2 \cdot (l_g \cdot m_g - n_g)}{n_g - 1}$
a_1	0	1	$\frac{l_g \cdot (l_g - 1) - m_g \cdot (m_g - 1) - 2 \cdot l_g \cdot m_g}{n \cdot (n-1)}$	$\frac{l_g \cdot (l_g - 1) - m_g \cdot (m_g - 1) - 2 \cdot (m_g - 1) \cdot n_g}{n \cdot (n-1)}$
a_2	0	1	$\frac{-l_g \cdot (l_g - 1) - m_g \cdot (m_g - 1) - 2 \cdot l_g \cdot m_g}{n_g \cdot (n_g - 1)}$	$\frac{l_g \cdot (l_g - 1) - m_g \cdot (m_g - 1) - 2 \cdot (l_g - 1) \cdot n_g}{n \cdot (n-1)}$
a_3	$1/\varepsilon_\alpha$	0	$\frac{2 \cdot m_g}{n_g \cdot (n_g - 1)}$	$\frac{2 \cdot (m_g - 1)}{n_g \cdot (n_g - 1)}$
a_4	$1/\varepsilon_\alpha$	0	$\frac{2 \cdot l_g}{n_g \cdot (n_g - 1)}$	$\frac{2 \cdot (l_g - 1)}{n_g \cdot (n_g - 1)}$

The parameters l_g, m_g and n_g can be determined using Equation 6.54 to Equation 6.56 with $l_g, m_g and\ n_g \in \mathbb{Z}$ [32].

$$\epsilon_1 \in \left[l_g - 1 : l_g\right] \quad \text{Equation 6.54}$$

$$\epsilon_2 \in \left[m_g - 1 : m_g\right] \quad \text{Equation 6.55}$$

$$\epsilon_\alpha \in \left[n_g - 1 : n_g\right] \quad \text{Equation 6.56}$$

So the gear mesh power loss depends on the transmitted power, the average coefficient of friction in the gear contact and a gear loss factor, H_v, as suggested in Equation 6.57.

$$P_{VZP} = P_a \cdot \mu_m \cdot H_v \quad \text{Equation 6.57}$$

Where:

- P_a is the transmitted power;
- μ_m is the mean coefficient of friction calculated according to Höhn et al. [22];
- H_v is a gear loss factor.

The transmitted power can be calculated using Equation 6.58.

$$P_a = F_N^{máx} \cdot \omega \cdot r_b \quad \text{Equation 6.58}$$

An example of results for gears power loss is given in Table 11 considering a 10 rad/s ($\approx 100rpm$) speed input and 1000 Nm torque input for the sun/planet contact for the MINR gear oil. The input is considered to be in the planet carrier.

Table 11. Example for 100rpm and 1000 Nm (Gear power loss – sun/planet contact).

	Variables	Results
Corrected film thickness [µm]	h_{0T}	0.566
Specific film thickness [/]	Λ	0.799
Transverse contact ratio [/]	ϵ_α	1.550
Tip contact ratio (pinion) [/]	ϵ_1	0.775
Tip contact ratio (gear) [/]	ϵ_2	0.775
Coefficient of the gear loss factor [/]	a_0	1
Coefficient of the gear loss factor [/]	a_1	-1
Coefficient of the gear loss factor [/]	a_2	-1
Coefficient of the gear loss factor [/]	a_3	1
Coefficient of the gear loss factor [/]	a_4	1
Gear loss factor [/]	H_v	0.1152
Normal force [N]	F_N^{max}	2463.4
Transmitted power [W]	P_a	2653.6
Coefficient of friction [/]	μ_M	0.0409
Gear mesh power loss [W]	P_{VZP}	12.5

The coefficient of friction used to calculate the gears power loss in this work is the one defined by Höhn et al. [22]. The other proposed methods for the calculation of the coefficient of friction were not showed in the example given in Table 11 since an analysis of their values is presented later in this work.

6.5.1. No-Load Power Loss

Several experimental and analytical studies by different authors, related to the no-load power loss in gears (churning losses), are available [33] [34] [35] [31] [36] [37] [38] [39].

Using gears with modules that ranged from 2 to 8 mm, Terekhov [33], studied the gear churning losses caused by high viscosity lubricants (200-2000 cSt) at low speeds. Lauster and Boos [34] studied gear churning losses in truck transmissions. Boness [35] studied churning losses of partially submerged rotating discs and gears in different fluids like water and oil. Höhn et al. [31] did an experimental study of no-load and load dependent gear power losses in cylindrical and bevel gears as a function of lubricant type and viscosity, load, speed and temperature, presenting a viscosity independent single flow regime model for the gear churning power losses in a pinion/wheel. Seetharaman et al. [36] suggested a physics-based fluid mechanics model that predicted spin power losses of gear pairs due to oil churning and

windage. Changenet et al. [37] deducted a set of equations that can calculate a dimensionless gear drag torque. These equations are directly influenced by the different flow regimes dependent upon a critical Reynolds number, which is related to the flow nature, and a centrifugal acceleration parameter, which in turn is related to fluid projection caused by the rotating gears. LePrince et al. [38] proposed a simplified model, based on surface tension and lubricant aeration, in order to quantify the influence of oil sump aeration on churning losses therefore reporting a relationship between lubricant aeration and gear churning power loss. Changenet et al. [39] shown that the internal housing geometry of a gearbox significantly influences the churning power loss.

None of the aforementioned studies encompass planetary gearboxes. The multitude of planetary gearbox designs coupled with complex fluid/geometry interactions may be the reason behind the lack of this type of models for planetary gearboxes.

A CFD (computer fluid dynamics) analysis could accurately predict churning power losses in the planetary gearbox studied in this work.

In an ideal simulation, in other words, a simulation with unlimited computational resources and numerical models with no limitations, every detail of the geometry and fluid/geometry interaction should be considered. However there are always limitations related with the computational resources and also with the models applied to the problem.

In a CFD analysis of a planetary gearbox the following fluid geometry interactions, which correspond to the churning power losses in a planetary gearbox, should be considered:

- Interaction of the rotating planet carrier with the oil sump;
- Interaction of the rotating sun with the oil sump (different rotational speed between the sun and the planet carrier);
- Interaction of the rotating planets with the oils sump considering two relative motions, one that considers the orbit of the planet relatively to the sun and the other one relative to its own rotation.
- Constant compression/expansion of volume due to the meshing gears (pocketing effects).

These phenomena occur simultaneously and there is a large possibility that they are simultaneously affected by each other, making the separate sum of each power loss different from the power loss obtained from their joint effect.

The no-load power loses will be analysed later together with the experimental results.

6.6. Rolling bearings power loss

The bearing power loss is directly related with the frictional moment in a rolling bearing and the rotational speed of the shaft (as shown in Equation 6.59).

$$P_{V\,L} = M \cdot n \cdot \frac{\pi}{30} \cdot 10^{-3} \qquad \text{Equation 6.59}$$

According to *SKF Rolling Bearings Catalogue 10000/1 EN* [40] the friction in a rolling bearing determines the amount of heat generated by the bearing. The amount of friction depends on the loads and several other factors, including: bearing type and size, operating speed and properties and volume of lubricant.

This resistance to rotation is, in a bearing, the result of rolling and sliding friction in the contact areas, between the rolling elements and raceways, between the rolling elements and cage, and between the rolling elements and other guiding surfaces. Friction can also be generated by lubricant drag and contact seals.

In order to determine the frictional moment of the bearings in question the SKF model for calculation of the frictional moment was used.

The total frictional moment, *M*, of a rolling bearing is calculated according to Equation 6.60 [40]:

$$M = M_{rr} + M_{sl} + M_{seal} + M_{drag} \qquad \text{Equation 6.60}$$

Where:

- M is the total frictional moment;
- M_{rr} is the rolling frictional moment;
- M_{sl} is the sliding frictional moment;
- M_{seal} is the frictional moment of seals;
- M_{drag} is the frictional moment of drag losses, churning, splashing etc.

6.6.1. Rolling frictional moment

The rolling frictional moment can be calculated using Equation 6.61 [40].

$$M_{rr} = \phi_{ish} \cdot \phi_{rs} \cdot G_{rr} \cdot (\nu \cdot n)^{0.6} \qquad \text{Equation 6.61}$$

Where:

- M_{rr} is the rolling frictional moment [N·mm];
- ϕ_{ish} is the inlet shear heating reduction factor;

- ϕ_{rs} is the kinematic replenishment/starvation reduction factor;
- G_{rr} is a variable that depends on the bearing type and mean diameter (d_m=0.5(d+D)) and on the radial and axial load;
- n is the rotational speed [rpm];
- v is the kinematic viscosity at operating temperature of the oil or the base oil viscosity of the grease [cSt].

For deep groove ball bearings, G_{rr} is determined using one of the following equations [40]:

When $F_a = 0$ $$G_{rr} = R_1 \cdot d_m^{1.96} \cdot F_r^{0.54}$$ Equation 6.62

When $F_a > 0$ $$G_{rr} = R_1 \cdot d_m^{1.96} \cdot \left(F_r + \frac{R_2}{\sin(\alpha_{FSKF})} \cdot F_a\right)^{0.54}$$ Equation 6.63

And for tapered roller bearings, Grr is determined using the following equation [40]:

$$G_{rr} = R_1 \cdot d_m^{2.38} \cdot (F_r + R_2 \cdot Y \cdot F_a)^{0.31}$$ Equation 6.64

Where:

- R_1 and R_2 are geometric constants for rolling frictional moment that depend on the type and series of a bearing;
- Y is the axial load factor for single row bearings;
- d_m is the mean diameter;
- F_r is the radial load;
- F_a is the axial load;
- $\alpha_{FSKF} = 24.6 \cdot \left(\frac{F_a}{C_0}\right)^{0.24}$.

6.6.2. Inlet shear heating reduction factor

Only a tiny amount of lubricant is used to form a hydrodynamic film. Therefore, some of the oil close to the contact area inlet is rejected and produces a reverse flow. This phenomenon is shown in Figure 35 [40].

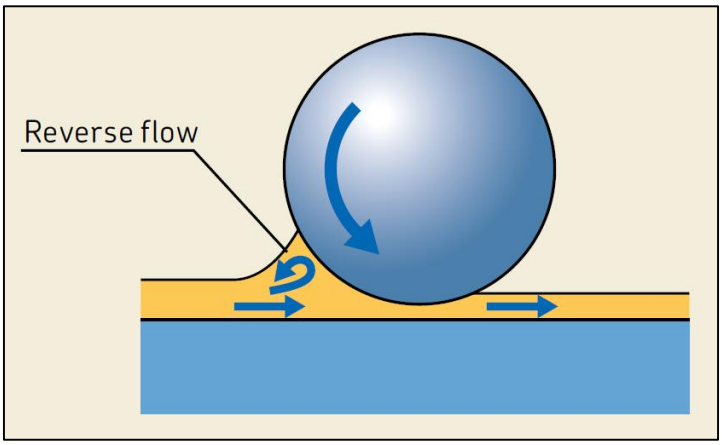

Figure 35. Reverse flow in a ball bearing [40].

This reverse flow shears the lubricant, generating heat, which lowers the oil viscosity and reduces the film thickness and rolling friction. For the effect described above, the inlet shear heating reduction factor can be estimated using Equation 6.65 [40].

$$\phi_{ish} = \frac{1}{1 + 1.84 \cdot 10^{-9} \cdot (n \cdot d_m)^{1.28} \cdot \nu^{0.64}} \qquad \text{Equation 6.65}$$

Where:

- ϕ_{ish} is the inlet shear heating reduction factor;
- n is the rotational speed [rpm];
- d_m is the bearing mean diameter [mm];
- v is the kinematic viscosity at operating temperature of the oil or the base oil viscosity of the grease [cSt].

6.6.3. Kinematic replenishment/starvation reduction factor

In applications where viscosity or speeds are high, the lubricant may not have sufficient time to replenish the raceways, causing a “kinematic starvation” effect. Kinematic starvation reduces the thickness of the hydrodynamic film and rolling friction [40].

For the type of lubrication methods described above, the kinematic replenishment/starvation reduction factor can be estimated using Equation 6.66 [40].

$$\phi_{rs} = \frac{1}{e^{\left[K_{rs} \cdot \nu \cdot (d+D) \cdot \sqrt{\frac{K_z}{2 \cdot (D-d)}}\right]}} \qquad \text{Equation 6.66}$$

Where:

- ϕ_{rs} is the kinematic replenishment/starvation reduction factor;
- K_{rs} is the replenishment/starvation constant: for low level oil bath and oil jet lubrication $K_{rs} = 3 \cdot 10^{-8}$, for grease and oil-air lubrication $K_{rs} = 6 \cdot 10^{-8}$;
- K_Z is a bearing type related geometric constant;
- v is the kinematic viscosity at operating temperature of the oils or the base oil viscosity of the grease [cSt];
- n is the rotational speed [rpm];
- d is the bearing bore diameter [mm];
- D is the bearing outside diameter [mm].

According to the online SKF bearing calculator [41], for a tapered roller bearing 32022 X/Q, Equation 6.66 is only valid if the oil level is below 7.525 [mm]. If this does not verify then ϕ_{rs} should be considered to be $\phi_{rs} = 1$.

6.6.4. Sliding frictional moment

The sliding frictional moment can be calculated using Equation 6.67 [40]:

$$M_{sl} = G_{sl} \cdot \mu_{sl} \qquad \text{Equation 6.67}$$

Where:

- M_{sl} is the sliding frictional moment [N·mm];
- G_{sl} is a variable that depends on the bearing type, the bearing mean diameter, the radial and axial load;
- μ_{sl} is the sliding friction coefficient.

For deep groove ball bearings one of the following equations can be used to calculate G_{sl} [40].

When $F_a = 0$

$$G_{sl} = S_1 \cdot d_m^{-0.26} \cdot F_r^{\frac{5}{3}} \qquad \text{Equation 6.68}$$

When $F_a > 0$

$$G_{sl} = S_1 \cdot d_m^{-0.145} \cdot \left(F_r^5 + \frac{S_2 \cdot d_m^{1.5}}{\sin(\alpha_F)} \cdot F_a^4\right)^{\frac{1}{3}} \qquad \text{Equation 6.69}$$

And for tapered roller bearings, G_{sl} is determined by using Equation 6.70 [40].

$$G_{sl} = S_1 \cdot d_m^{0.82} \cdot (F_r + S_2 \cdot Y \cdot F_a) \qquad \text{Equation 6.70}$$

Where:

- S1 and S2 are geometric constants for sliding frictional moments.

The sliding friction coefficient for full-film and mixed lubrication conditions can be estimated using Equation 6.71 [40].

$$\mu_{sl} = \phi_{bl} \cdot \mu_{bl} + (1 - \phi_{bl}) \cdot \mu_{EHL} \qquad \text{Equation 6.71}$$

Where:

- μ_{sl} is the sliding friction coefficient;
- n is the rotational speed [rpm];
- v is the viscosity at operating temperature of the oil or the base oil viscosity of the grease [cSt];
- d_m is the bearing mean diameter [mm];
- μ_{bl} is a coefficient that depends on the additive package in the lubricant, generally =0.15.

The weighting factor for the sliding friction coefficient, ϕ_{bl}, can be calculated using Equation 6.72 [40].

$$\phi_{bl} = 1/(e^{2.6 \cdot 10^{-8} \cdot (v \cdot n)^{1.4} \cdot d_m}) \qquad \text{Equation 6.72}$$

Usual values for the sliding friction coefficient in full-film conditions, μ_{EHL}, are:

- 0.02 for cylindrical roller bearings;
- 0.002 for tapered roller bearings;
- For other bearings:
    - 0.05 for lubrication with mineral oils;
    - 0.04 for lubrication with synthetic oils.

6.6.5. Drag losses

The drag losses that occur when the bearing is rotating in an oil bath contribute to the total frictional moment and should not be neglected. These are not only influenced by bearing speed, oil viscosity and oil level, but also by the size and geometry of the oil reservoir. External oil agitation, which can originate from mechanical elements, like gears or cams, in close proximity to the bearing should also be taken into consideration.

The SKF model for calculating the drag losses in oil bath lubrication considers resistance of the rolling elements when moving through the oil and includes the effects of the viscosity of the oil. The oil level *H* is measured from the lowest contact point between the outer ring raceway and the rolling element (as shown in Figure 36).

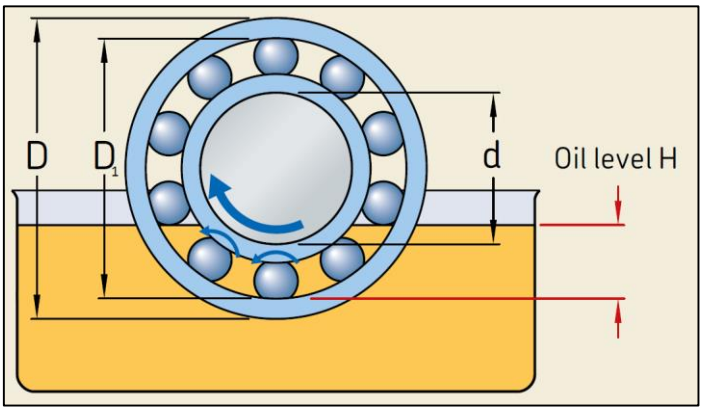

Figure 36. Oil level H measurement [40].

For tapered roller bearing the lowest point should be the outside diameter D and for all other rolling bearings, the outer ring mean diameter (=0.5*(D+D_1)).

The frictional moment of drag losses for ball bearings can be estimated using Equation 6.73 [40].

$$M_{drag} = 0.4 \cdot V_M \cdot K_{ball} \cdot d_m^5 \cdot n^2 + 1.093 \cdot 10^{-7} \cdot n^2 \cdot d_m^3 \cdot \left(\frac{n \cdot d_m^2 \cdot f_t}{\nu}\right)^{-1.379} \cdot R_s \quad \text{Equation 6.73}$$

And the frictional moment of drag losses for roller bearings can be estimated using Equation 6.74 [40].

$$M_{drag} = 4 \cdot V_M \cdot K_{rol} \cdot C_W \cdot B \cdot d_m^4 \cdot n^2 + 1.093 \cdot 10^{-7} \cdot n^2 \cdot d_m^3 \cdot \left(\frac{n \cdot d_m^2 \cdot f_t}{\nu}\right)^{-1.379} \cdot R_s \quad \text{Equation 6.74}$$

The rolling element related constant is, for ball bearings, calculated according to Equation 6.75 [40].

$$K_{ball} = \frac{i_{rw} \cdot K_Z \cdot (d + D)}{D - d} \cdot 10^{-12} \quad \text{Equation 6.75}$$

And for roller bearings:

$$K_{roll} = \frac{K_L \cdot K_Z \cdot (d + D)}{D - d} \cdot 10^{-12} \quad \text{Equation 6.76}$$

The rest of the variables and functions used in the equations for the frictional moment of drag losses are stated in Equation 6.77 to Equation 6.82 [40].

$$C_W = 2.789 \cdot 10^{-10} \cdot l_D^3 - 2.786 \cdot 10^{-4} \cdot l_D^2 + 0.0195 \cdot l_D + 0.6439 \quad \text{Equation 6.77}$$

$$l_D = 5 \cdot \frac{K_L \cdot B}{d_m}$$ Equation 6.78

$$f_t = \begin{cases} \sin(0.5 \cdot t), when\ 0 \le t \le \pi \\ 1, when\ \pi < t\ < 2 \cdot \pi \end{cases}$$ Equation 6.79

$$R_s = 0.36 \cdot d_m^2 \cdot (t - \sin(t)) \cdot f_A$$ Equation 6.80

When H ≥d_m, use H=d_m

$$t = 2 \cdot \cos^{-1}\left(\frac{0.6 \cdot d_m - H}{0.6 \cdot d_m}\right)$$ Equation 6.81

$$f_A = 0.05 \cdot \frac{K_Z \cdot (D + d)}{D - d}$$ Equation 6.82

Where:

- M_{drag} is the frictional moment of drag losses [N·mm];
- V_M is the drag loss factor;
- B is the bearing width [mm]:
  - For tapered roller bearings use T;
  - For Thrust bearings use H;
- d_m is the bearing mean diameter [mm];
- d is the bearing bore diameter [mm];
- D is the bearing outside diameter [mm];
- H is the oil level [mm];
- i_{rw} is the number of ball rows
- K_Z is a bearing type related geometric constant;
- K_L is a rolling bearing type related geometric constant;
- n is the rotational speed [rpm];
- v is the kinematic viscosity at operating.

The drag loss factor can be determined using Figure 37.

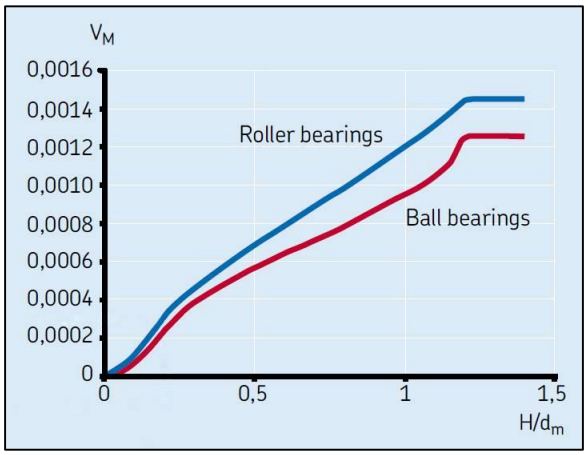

Figure 37. Drag loss factor graph for roller and ball bearings [40].

6.6.6. Preload

The calculated axial and radial forces acting in the tapered roller bearings took into consideration the preload force.

Figure 38 shows an example of an arrangement for two tapered roller bearings. The case shown in Figure 38 consists of two different size tapered roller bearings, A and B, with different spring constants c_A and c_B. However in the case studied in this work the bearings in question have the same size.

Both bearings are usually subjected to a preload force F_0. If the bearings had not been preloaded, in the case of an axial force K_a acting on bearing A, bearing B would become unloaded, and the additional load acting on bearing A would result in an axial displacement δ_a, smaller than it would be if the bearings had not been preloaded.

To prevent bearing B from becoming unloaded when bearing A is subjected to an axial force K_a, the preload force calculated in Equation 6.83 is required.

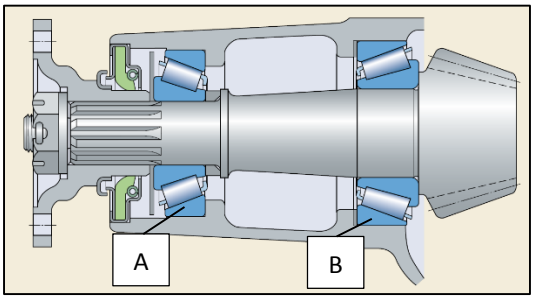

Figure 38. Example of an arrangement for two tapered roller bearings.

$$F_0 = K_a \cdot \left(\frac{c_B}{c_A + c_B}\right)$$ Equation 6.83

In the studied gearbox the tapered bearings were considered to be equal. Therefore the spring constants c_A and c_B were equal turning Equation 6.83 into Equation 6.84.

$$F_0 = \frac{1}{2} \cdot K_a$$ Equation 6.84

The value of K_a is the sum of a value determined based on the Wittenstein catalogue [19] for the maximum axial force allowed on the output shaft and the axial force caused by the maximum input torque for each test.

An example of results for the tapered roller bearing (TPRB) and deep groove ball bearing (DGBB) power loss is given in Table 12 Table 11considering a 10 rad/s ($\approx 100rpm$) speed input and 1000 Nm torque input for the MINR gear oil. The input is considered to be in the planet carrier.

Table 12. Example for 100 rpm and 1000 Nm (TPRB and DGBB power loss).

	Variables	Results	
		TPRB	DGBB
Preload [N]	F_0	16×10^3	
Inlet shear heating reduction factor [/]	ϕ_{ish}	0.9889	0.9745
Kinematic replenishment/starvation reduction factor [/]	ϕ_{rs}	1	0.9427
Variable of the rolling frictional moment [/]	G_{rr}	14.599	0.7335
Rolling frictional moment [N·m]	M_{rr}	5.578	0.308
Variable of the sliding frictional moment [N·m]	G_{sl}	41.8635	1.3623
Sliding friction coefficient [/]	μ_{sl}	0.0048	0.0507
Weighting factor for the sliding coefficient [/]	ϕ_{bl}	0.0191	0.0073
Sliding frictional moment [N·m]	M_{sl}	0.202	0.069
Frictional moment of drag losses [N·m]	M_{drag}	0.209	0*
Total frictional moment [N·m]	M	5.990	0.377

For grease lubricated rolling bearings the *SKF* model considers $M_{drag} = 0$ which is the case for the deep groove ball bearing of the test gearbox.

6.7. Needle roller bearings power loss

The frictional moment of a needle roller bearing (Equation 6.85) was calculated by using the SKF Needle roller bearing Catalogue [42] and the Höhn et al. [31] model based also on Eschmann et al. [43].

$$T_{VL} = T_{VL0} + T_{VLP1} + T_{VLP2} \quad \text{Equation 6.85}$$

The no-load component, T_{VL0}, can be calculated using Equation 6.86 or Equation 6.87.

When $\nu \cdot n < 2000$ $$T_{VL0} = 1.6 \cdot 10^{-8} \cdot f_0 \cdot \mathrm{d_m^3} \quad \text{Equation 6.86}$$

When $\nu \cdot n \geq 2000$ $$T_{VL0} = 10^{-10} \cdot f_0 \cdot (\nu \cdot n)^{\frac{2}{3}} \cdot \mathrm{d_m^3} \quad \text{Equation 6.87}$$

Where:

- T_{VL0} is the no-load frictional moment [N·m];
- f_0 is a coefficient that depends on the bearing design and lubrication method ($f_0 = 12$);
- ν is the kinematic viscosity of the oil [mm^2/s];
- n is the rotational speed [rpm]
- d_m is the bearing mean diameter [mm].

The load component, T_{VLP1}, can be calculated using Equation 6.88 [31].

$$T_{VLP1} = 10^{-3} \cdot f_1 \cdot P_1 \cdot d_m \quad \text{Equation 6.88}$$

Where:

- P_1 is the equivalent bearing load;
- f_1 is a coefficient taking into account the direction of load application (f_1=0.002).

And the load component can be calculated using Equation 6.89.

$$T_{VLP2} = f_2 \cdot F_a \cdot d_m \cdot 10^{-3} \quad \text{Equation 6.89}$$

An example of results for the needle roller bearing power loss is given in Table 13 considering a 10 rad/s ($\approx 100rpm$) speed input and 1000 Nm torque input for the MINR gear oil. The input is considered to be in the planet carrier.

Table 13. Example for 100 rpm and 1000 Nm (Needle bearing power loss).

	Variables	Results
No-Load component of the frictional moment [N·m]	T_{VL0}	0.1593
Load component of the frictional moment [N·m]	T_{VLP1}	0.4197
Load component of the frictional moment [N·m]	T_{VLP2}	0
Total needle bearing torque loss [N·m]	T_{VL}	0.5790

6.8. Seals power loss

Seal power losses represent, in most applications, a very small fraction of the nominal transmitted power and are almost negligible compared to other losses in a gear drive. Nonetheless an approximation is given in Equation 6.90 [31].

$$P_{V\,D} = 7.69 \times 10^{-6} \times d_{sh}^2 \times n \qquad \text{Equation 6.90}$$

Where:

- d_{sh} is the shaft diameter [mm];
- n is the rotational speed of the shaft [rpm].

The seal power loss is independent of the transmitted power and can therefore be more relevant in the regime of partial power transmission. Different seal materials can also influence the value of P_{VD} [31].

An example of results for the needle roller bearing power loss is given in Table 14 Table 11considering a 10 rad/s ($\approx 100\ rpm$) speed input and 1000 Nm torque input for the MINR gear oil. The input is considered to be in the planet carrier.

Table 14. Example for 100 rpm and 1000 Nm (Seal power loss)

	Variables	Results
Seal power loss [W]	T_{VL0}	0.1593

6.9. Heat balance

When the thermal equilibrium is reached, according to thermodynamic laws, the heat dissipation through the gearbox must be equal to the sum of the power losses produced in the gearbox.

The energetic equilibrium of a gear transmission results from the sum of the energy flux that occurs in the transmission. The balance of the energetic fluxes lead to the thermal stabilization of the system:

$$P_V = \dot{Q}_{total} \quad \text{Equation 6.91}$$

And:

$$\dot{Q}_{total} = \dot{Q}_{rad} + \dot{Q}_{cv} + \dot{Q}_{cd} \quad \text{Equation 6.92}$$

Where:

- $\dot{Q}_{rad}$ is the heat flow rate due to radiation;
- $\dot{Q}_{cv}$ is the heat flow rate due to convection;
- $\dot{Q}_{cd}$ is the heat flow rate due to conduction.

These are the predominant heat transfer mechanisms of an oil bath lubricated gearbox. Convection and radiation heat transfer happens through the external surface of the housing of the gearbox. While a small part of the heat is transferred through the shafts, couplings and foundations due to thermal conduction.

According to Höhn et al. [31] measurements of temperature distribution over the gear housing showed that even for different applications there's only a small variation of temperature occurring. This variation is within a range of about 5 °C. Yet this is only valid for cases where the gear drives are splash lubricated with an adequate oil quantity. Since for gear drives with a low oil volume the generated heat in the gear mesh and the bearings cannot uniformly be distributed to the inner walls of the housing causing, in some cases, hot spots to occur. So the average temperature of the housing can be used in further calculations guarantying that there will not be significant errors. Also because the difference between the housing and the oil temperature is very small the heat flow rate can be written as a function of the oil temperature.

In many applications of stationary gear drives the heat transmission can be approximated only by the external heat transfer as the governing portion [31]. Yet for cases where there is external forced convection with high air speeds the internal heat transfer has to be taken into account [31].

So the total heat flow rate, as suggested by Höhn et al. [31], can be calculated as it is showed in Equation 6.93.

$$\dot{Q}_{total} = \alpha_{Heat} \cdot A \cdot (T_{oil} - T_{room}) \qquad \text{Equation 6.93}$$

Where:

- α_{Heat} is the heat transfer coefficient (which takes into consideration the radiation and convection heat transfer coefficients);
- A is the external area of the gearbox housing;
- T_{oil} is the oil temperature;
- T_{room} is the ambient room temperature.

There were no changes made to the components of the gearbox except for the lubricating oil that was, as it was previously mentioned, changed for each series of tests, so the heat transfer coefficient could be found using the values of the stabilized operating temperatures, $\Delta T = T_{oil} - T_{room}$, which were measured during the tests. Therefore $\Delta T = T_{oil} - T_{room}$ can also be taken as an indication of the power loss in the gearbox.

By way of example, the values of $\alpha \cdot A$, in this application, ranged from 10 to 16 W/m°C.

7. Experimental and numerical results

7.1. Comparison between before and after running-in

The stabilized operating temperature of the MINR oil test during running-in and in normal conditions are compared in Figure 39.

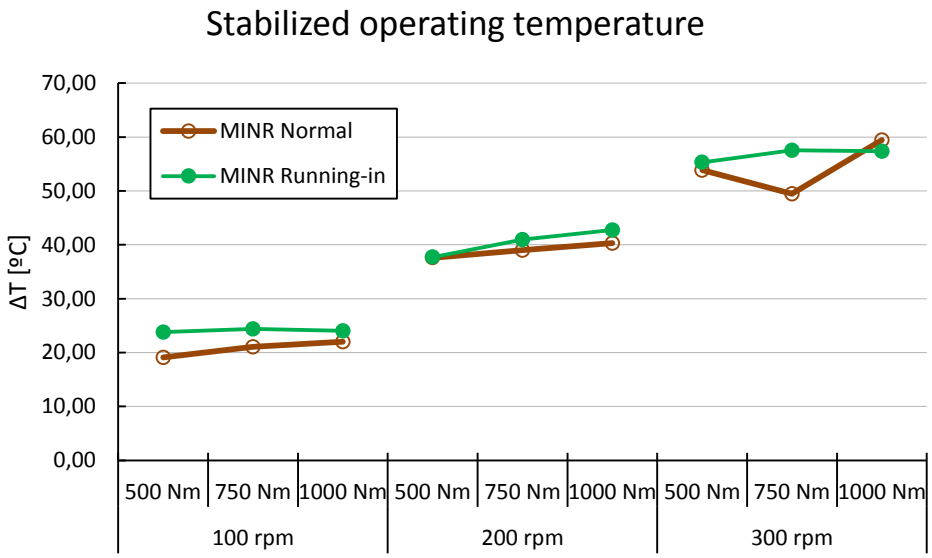

Figure 39. Comparison of the stabilized operating temperature between the normal MINR and Running-in MINR.

The difference between them ranged from almost 0% to approximately 25% (@300rpm/750Nm the relative air humidity was higher). The difference was not that great however the running-in MINR showed in almost every test higher temperatures.

Even if this comparison showed a small difference between the tests the wear performance of the MINR running-in was difficult to measure due to the high quantity of particles found in the oil samples.

Figure 40 compares the ferrograms of MINR oil before and after running-in.

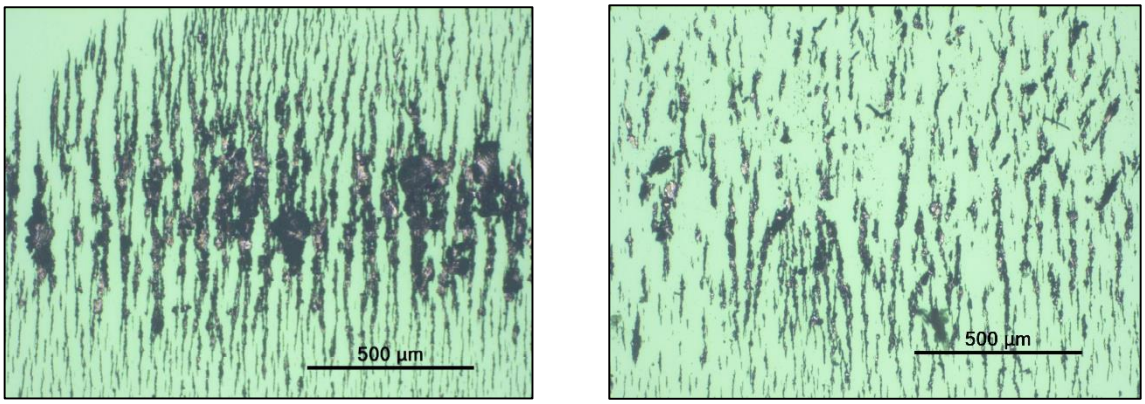

(a) Running-in: d=0.01 (b) Normal: d=0.1

Figure 40. Ferrograms of the MINR oil samples: (a) MINR running-in with 0.01 dilution factor; (b) MINR normal with 0.1 dilution factor.

It's visible that the running-in MINR ferrogram shows a much greater amount of particles in spite of its dilution which is 10 times higher. In other words if the dilution had been the same for both samples the amount of particles in the MINR running-in would be 10 times more than what is shown in Figure 40.

7.2. Lubricant contamination

During a second run of the MINR tests an abnormal increase of temperature was observed. In Figure 41 it's possible to observe this abnormality.

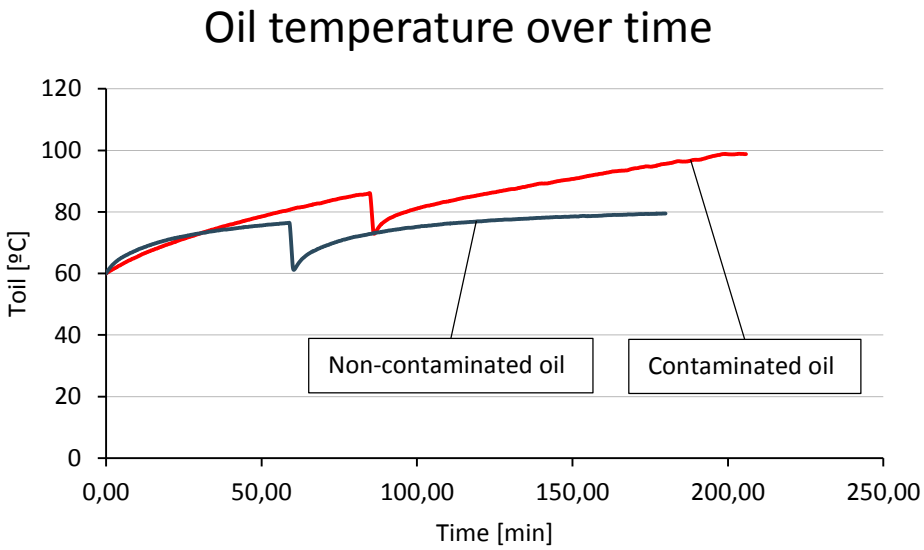

Figure 41. Comparison of the oil temperature over time between a contaminated and non-contaminated oil (300 rpm 750 Nm).

Figure 41 shows the MINR oil temperature during a test with 300 rpm and 750 Nm as inputs. The zero mark of the time was set as the time at which both tests were at 60°C. The curves shown on the graph should overlap each other since they are tests done under the same operating condition and with the same lubricant, yet this obviously doesn't happen. It was observed that the contaminated oil reached a much higher temperature, 98.78°C, than the non-contaminated oil, 79.57°C, at the end of the test. Furthermore in the last 30 minutes of the test, the contaminated oil suffered an increase in temperature of approximately 4.12°C while the non-contaminated oil only had an increase of 0.97°C that means that the non-contaminated oil was much closer to attaining thermal stability than the contaminated one. Another way of easily observing this, is by looking at the displayed curves where it's possible to understand that the slopes, near the end, of the contaminated and non-contaminated oil are significantly different and it's also possible to observe that the contaminated oil should likely keep on increasing its temperature way above 100°C while the non-contaminated oil should keep its temperature closer to 80°C.

There is also a sudden decrease in temperature close to the 60 minutes mark for the non-contaminated oil and 90 minutes mark for the contaminated oil. This happened because the test was stopped so that it would be possible to do a calibration. So the decrease has to

do with the test rig being stopped which in turn caused a cooling down of the gearbox and nothing to do with the behaviour of the oil or the gearbox. Furthermore, the central control software stops counting time while the test rig is stopped thus explaining why the temperature in both tests decreased so abruptly when it came close to the aforementioned times.

The FTIR spectra of two contaminated samples, both MINR oil one from the 100rpm tests and the other from the 300rpm tests, and a fresh sample of MINR oil are shown in Figure 42.

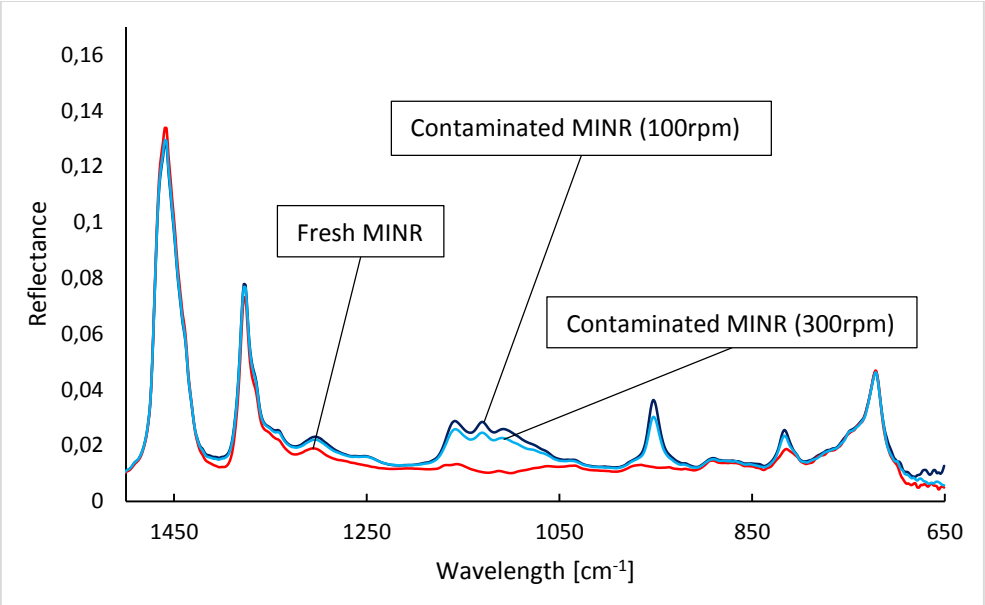

Figure 42. Spectra of contaminated oil samples and a fresh sample of MINR oil.

Analysing the spectra shown in Figure 42 it's possible to conclude that between the 1200 and 900 wavelength there are common peaks for both contaminated oil samples which are different from the ones displayed by the fresh oil. Thus proving that there was indeed a different compound present in the lubricating oil.

Since the tests that showed the aforementioned behaviour were done after the PAGD tests and because the solvent used to clean the gearbox was propanol it was decided to artificially contaminate a fresh sample of MINR with propanol and PAGD. Analysing this new sample with the FTIR technique Figure 43 was obtained.

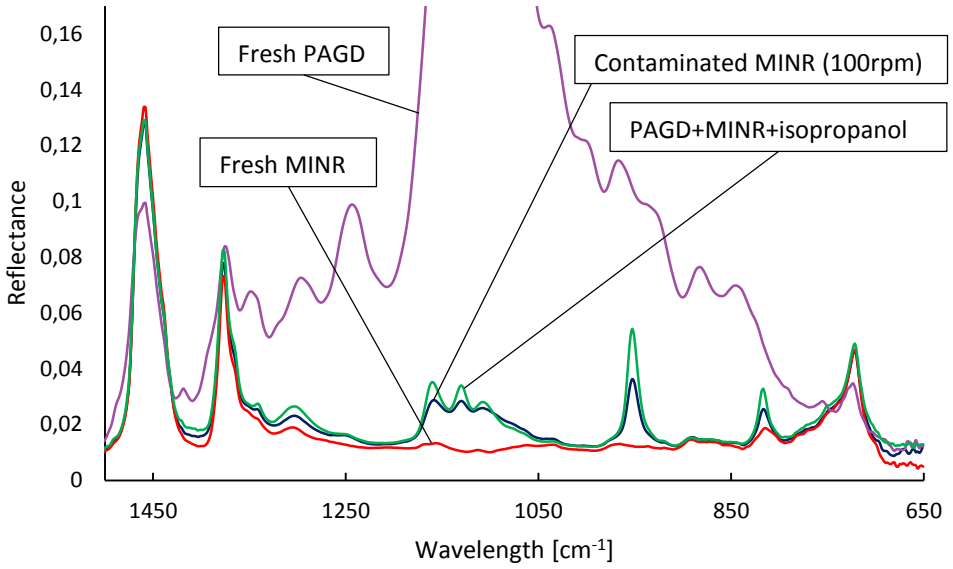

Figure 43. Spectra of fresh MINR and PAGD, a mixture of PAGD, MINR and isopropanol and a contaminated MINR oil samples.

Observing Figure 43 it's possible to conclude that the artificially contaminated MINR oil sample has a curve that differs from the fresh MINR in between the 1200 and 900 wavelength in the same manner of that of the contaminated oil sample from the gearbox.

So the most credible hypothesis for what happened is that when the change between oils occurred, residues of the remnants of PAGD oil and of the solvent, isopropanol, got lodged somewhere inside the gearbox. So when the gearbox was filled with MINR oil in order to perform the next test, a reaction between the contaminants (PAGD and isopropanol) must have occurred which resulted in much higher operating temperatures for the same operating conditions.

7.3. Experimental results

As suggested in section 6.7., the stabilized operating temperatures, $\Delta T=T_{oil}-T_{room}$, can be an indication of the power loss in the test gearbox.

The results of the stabilized operating temperatures, $\Delta T=T_{oil}-T_{room}$, are shown in Figure 44.

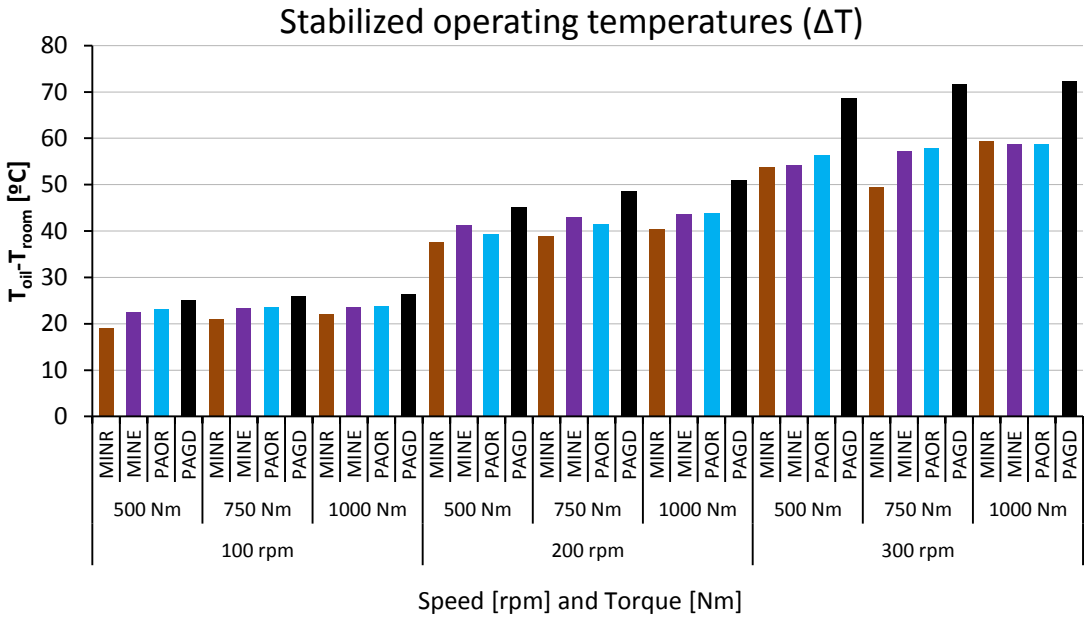

Figure 44. Stabilized operating temperatures ($\Delta T=T_{oil}-T_{room}$).

Detailed information (e.g. exact values for each of the tests performed) about the stabilized operating temperatures can be found in the Appendix.

The PAGD oil was the one that showed the highest stabilized operating temperatures for every case while the MINR oil showed exactly the opposite by showing the lowest temperatures in every situation. The PAOR and MINE oils both showed similar stabilized operating temperatures which were in some tests similar to those of the MINR oil or between the PAGD and MINR oil.

Also worthy of mention is that the speed has a much greater influence on the temperature than the torque. The MINE gear oil, for example, showed an almost similar temperature (variation of approximately 5%) for the 100 rpm tests even though the torque doubled from the first to last test of this series. This also happened in the 200 and 300 rpm test series. Furthermore between the 100 rpm 1000 Nm and the 200 rpm 500 Nm test, which have the same operating power (≈ 10500 W), there was an increase that ranged from about

50% to almost 100% in the stabilized operating temperature thus proving the major role of the speed in the stabilized operating temperature.

Using the power loss model described in section 6. it was possible to calculate the power loss of the gearbox. The calculation of the power loss was done using the absolute temperatures given by the temperature sensors in order to calculate the gear oil operating viscosities and densities. Before introducing the results of the numerical power loss, the operating power is presented.

The values of the viscosity for each oil for each test were calculated using the *ASTM D341* standard and are displayed in Figure 45.

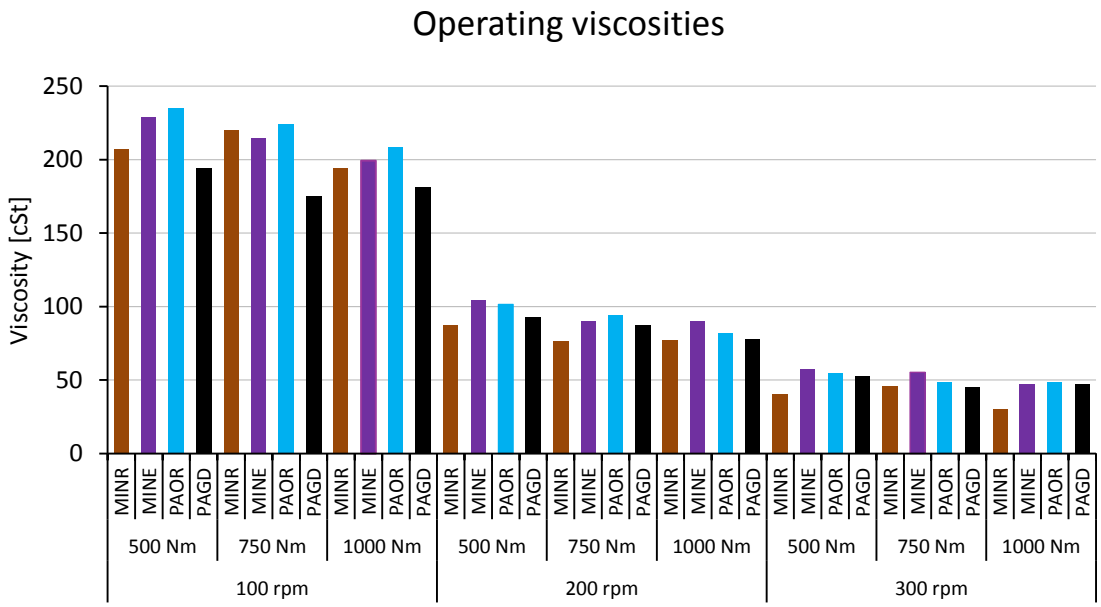

Figure 45. Operating viscosities [cSt].

Detailed information (e.g. exact values for each of the tests performed) about the operating viscosities can be found in the Appendix Table 17.

The MINR gear oil presented the lowest viscosity and temperature in the 200 and 300 rpm test. The PAOR and the MINE gear oils showed similar viscosities and for almost every test had higher viscosities then those of the MINR and PAGD oils. Despite its higher viscosity index, PAGD showed much higher operating temperatures at 200 and 300rpm, resulting in similar operating viscosities to MINE and PAOR at these speeds.

Viscosity is directly related to temperature so the small variations with torque and the large variations with speed that were mentioned in previous paragraphs about the stabilized operating temperature are also valid for the analysis of the viscosity variation.

The specific film thicknesses for the sun/planet contact and for the planet/internal gear contact were calculated at the pitch point by the D. Dowson and G.R. Higginson model [23] using the temperatures obtained in the respective test. The calculated specific film thicknesses are shown in Figure 46 and Figure 47 respectively.

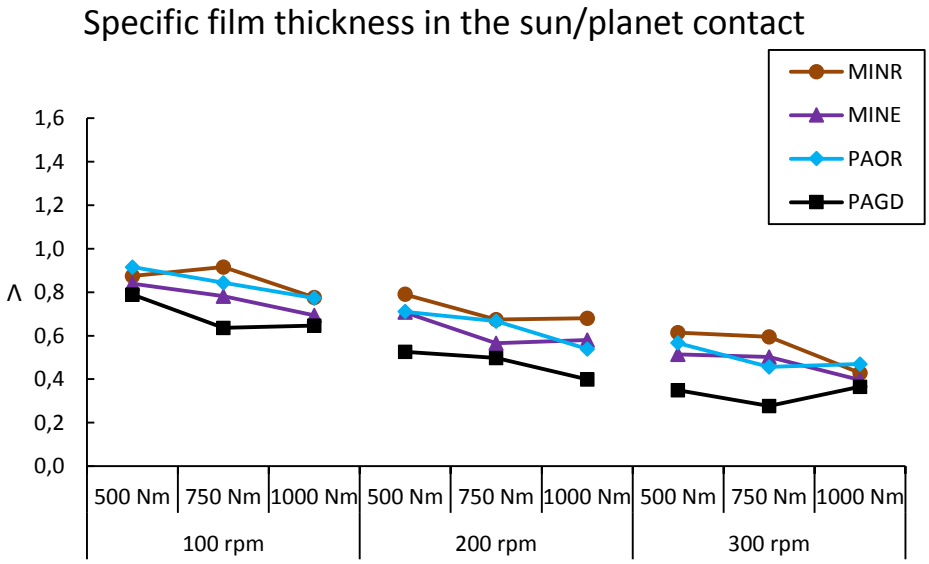

Figure 46. Specific film thickness in the sun/planet contact.

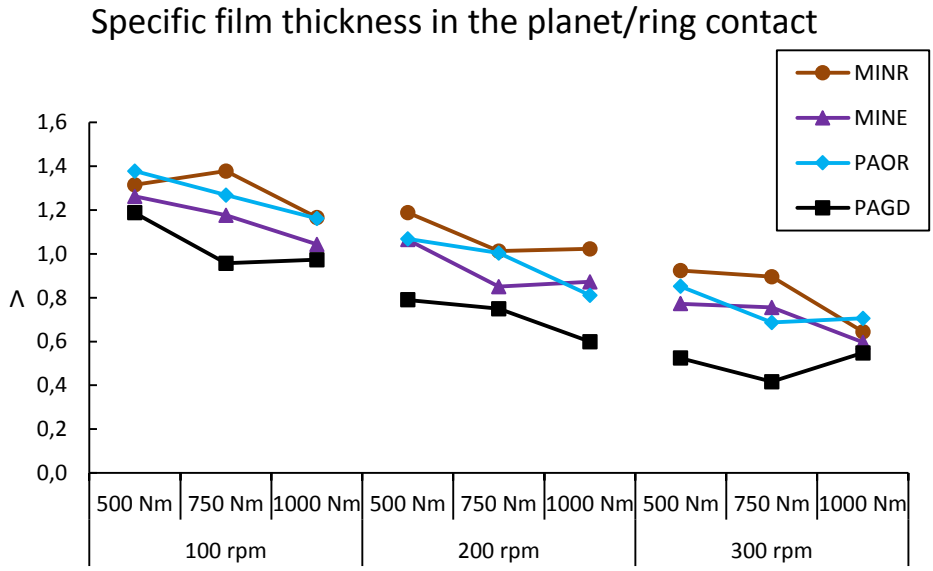

Figure 47. Specific film thickness in the planet/ring contact.

The specific films thickness is for the most part higher than 0.7 which means that for the majority of the tests, the lubrication regime was mixed film. The specific film thickness is

higher for the planet/ring contacts mainly due to the higher equivalent radius and lower load line of this contact.

7.3.1. Ferrography results

The number of cycles for each speed and each oil should be the same, and it's indeed quite similar for the MINE, PAOR and PAGD oils, yet this isn't true for the MINR oil since there were other tests made with that oil before the actual tests.

The results of the wear indexes found for each speed for all tested oils are presented in Table 15:

Table 15. Wear indexes for each speed for all tested oils.

Oil	Speed	Cycles	d	D_L	D_S	ISUC	CPUC
MINE	100	72000	0.1	73.1	11.9	$5.2x10^5$	850.0
	200	264000	0.1	74.2	12.4	$5.4x10^5$	866.0
	300	480000	0.1	53.4	10.1	$2.7x10^5$	635.0
PAOR	100	60000	0.1	27.9	5.8	$7.4x10^4$	337.0
	200	192000	0.1	29.9	2.6	$8.9x10^4$	325.0
	300	408000	0.1	41.4	4.9	$1.7x10^5$	463.0
PAGD	100	73000	0.1	4.5	1.6	$1.8x10^3$	61.0
	200	217000	0.1	14.3	11.1	$8.1x10^4$	254.0
	300	433000	0.1	31.4	18.8	$6.3x10^5$	502.0
MINR	100	730000	0.1	35.4	4.8	$1.2x10^5$	402.0
	200	874000	0.1	26.0	5.4	$6.5x10^4$	314.0
	300	658000	0.1	39.3	5.4	$1.5x10^5$	447.0

The evolution of the wear indexes with the number of cycles can be seen in Figure 48 and Figure 49:

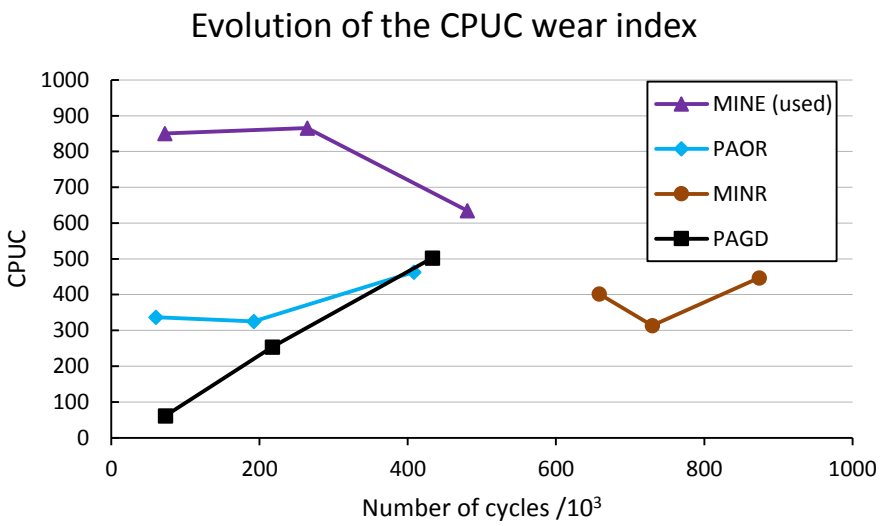

Figure 48. Evolution of the CPUC wear index.

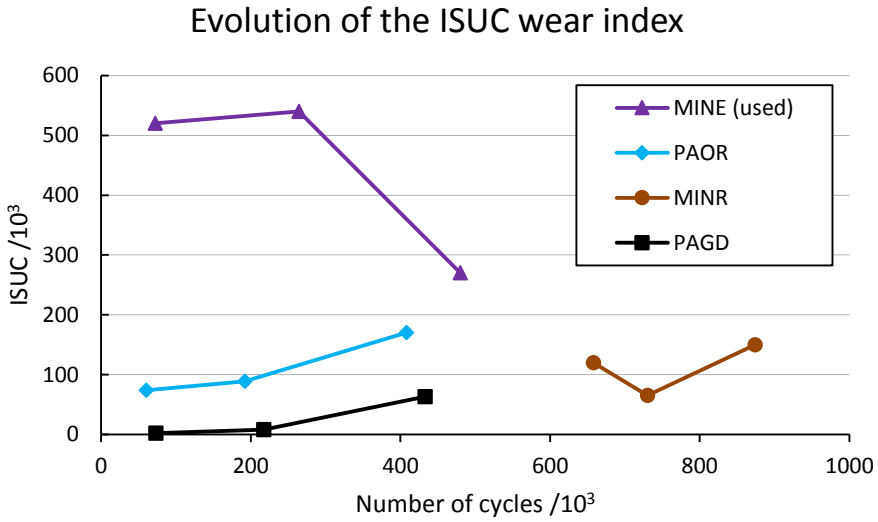

Figure 49. Evolution of the ISUC wear index.

The lubricant analysis reports can be found in the Appendix.

The values obtained for the MINE oil may have been influenced by the running-in period because the MINE power loss tests were done right after MINR's. There wasn't any fresh MINE gear oil available, so the MINE tests were done with used oil. This can explain the great difference of the CPUC and ISUC values between the MINE and MINR /PAOR/PAGD oils. MINR and PAOR promoted similar wear indexes (Figure 49).

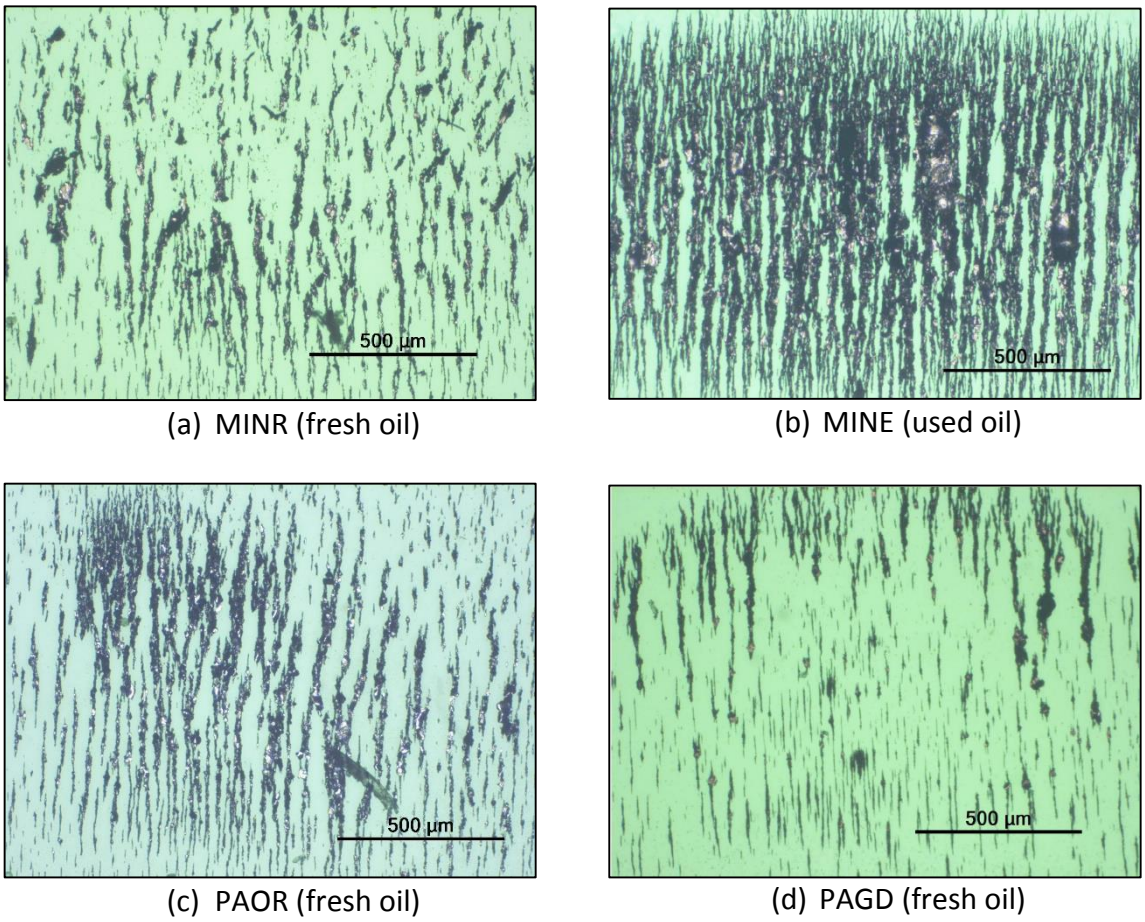

(a) MINR (fresh oil) (b) MINE (used oil)

(c) PAOR (fresh oil) (d) PAGD (fresh oil)

Figure 50. Entry of the ferrogram.

In Figure 50 it's possible to observe a significant difference between the MINE gear oil and the other oils, which is in accordance with the wear indexes shown in Figure 48 and Figure 49.

All samples showed some oxidized particles.

Observing the ferrrograms it's also possible to say that the PAOR gear oil shows more particles than the MINR oil, even though the wear indexes suggest that the PAOR and the MINR gear oils should have the same amount of particles. This apparent inconsistency may be related to the somewhat statistical nature of the particle distribution in the ferrogram.

The PAGD gear oil showed the lowest amount of particles, among all samples, which is consistent with the ISUC results shown in Figure 49. Therefore, the oil that showed the best wear performance was the PAGD gear oil, even though it was not that different from the PAOR and MINR gear oils, while the one that showed the worse was the MINE gear oil.

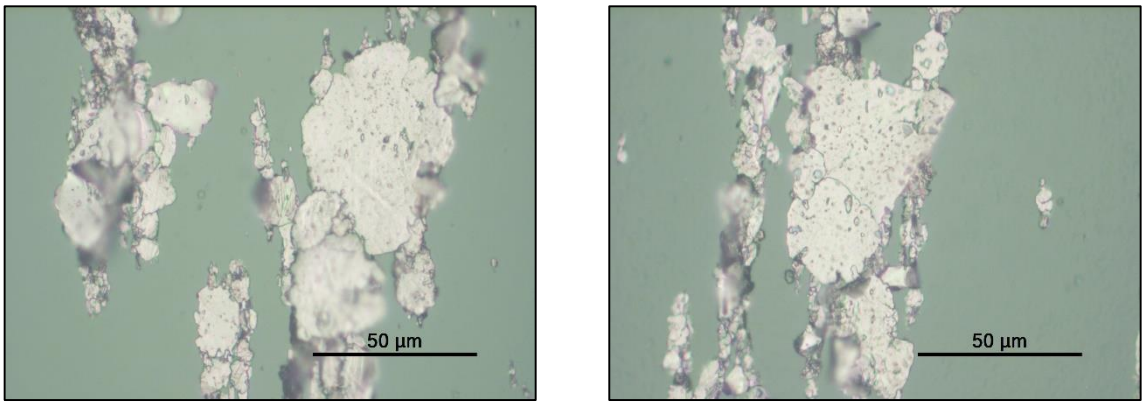

(a) MINR (fresh oil) (b) MINE (used oil)

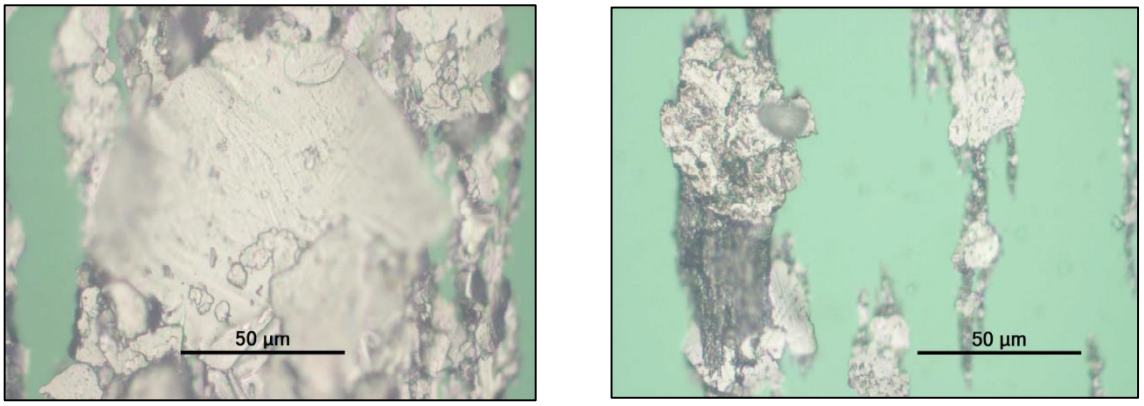

(c) PAOR (fresh oil) (d) PAGD (fresh oil)

Figure 51. Magnification of found particles in the samples.

The ferrograms showed that similar particles can be found in all gear oils. These were usually large, thin and reveal fractured edges which are typical wear and fatigue particles.

After applying heat treatment to a ferrogram the particles changed its colour. The blue tone means that it is a low alloyed steel while the brownish tones mean that it is a medium

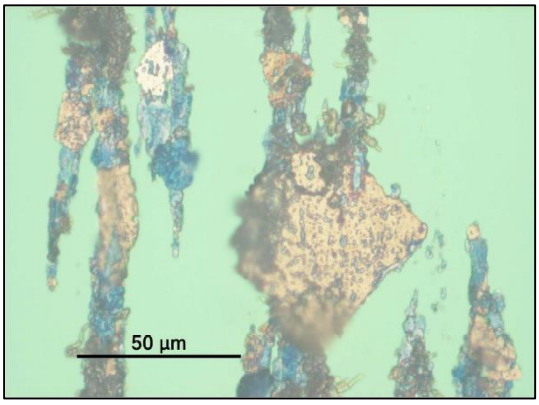

Figure 52. MINR particle after heat treatment.

alloyed steel. Meaning that the origin of this particle may be from the gears or from any other component inside the gearbox.

Figure 53 shows friction polymers found in the ferrogram of the PAGD oil sample.

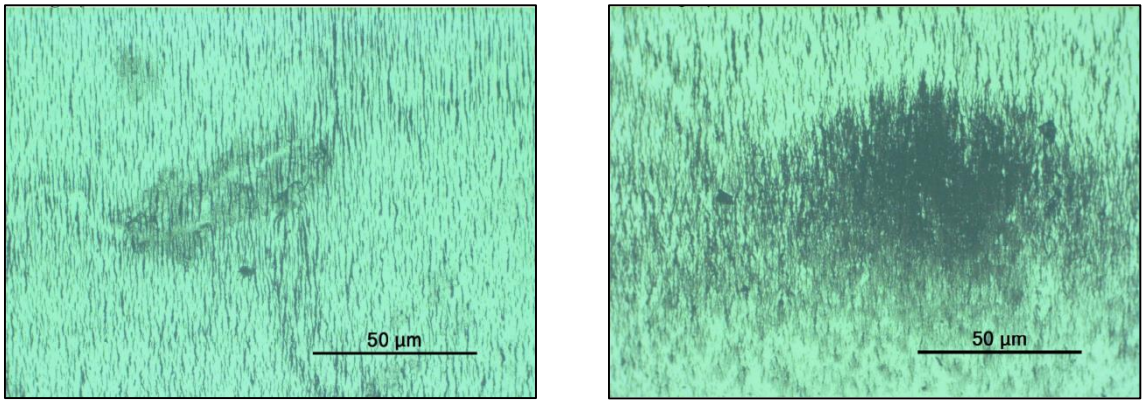

Figure 53. Friction polymers in the PAGD oil sample.

Friction polymers are thought to be created by overstress on a lubricant in critical conditions [44]. According to the Wear Particle Atlas [44] the structure of friction polymers is a result of the polymerization of the oil molecules to form a large coherent structure. These are generally produced under the influence of heavy load and may or not appear depending on the oil formulation.

7.3.2. No-Load torque loss results

The results of the gearbox torque loss for the no-load tests are shown in Figure 54.

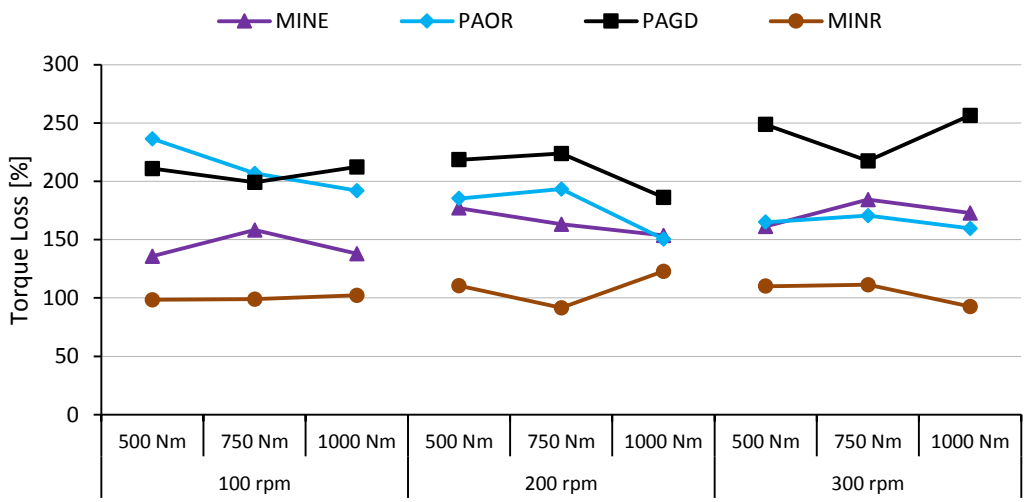

Figure 54. Relative no-load gearbox torque loss.

In Figure 54 the gearbox torque loss of the gear oils is presented relatively to the average of the MINR oil at 100 rpm no-load torque loss results. It's important to mention that the abscissa of the graphic in Figure 54 does not reflect the actual operating conditions, it just identifies the no-load test that is related to the referenced "loaded" test point.

MINR oil generates almost constant no-load torque loss for all operating conditions.

With the exception of the PAOR oil all oils show increasing no-load torque loss with the increase of speed.

The MINR oil shows the lowest no-load torque loss for every test while PAGD shows the highest. The MINE and PAOR oils show similar behaviour for the 200 and 300 rpm tests, while at 100 rpm PAOR shows similar behaviour to PAGD.

The dynamic viscosity and the absolute operating temperatures at no-load conditions are showed in Figure 55.

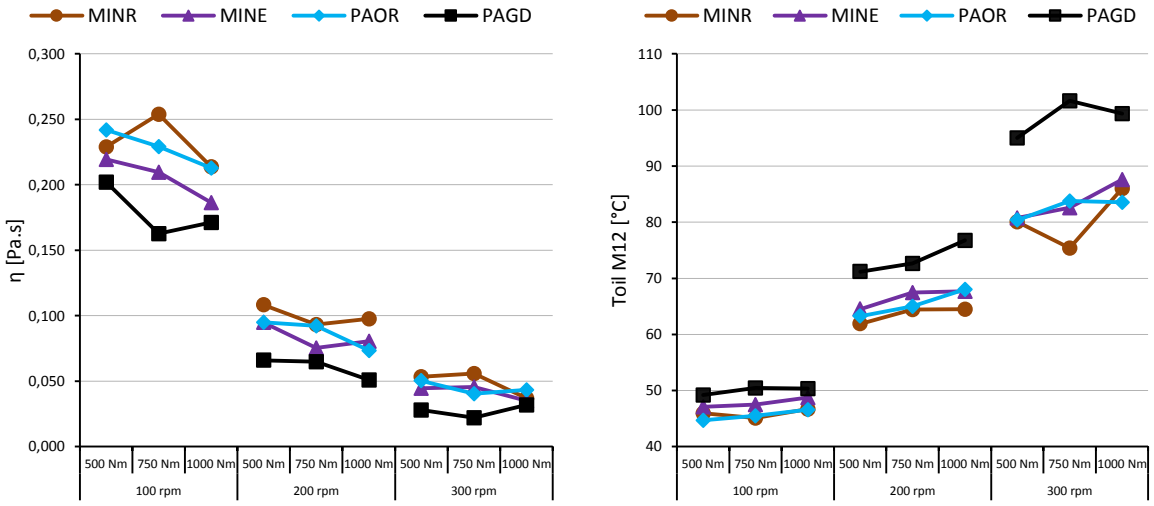

(a) Dynamic viscosity (b) Absolute operating temperatures

Figure 55. Dynamic viscosity and absolute operating temperatures of the no-load tests.

Observing Figure 55 it's possible to conclude that for all oils the dynamic viscosity lowers with speed, which is a result of the increasing operating temperatures. The PAGD oil shows the lowest dynamic viscosity in all tests while MINR shows the highest, being sometimes close to the dynamic viscosity of the PAOR oil.

The absolute operating temperatures show an increase with increasing speeds, this behaviour is similar for all oils. The PAGD oil shows the highest absolute operating temperatures in every test, standing out from the rest of the oils (@300rpm PAGD 15°C > MINR/MINE/PAOR).

The dynamic viscosity and the absolute operating temperatures are, obviously, related, as it has been shown in Section 3, since the dynamic viscosity is a directly correlated with the kinematic viscosity and the density, both, in turn, having a direct correlation with the temperature of the oil sump.

So as the temperature rises the dynamic viscosity lowers.

The PAGD oil shows a distinguishable behaviour from the other oils in all of the mentioned results.

For the 300 rpm tests MINE/PAOR/PAGD have similar dynamic viscosity. Yet, for these conditions, PAGD shows a much higher relative no-load torque loss than MINE and PAOR.

Considering the same geometry and similar dynamic viscosity and operating conditions, these results become interesting. A possible explanation for this phenomenon will be presented along with the analysis of the numerical results.

7.4. Numerical results

The numerical power loss results are shown in Figure 56.

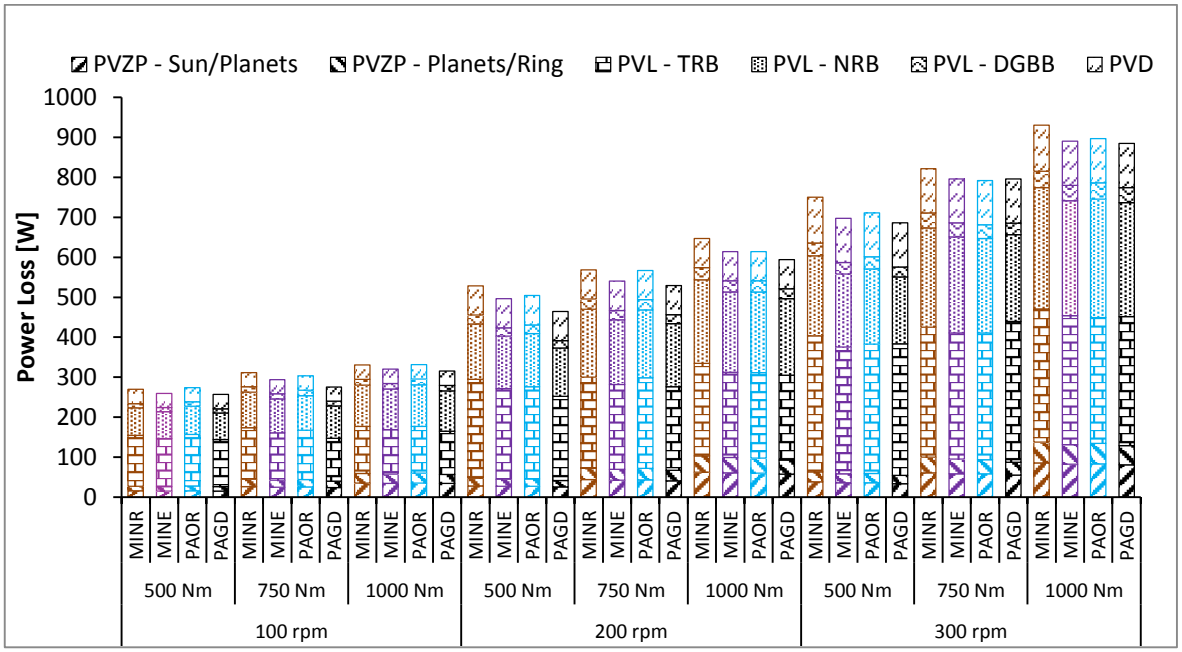

Figure 56. Power loss model results: Total Power Loss [W].

Detailed information (e.g. exact values for each of the tests performed) about the power loss model results can be found in the Appendix Table 18.

Before any observation is made about the results displayed in Figure 56 one consideration has to be taken into account, the power loss model doesn't contemplate the churning losses. Even though Changenet et al. [37] and Gorla et al. [45] showed that the results of their experiments validate CFD analysis as a valid method to predict power losses, the same may possibly not be true since there are some crucial differences between this and the aforementioned researcher's works:

- The internal geometry of the planetary gearbox is much more complex than the one used on Changenet et al. [37] and Gorla et al. [45] works. And this is relevant because the internal geometry of a gearbox has great influence over the churning power loss;
- There are several components rotating and moving relatively to each other, like the planets that rotate around their own axis and around the sun or planet carrier axis creating therefore complex flow conditions.

Analysing the results in Figure 56 it is observable that even though the stabilized temperatures indicated that the PAGD gear oil would have the highest power loss and the MINR gear oil the lowest, it turned out, according to the power loss model, that it was actually

the opposite. This is due to the absence of a churning power loss model. According to Marques et al. [18] density, viscosity, rotational speed, geometry and the flow regime are all factors to take into consideration when evaluating the churning power losses in a gearbox.

Analysing the results of the no-load torque loss it's possible to observe, as it has been mentioned, a higher no-load loss for the PAGD, compared to the MINR oil, which is in accordance with what has been explained in the previous paragraphs of this section, yet, the difference between the MINR and PAGD observed in the no-load torque loss results are not sufficient to explain the difference between the numerical and the experimental results of the power loss, which means that the power loss model not only lacks a churning power loss model but it also needs to be improved not only because of this reason but also because there's a lack of accurate information about the inside geometry and components of the tested gearbox, as it has been mentioned in previous sections of this work.

The power loss model shows a power loss increase with increasing input torques, which is in accordance to the temperature evolution for higher input torques (there is a tendency to a small temperature increase with input torque).

In Figure 57 the different components of the power loss are shown. The gear mesh power loss (P_{VZP} - planet/ring and P_{VZP} - sun/planet) are a lot less significant than the power loss of the bearings, which correspond to approximately 69-77% of the total power loss in every test.

Figure 57 shows the evolution of the power loss of each component.

Analysing Figure 57 it is possible to conclude that there is not a significant change in the gear mesh power loss, when compared to the total power loss.

The needle roller bearings power loss show an almost direct relationship with the increase in power.

Figure 57 shows that the tapered roller bearings (TRBs) are the most important power loss source under the tested operating conditions. The power loss generated by the TRBs increases with increasing input speeds, but shows a slight decrease for increasing torques at the same speed. This apparently strange phenomena can be explained. The pre-load applied on the TRBs is orders of magnitude higher than the axial force introduced by the helical gears on the planetary gearbox, thus the axial force due to the helical hears has a small influence on the torque loss generated by the TRBs.

Nevertheless, increasing the input torque will drastically increase the power loss generated by the needle roller bearings, (NRbs), since from 500 to 1000 Nm the power loss generated by the NRBs almost doubles. The increase in the power loss with increasing torques

due to the meshing gears and NRBs results on a higher operating temperature, which lowers the operating viscosity, thus lowering the power loss generated by the TRBs.

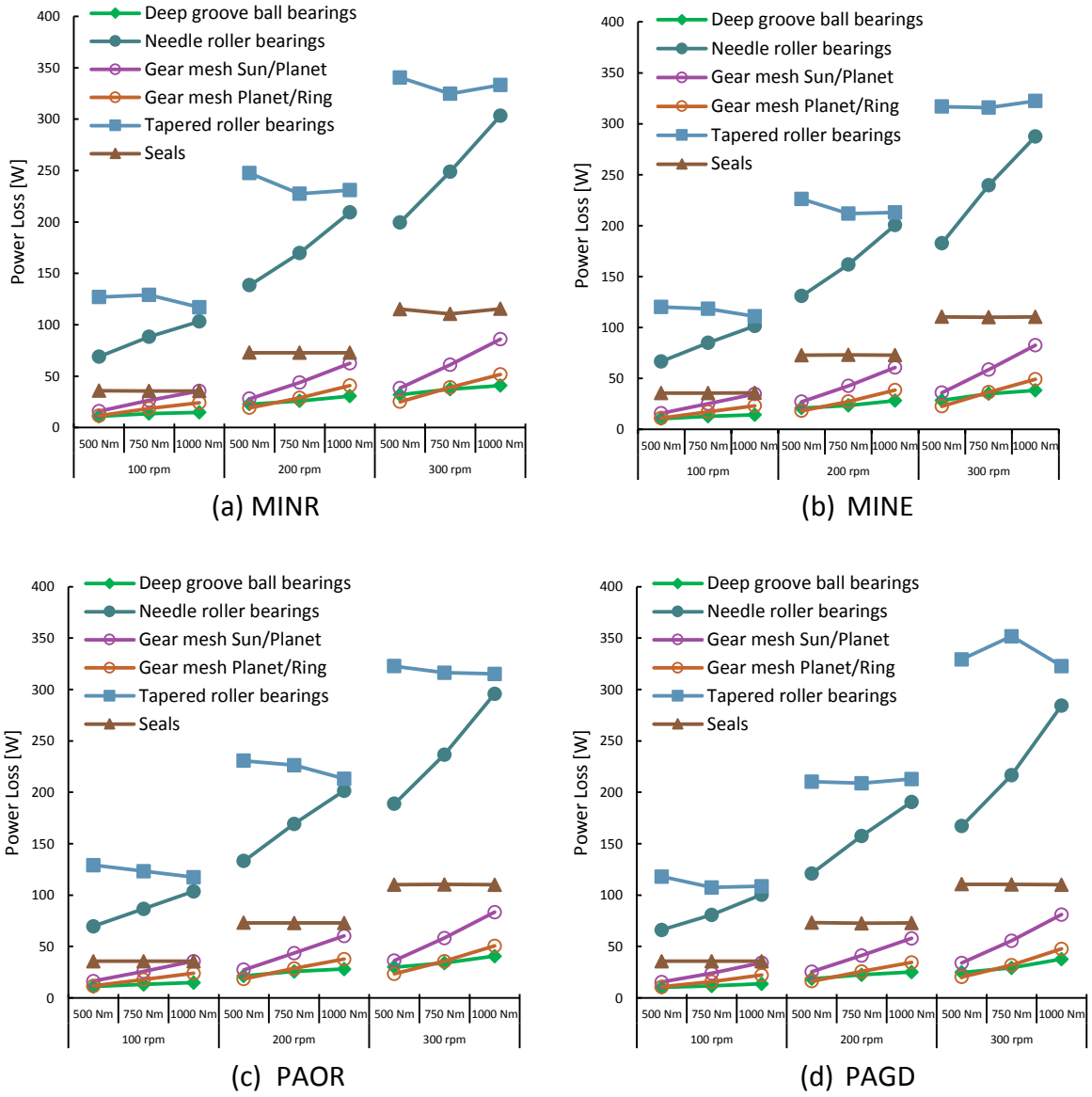

Figure 57. Power loss results of the components of the Power Loss Model: (a) MINR; (b) MINE; (c) PAOR; (d) PAGD.

7.4.1. Heat transfer coefficient

The global heat transfer coefficients were calculated using the results obtained with the power loss model (Figure 58).

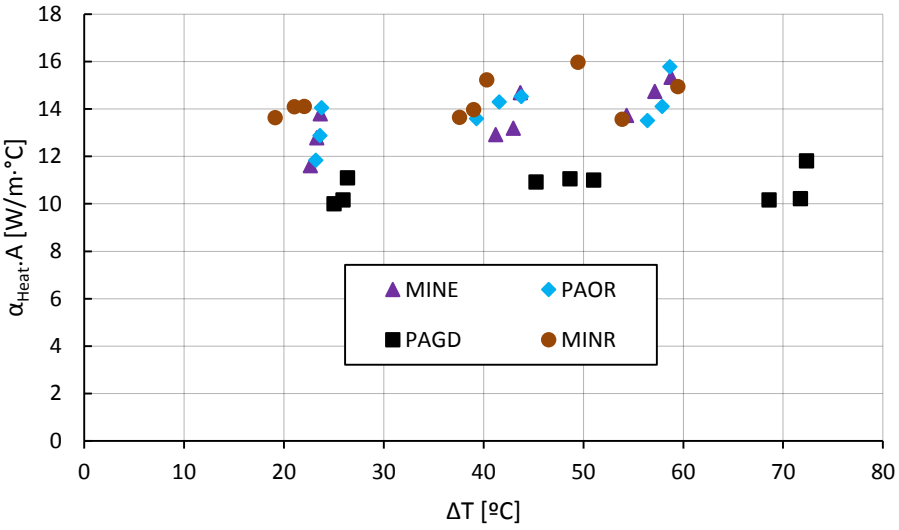

Figure 58. Heat transfer coefficient.

In an ideal situation the heat transfer coefficient is given by a linear equation that is dependent upon temperature. The results on Figure 58 suggest that the model actually gives consistent results for the MINR, MINE and PAOR gear oils and even though there is a slight scattering they show the same tendency. Yet PAGD shows a very different tendency, the global heat transfer coefficient is always smaller than those observed for the other gear oils.

The absence of a churning loss model may explain these differences, but, for similar operating dynamic viscosities, speeds and oil level a churning loss model would give the same churning power loss results and yet, at 300rpm, MINE, PAGD and PAOR show similar operating viscosities, but PAGD promotes much higher operating temperatures.

The volumetric expansion of the oil caused by thermal effects, influences the immersion depth of the mechanical elements on the planetary gearbox. Nevertheless, even considering that PAGD has the highest thermal expansion coefficient, a tremendous increase on the churning power loss due to a slight increase on immersion depth shouldn't be expected.

The chemical properties of the lubricant can also have an influence on the power loss due to fluid-geometry interactions. Surface tension has an influence on the amount of air bubbles on the oil sump. Changenet et al. [38] suggested that the amount of air bubbles in an oil sump lubricated gearbox can increase the churning power loss.

At 300 rpm PAGD shows the lowest operating film thickness. In similar operating conditions (temperature, load and speed) the power loss due to power transmitting contacts generated by PAGD should be the lowest. This is suggested by results obtained in the FZG test rig by Höhn et al. [22].

If PAGD usually generates lower load loss, then the great increase on the operating temperature at 300rpm (relative to the other gear oils) should be related to a no-load power loss source.

Higher temperatures due to no-load power loss would decrease the lubricant operating viscosity which would also decrease the specific film thickness. At 300rpm PAGD, PAOR and MINE show similar operating viscosities but very different specific film thickness, as shown in Figure 45, Figure 46 and Figure 47. The specific film thickness is lower because for the same operating viscosity, PAGD has the lowest piezoviscosity.

At 300rpm PAGD specific film thickness is below 0.7 which may indicate boundary lubrication conditions. In boundary lubrication conditions the power loss in the gear mesh will generally increase.

The increase in temperature caused by the no-load losses causes a diminution in the specific film thickness which in turn causes an increase in the gear contacts power loss, due to the diminished specific film thickness.

A linear regression of the global heat transfer coefficient is shown in Figure 59.

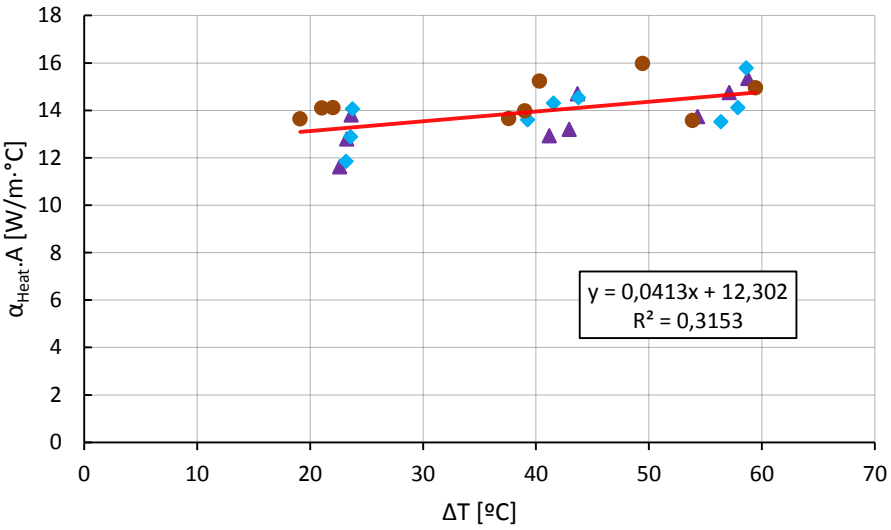

Figure 59. Heat transfer coefficient with linear regression (PAGD excluded).

7.4.2. Coefficient of friction comparison

A comparison between the calculated coefficient of friction (COF) in the sun/planet and planet/ring contact for the MINR, MINE, PAOR and PAGD gear oil tests is shown in Figure 60, Figure 61, Figure 62 and Figure 63 respectively.

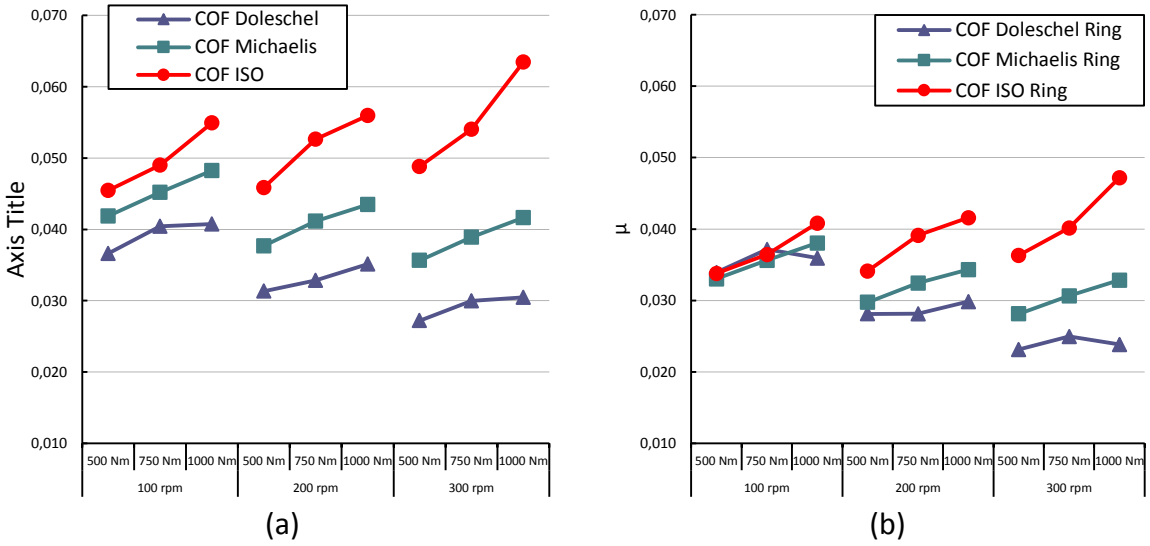

Figure 60. COF comparison of MINR gear oil; (a) Sun/planet; (b) Planet/ring.

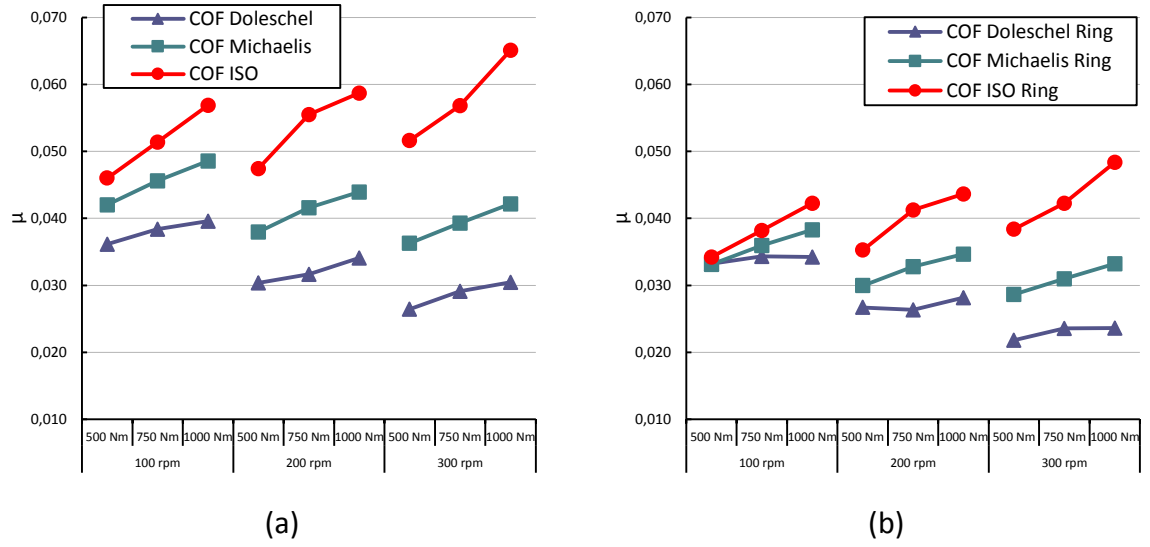

Figure 61. COF comparison of MINE gear oil; (a) Sun/planet; (b) Planet/ring.

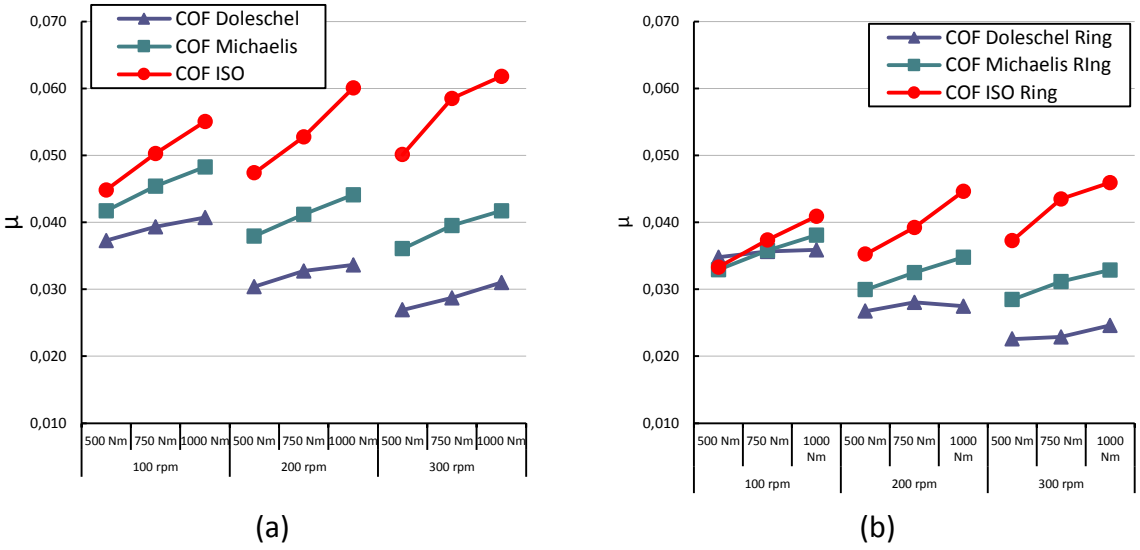

(a) (b)

Figure 62. COF comparison of PAOR gear oil; (a) Sun/planet; (b) Planet/ring.

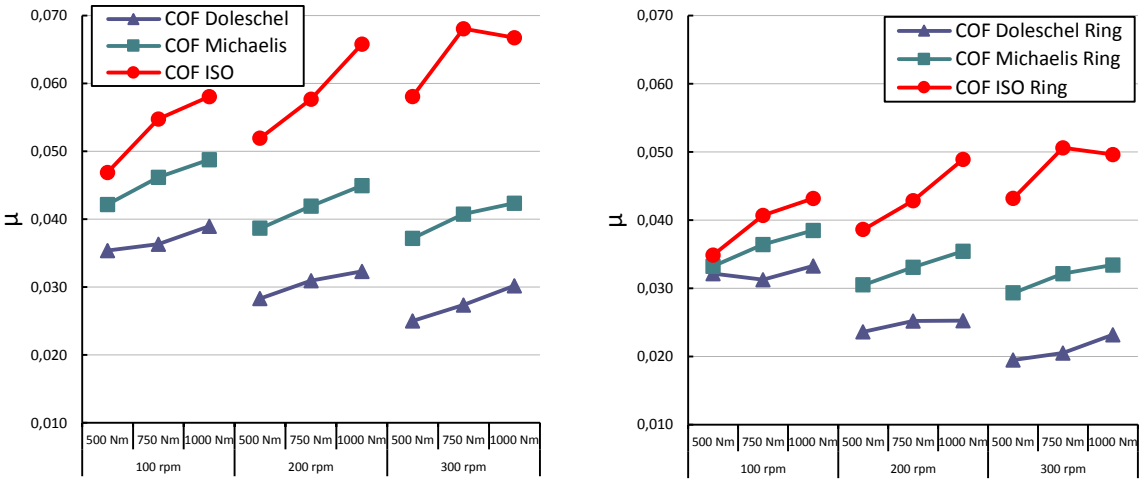

(a) (b)

Figure 63. COF comparison of PAGD gear oil; (a) Sun/planet; (b) Planet/ring.

Analysing Figure 60 through Figure 63 it is observable that the coefficient of friction suggested by the ISO standard shows higher values of the coefficient of friction in almost every situation. The Doleschel coefficient of friction and the Michaelis coefficient of friction are similar in the planet/ring contact for the 200 and 300 rpm series of tests. For the sun/planet contact the coefficient of friction is very different for each model and it shows an increasing tendency in each series of speed corresponding to the increase of torque.

An interesting detail is that for the same torque and increasing speeds the coefficient of friction lessens for the Michaelis and Doleschel models while for the ISO model it shows a different tendency, in other words, it increases with the increase of speed for a constant torque.

The planet/ring contact shows lower coefficient of friction in every test, when compared to the sun/planet contact. This is due to a lower load parameter caused by a higher average sum of contacting lines length, since the normal forces are the same in both contacts (section 6). The equivalent radius is also much larger in the case of the planet/ring contacts. The average sum of contacting lines length is $\ell^{sun/planet} = 0.066$ while $\ell^{planet/ring} = 0.072$. regarding the equivalent radius at pitch point: $R_X^{sun/planet} = 0.0139$ while $R_x^{planet/ring} = 0.0417$.

The loss factor, H_V, for the planet/ring contacts is also lower than the one for the sun/planet contacts., lowering even more the calculated power loss for the planet/ring ($H_V^{sun/planet} = 0.1152$ while $H_V^{planet/ring} = 0.0884$).

8. Conclusions

8.1. Conclusions based on experimental results

The results of the stabilized operating temperatures showed that the MINR oil has the lowest stabilized operating temperature in all tests except for the 300 rpm 1000 Nm where it showed a slightly higher temperature ($\approx 1°C$) than the PAOR and MINE oils.

The PAGD oil had the highest stabilized operating temperatures in all tests showing even a $\approx 10°C$ difference for the most severe conditions.

The MINE and PAOR oils showed similar stabilized operating temperatures which were in almost every conditions in between the MINR and PAGD temperatures.

Observing the results of the stabilized operating conditions one can also conclude that the torque doesn't have that much of an influence on the stabilized operating temperatures, the speed being the dominating factor. This can be observed by comparing the 100rpm 1000Nm and 200rpm 500Nm where the operating power is almost the same and yet there is an increase of the stabilized temperature that ranged from 50% to almost 100%.

PAGD showed much higher operating temperatures at 200 and 300 rpm, which resulted in similar operating viscosities to MINE and PAOR. This was due to its viscosity index.

The wear performance of the MINR and PAOR oils were similar while the MINE oil had much higher wear indexes. It was concluded that this difference was probably due to the fact that the MINE tests were done with used oil because there wasn't any fresh MINE gear oil available, furthermore these tests were performed right after the running-in test performed with the MINR oil.

There were some oxidised particles found all over the ferrograms and the PAGD oil samples had traces of friction polymers.

The no-load torque loss results showed that the MINR oil had the lowest no-load torque loss while PAGD showed the highest. MINE and PAOR performed similarly for the 200 and 300 rpm tests. At 100 rpm PAOR and PAGD showed similar behaviour.

By analysing the results of the dynamic viscosity and the absolute operating temperatures for the no-load tests it's possible to conclude that the absolute operating temperatures increase with increasing speeds and the same is verified for the dynamic viscosity since there is a correlation between these two results.

The PAGD oil shows a distinguishable behaviour from the other oils in all of the mentioned results. Having much lower dynamic viscosities and much higher absolute temperatures at 300 rpm.

8.2. Conclusions based on the numerical results

The numerical results showed the opposite of the experimental results regarding the oil with the higher and the one with the lowest power loss. In other words, the stabilized operating temperatures that can be directly related to the power loss, showed that the oil with the highest power loss was the PAGD and the lowest was the MINR while the calculations based on the power loss model showed that the PAGD had the lowest and MINR had the highest power loss. This difference was explained as being partially caused by the lack of a churning power loss model and by the fact that the power loss model itself could still be improved since there is a lack of accurate information about the inside geometry and components of the tested gearbox.

The numerical results also showed that the power loss is more dependent upon the speed than upon the torque, which is in agreement with the experimental results.

Analysing the components of the power loss it was concluded that the bearings are the main cause of the power loss representing 50% to 70% of the total power loss.

The power loss caused by the gear contacts is low, when comparing to the bearings losses.

The needle roller bearings are very influenced by the torque and also by the speed, showing an almost direct correlation (linear) with the increase of the transmitted power.

The tapered roller bearings are the most influential power loss source in the gearbox. These bearings are mainly influenced by the speed showing an unexpected behaviour regarding the torque, since, by increasing the torque, the power loss generated by these components lowered. This was explained by the high applied preload on these bearings.

A heat transfer coefficient was calculated based on the numerical results. The results showed that the power loss model gave consistent results for the MINR, MINE and PAOR oils. Yet the model for PAGD oil showed a different tendency, resulting in a much lower global heat transfer coefficient. These differences were explained as being caused by the lack of a churning power loss model.

A comparison between the different calculated coefficients of friction was made and it was observed that the ISO standard shows the higher values of the coefficient of friction in almost every tested situation. The Doleschel coefficient of friction and the Michaelis

coefficient of friction were proved to be similar in the planet/ring contact for the 200 and 300 rpm series of tests. In the sun/planet contact the coefficient of friction is very different for each model and it shows an increasing tendency in each series of speed corresponding to the increase of torque.

The planet/ring contact shows lower coefficient of friction and power loss in every test, compared to the sun/planet contact. This is due to differences in the average sum of contacting lines length, the equivalent radius and the gear loss factor.

8.3. Lubricant contamination and running-in conclusions

The running-in tests showed slightly higher stabilized operating conditions but a much higher amount of particles when comparing to a normal test.

In a performed test of the MINR oil the temperatures were attaining unusual values and it was verified that this problem was caused by lubricant contamination. By doing FTIR analysis it was demonstrated that these contaminants were a mixture of PAGD oil and isopropanol, which was used as a solvent when removing the PAGD oil from the gearbox.

9. Future works

More lubricants with different base oils, different additive packages and different viscosity grades should be tested to further comprehend the power loss process in a planetary multiplier gearbox and to improve the power loss model.

A computer fluid dynamics analysis, even though it may not take into account the particular lubricant chemistry, should be done in the planetary multiplier gearbox in order to evaluate the churning power losses and to understand the influence of the oil formulation in this power loss source. This is one of the most important things that has to be done since it is, as it was shown, one of the most important factors that contribute to the total power loss.

The tested gearbox should be disassembled to check if the prediction of the components were correct and to see if a problem occurred with any of the components.

The output torque sensors should be repaired so that the torque loss can be precisely measured using the measured torques instead of the stabilized operating conditions.

A torque sensor next to the motor should be installed in order to have more precise measurements of the torque loss.

Bibliography

1. Council, G.W.E., *Global wind report.* Annual Market Update, 2012.
2. http://www.hkelectric.com/. *(visited 28, June, 2013)*.
3. W. Musial, S.B., *Improving Wind Turbine Gearbox Reliability*, in *European Wind Energy Conference*. 2007: Milan, Italy.
4. Standardization, I.O.f., *Wind Turbines – Part 4: Standard for Design and Specification of Gearboxes*. 2005: Geneva, Switzerland.
5. Aaron Paul Thaler, *A High Fidelity Finite Element and Contact Analysis Investigation of Stresses and Motions of a Wind Turbine Gearbox*. 2011, Ohio State University.
6. Jorge Seabra, A.C., Alexandre Sottomayor, *Lubrificação Elastohidródinamica.* Departamento de Engenharia Mecânica e Gestão Industrial, Porto, 2002. Secção de Mecânica Aplicada.
7. Fox, M.F., *Chemistry and Technology of Lubricants*. Third Edition ed, ed. S.T.O. Roy M. Mortier. 2010: Springer.
8. Gonçalves, D., *Efficiency of a Gearbox Lubricated with Wind Mill gear Oils*. 2011, FEUP.
9. Bernard J. Hamrock, S.R.S., Bo O. Jacobson, *Fundamental of Fluid Film Lubrication*. 2004, New york: MARCEL DEKKER, INC.
10. Marques, P.M.T., *Efficiency of a Gearbox Lubricated with Wind Turbine Gear Oils*, in *DEM*. 2012, FEUP.
11. Hamrock, B.J., *Lubrication of Machine Elements.* NASA, 1984.
12. Denis, J., J. Briant, and J.C. Hipeaux, *Physico-Chimie Des Lubrifiants: Analyses Et Essais*. 1997: Editions Technip.
13. http://www.api.org/. *(visited 28, June, 2013)*.
14. http://www.blauer-engel.de/, *(visited 28, June, 2013).*
15. http://ec.europa.eu/environment/ecolabel/, *(visited 28, June, 2013).*
16. http://www.svanen.se/en/, *(visited 28, June, 2013)*
17. http://www.greenseal.org/, *(visited 28, June, 2013).*
18. Pedro M.T. Marques, C.M.C.G.F., Ramiro C. Martins, Jorge H.O. Seabra, *Power losses at low speed in a gearbox lubricated with wind turbine gear oils with special focus on churning losses.* Tribology International, 2013.
19. http://www.wittenstein-us.com/, *(visited 28, June, 2013).*
20. Barton, P.M.J., *A Forensic Investigation on Single Human Hair Fibres using FTIR-ATR Spectroscopy and Chemometrics*. 2011, Queensland University of Technology.
21. Neil E. Anderson, S.H.L., Joseph D. Black, *An Analytical Method To Predict Efficiency of Aircraft Gearboxes*. 1984, NASA.
22. Bernd-Robert Höhn, K.M.a.M.H., *OPTIMIZATION OF GEARBOX EFFICIENCY.* goriva i maziva, 2009. 48(4): p. 441-480.
23. Seabra, J., *Engrenagens - Lubrificação, Rendimento e Avarias.* Departamento de Engenharia Mecânica e Gestão Industrial, Porto, 2005. Secção de Mecânica Aplicada.
24. Higginson, D.D.e.G.R., *Elasto-hydrodynamic lubrication*. SI edition, ed. 1977, Oxford, UK: Pergamon Press.

25. Brandão, J.A., et al., *Comparative overview of five gear oils in mixed and boundary film lubrication.* Tribology International, 2012. 47: p. 50-61.
26. Simner, D., *Quantifying the potential fuel economy benefict of transmission lubricants.* Industrial and Automotive Lubrication, 1998. Vol. 2: p. 8.
27. Roux, F., *Notion de tribologie.* La Lubrifiaction Industrielle, Transmissions Compresseurs, Turbines, Publications de l'Institue Français du Pétrole, 1984. Tome 1.
28. P.W. Gold, A.S., H. Dicke, J. Loos, C. Assmann, *Viscosity-Pressure-Temperature Behaviour of Mineral and Synthetic oils.* Journal of Synthetic Lubrication, April 2001. Vol. 18(1): p. 51-79.
29. Fernandes, C.M.C.G., et al., *Torque loss in thrust ball bearings lubricated with wind turbine gear oils at constant temperature.* Tribology International, 2013. 66(0): p. 194-202.
30. *ISO-DIS 6336 part 4.* 1996.
31. Bernd-Robert Höhn, K.M., Thomas VoIlmer, *Thermal Rating of Gear Drives - Balance Between Power Loss and Heat Dissipation.* AGMA, 1996.
32. Wimmer, A.J., *Lastverluste von Stirnradverzahnungen*. 2005, Fakultät für Maschinenwesen der Technischen Universität München.
33. Terekhov, A., *Hydraulic losses in gearboxes with oil immersion.* Vestnik Mashinostroeniya, 1975. 55(5): p. 13-17.
34. Boos, E.L.a.M., *Zum Wärmehaushalt mechanischer Schaltgetriebe für Nutzfahrzeuge.* VDI-Berichte, 1983. vol. 488: p. pp. 45–55.
35. Boness, R.J. *Churning losses of discs and gears running partially submerged in oil*. 1989.
36. Seetharaman, S. and A. Kahraman, *Load-Independent Spin Power Losses of a Spur Gear Pair: Model Formulation.* Journal of Tribology, 2009. 131(2): p. 022201-022201.
37. C. Changenet, G.L., F. Ville, P. Velex, *A Note on Flow Regimes and Churning Loss Modeling.* Journal of Mechanical Design, 2011. 133.
38. LePrince, G., et al., *Influence of Aerated Lubricants on Gear Churning Losses–An Engineering Model.* Tribology Transactions, 2011. 54(6): p. 929-938.
39. Changenet, C. and P. Velex, *Housing Influence on Churning Losses in Geared Transmissions.* Journal of Mechanical Design, 2008. 130(6): p. 062603-062603.
40. SKF, *Rolling Bearings Catalogue 10000/1 EN.* February 2013.
41. http://webtools3.skf.com/BearingCalc/, *(visited 28, June, 2013).*
42. SKF, *Needle roller bearings Catalogue 06003/1 EN.* March 2010.
43. Eschmann, P., et al., *Ball and roller bearings: theory, design, and application*. 1985: R. Oldenbourg.
44. Bowen, E.R., *Wear Particle Atlas*. 1976: Foxboro Analytical.
45. Gorla, C., et al., *CFD Simulations of Splash Losses of a Gearbox.* Advances in Tribology, 2012. 2012: p. 1-10.

Appendix

A. Reports from the experimental tests

A.1. MINE Oil

Test number: 1	Date: 27/03/2013	By: Diogo Pereira
OIL:	MINE	
	Imposed working conditions	Units
n_{in}	100	rpm
TQ_{in}	500	N·m
Test period	240	min
	Actual working conditions (average of the last 30min)	Units
n_{in}	95.23	rpm
n_{out}	378.93	rpm
TQ_{in}	499.04	N·m
	Temperature readings (average of the last 30min)	Units
T_{oil} (M5 sensor)	47.48	$°C$
T_{wall}	44.05	$°C$
T_{oil} (M12 sensor)	46.02	$°C$
T_{amb}	24.84	$°C$
	Additional information	Units
ΔT	22.63	$°C$

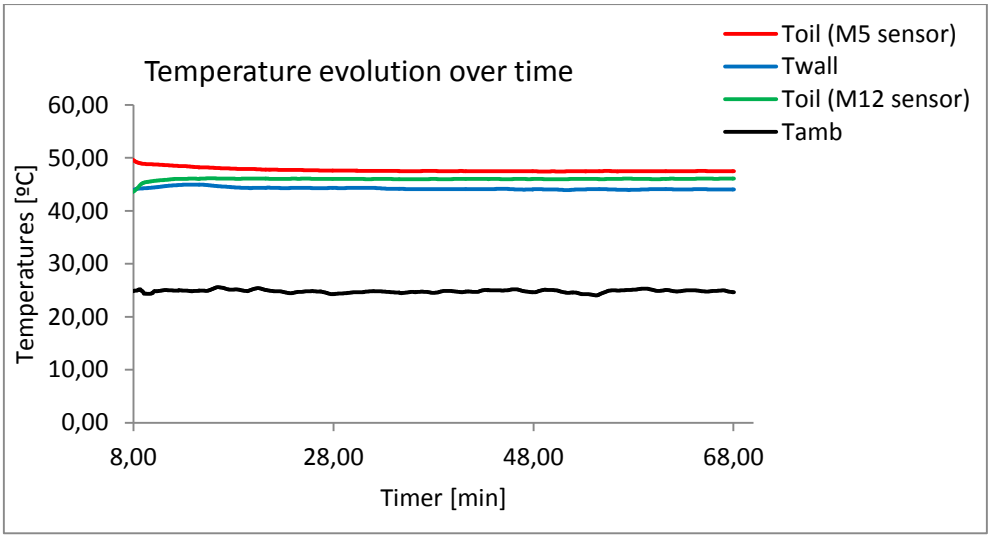

Test number: 2	Date: 28/03/2013	By: Diogo Pereira
OIL:	MINE	
	Imposed working conditions	Units
n_{in}	100	rpm
TQ_{in}	750	N·m
Test period	240	min
	Actual working conditions (average of the last 30min)	Units
n_{in}	96.24	rpm
n_{out}	382.57	rpm
TQ_{in}	749.48	N·m
	Temperature readings (average of the last 30min)	Units
T_{oil} (M5 sensor)	48.91	$°C$
T_{wall}	45.38	$°C$
T_{oil} (M12 sensor)	47.75	$°C$
T_{amb}	25.64	$°C$
	Additional information	Units
ΔT	23.26	$°C$

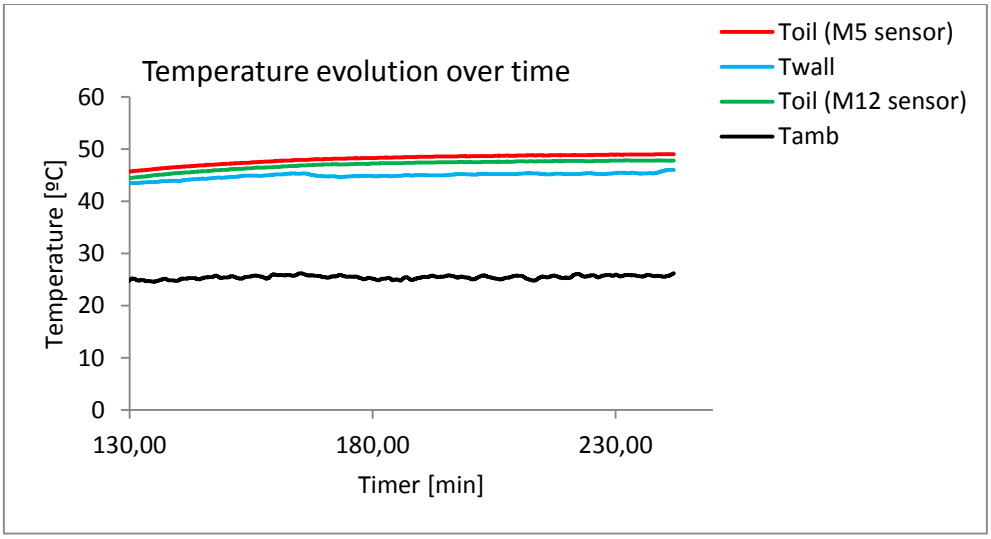

Test number: 3	Date: 28/03/2013	By: Diogo Pereira
OIL:	MINE	
	Imposed working conditions	Units
n_{in}	100	rpm
TQ_{in}	1000	N·m
Test period	240	min
	Actual working conditions (average of the last 30min)	Units
n_{in}	96.13	rpm
n_{out}	382.23	rpm
TQ_{in}	997.80	N·m
	Temperature readings (average of the last 30min)	Units
T_{oil} (M5 sensor)	50.54	$°C$
T_{wall}	46.82	$°C$
T_{oil} (M12 sensor)	49.71	$°C$
T_{amb}	26.90	$°C$
	Additional information	Units
ΔT	23.64	$°C$

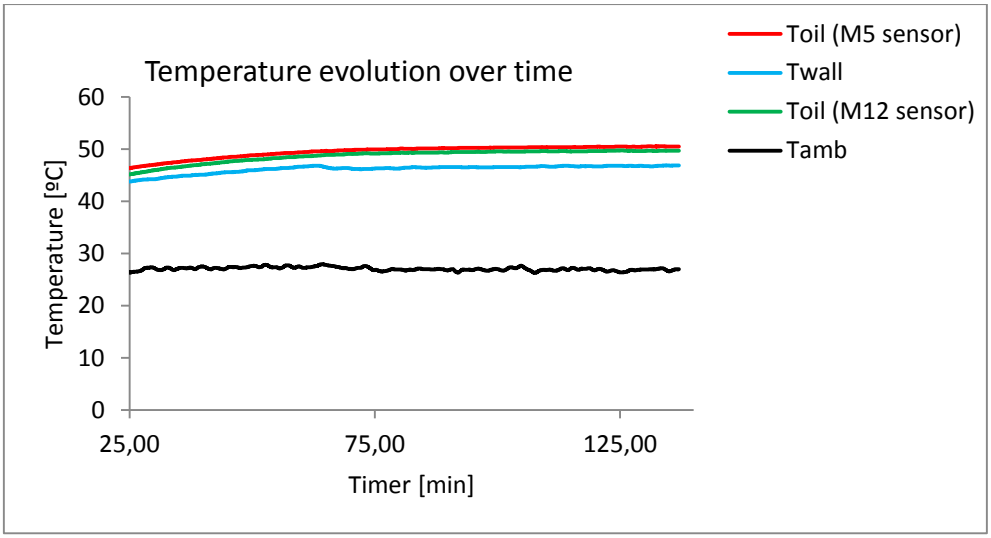

Test number: 4	Date: 01/04/2013	By: Diogo Pereira
OIL:	MINE	
	Imposed working conditions	Units
n_{in}	200	rpm
TQ_{in}	500	N·m
Test period	240	min
	Actual working conditions (average of the last 30min)	Units
n_{in}	196.05	rpm
n_{out}	784.25	rpm
TQ_{in}	500.69	N·m
	Temperature readings (average of the last 30min)	Units
T_{oil} (M5 sensor)	66.76	$°C$
T_{wall}	60.32	$°C$
T_{oil} (M12 sensor)	63.78	$°C$
T_{amb}	25.58	$°C$
	Additional information	Units
ΔT	41.18	$°C$

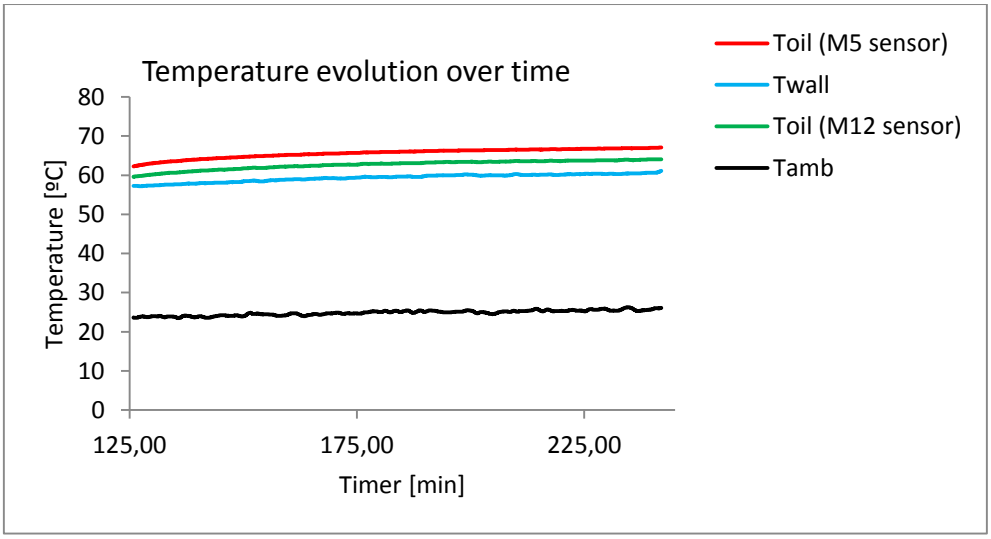

Test number: 5	Date: 01/04/2013	By: Diogo Pereira
OIL:	MINE	
	Imposed working conditions	Units
n_{in}	200	rpm
TQ_{in}	750	N·m
Test period	240	min
	Actual working conditions (average of the last 30min)	Units
n_{in}	196.01	rpm
n_{out}	784.15	rpm
TQ_{in}	748.98	N·m
	Temperature readings (average of the last 30min)	Units
T_{oil} (M5 sensor)	70.83	$°C$
T_{wall}	64.02	$°C$
T_{oil} (M12 sensor)	68.24	$°C$
T_{amb}	27.87	$°C$
	Additional information	Units
ΔT	42.96	$°C$

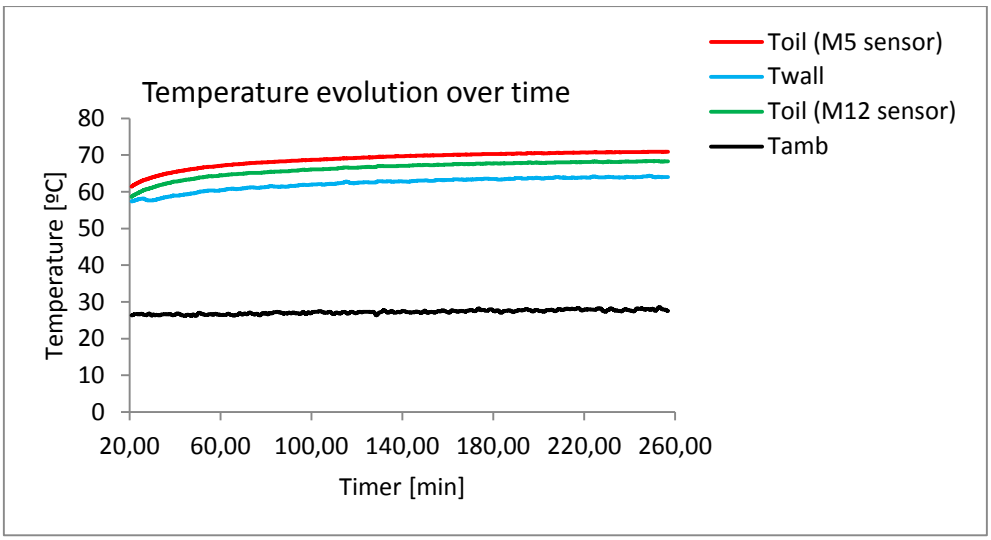

Test number: 6	Date: 02/04/2013	By: Diogo Pereira
OIL:	MINE	
	Imposed working conditions	Units
n_{in}	200	rpm
TQ_{in}	1000	N·m
Test period	240	min
	Actual working conditions (average of the last 30min)	Units
n_{in}	195.92	rpm
n_{out}	783.72	rpm
TQ_{in}	998.62	N·m
	Temperature readings (average of the last 30min)	Units
T_{oil} (M5 sensor)	66.76	$°C$
T_{wall}	60.32	$°C$
T_{oil} (M12 sensor)	63.78	$°C$
T_{amb}	25.58	$°C$
	Additional information	Units
ΔT	41.18	$°C$

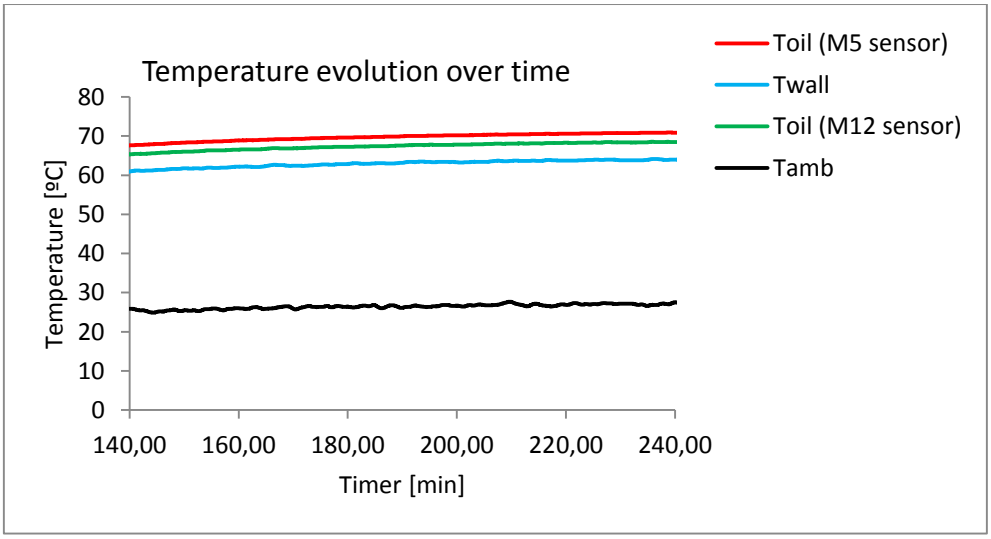

Test number: 7	Date: 02/04/2013	By: Diogo Pereira
OIL:	MINE	
	Imposed working conditions	Units
n_{in}	300	rpm
TQ_{in}	500	N·m
Test period	240	min
	Actual working conditions (average of the last 30min)	Units
n_{in}	296.25	rpm
n_{out}	1185.11	rpm
TQ_{in}	500.16	N·m
	Temperature readings (average of the last 30min)	Units
T_{oil} (M5 sensor)	84.66	$°C$
T_{wall}	76.04	$°C$
T_{oil} (M12 sensor)	80.34	$°C$
T_{amb}	30.36	$°C$
	Additional information	Units
ΔT	54.31	$°C$

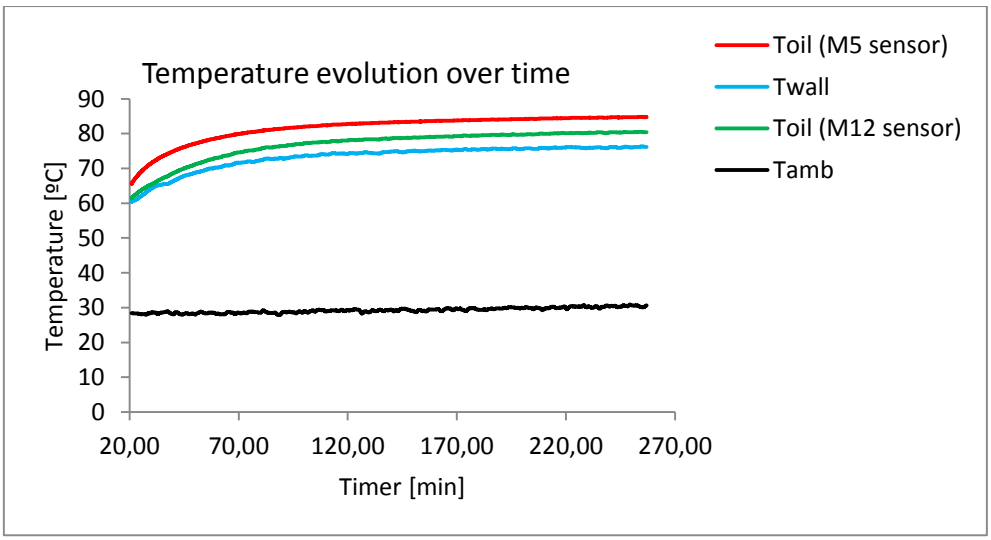

Test number: 8	Date: 03/04/2013	By: Diogo Pereira
OIL:	MINE	
	Imposed working conditions	Units
n_{in}	300	rpm
TQ_{in}	750	N·m
Test period	240	min
	Actual working conditions (average of the last 30min)	Units
n_{in}	296.22	rpm
n_{out}	1184.99	rpm
TQ_{in}	749.16	N·m
	Temperature readings (average of the last 30min)	Units
T_{oil} (M5 sensor)	86.11	$°C$
T_{wall}	77.17	$°C$
T_{oil} (M12 sensor)	82.02	$°C$
T_{amb}	28.98	$°C$
	Additional information	Units
ΔT	57.13	$°C$

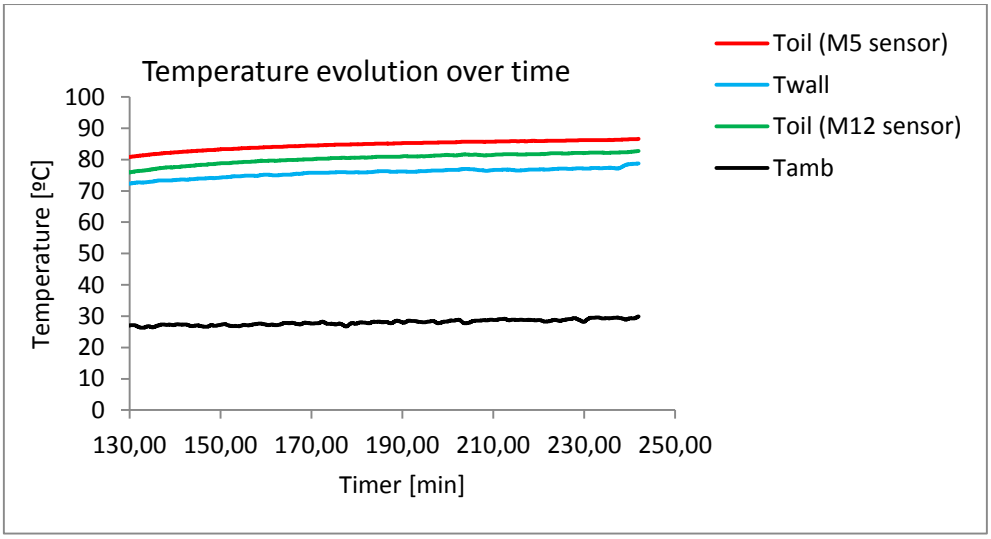

Test number: 9	Date: 03/04/2013	By: Diogo Pereira
OIL:	MINE	
	Imposed working conditions	Units
n_{in}	300	rpm
TQ_{in}	1000	N·m
Test period	240	min
	Actual working conditions (average of the last 30min)	Units
n_{in}	296.16	rpm
n_{out}	1184.65	rpm
TQ_{in}	998.64	N·m
	Temperature readings (average of the last 30min)	Units
T_{oil} (M5 sensor)	91.59	$°C$
T_{wall}	82.27	$°C$
T_{oil} (M12 sensor)	88.64	$°C$
T_{amb}	32.82	$°C$
	Additional information	Units
ΔT	58.77	$°C$

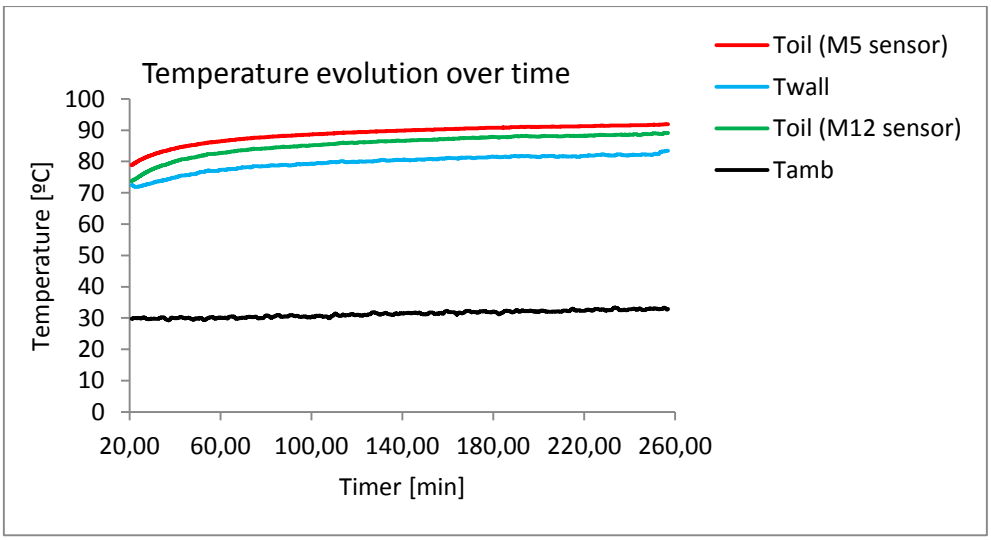

A.2. PAOR Oil

Test number: 10	Date: 08/04/2013	By: Diogo Pereira
OIL:	PAOR	
	Imposed working conditions	Units
n_{in}	100	rpm
TQ_{in}	500	N·m
Test period	240	min
	Actual working conditions (average of the last 30min)	Units
n_{in}	96.08	rpm
n_{out}	381.54	rpm
TQ_{in}	499.91	N·m
	Temperature readings (average of the last 30min)	Units
T_{oil} (M5 sensor)	45.68	$°C$
T_{wall}	42.50	$°C$
T_{oil} (M12 sensor)	44.17	$°C$
T_{amb}	22.49	$°C$
	Additional information	Units
ΔT	23.19	$°C$

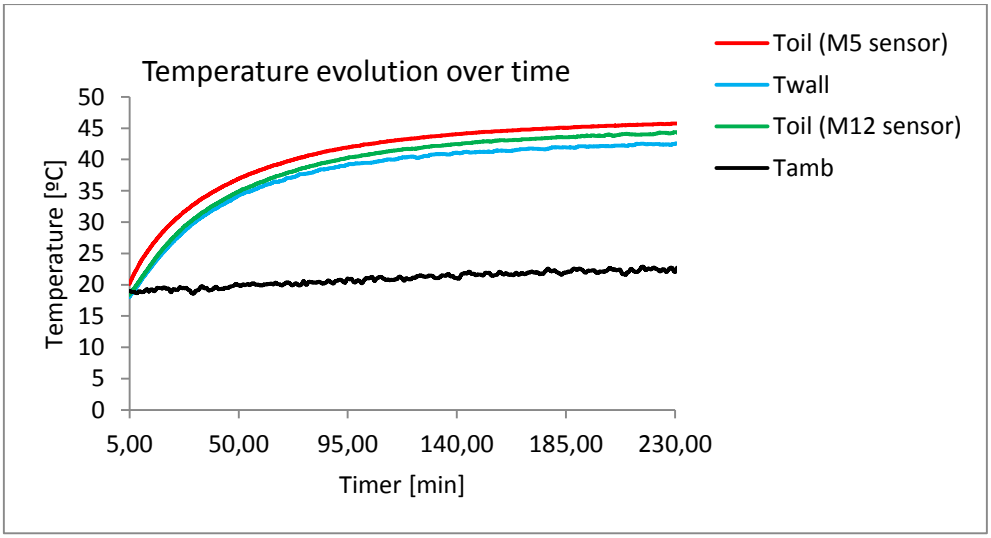

Test number: 11	Date: 09/04/2013	By: Diogo Pereira
OIL:	PAOR	
	Imposed working conditions	Units
n_{in}	100	rpm
TQ_{in}	750	N·m
Test period	240	min
	Actual working conditions (average of the last 30min)	Units
n_{in}	95.96	rpm
n_{out}	1149.99	rpm
TQ_{in}	749.93	N·m
	Temperature readings (average of the last 30min)	Units
T_{oil} (M5 sensor)	46.66	$°C$
T_{wall}	43.36	$°C$
T_{oil} (M12 sensor)	45.56	$°C$
T_{amb}	23.06	$°C$
	Additional information	Units
ΔT	23.60	$°C$

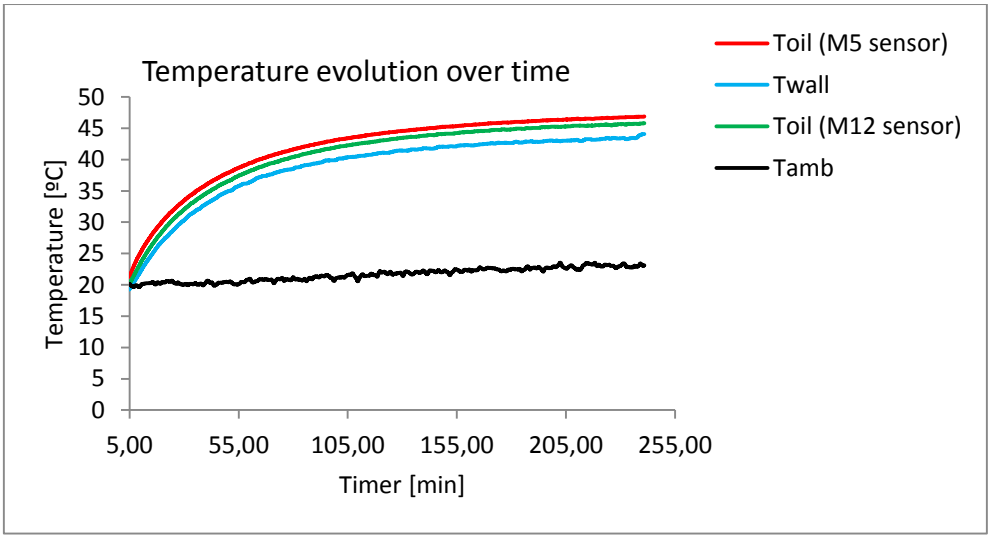

Test number: 12	Date: 09/04/2013	By: Diogo Pereira
OIL:	PAOR	
	Imposed working conditions	Units
n_{in}	100	rpm
TQ_{in}	1000	N·m
Test period	240	min
	Actual working conditions (average of the last 30min)	Units
n_{in}	95.81	rpm
n_{out}	381.68	rpm
TQ_{in}	998.31	N·m
	Temperature readings (average of the last 30min)	Units
T_{oil} (M5 sensor)	48.17	$°C$
T_{wall}	44.72	$°C$
T_{oil} (M12 sensor)	47.27	$°C$
T_{amb}	24.42	$°C$
	Additional information	Units
ΔT	23.75	$°C$

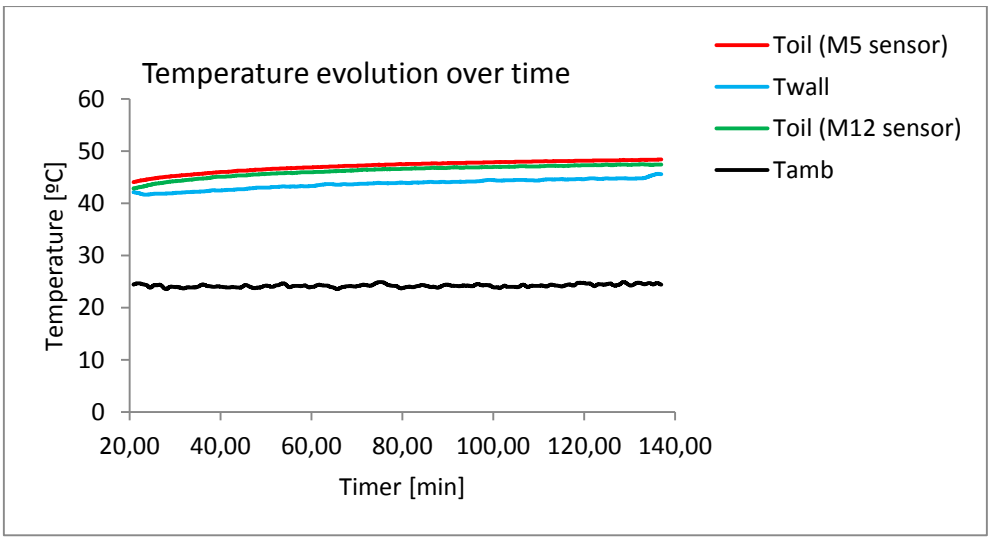

Test number: 13	Date: 09/04/2013	By: Diogo Pereira
OIL:	PAOR	
	Imposed working conditions	Units
n_{in}	200	rpm
TQ_{in}	500	N·m
Test period	240	min
	Actual working conditions (average of the last 30min)	Units
n_{in}	196.09	rpm
n_{out}	784.36	rpm
TQ_{in}	500.39	N·m
	Temperature readings (average of the last 30min)	Units
T_{oil} (M5 sensor)	65.20	$°C$
T_{wall}	59.39	$°C$
T_{oil} (M12 sensor)	61.90	$°C$
T_{amb}	25.92	$°C$
	Additional information	Units
ΔT	39.27	$°C$

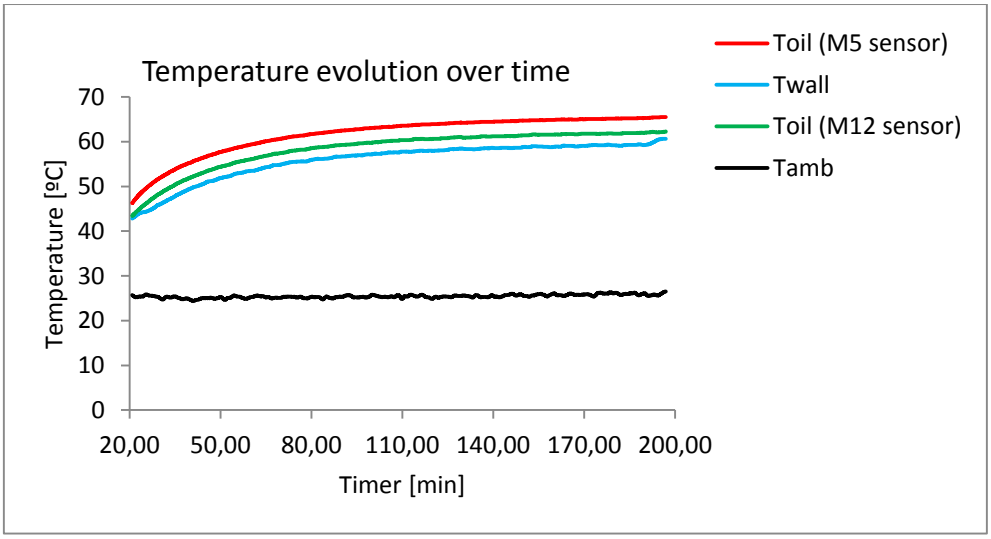

Test number: 14	Date: 10/04/2013	By: Diogo Pereira
OIL:	PAOR	
	Imposed working conditions	Units
n_{in}	200	rpm
TQ_{in}	750	N·m
Test period	240	min
	Actual working conditions (average of the last 30min)	Units
n_{in}	196.03	rpm
n_{out}	784.14	rpm
TQ_{in}	748.92	N·m
	Temperature readings (average of the last 30min)	Units
T_{oil} (M5 sensor)	67.11	$°C$
T_{wall}	61.13	$°C$
T_{oil} (M12 sensor)	63.72	$°C$
T_{amb}	25.56	$°C$
	Additional information	Units
ΔT	41.55	$°C$

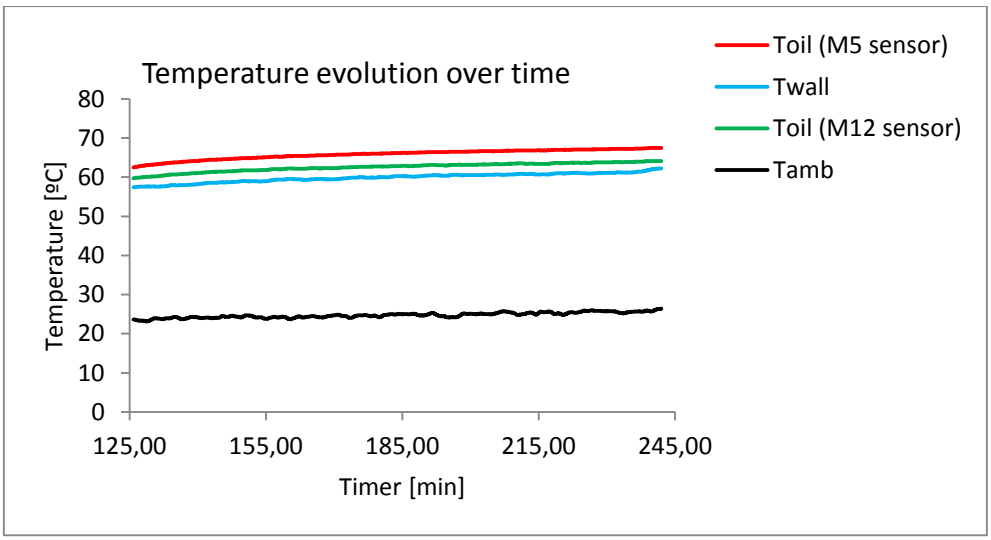

Test number: 15	Date: 10/04/2013	By: Diogo Pereira
OIL:	PAOR	
	Imposed working conditions	Units
n_{in}	200	rpm
TQ_{in}	1000	N·m
Test period	240	min
	Actual working conditions (average of the last 30min)	Units
n_{in}	195.96	rpm
n_{out}	783.88	rpm
TQ_{in}	997.82	N·m
	Temperature readings (average of the last 30min)	Units
T_{oil} (M5 sensor)	71.00	$°C$
T_{wall}	64.61	$°C$
T_{oil} (M12 sensor)	67.30	$°C$
T_{amb}	27.23	$°C$
	Additional information	Units
ΔT	43.77	$°C$

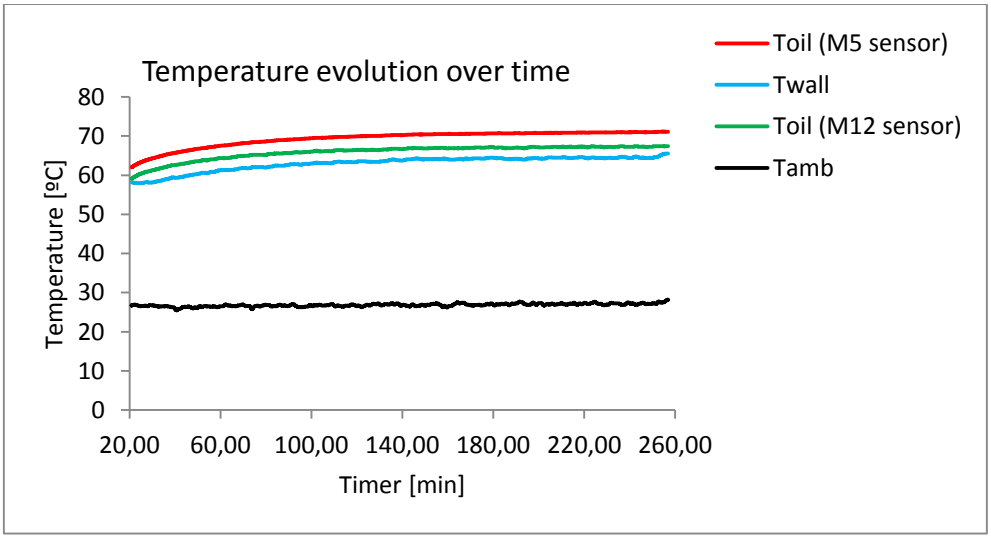

Test number: 16	Date: 11/04/2013	By: Diogo Pereira
OIL:	PAOR	
	Imposed working conditions	Units
n_{in}	300	rpm
TQ_{in}	500	N·m
Test period	240	min
	Actual working conditions (average of the last 30min)	Units
n_{in}	296.28	rpm
n_{out}	1185.23	rpm
TQ_{in}	499.86	N·m
	Temperature readings (average of the last 30min)	Units
T_{oil} (M5 sensor)	82.95	$°C$
T_{wall}	74.66	$°C$
T_{oil} (M12 sensor)	77.89	$°C$
T_{amb}	26.57	$°C$
	Additional information	Units
ΔT	56.38	$°C$

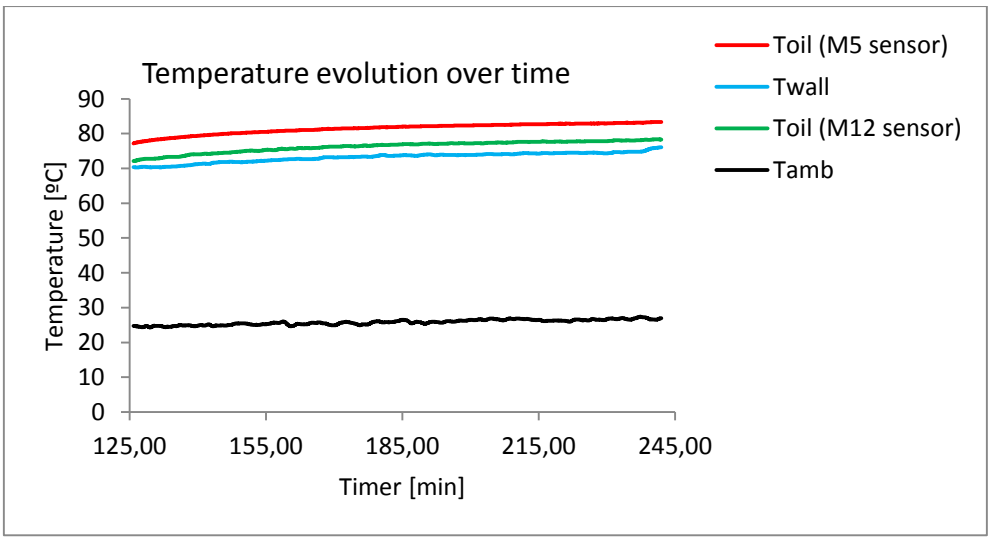

Test number: 17	Date: 11/04/2013	By: Diogo Pereira
OIL:	PAOR	
	Imposed working conditions	Units
n_{in}	300	rpm
TQ_{in}	750	N·m
Test period	240	min
	Actual working conditions (average of the last 30min)	Units
n_{in}	296.23	rpm
n_{out}	1184.83	rpm
TQ_{in}	748.59	N·m
	Temperature readings (average of the last 30min)	Units
T_{oil} (M5 sensor)	87.24	$°C$
T_{wall}	78.55	$°C$
T_{oil} (M12 sensor)	82.96	$°C$
T_{amb}	29.36	$°C$
	Additional information	Units
ΔT	57.88	$°C$

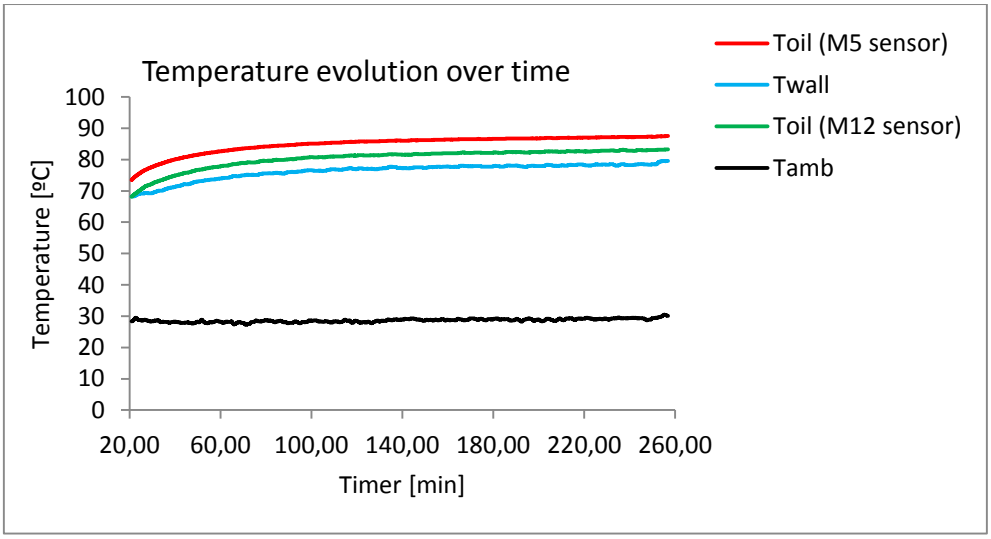

Test number: 18	Date: 12/04/2013	By: Diogo Pereira
OIL:	PAOR	
	Imposed working conditions	Units
n_{in}	300	rpm
TQ_{in}	1000	N·m
Test period	240	min
	Actual working conditions (average of the last 30min)	Units
n_{in}	296.19	rpm
n_{out}	1184.76	rpm
TQ_{in}	998.57	N·m
	Temperature readings (average of the last 30min)	Units
T_{oil} (M5 sensor)	87.08	$°C$
T_{wall}	78.52	$°C$
T_{oil} (M12 sensor)	83.00	$°C$
T_{amb}	28.44	$°C$
	Additional information	Units
ΔT	58.63	$°C$

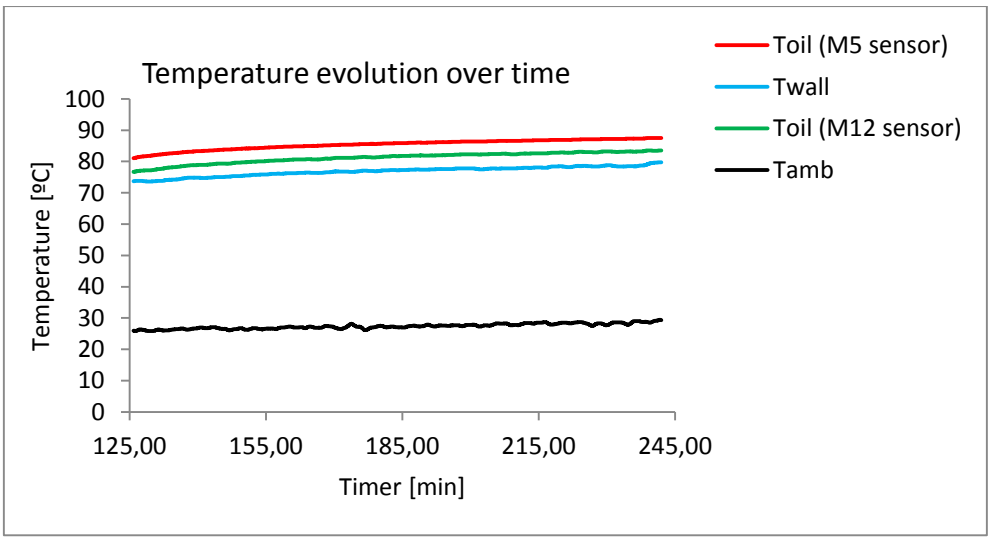

A.3. PAGD Oil

Test number: 19	Date: 16/04/2013	By: Diogo Pereira
OIL:	PAGD	
	Imposed working conditions	Units
n_{in}	100	rpm
TQ_{in}	500	N·m
Test period	240	min
	Actual working conditions (average of the last 30min)	Units
n_{in}	96.12	rpm
n_{out}	382.94	rpm
TQ_{in}	500.00	N·m
	Temperature readings (average of the last 30min)	Units
T_{oil} (M5 sensor)	50.06	$°C$
T_{wall}	46.63	$°C$
T_{oil} (M12 sensor)	48.30	$°C$
T_{amb}	25.04	$°C$
	Additional information	Units
ΔT	25.02	$°C$

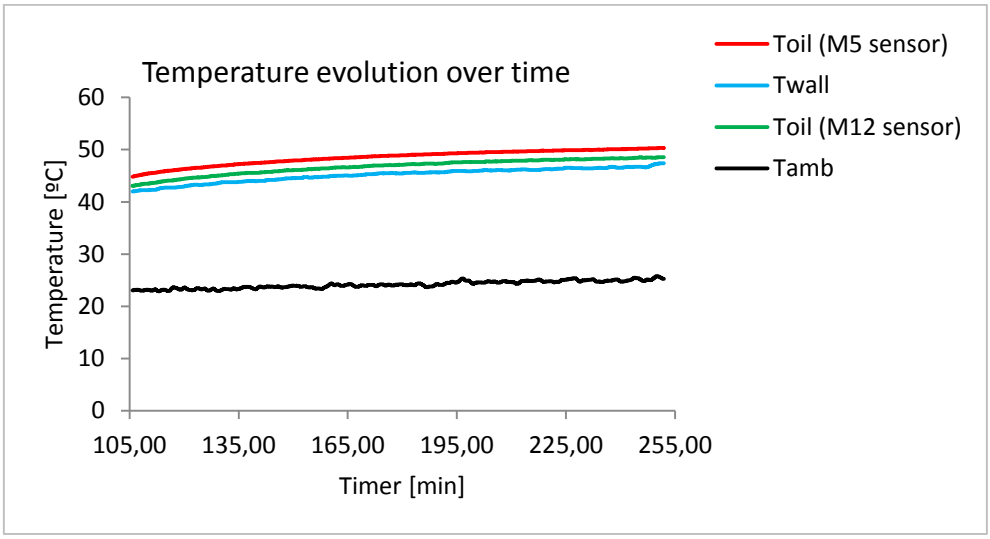

Test number: 20	Date: 16/04/2013	By: Diogo Pereira
OIL:	PAGD	
	Imposed working conditions	Units
n_{in}	100	rpm
TQ_{in}	750	N·m
Test period	240	min
	Actual working conditions (average of the last 30min)	Units
n_{in}	96.16	rpm
n_{out}	382.90	rpm
TQ_{in}	749.90	N·m
	Temperature readings (average of the last 30min)	Units
T_{oil} (M5 sensor)	52.90	$°C$
T_{wall}	49.19	$°C$
T_{oil} (M12 sensor)	51.64	$°C$
T_{amb}	27.00	$°C$
	Additional information	Units
ΔT	25.90	$°C$

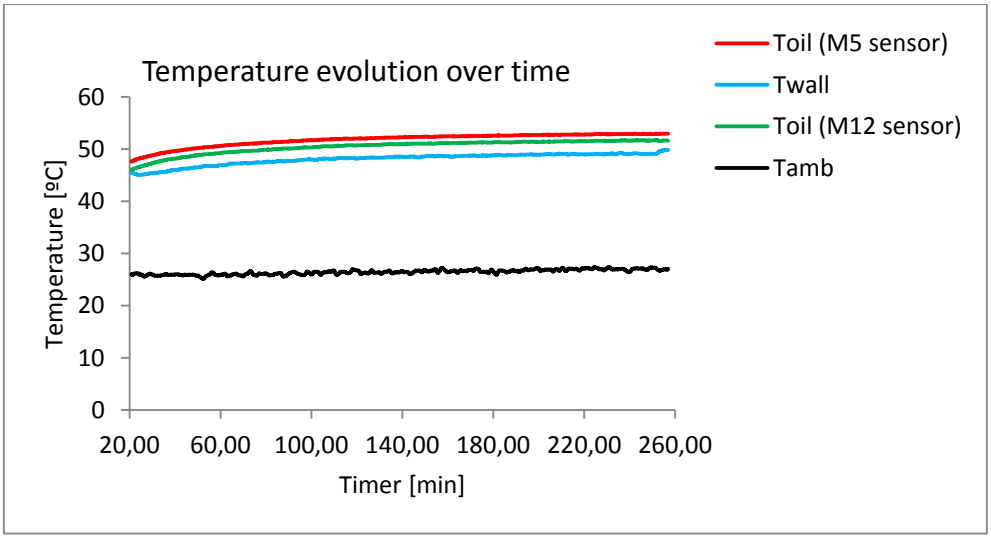

Test number: 21	Date: 17/04/2013	By: Diogo Pereira
OIL:	PAGD	
	Imposed working conditions	Units
n_{in}	100	rpm
TQ_{in}	1000	N·m
Test period	240	min
	Actual working conditions (average of the last 30min)	Units
n_{in}	96.12	rpm
n_{out}	382.59	rpm
TQ_{in}	998.07	N·m
	Temperature readings (average of the last 30min)	Units
T_{oil} (M5 sensor)	51.93	$°C$
T_{wall}	48.24	$°C$
T_{oil} (M12 sensor)	50.83	$°C$
T_{amb}	25.57	$°C$
	Additional information	Units
ΔT	26.36	$°C$

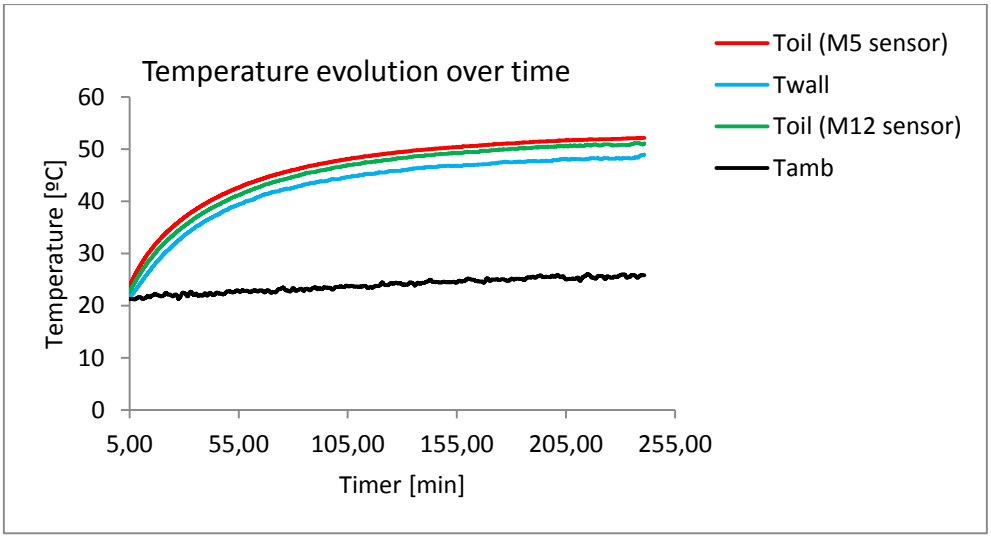

Test number: 22	Date: 17/04/2013	By: Diogo Pereira
OIL:	PAGD	
	Imposed working conditions	Units
n_{in}	200	rpm
TQ_{in}	500	N·m
Test period	240	min
	Actual working conditions (average of the last 30min)	Units
n_{in}	196.09	rpm
n_{out}	784.33	rpm
TQ_{in}	499.76	N·m
	Temperature readings (average of the last 30min)	Units
T_{oil} (M5 sensor)	73.64	$°C$
T_{wall}	67.00	$°C$
T_{oil} (M12 sensor)	69.99	$°C$
T_{amb}	28.42	$°C$
	Additional information	Units
ΔT	45.22	$°C$

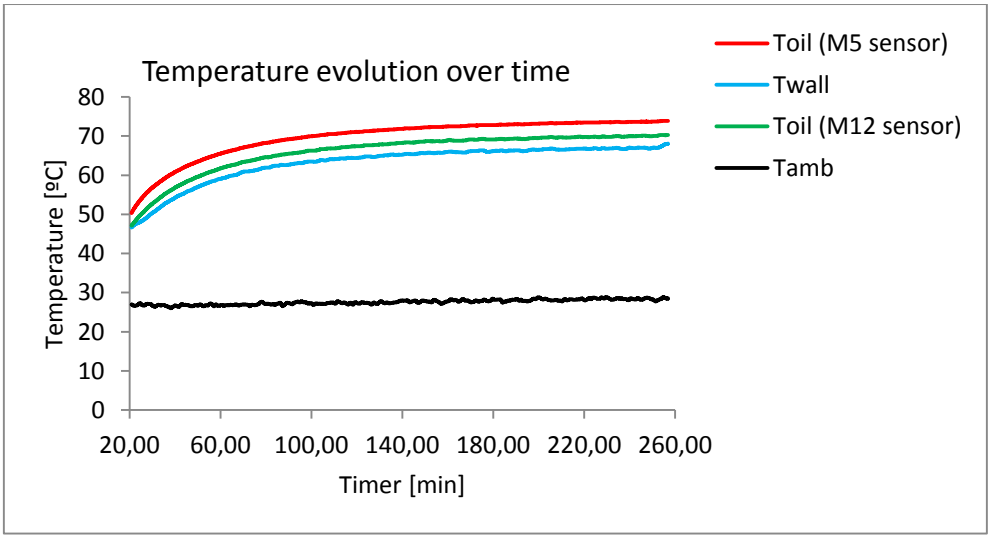

Test number: 23	Date: 18/04/2013	By: Diogo Pereira
OIL:	PAGD	
	Imposed working conditions	Units
n_{in}	200	rpm
TQ_{in}	750	N·m
Test period	240	min
	Actual working conditions (average of the last 30min)	Units
n_{in}	195.98	rpm
n_{out}	783.96	rpm
TQ_{in}	749.48	N·m
	Temperature readings (average of the last 30min)	Units
T_{oil} (M5 sensor)	75.88	$°C$
T_{wall}	68.92	$°C$
T_{oil} (M12 sensor)	72.27	$°C$
T_{amb}	27.25	$°C$
	Additional information	Units
ΔT	48.63	$°C$

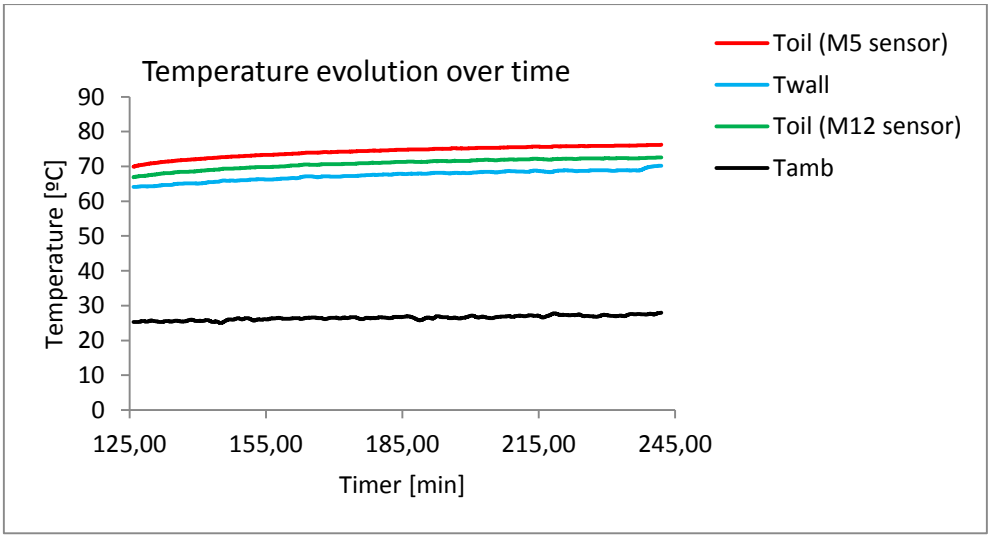

Test number: 24	Date: 18/04/2013	By: Diogo Pereira
OIL:	PAGD	
	Imposed working conditions	Units
n_{in}	200	rpm
TQ_{in}	1000	N·m
Test period	240	min
	Actual working conditions (average of the last 30min)	Units
n_{in}	195.95	rpm
n_{out}	783.89	rpm
TQ_{in}	998.28	N·m
	Temperature readings (average of the last 30min)	Units
T_{oil} (M5 sensor)	80.35	$°C$
T_{wall}	72.81	$°C$
T_{oil} (M12 sensor)	76.83	$°C$
T_{amb}	29.36	$°C$
	Additional information	Units
ΔT	51.00	$°C$

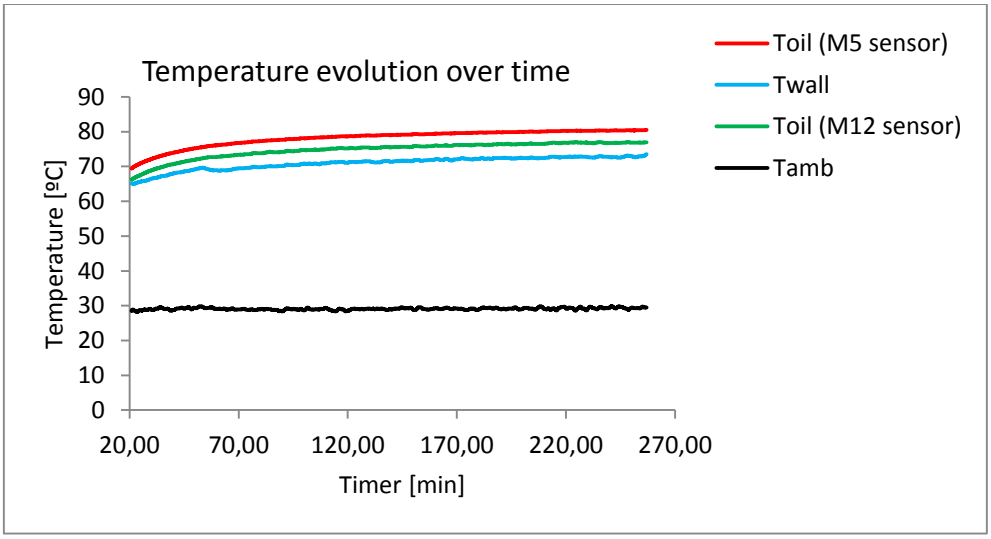

Test number: 25	Date: 17/04/2013	By: Diogo Pereira
OIL:	PAGD	
	Imposed working conditions	Units
n_{in}	300	rpm
TQ_{in}	500	N·m
Test period	240	min
	Actual working conditions (average of the last 30min)	Units
n_{in}	196.09	rpm
n_{out}	784.33	rpm
TQ_{in}	499.76	N·m
	Temperature readings (average of the last 30min)	Units
T_{oil} (M5 sensor)	73.64	$°C$
T_{wall}	67.00	$°C$
T_{oil} (M12 sensor)	69.99	$°C$
T_{amb}	28.42	$°C$
	Additional information	Units
ΔT	45.22	$°C$

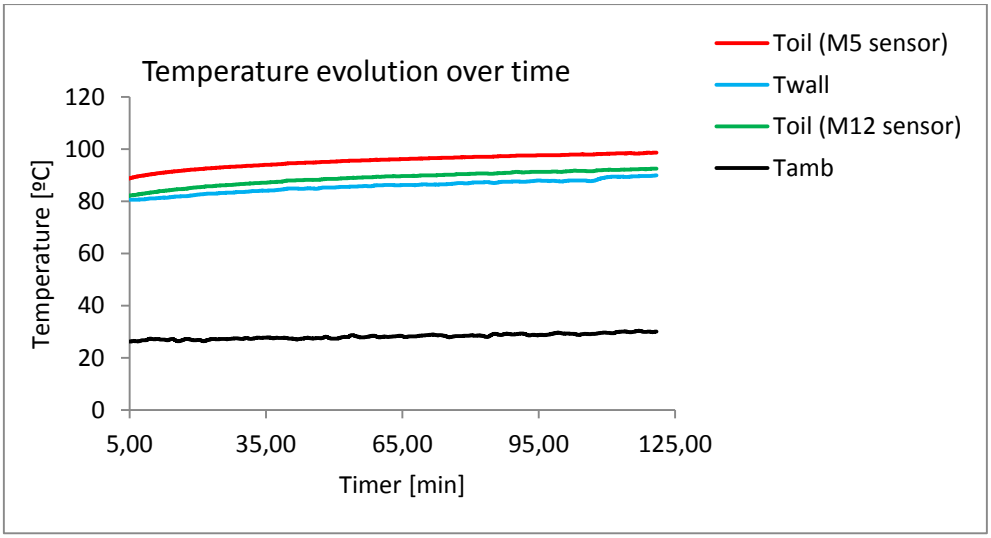

Test number: 26	Date: 18/04/2013	By: Diogo Pereira
OIL:	PAGD	
	Imposed working conditions	Units
n_{in}	300	rpm
TQ_{in}	750	N·m
Test period	240	min
	Actual working conditions (average of the last 30min)	Units
n_{in}	195.98	rpm
n_{out}	783.96	rpm
TQ_{in}	749.48	N·m
	Temperature readings (average of the last 30min)	Units
T_{oil} (M5 sensor)	75.88	$°C$
T_{wall}	68.92	$°C$
T_{oil} (M12 sensor)	72.27	$°C$
T_{amb}	27.25	$°C$
	Additional information	Units
ΔT	48.63	$°C$

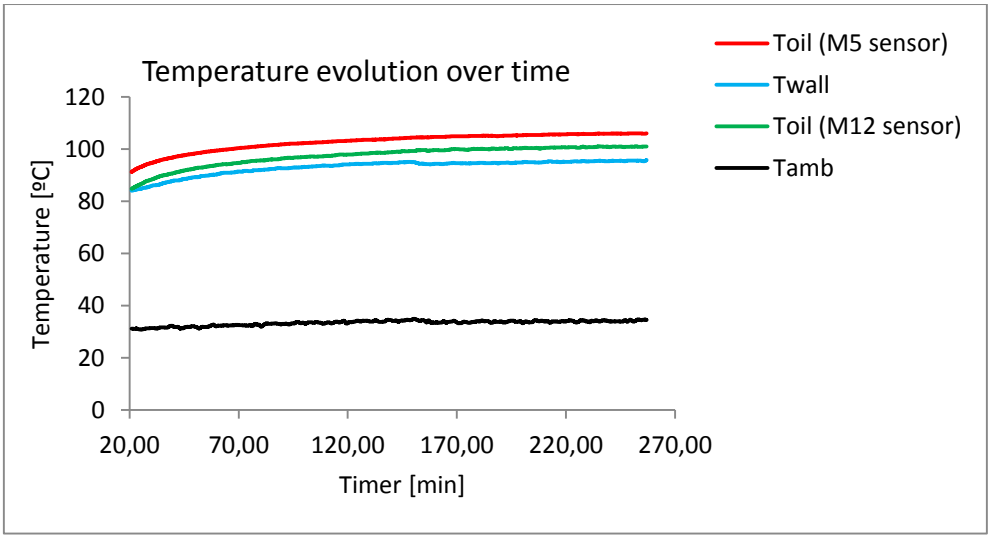

Test number: 27	Date: 18/04/2013	By: Diogo Pereira
OIL:	PAGD	
	Imposed working conditions	Units
n_{in}	300	rpm
TQ_{in}	1000	N·m
Test period	240	min
	Actual working conditions (average of the last 30min)	Units
n_{in}	195.95	rpm
n_{out}	783.89	rpm
TQ_{in}	998.28	N·m
	Temperature readings (average of the last 30min)	Units
T_{oil} (M5 sensor)	80.35	$°C$
T_{wall}	72.81	$°C$
T_{oil} (M12 sensor)	76.83	$°C$
T_{amb}	29.36	$°C$
	Additional information	Units
ΔT	51.00	$°C$

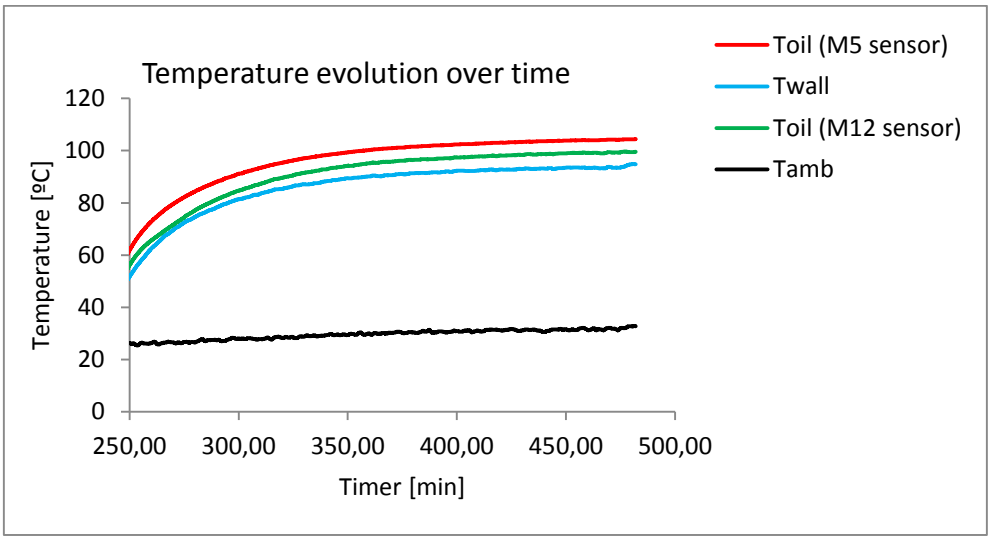

A.4. MINR Oil

Test number: 28	Date: 15/05/2013	By: Diogo Pereira
OIL:	MINR	
	Imposed working conditions	Units
n_{in}	100	rpm
TQ_{in}	500	N·m
Test period	240	min
	Actual working conditions (average of the last 30min)	Units
n_{in}	96.42	rpm
n_{out}	383.60	rpm
TQ_{in}	501.30	N·m
	Temperature readings (average of the last 30min)	Units
T_{oil} (M5 sensor)	47.02	$°C$
T_{wall}	45.08	$°C$
T_{oil} (M12 sensor)	46.51	$°C$
T_{amb}	27.90	$°C$
	Additional information	Units
ΔT	19.12	$°C$

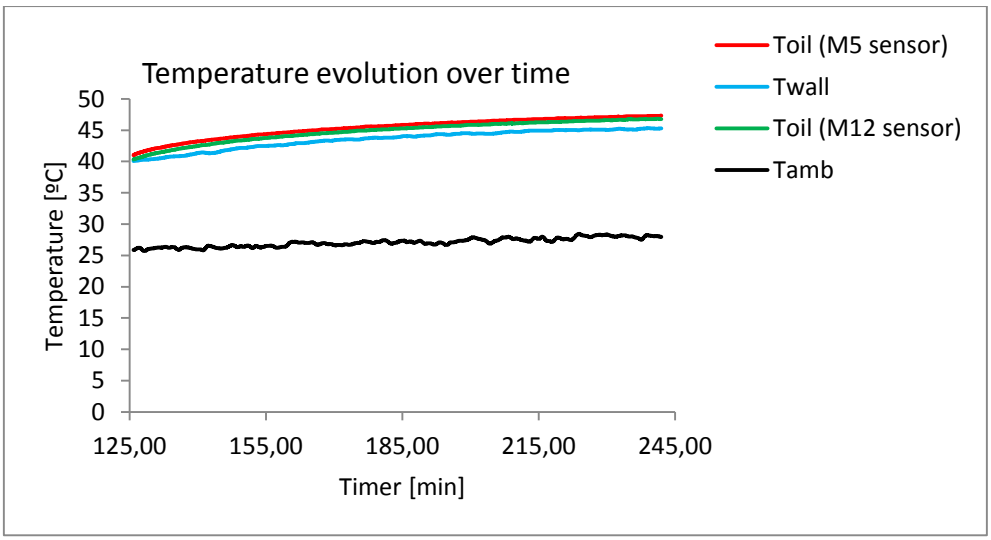

Test number: 29	Date: 16/05/2013	By: Diogo Pereira
OIL:	MINR	
	Imposed working conditions	Units
n_{in}	100	rpm
TQ_{in}	750	N·m
Test period	240	min
	Actual working conditions (average of the last 30min)	Units
n_{in}	96.38	rpm
n_{out}	383.39	rpm
TQ_{in}	749.88	N·m
	Temperature readings (average of the last 30min)	Units
T_{oil} (M5 sensor)	45.98	$°C$
T_{wall}	43.15	$°C$
T_{oil} (M12 sensor)	45.60	$°C$
T_{amb}	24.94	$°C$
	Additional information	Units
ΔT	21.05	$°C$

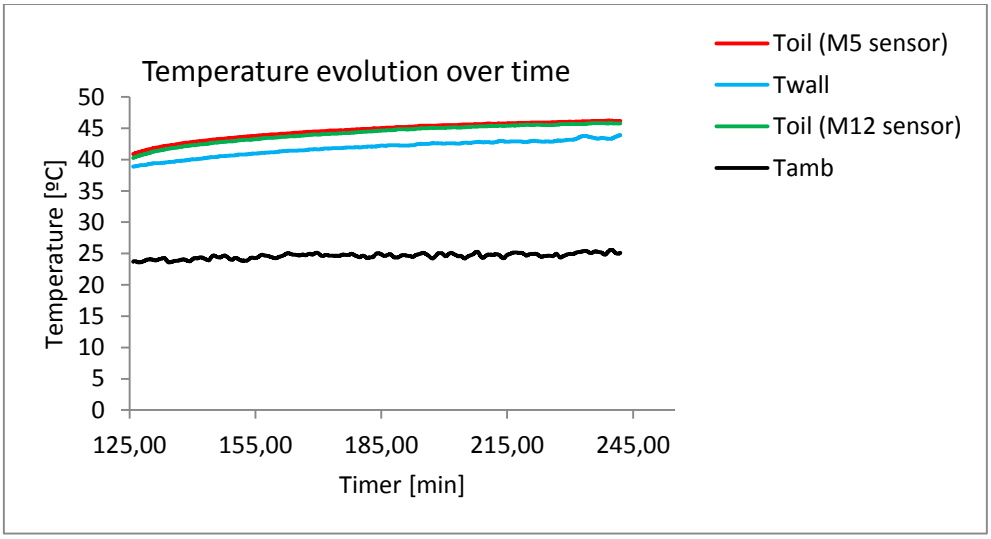

Test number: 30	Date: 16/05/2013	By: Diogo Pereira
OIL:	MINR	
	Imposed working conditions	Units
n_{in}	100	rpm
TQ_{in}	1000	N·m
Test period	240	min
	Actual working conditions (average of the last 30min)	Units
n_{in}	96.27	rpm
n_{out}	383.32	rpm
TQ_{in}	999.20	N·m
	Temperature readings (average of the last 30min)	Units
T_{oil} (M5 sensor)	48.15	$°C$
T_{wall}	45.04	$°C$
T_{oil} (M12 sensor)	48.14	$°C$
T_{amb}	26.13	$°C$
	Additional information	Units
ΔT	22.02	$°C$

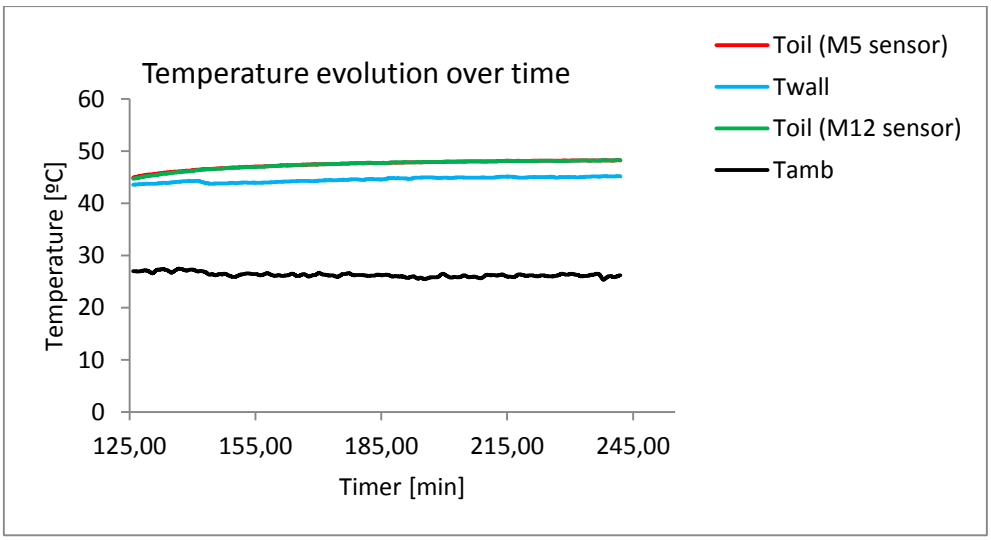

Test number: 31	Date: 17/05/2013	By: Diogo Pereira
OIL:	MINR	
	Imposed working conditions	Units
n_{in}	200	rpm
TQ_{in}	500	N·m
Test period	240	min
	Actual working conditions (average of the last 30min)	Units
n_{in}	196.11	rpm
n_{out}	784.46	rpm
TQ_{in}	500.28	N·m
	Temperature readings (average of the last 30min)	Units
T_{oil} (M5 sensor)	63.56	$°C$
T_{wall}	58.30	$°C$
T_{oil} (M12 sensor)	60.62	$°C$
T_{amb}	25.97	$°C$
	Additional information	Units
ΔT	37.59	$°C$

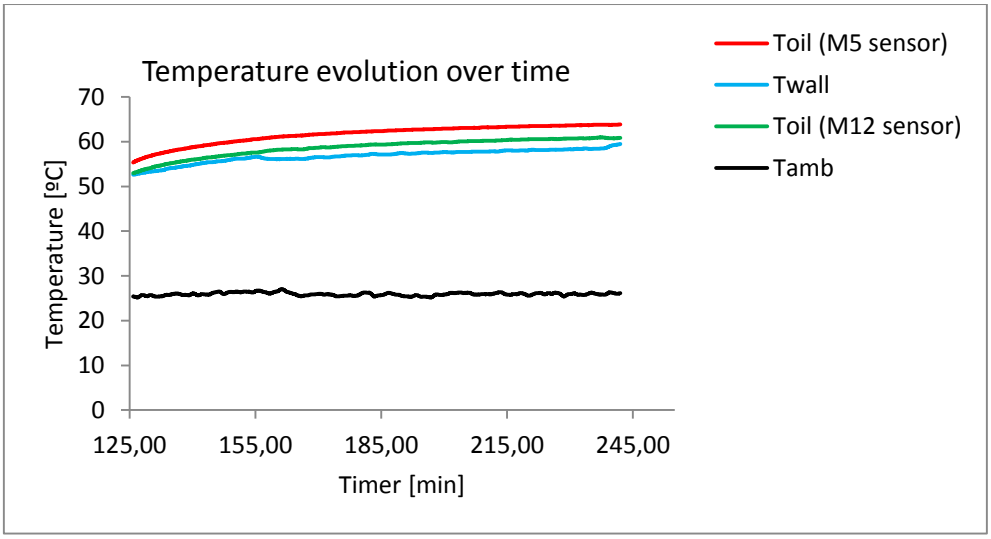

Test number: 32	Date: 17/05/2013	By: Diogo Pereira
OIL:	MINR	
	Imposed working conditions	Units
n_{in}	200	rpm
TQ_{in}	750	N·m
Test period	240	min
	Actual working conditions (average of the last 30min)	Units
n_{in}	196.09	rpm
n_{out}	784.35	rpm
TQ_{in}	748.52	N·m
	Temperature readings (average of the last 30min)	Units
T_{oil} (M5 sensor)	66.48	$°C$
T_{wall}	60.97	$°C$
T_{oil} (M12 sensor)	63.84	$°C$
T_{amb}	27.48	$°C$
	Additional information	Units
ΔT	39.00	$°C$

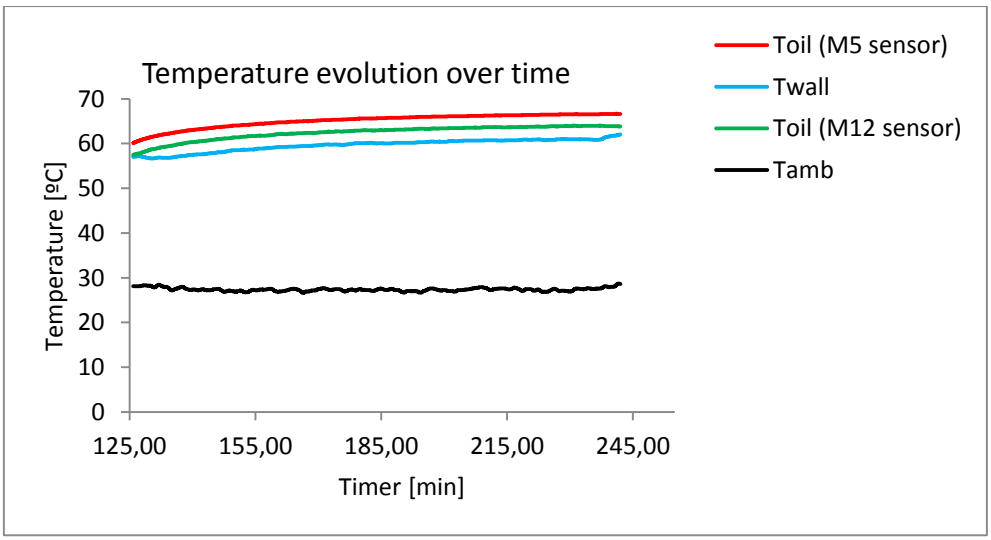

Test number: 33	Date: 20/05/2013	By: Diogo Pereira
OIL:	MINR	
	Imposed working conditions	Units
n_{in}	200	rpm
TQ_{in}	1000	N·m
Test period	240	min
	Actual working conditions (average of the last 30min)	Units
n_{in}	196.00	rpm
n_{out}	784.04	rpm
TQ_{in}	998.95	N·m
	Temperature readings (average of the last 30min)	Units
T_{oil} (M5 sensor)	66.22	$°C$
T_{wall}	60.91	$°C$
T_{oil} (M12 sensor)	63.85	$°C$
T_{amb}	25.91	$°C$
	Additional information	Units
ΔT	40.31	$°C$

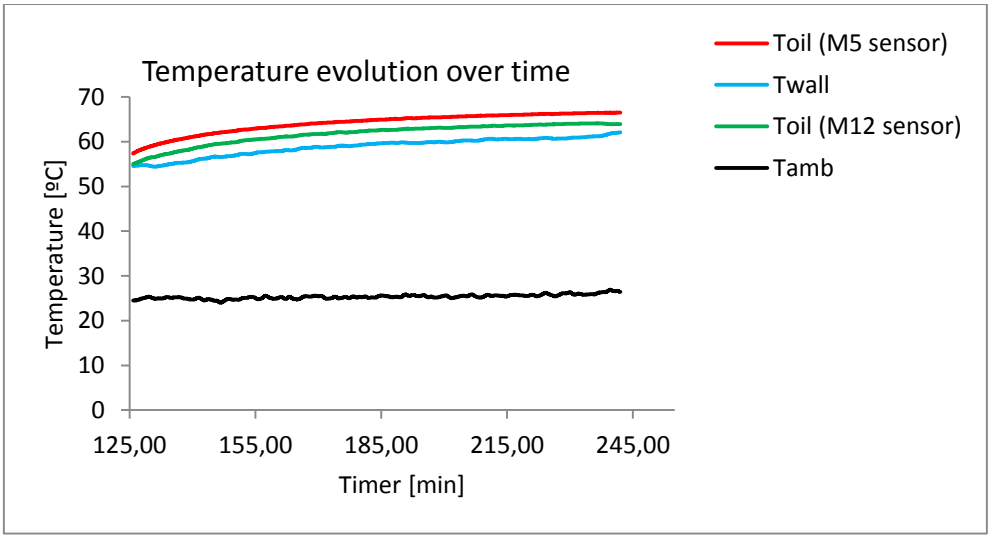

Test number: 34	Date: 14/05/2013	By: Diogo Pereira
OIL:	MINR	
	Imposed working conditions	Units
n_{in}	300	rpm
TQ_{in}	500	N·m
Test period	240	min
	Actual working conditions (average of the last 30min)	Units
n_{in}	309.89	rpm
n_{out}	1239.59	rpm
TQ_{in}	500.29	N·m
	Temperature readings (average of the last 30min)	Units
T_{oil} (M5 sensor)	82.18	$°C$
T_{wall}	74.65	$°C$
T_{oil} (M12 sensor)	79.60	$°C$
T_{amb}	28.33	$°C$
	Additional information	Units
ΔT	53.85	$°C$

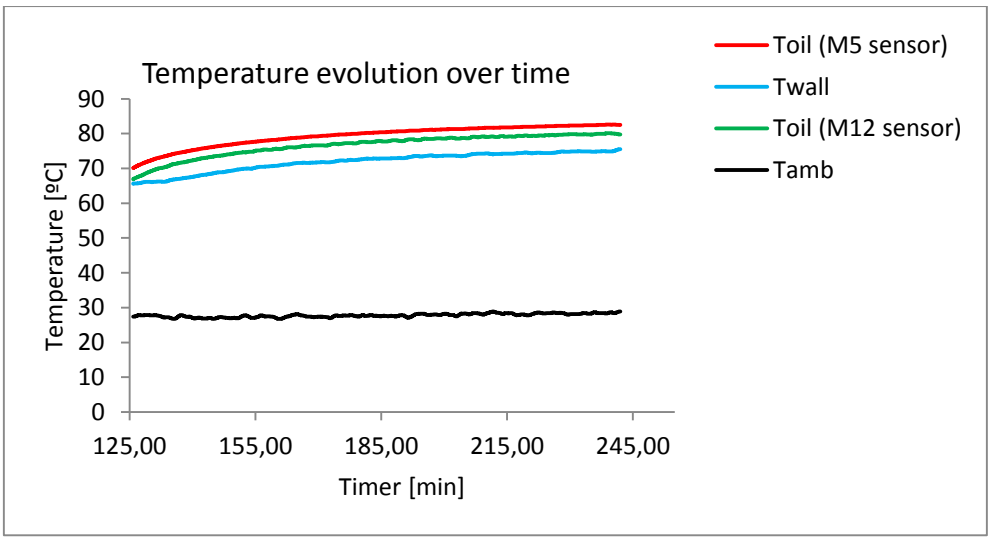

Test number: 35	Date: 13/05/2013	By: Diogo Pereira
OIL:	MINR	
	Imposed working conditions	Units
n_{in}	300	rpm
TQ_{in}	750	N·m
Test period	240	min
	Actual working conditions (average of the last 30min)	Units
n_{in}	296.25	rpm
n_{out}	1184.96	rpm
TQ_{in}	749.42	N·m
	Temperature readings (average of the last 30min)	Units
T_{oil} (M5 sensor)	79.01	$°C$
T_{wall}	72.17	$°C$
T_{oil} (M12 sensor)	77.46	$°C$
T_{amb}	29.56	$°C$
	Additional information	Units
ΔT	49.45	$°C$

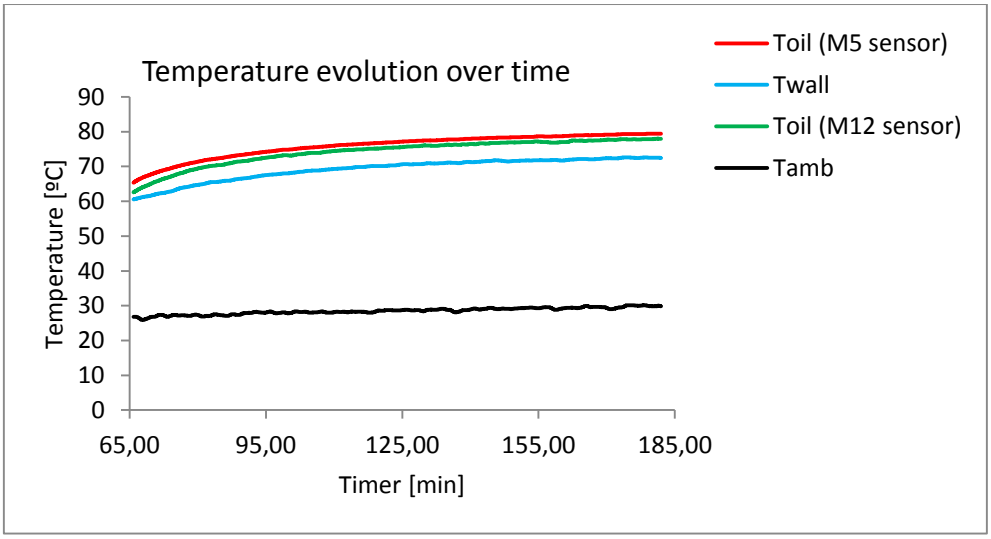

Test number: 36	Date: 14/05/2013	By: Diogo Pereira
OIL:	MINR	
	Imposed working conditions	Units
n_{in}	300	rpm
TQ_{in}	1000	N·m
Test period	240	min
	Actual working conditions (average of the last 30min)	Units
n_{in}	310.78	rpm
n_{out}	1243.23	rpm
TQ_{in}	998.77	N·m
	Temperature readings (average of the last 30min)	Units
T_{oil} (M5 sensor)	90.55	$°C$
T_{wall}	81.96	$°C$
T_{oil} (M12 sensor)	89.11	$°C$
T_{amb}	31.10	$°C$
	Additional information	Units
ΔT	59.45	$°C$

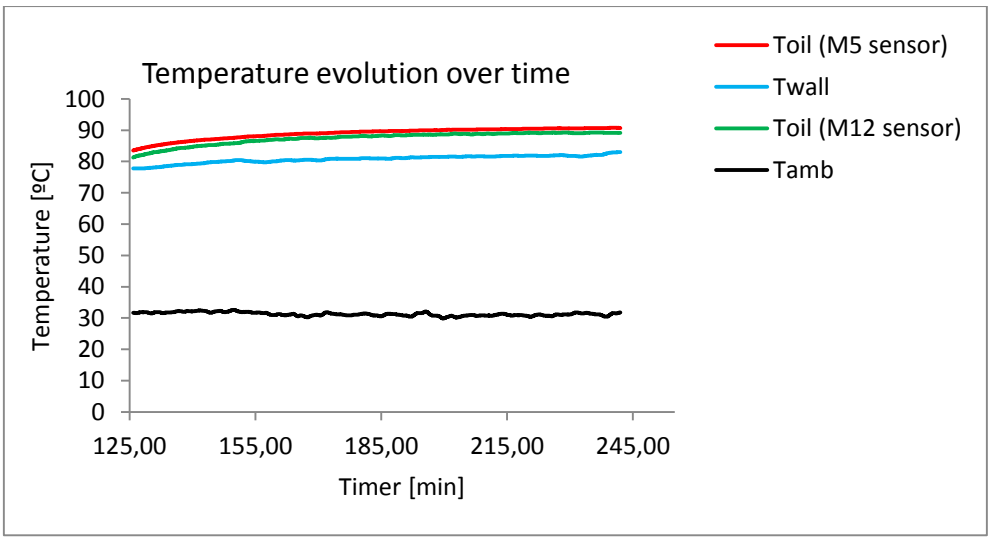

B. Lubricant Analysis Reports

B.1. MINE Oil

Relatório
de
Análise de Lubrificantes

Análise nº:	19 - 21 / 13
Tipo de análise:	Ferrometria e Ferrografia Analítica
Confidencialidade:	1
Cliente:	INEGI - Cetrib
Morada:	Porto
Telefone / Fax:	
Equipamento:	BANCO - Ensaios de Eficiência, Caixas Planetárias
Lubrificante:	Mineral E
Dossier:	/
Nº de páginas:	6
Data:	11/04/13
Responsável:	Beatriz Graça – Jorge Seabra
Rúbrica:	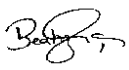 

OBJECTIVO

Análise de três amostras de óleo lubrificante MINE, resultantes de Ensaios de Eficiência no Banco de Ensaios com Caixas Planetárias para avaliação do desgaste presente.

As amostras analisadas foram as seguintes:

Amostra Nº (rpm)	Análises efectuadas	
	Ferrometria	Ferrografia Analítica
100	X	X
200	X	-
300	X	X

RESULTADOS DAS ANÁLISES

Nas páginas seguintes são apresentados os resultados referentes às análises de Ferrometria (DR III) e Ferrografia Analítica (FM III).

	CLIENTE: ***INEGI***			MÁQUINA: Caixas Planetárias (Banco)				
	MORADA: Porto			Ref. ÓLEO: MinE				
	DATA: 11/04/13			ENSAIOS de EFICIÊNCIA				
IDENTIFICAÇÃO								
Amostra nº:	100rpm	200rpm	300rpm					
Data amostra:	Abr-13	Abr-13	Abr-13					
Análise nº:	19/13	20/13	21/13					
Ciclos/Máquina:	-	-	-					
Ciclos/Óleo:	-	-	-					
FERROMETRIA								
d:	0,1	0,1	0,1					
DL:	73,1	74,2	53,4					
DS:	11,9	12,4	10,1					
CPUC:	850,0	866,0	635,0					
ISUC:	5,2E+05	5,4E+05	2,7E+05					
FERROGRAFIA:								
Desgaste normal								
Desgaste severo								
Desgaste de abrasão								
Desgaste combinado								
Desgaste fadiga								
Esferas Metálicas								
Polímeros de atrito								
Óxidos Vermelhos								
Minerais/Orgânicos								
OILVIEW:								
Índice OilLife:								
Índice Oxidação:								
Índice Contaminação:								
Índice Ferromagnético:								
Grandes Contaminantes:								
Constante Dieléctrica:								
FILTRAGEM								
(Nº Partículas/10 ml)								
5 - 15 µm								
15 - 25 µm								
25 - 50 µm								
50 - 100 µm								
> 100 µm								
VISCOSIDADE								
(cSt a 40° C):								
(cSt a 80° C):								
(cSt a 100° C):								
ACIDEZ (TAN)								
(mg KOH)								
P. INFLAMAÇÃO								
(° C)								
DIAGNÓSTICO:								

LEGENDA	**DL** - Índice de partículas grandes		Não existe
	DS - Índice de partículas pequenas	f	Fraco
	CPUC - Concentração de partículas de desgaste	M	Médio
	ISUC - Índice de severidade de desgaste	F	Forte

CLIENTE: ***INEGI***	MÁQUINA: Caixas Planetárias (Banco)
MORADA: Porto	Ref. ÓLEO: MinE 100RPM
DATA: 11/04/13	ENSAIOS de EFICIÊNCIA

Fotografia 1

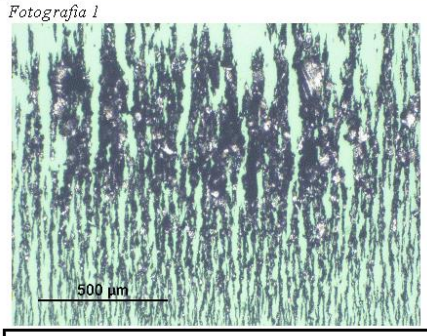

Fotografia 2

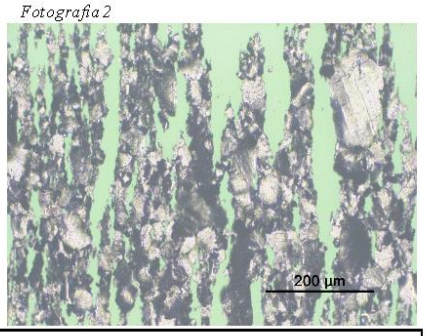

Ampliação: x 100 / x 200 Diluição: 0.1 Luz: Branca / Verde

Observações: Presença significativa de partículas ferrosas de grandes dimensões, algumas oxidadas.

Fotografia 3

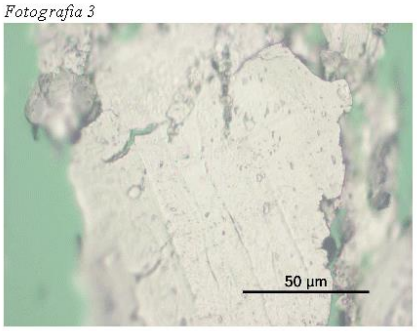

Fotografia 4

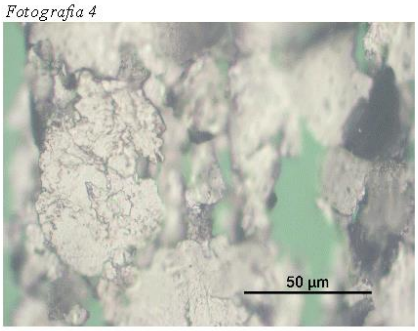

Ampliação: x 1000 Diluição: 0.1 Luz: Branca / Verde

Observações: Ampliações da Fotografia 2. Partículas ferrosas, de grandes dimensões, típicas de desgaste de fadiga.

Fotografia 5

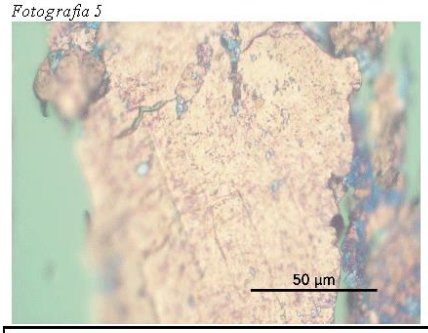

Fotografia 6

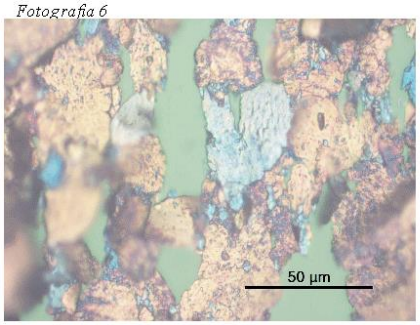

Ampliação: x 1000 Diluição: 0.1 Luz: Branca / Verde

Observações: Partículas anteriores após tratamento térmico. A mudança de tonalidade para azul significa que são partículas de aço de baixa liga e para tons acastanhados são partículas de média liga de aço.

CLIENTE: ***INEGI***	MÁQUINA: Caixas Planetárias (Banco)
MORADA: Porto	Ref. ÓLEO: MinE 300RPM
DATA: 11/04/13	ENSAIOS de EFICIÊNCIA

Fotografia 7

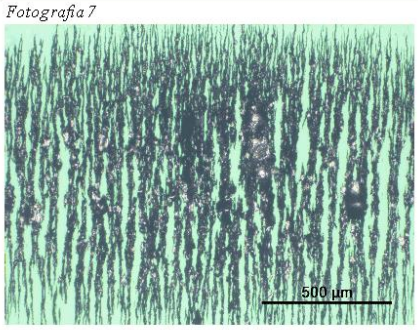

Fotografia 8

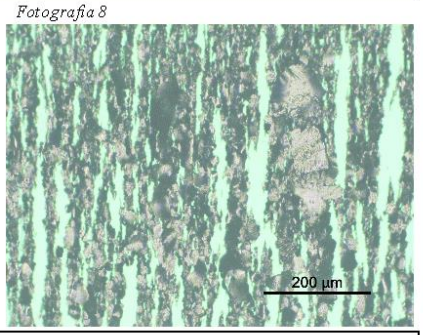

Ampliação: x 100 / x 200 Diluição: 0.1 Luz: Branca / Verde

Observações: Presença significativa de partículas ferrosas de grandes dimensões, algumas oxidadas.

Fotografia 9

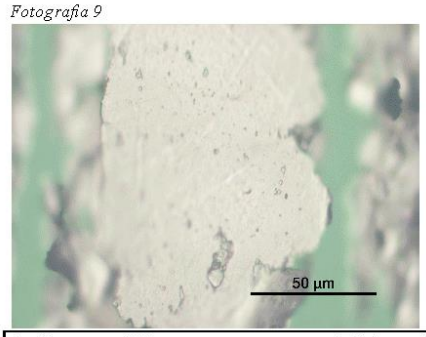

Fotografia 10

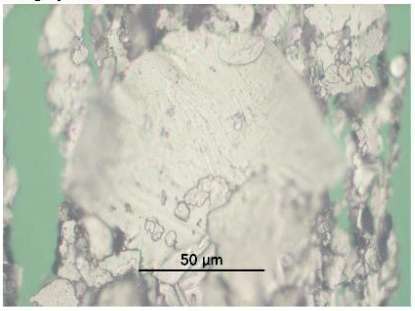

Ampliação: x 1000 Diluição: 0.1 Luz: Branca / Verde

Observações: Ampliações da Fotografia 8. Partículas ferrosas, de grandes dimensões, típicas de desgaste de fadiga.

Fotografia 11

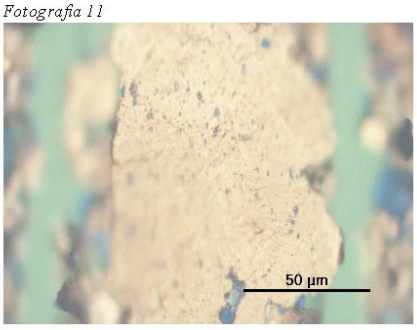

Fotografia 12

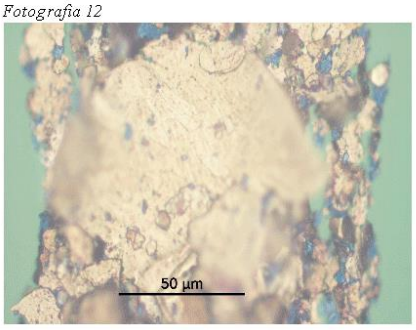

Ampliação: x 1000 Diluição: 0.1 Luz: Branca / Verde

Observações: Partículas anteriores após tratamento térmico. A mudança de tonalidade para azul significa que são partículas de aço de baixa liga e para tons acastanhados são partículas de média liga de aço.

B.2. PAOR Oil

Relatório
de
Análise de Lubrificantes

Análise nº:	42 - 44 / 13
Tipo de análise:	Ferrometria e Ferrografia Analítica
Confidencialidade:	1
Cliente:	INEGI - Cetrib
Morada:	Porto
Telefone / Fax:	
Equipamento:	BANCO - Ensaios de Eficiência, Caixas Planetárias
Lubrificante:	PAO R
Dossier:	/
Nº de páginas:	4
Data:	11/06/13
Responsável:	Beatriz Graça – Jorge Seabra
Rúbrica:	

OBJECTIVO

Análise de três amostras de óleo lubrificante PAOR, resultantes de Ensaios de Eficiência no Banco de Ensaios com Caixas Planetárias para avaliação do desgaste presente.

As amostras analisadas foram as seguintes:

Amostra Nº (rpm)	Análises efectuadas	
	Ferrometria	Ferrografia Analítica
100	X	-
200	X	-
300	X	X

RESULTADOS DAS ANÁLISES

Nas páginas seguintes são apresentados os resultados referentes às análises de Ferrometria (DR III) e Ferrografia Analítica (FM III).

	CLIENTE: *INEGI*			MÁQUINA: Caixas Planetárias (Banco)				
	MORADA: Porto			Ref. ÓLEO: PAOR				
	DATA: 11/06/13			ENSAIOS de EFICIÊNCIA				
IDENTIFICAÇÃO								
Amostra n°:	100rpm	200rpm	300rpm					
Data amostra:	Jun-13	Jun-13	Jun-13					
Análise n°:	42/13	43/13	44/13					
Ciclos/Máquina:	-	-	-					
Ciclos/Óleo:	-	-	-					
FERROMETRIA								
d:	0,1	0,1	0,1					
DL:	27,9	29,9	41,4					
DS:	5,8	2,6	4,9					
CPUC:	337,0	325,0	463,0					
ISUC:	7,4E+04	8,9E+04	1,7E+05					
FERROGRAFIA:								
Desgaste normal								
Desgaste severo								
Desgaste de abrasão								
Desgaste combinado								
Desgaste fadiga								
Esferas Metálicas								
Polímeros de atrito								
Óxidos Vermelhos								
Minerais/Orgânicos								
OILVIEW:								
Índice OilLife:								
Índice Oxidação:								
Índice Contaminação:								
Índice Ferromagnético:								
Grandes Contaminantes:								
Constante Dieléctrica:								
FILTRAGEM								
(Nº Partículas/10 ml)								
5 - 15 µm								
15 - 25 µm								
25 - 50 µm								
50 - 100 µm								
> 100 µm								
VISCOSIDADE								
(cSt a 40° C):								
(cSt a 80° C):								
(cSt a 100° C):								
ACIDEZ (TAN)								
(mg KOH)								
P. INFLAMAÇÃO								
(° C)								
DIAGNÓSTICO:								

LEGENDA	DL - Índice de partículas grandes		Não existe
	DS - Índice de partículas pequenas	f	Fraco
	CPUC - Concentração de partículas de desgaste	M	Médio
	ISUC - Índice de severidade de desgaste	F	Forte

CLIENTE: ***INEGI***	MÁQUINA: Caixas Planetárias (Banco)
MORADA: Porto	Ref. ÓLEO: PAOR **300RPM**
DATA: 11/06/13	ENSAIOS de EFICIÊNCIA

Fotografia 1

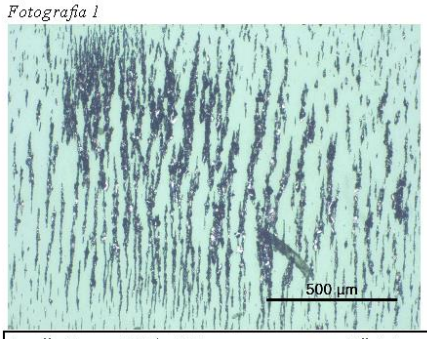

Fotografia 2

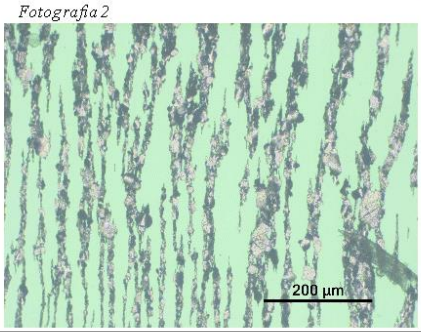

Ampliação: x 100 / x 200 Diluição: 0.1 Luz: Branca / Verde

Observações: Presença significativa de partículas ferrosas de grandes dimensões, algumas oxidadas.

Fotografia 3

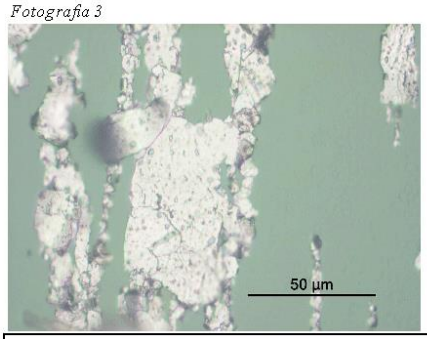

Fotografia 4

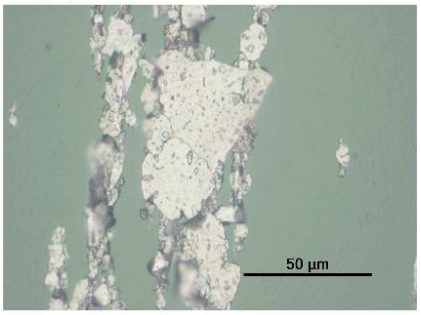

Ampliação: x 1000 Diluição: 0.1 Luz: Branca / Verde

Observações: Ampliações da Fotografia 2. Partículas ferrosas, de grandes dimensões, típicas de desgaste de fadiga.

Fotografia 5

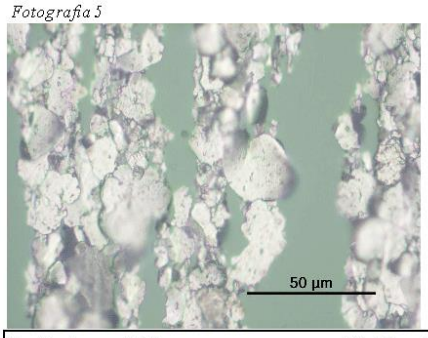

Fotografia 6

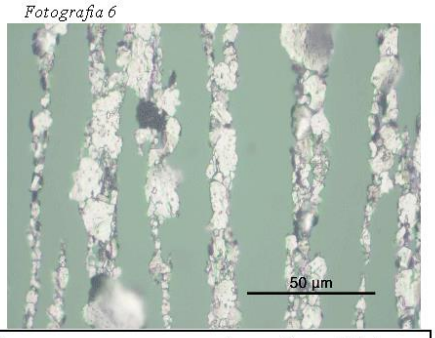

Ampliação: x 1000 Diluição: 0.1 Luz: Branca / Verde

Observações: Partículas ferrosas de desgaste típicas de micropitting (<30µm).

B.3. MINR Oil

Relatório
de
Análise de Lubrificantes

Análise nº:	16 - 18 / 13
Tipo de análise:	Ferrometria e Ferrografia Analítica
Confidencialidade:	1
Cliente:	INEGI - Cetrib
Morada:	Porto
Telefone / Fax:	
Equipamento:	BANCO - Ensaios de Eficiência, Caixas Planetárias
Lubrificante:	Mineral R
Dossier:	/
Nº de páginas:	6
Data:	11/04/13
Responsável:	Beatriz Graça – Jorge Seabra
Rúbrica:	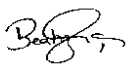 

OBJECTIVO

Análise de três amostras de óleo lubrificante MINR, resultantes de Ensaios de Eficiência no Banco de Ensaios com Caixas Planetárias para avaliação do desgaste presente.

As amostras analisadas foram as seguintes:

Amostra Nº (rpm)	Análises efectuadas	
	Ferrometria	Ferrografia Analítica
100	X	X
200	X	-
300	X	X

RESULTADOS DAS ANÁLISES

Nas páginas seguintes são apresentados os resultados referentes às análises de Ferrometria (DR III) e Ferrografia Analítica (FM III).

	CLIENTE: ***INEGI***			MÁQUINA: Caixas Planetárias (Banco)				
	MORADA: Porto			Ref. ÓLEO: MinR				
	DATA: 11/04/13			ENSAIOS de EFICIÊNCIA				
IDENTIFICAÇÃO								
Amostra nº:	100rpm	200rpm	300rpm					
Data amostra:	Abr-13	Abr-13	Abr-13					
Análise nº:	16/13	17/13	18/13					
Ciclos/Máquina:	-	-	-					
Ciclos/Óleo:	-	-	-					
FERROMETRIA								
d:	0,01	0,01	0,01					
DL:	44,3	48,7	50,6					
DS:	6,7	9,1	11,3					
CPUC:	5100,0	5780,0	6190,0					
ISUC:	1,9E+07	2,3E+07	2,4E+07					
FERROGRAFIA:								
Desgaste normal								
Desgaste severo								
Desgaste de abrasão								
Desgaste combinado								
Desgaste fadiga								
Esferas Metálicas								
Polímeros de atrito								
Óxidos Vermelhos								
Minerais/Orgânicos								
OILVIEW:								
Índice OilLife:								
Índice Oxidação:								
Índice Contaminação:								
Índice Ferromagnético:								
Grandes Contaminantes:								
Constante Dieléctrica:								
FILTRAGEM								
(Nº Partículas/10 ml)								
5 - 15 µm								
15 - 25 µm								
25 - 50 µm								
50 - 100 µm								
> 100 µm								
VISCOSIDADE								
(cSt a 40° C):								
(cSt a 80° C):								
(cSt a 100° C):								
ACIDEZ (TAN)								
(mg KOH)								
P. INFLAMAÇÃO								
(° C)								
DIAGNÓSTICO:								

LEGENDA	**DL** - Índice de partículas grandes		Não existe
	DS - Índice de partículas pequenas	f	Fraco
	CPUC - Concentração de partículas de desgaste	M	Médio
	ISUC - Índice de severidade de desgaste	F	Forte

CLIENTE: ***INEGI***	MÁQUINA: Caixas Planetárias (Banco)
MORADA: Porto	Ref. ÓLEO: MinR 100RPM
DATA: 11/04/13	ENSAIOS de EFICIÊNCIA

Fotografia 1

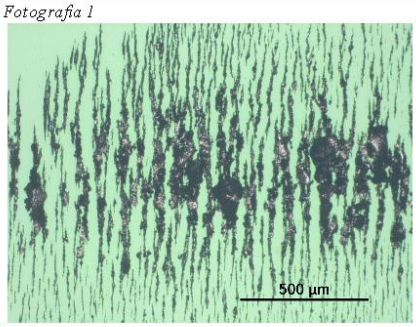

Fotografia 2

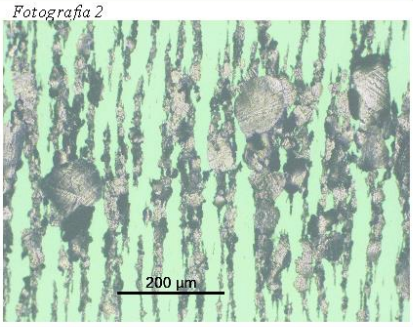

Ampliação: x 100 / x 200 Diluição: 0.01 Luz: Branca / Verde

Observações: Presença significativa de partículas ferrosas de grandes dimensões, algumas oxidadas.

Fotografia 3

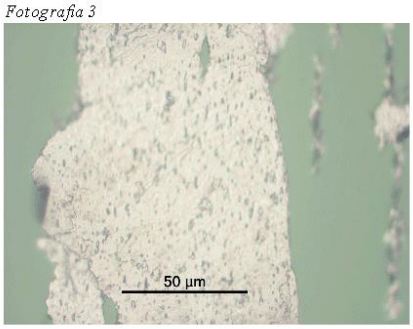

Fotografia 4

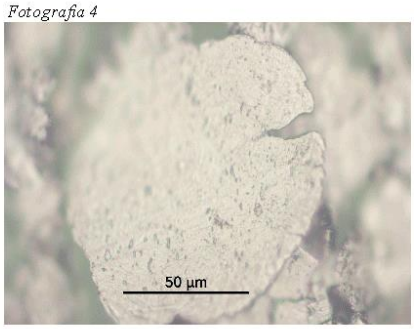

Ampliação: x 1000 Diluição: 0.01 Luz: Branca / Verde

Observações: Ampliações da Fotografia 2. Partículas ferrosas, de grandes dimensões, típicas de desgaste de fadiga.

Fotografia 5

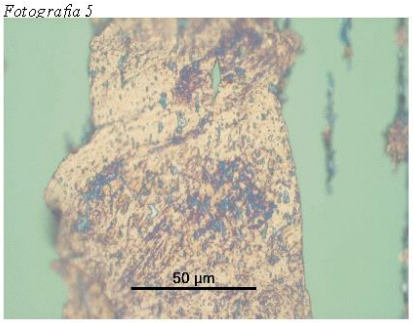

Fotografia 6

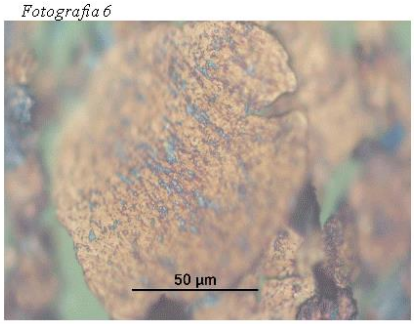

Ampliação: x 1000 Diluição: 0.01 Luz: Branca / Verde

Observações: Partículas anteriores após tratamento térmico. A mudança de tonalidade para azul significa que são partículas de aço de baixa liga e para tons acastanhados são partículas de média liga de aço.

CLIENTE: ***INEGI***	MÁQUINA: Caixas Planetárias (Banco)
MORADA: Porto	Ref. ÓLEO: MinR 500RPM
DATA: 11/04/13	ENSAIOS de EFICIÊNCIA

Fotografia 7

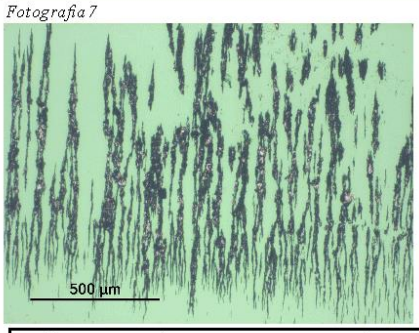

Fotografia 8

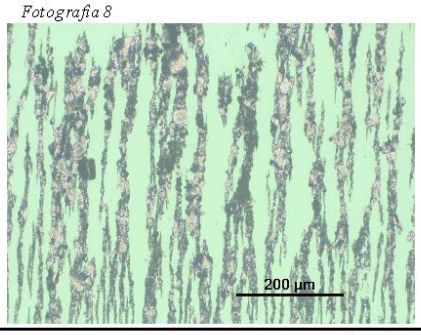

Ampliação: x 100 / x 200 Diluição: 0.01 Luz: Branca / Verde

Observações: Presença significativa de partículas ferrosas de pequenas e grandes dimensões.

Fotografia 9

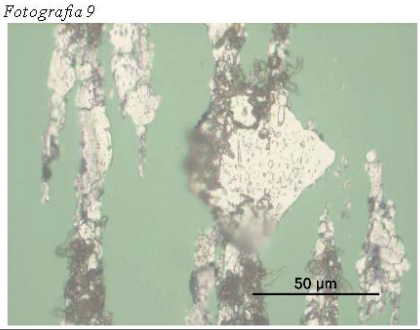

Fotografia 10

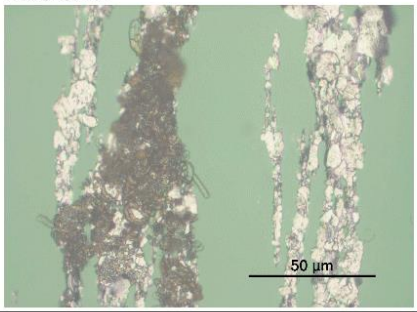

Ampliação: x 1000 Diluição: 0.01 Luz: Branca / Verde

Observações: Ampliações da Fotografia 8. Partículas ferrosas, algumas de grandes dimensões outras revestidas com polímeros de atrito.

Fotografia 11

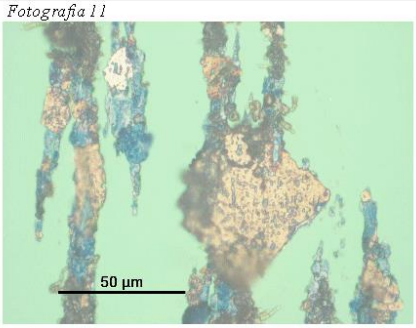

Fotografia 12

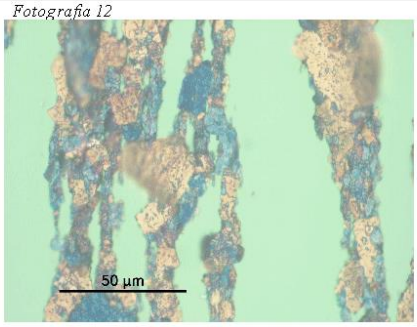

Ampliação: x 1000 Diluição: 0.01 Luz: Branca / Verde

Observações: Partículas anteriores após tratamento térmico. A mudança de tonalidade para azul significa que são partículas de aço de baixa liga e para tons acastanhados são partículas de média liga de aço.

B.4. PAGD oil

Relatório
de
Análise de Lubrificantes

Análise nº:	48 - 53 / 13
Tipo de análise:	Ferrometria e Ferrografia Analítica
Confidencialidade:	1
Cliente:	INEGI - Cetrib
Morada:	Porto
Telefone / Fax:	
Equipamento:	BANCO - Ensaios de Eficiência, Caixas Planetárias
Lubrificante:	PAG
Dossier:	/
Nº de páginas:	4
Data:	13/06/13
Responsável:	Beatriz Graça – Jorge Seabra
Rúbrica:	

OBJECTIVO

Análise de três amostras de óleo lubrificante PAG, resultantes de Ensaios de Eficiência no Banco de Ensaios com Caixas Planetárias para avaliação do desgaste presente.

As amostras analisadas foram as seguintes:

Amostra Nº (rpm)	Análises efectuadas	
	Ferrometria	Ferrografia Analítica
100	X	-
200	X	-
300	X	X

RESULTADOS DAS ANÁLISES

Nas páginas seguintes são apresentados os resultados referentes às análises de Ferrometria (DR III) e Ferrografia Analítica (FM III).

	CLIENTE: ***INEGI***			MÁQUINA: Caixas Planetárias (Banco)				
	MORADA: Porto			Ref. ÓLEO: PAG				
	DATA: 13/06/13			ENSAIOS de EFICIÊNCIA				
IDENTIFICAÇÃO								
Amostra nº:	100rpm	200rpm	300rpm					
Data amostra:	Jun-13	Jun-13	Jun-13					
Análise nº:	48/13	52/13	53/13					
Ciclos/Máquina:	-	-	-					
Ciclos/Óleo:	-	-	-					
FERROMETRIA								
d:	0,1	0,1	0,1					
DL:	4,5	14,3	31,4					
DS:	1,6	11,1	18,8					
CPUC:	61,0	254,0	502,0					
ISUC:	1,8E+03	8,1E+03	6,3E+04					
FERROGRAFIA:								
Desgaste normal								
Desgaste severo								
Desgaste de abrasão								
Desgaste combinado								
Desgaste fadiga								
Esferas Metálicas								
Polímeros de atrito								
Óxidos Vermelhos								
Minerais/Orgânicos								
OILVIEW:								
Índice OilLife:								
Índice Oxidação:								
Índice Contaminação:								
Índice Ferromagnético:								
Grandes Contaminantes:								
Constante Dieléctrica:								
FILTRAGEM								
(Nº Partículas/10 ml)								
5 - 15 µm								
15 - 25 µm								
25 - 50 µm								
50 - 100 µm								
> 100 µm								
VISCOSIDADE								
(cSt a 40° C):								
(cSt a 80° C):								
(cSt a 100° C):								
ACIDEZ (TAN)								
(mg KOH)								
P. INFLAMAÇÃO								
(° C)								
DIAGNÓSTICO:								

LEGENDA			
	DL - Índice de partículas grandes		Não existe
	DS - Índice de partículas pequenas	f	Fraco
	CPUC - Concentração de partículas de desgaste	M	Médio
	ISUC - Índice de severidade de desgaste	F	Forte

CLIENTE: ***INEGI***	MÁQUINA: Caixas Planetárias (Banco)
MORADA: Porto	Ref. ÓLEO: PAG **300RPM**
DATA: 13/06/13	ENSAIOS de EFICIÊNCIA

Fotografia 1

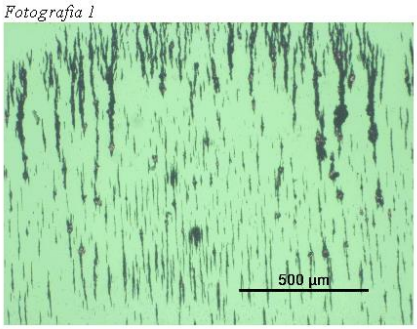

Fotografia 2

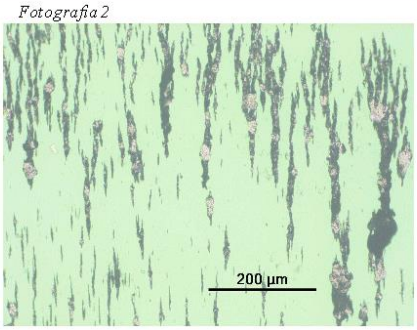

Ampliação: x 100 / x 200 Diluição: 0.1 Luz: Branca / Verde

Observações: Presença de partículas ferrosas de médias e grandes dimensões, algumas oxidadas.

Fotografia 3

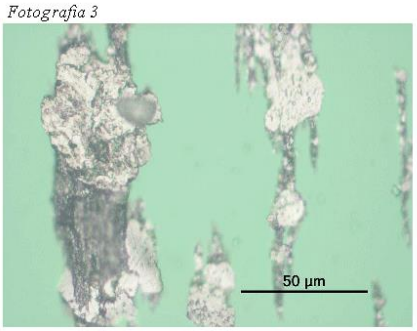

Fotografia 4

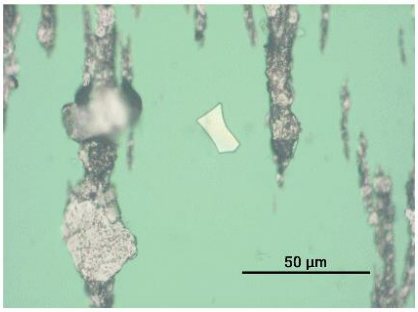

Ampliação: x 1000 Diluição: 0.1 Luz: Branca / Verde

Observações: Ampliações da Fotografia 2. Partículas ferrosas de médias e grandes dimensões, algumas oxidadas.

Fotografia 5

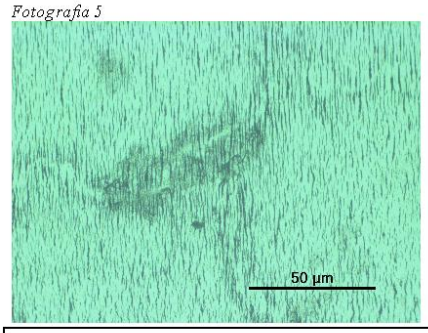

Fotografia 6

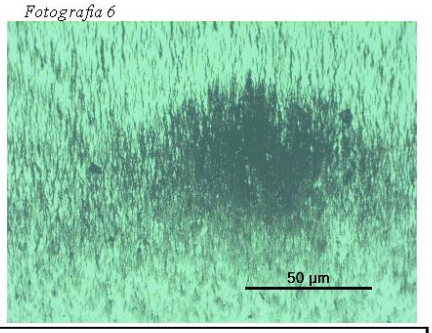

Ampliação: x 1000 Diluição: 0.1 Luz: Branca / Verde

Observações: Presença de alguns polímeros de atrito de grandes dimensões.

B.5. Running-in MINR Oil

Relatório
de
Análise de Lubrificantes

Análise nº:	45 - 47 / 13
Tipo de análise:	Ferrometria e Ferrografia Analítica
Confidencialidade:	1
Cliente:	INEGI - Cetrib
Morada:	Porto
Telefone / Fax:	
Equipamento:	BANCO - Ensaios de Eficiência, Caixas Planetárias
Lubrificante:	MIN R
Dossier:	/
Nº de páginas:	4
Data:	11/06/13
Responsável:	Beatriz Graça – Jorge Seabra
Rúbrica:	

OBJECTIVO

Análise de três amostras de óleo lubrificante MINR, resultantes de Ensaios de Eficiência no Banco de Ensaios com Caixas Planetárias para avaliação do desgaste presente.

As amostras analisadas foram as seguintes:

Amostra Nº (rpm)	Análises efectuadas	
	Ferrometria	Ferrografia Analítica
100	X	-
200	X	-
300	X	X

RESULTADOS DAS ANÁLISES

Nas páginas seguintes são apresentados os resultados referentes às análises de Ferrometria (DR III) e Ferrografia Analítica (FM III).

	CLIENTE: *INEGI*			MÁQUINA: Caixas Planetárias (Banco)				
	MORADA: Porto			Ref. ÓLEO: MINR				
	DATA: 11/06/13			ENSAIOS de EFICIÊNCIA				
IDENTIFICAÇÃO								
Amostra nº:	100rpm	200rpm	300rpm					
Data amostra:	Jun-13	Jun-13	Jun-13					
Análise nº:	45/13	46/13	47/13					
Ciclos/Máquina:	-	-	-					
Ciclos/Óleo:	-	-	-					
FERROMETRIA								
d:	0,1	0,1	0,1					
DL:	35,4	26,0	39,3					
DS:	4,8	5,4	5,4					
CPUC:	402,0	314,0	447,0					
ISUC:	1,2E+05	6,5E+04	1,5E+05					
FERROGRAFIA:								
Desgaste normal								
Desgaste severo								
Desgaste de abrasão								
Desgaste combinado								
Desgaste fadiga								
Esferas Metálicas								
Polímeros de atrito								
Óxidos Vermelhos								
Minerais/Orgânicos								
OILVIEW:								
Índice OilLife:								
Índice Oxidação:								
Índice Contaminação:								
Índice Ferromagnético:								
Grandes Contaminantes:								
Constante Dieléctrica:								
FILTRAGEM								
(Nº Partículas/10 ml)								
5 - 15 µm								
15 - 25 µm								
25 - 50 µm								
50 - 100 µm								
> 100 µm								
VISCOSIDADE								
(cSt a 40° C):								
(cSt a 80° C):								
(cSt a 100° C):								
ACIDEZ (TAN)								
(mg KOH)								
P. INFLAMAÇÃO								
(° C)								
DIAGNÓSTICO:								

LEGENDA	DL - Índice de partículas grandes		Não existe
	DS - Índice de partículas pequenas	f	Fraco
	CPUC - Concentração de partículas de desgaste	M	Médio
	ISUC - Índice de severidade de desgaste	F	Forte

CLIENTE: ***INEGI***	MÁQUINA: Caixas Planetárias (Banco)
MORADA: Porto	Ref. ÓLEO: MinE **300RPM**
DATA: 11/06/13	ENSAIO de EFICIÊNCIA

Fotografia 1

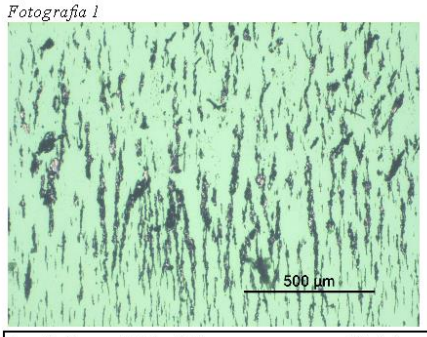

Fotografia 2

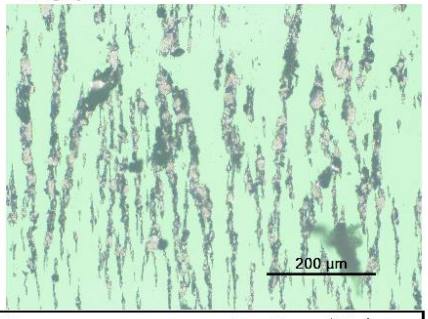

Ampliação: x 100 / x 200 Diluição: 0.1 Luz: Branca / Verde

Observações: Presença significativa de partículas ferrosas de grandes dimensões, algumas oxidadas.

Fotografia 3

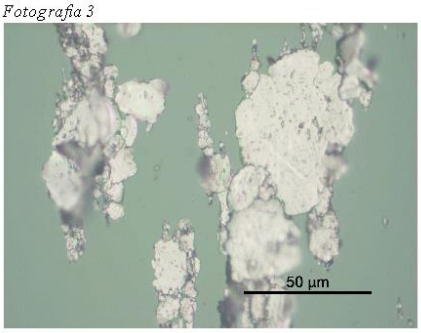

Fotografia 4

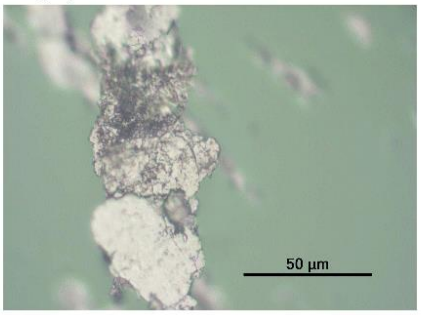

Ampliação: x 1000 Diluição: 0.1 Luz: Branca / Verde

Observações: Ampliações da Fotografia 2. Partículas ferrosas, de grandes dimensões, típicas de desgaste de fadiga.

Fotografia 5

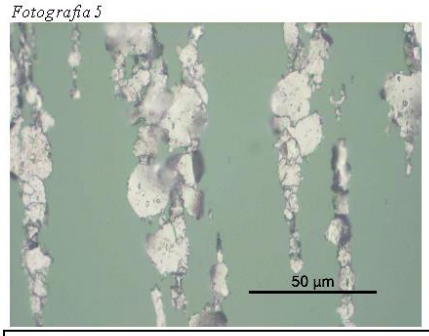

Fotografia 6

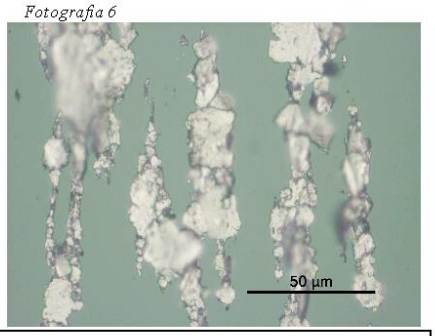

Ampliação: x 1000 Diluição: 0.1 Luz: Branca / Verde

Observações: Partículas ferrosas de desgaste típicas de micropitting (<30µm).

C. Results in tabular form

Table 16. Stabilized operating temperatures.

		ΔT [°C]			
		MINR	MINE	PAOR	PAGD
100 rpm	500 Nm	19.122	22.635	23.191	25.022
	750 Nm	21.045	23.264	23.596	25.902
	1000 Nm	22.021	23.638	23.750	26.364
200 rpm	500 Nm	37.586	41.181	39.273	45.220
	750 Nm	38.998	42.957	41.550	48.629
	1000 Nm	40.313	43.681	43.769	50.997
300 rpm	500 Nm	53.849	54.306	56.377	68.583
	750 Nm	49.449	57.128	57.876	71.731
	1000 Nm	59.451	58.766	58.633	72.322

Table 17. Kinematic viscosities at operating temperature.

		v [cSt]			
		MINR	MINE	PAOR	PAGD
100 rpm	500 Nm	207.18	228.80	235.08	194.25
	750 Nm	220.21	214.35	224.22	175.30
	1000 Nm	194.02	199.23	208.64	181.44
200 rpm	500 Nm	87.62	104.03	101.49	92.74
	750 Nm	76.73	90.07	94.47	87.46
	1000 Nm	77.63	90.46	82.03	78.17
300 rpm	500 Nm	40.66	57.77	55.20	53.00
	750 Nm	45.78	55.36	48.48	45.58
	1000 Nm	30.35	47.36	48.72	47.12

Table 18. Total calculated Power Loss of each test.

		Power Loss [W]			
		MINR	MINE	PAOR	PAGD
100 rpm	500 Nm	272.30	261.85	276.49	259.21
	750 Nm	315.42	297.76	307.00	279.82
	1000 Nm	335.91	326.03	337.04	321.25
200 rpm	500 Nm	532.94	500.46	508.31	469.06
	750 Nm	575.79	547.44	574.00	536.54
	1000 Nm	657.36	624.07	624.68	605.37
300 rpm	500 Nm	756.89	703.38	717.48	692.42
	750 Nm	831.89	806.59	802.52	807.36
	1000 Nm	946.43	906.11	911.62	900.07

D. KISSSOFT analysis of the planetary gearbox

D.1. Geometry

KISSsoft
Calculation programs for machine design

KISSsoft - Release 03-2011L
LND-7330757468@CS

File
Name : redut epicic 1
Changed by : pedromarques on: 15.07.2013 at: 11:24:48

CALCULATION OF A HELICAL PLANETARY GEAR

Drawing or article number:
Gear 1: 0.000.0
Gear 2: 0.000.0
Gear 3: 0.000.0

Calculation method Static calculation

		Gear 1	Gear 2	Gear 3
Number of planets	[p]	(1)	3	(1)
Power (kW)	[P]		10.47	
Speed (1/min)	[n]	400.0		0.0
Speed difference for planet bearing calculation (1/min)	[n2]		300.0	
Speed planet carrier (1/min)	[nSteg]		100.0	
Torque (Nm)	[T]	250.0	0.0	750.0
Torque Pl.-Carrier (Nm)	[TSteg]		1000.000	
Application factor	[KA]		1.00	
Power distribution factor	[Kgam]		1.00	
Required service life	[H]		0.00	
Gear driving (+) / driven (-)		+	-/+	-

1. TOOTH GEOMETRY AND MATERIAL

(Geometry calculation according ISO 21771)

		Gear 1	Gear 2	Gear 3
Center distance (mm)	[a]		74.000	
Centre distance tolerance			ISO 286 Measure js7	
Normal module (mm)	[mn]		2.0000	
Pressure angle at normal section (°)	[alfn]		20.0000	
Helix angle at reference circle (°)	[beta]		10.0000	
Number of teeth	[z]	36	36	-108
Facewidth (mm)	[b]	42.00	42.00	42.00
Hand of gear		right	left	left
Planetary axles can be placed in regular pitch.:			120°	
Accuracy grade	[Q-ISO1328]	6	6	6
Inner diameter (mm)	[di]	0.00	0.00	
External diameter (mm)	[di]			0.00
Inner diameter of gear rim (mm)	[dbi]	0.00	0.00	
Outer diameter of gear rim (mm)	[dbi]			0.00

Material
Gear 1: 18CrNiMo7-6, Case-carburized steel, case-hardened
ISO 6336-5 Figure 9/10 (MQ), core strength >=25HRC Jominy J=12mm<HRC28
Gear 2: 18CrNiMo7-6, Case-carburized steel, case-hardened
ISO 6336-5 Figure 9/10 (MQ), core strength >=25HRC Jominy J=12mm<HRC28
Gear 3: 18CrNiMo7-6, Case-carburized steel, case-hardened
ISO 6336-5 Figure 9/10 (MQ), core strength >=25HRC Jominy J=12mm<HRC28

		Gear 1	Gear 2	Gear 3
Surface hardness		HRC 61	HRC 61	HRC 61
Fatigue strength. tooth root stress (N/mm²)	[sigFlim]	430.00	430.00	430.00
Fatigue strength for Hertzian pressure (N/mm²)	[sigHlim]	1500.00	1500.00	1500.00
Yield point (N/mm²)	[sigs]	850.00	850.00	850.00
Young's modulus (N/mm²)	[E]	206000	206000	206000

Poisson's ratio	[ny]	0.300	0.300
0.300			
Average roughness, Ra, tooth flank (µm)	[RAH]	0.60	0.60
0.60			
Mean roughness height, Rz, flank (µm)	[RZH]	4.80	4.80
4.80			
Mean roughness height, Rz, root (µm)	[RZF]	20.00	20.00
20.00			

Tool or reference profile of gear 1 :

Reference profile 1.25 / 0.38 / 1.0 ISO 53.2 Profil A		
Addendum coefficient	[haP*]	1.000
Dedendum coefficient	[hfP*]	1.250
Tip radius factor	[rhoaP*]	0.000
Root radius factor	[rhofP*]	0.380
Tip form height coefficient	[hFaP*]	0.000
Protuberance height factor	[hprP*]	0.000
Protuberance angle	[alfprP]	0.000
Ramp angle	[alfKP]	0.000
		not topping

Tool or reference profile of gear 2 :

Reference profile 1.25 / 0.38 / 1.0 ISO 53.2 Profil A		
Addendum coefficient	[haP*]	1.000
Dedendum coefficient	[hfP*]	1.250
Tip radius factor	[rhoaP*]	0.000
Root radius factor	[rhofP*]	0.380
Tip form height coefficient	[hFaP*]	0.000
Protuberance height factor	[hprP*]	0.000
Protuberance angle	[alfprP]	0.000
Ramp angle	[alfKP]	0.000
		not topping

Tool or reference profile of gear 3 :

Reference profile 1.25 / 0.38 / 1.0 ISO 53.2 Profil A		
Addendum coefficient	[haP*]	1.000
Dedendum coefficient	[hfP*]	1.250
Tip radius factor	[rhoaP*]	0.000
Root radius factor	[rhofP*]	0.380
Tip form height coefficient	[hFaP*]	0.000
Protuberance height factor	[hprP*]	0.000
Protuberance angle	[alfprP]	0.000
Ramp angle	[alfKP]	0.000
		not topping

Summary of reference profile gears:

Dedendum reference profile (module)	[hfP*]	1.250	1.250
1.250			
Tooth root radius Refer. profile (module)			
	[rofP*]	0.380	0.380
0.380			
Addendum Reference profile (module)	[haP*]	1.000	1.000
1.000			
Protuberance height (module)	[hprP*]	0.000	0.000
Protuberance angle (°)	[alfprP]	0.000	0.000
Buckling root flank height (module)	[hFaP*]	0.000	0.000
Buckling root flank angle (°)	[alfKP]	0.000	0.000
Data for Grinding / Honing:			
Depth of immersion (module)	[hgrind*]	1.066	1.066
0.891			
Radius at cutter head (module)	[rgrind*]	0.100	0.100
0.100			

Type of profile modification:		none (only running-in)	
Tip relief (µm)	[Ca]	2.00	2.00
2.00			

Lubrication type	oil bath lubrication	
Type of oil	Oil: ISO-VG 320	
Lubricant base	Mineral-oil base	
Kinem. viscosity oil at 40 °C (mm²/s)	[nu40]	320.00
Kinem. viscosity oil at 100 °C (mm²/s)	[nu100]	22.00
FZG-Test A/8.3/90 step	[FZGtestA]	12
Specific density at 15 °C (kg/dm³)	[roOil]	0.900
Oil temperature (°C)	[TS]	42.500
Ambient temperature (°C)	[TU]	20.000

------- Gear 1 ------------ Gear 2 ------------ Gear 3 ---

Overall transmission ratio	[itot]		4.000	
Gear ratio	[u]		1.000	-3.000
Transverse module (mm)	[mt]		2.031	
Pressure angle at pitch circle (°)	[alft]		20.284	
Working transverse pressure angle (°)	[alfwt]		22.071	22.071
	[alfwt.e/i]	22.100 / 22.043	22.043 / 22.100	
Working pressure angle at normal section (°)	[alfwn]		21.760	21.760
Helix angle at operating pitch circle (°)	[betaw]		10.119	10.119
Base helix angle (°)	[betab]		9.391	
Reference centre distance (mm)	[ad]		73.111	-73.111
Sum of profile shift coefficients	[Summexi]		0.4637	-0.4637
Profile shift coefficient	[x]	0.2318	0.2318	-0.6955
Tooth thickness (Arc) (module)	[sn*]	1.7396	1.7396	1.0645
Tip alteration (mm)	[k*mn]	-0.038	-0.038	0.000
Reference diameter (mm)	[d]	73.111	73.111	-219.332
Base diameter (mm)	[db]	68.577	68.577	-205.731
Tip diameter (mm)	[da]	77.962	77.962	-218.114
(mm)	[da.e/i]	77.962 / 77.952	77.962 / 77.952	-218.114 / -218.124
Tip diameter allowances (mm)	[Ada.e/i]	0.000 / -0.010	0.000 / -0.010	0.000 / -0.010
Tip chamfer / tip rounding (mm)	[hK]	0.000	0.000	0.000
Tip form diameter (mm)	[dFa.e/i]	77.962 / 77.952	77.962 / 77.952	-218.114 / -218.124
Operating pitch diameter (mm)	[dw]	74.000	74.000 / 74.000	-222.000
(mm)	[dw.e]	74.015	74.015 / 73.985	-221.955
(mm)	[dw.i]	73.985	73.985 / 74.015	-222.045
Root diameter (mm)	[df]	69.038	69.038	-227.114
Generating Profile shift coefficient	[xE.e/i]	0.1837 / 0.1563	0.1837 / 0.1563	-0.7607 / -0.7951
Manufactured root diameter with xE (mm)	[df.e]	68.85	68.85	-227.38
(mm)	[df.i]	68.74	68.74	-227.51
Theoretical tip clearance (mm)	[c]	0.500	0.500/0.576	0.538
Tip clearance upper allowance (mm)	[c.e]	0.671	0.671/0.795	0.709
Tip clearance lower allowance (mm)	[c.i]	0.581	0.581/0.692	0.619
Active root diameter (mm)	[dNf]	71.036	71.036/70.613	-225.650
(mm)	[dNf.e]	71.062	71.062/70.639	-225.609
(mm)	[dNf.i]	71.015	71.015/70.594	-225.683
Root form diameter (mm)	[dFf]	70.530	70.530	-226.078
(mm)	[dFf.e/i]	70.402 / 70.331	70.402 / 70.331	-226.326 / -226.455
Internal toothing: Calculation dFf with pinion type cutter (z0=35, x0=0.000)				
Reserve (dNf-dFf)/2 (mm)	[cF.e/i]	0.365 / 0.306	0.154 / 0.096	0.423 / 0.321
Addendum (mm) [ha = mn * (haP*+x)]		2.426	2.426	0.609
(mm)	[ha.e/i]	2.426 / 2.421	2.426 / 2.421	0.609 / 0.604
Dedendum (mm) [hf = mn * (hfP*-x)]		2.036	2.036	3.891
(mm)	[hf.e/i]	2.133 / 2.187	2.133 / 2.187	4.021 / 4.090
Roll angle at dFa (°)	[xsi_dFa.e/i]	30.984 / 30.967	30.984 / 30.967	20.176 / 20.185
Roll angle to dNf (°)	[xsi_dNf.e/i]	15.564 / 15.413	15.564 / 15.413	
	[xsi_dNf.e/i]		14.157 / 13.998	25.788 / 25.838
Roll angle at dFf (°)	[xsi_dFf.e/i]	13.307 / 13.042	13.307 / 13.042	26.271 / 26.357
Tooth height (mm)	[H]	4.462	4.462	

4.500				
Virtual gear no. of teeth	[zn]	37.555	37.555	
-112.666				
Normal tooth thickness at tip cyl. (mm)	[san]	1.444	1.444	
1.686				
(mm)	[san.e/i]	1.375 / 1.327	1.375 / 1.327	1.595 /
1.542				
Normal spacewidth at root cylinder (mm)	[efn]	1.627	1.627	
1.026				
(mm)	[efn.e/i]	1.669 / 1.696	1.669 / 1.696	1.005 /
0.993				
Max. sliding velocity at tip (m/s)	[vga]	0.291	0.291/0.097	0.115
Specific sliding at the tip	[zetaa]	0.500	0.500/0.167	0.303
Specific sliding at the root	[zetaf]	-1.002	-1.002/-0.435	-0.200
Sliding factor on tip	[Kga]	0.251	0.251/0.084	0.099
Sliding factor on root	[Kgf]	-0.251	-0.251/-0.099	-0.084
Pitch on reference circle (mm)	[pt]		6.380	
Base pitch (mm)	[pbt]		5.984	
Transverse pitch on contact-path (mm)	[pet]		5.984	
Lead height (mm)	[pz]	1302.603	1302.603	
3907.810				
Axial pitch (mm)	[px]	36.183	36.183	
36.183				
Length of path of contact (mm)	[ga]		9.278	10.125
(mm)	[ga.e/i]	9.318 / 9.217	10.165 / 10.060	
Length T1-A (mm)	[T1A]	9.264	18.542/8.417	-36.223
Length T1-B (mm)	[T1B]	12.558	15.248/12.558	-40.364
Length T1-C (mm)	[T1C]	13.903	13.903/13.903	-41.710
Length T1-D (mm)	[T1D]	15.248	12.558/14.401	-42.208
Length T1-E (mm)	[T1E]	18.542	9.264/18.542	-46.349
Diameter of single contact point B (mm)	[d-B]	73.032	75.052/73.032	-221.003
(mm)	[d-B.e]	73.032	75.020/73.032	-221.032
(mm)	[d-B.i]	73.024	75.093/73.024	-220.966
Diameter of single contact point D (mm)	[d-D]	75.052	73.032/74.380	-222.376
(mm)	[d-D.e]	75.020	73.032/74.349	-222.376
(mm)	[d-D.i]	75.093	73.024/74.423	-222.388
Transverse contact ratio	[Eps.a]		1.550	1.692
Transverse contact ratio with allowances	[Eps.aEffe/i]	1.557 / 1.540	1.699 / 1.681	
Overlap ratio	[Eps.b]		1.161	1.161
Total contact ratio	[Eps.G]		2.711	2.853
Total contact ratio with allowances	[Eps.gEffe/i]	2.718 / 2.701	2.859 / 2.842	

2. FACTORS OF GENERAL INFLUENCE

		------- Gear 1	---------- Gear 2	---------- Gear
3 ---				
Nominal circum. force at pitch circle (N)				
	[Ft]	2279.648	2279.648	
Axial force (N)	[Fa]	402.0	402.0	
402.0				
Axial force (total) (N)	[Fa_ges]	1205.9		
1205.9				
Radial force (N)	[Fr]	842.524	842.524	
Normal force (N)	[Fnorm]	2463.4	2463.4	
2463.4				
Tangent.load at p.c.d.per mm (N/mm) (N/mm)				
	[w]	54.28	54.28	
Only as information: Forces at operating pitch circle:				
Nominal circumferential force (N)	[Ftw]	2252.253	2252.253	
Axial force (N)	[Fa]	402.0	402.0	
402.0				
Axial force (total) (N)	[Fa_ges]	1205.9		
1205.9				
Radial force (N)	[Fr]	913.235	913.235	
Circumferential speed pitch d.. (m/sec)	[v]		1.15	
Dynamic factor	[KV]	1.00	1.00	
Face load factor - flank	[KHb]	1.00	1.00	
- Tooth root	[KFb]	1.00	1.00	
- Scuffing	[KBb]	1.00	1.00	
Transverse load factor - flank	[KHa]	1.00	1.00	
- Tooth root	[KFa]	1.00	1.00	
- Scuffing	[KBa]	1.00	1.00	
Helical load factor scuffing	[Kbg]	1.00	1.00	

3. TOOTH ROOT STRENGTH

4/7

		------- Gear 1 ----------	Gear 2 ----------	Gear 3 ---
Calculation of Tooth form coefficients according method: B				
(Calculate tooth form factor YF with manufacturing addendum mod. xE.e)				
Tooth form factor	[YF]	1.35	1.35/1.14	0.92
Bending lever arm (mm)	[hF]	2.16	2.16/1.81	2.44
Working angle (°)	[alfen]	21.37	21.37/19.98	21.89
Tooth thickness at root (mm)	[sFn]	4.36	4.36/4.36	5.61
Tooth root radius (mm)	[roF]	0.96	0.96/0.96	1.04
(sFn* = 2.181/2.181/2.181/2.803 roF* = 0.482/0.482/0.482/0.520 dsFn = 69.61/69.61/69.61/-227.15 alfsFn = 30.0/ 30.0/ 30.0/ 60.0)				
Contact ratio factor	[Yeps]	1.00	1.00	
Helical load factor	[Ybet]	0.92	0.92	
Deep tooth factor	[YDT]	1.00	1.00	
Gear rim factor	[YB]	1.00	1.00	1.00
Effective facewidth (mm)	[beff]	42.00	42.00/42.00	42.00
Nominal shear stress at tooth root (N/mm²)	[sigF0]	33.58	33.58/28.46	22.89
Tooth root stress (N/mm²)	[sigF]	33.58	33.58/28.46	22.89

Calculation formulae:
sigF0 = Ft / beff / mn * YF * Yeps * Ybeta * YB * YDT
sigF = sigF0 * KA * KV * KFa * KFb
YF, YS : ISO6336-3

Yield point (N/mm²)	[sigs]	850.00	850.00	850.00
Tensile strength (N/mm²)	[sigb]	1200.00	1200.00	1200.00
Safety against plastic deformation	[Ss=sigs/sigF]	25.31	25.31/29.87	37.14
Safety for tensile stress	[Sb=sigb/sigF]	35.73	35.73/42.17	52.44

Extensions for aerospace industry:
Calculation formula:
sigF0 = Ft / beff / mn * YF * YS * Yeps * Ybeta * YB * YDT

Stress correction factor	[YS]	2.07	2.07/2.20	2.35
Safety against plastic deformation	[Ss=sigs/sigF]	12.23	12.23/13.55	15.82
Safety for tensile stress	[Sb=sigb/sigF]	17.26	17.26/19.13	22.34

6. MEASUREMENTS FOR TOOTH THICKNESS

		------- Gear 1 ----------	Gear 2 ----------	Gear 3 ---
Tooth thickness deviation		DIN3967 cd25	DIN3967 cd25	DIN3967 cd25
Tooth thickness allowance (normal section) (mm)	[As.e/i]	-0.070/-0.110	-0.070/-0.110	-0.095/-0.145
Number of teeth spanned	[k]	5.000	5.000	0.000
(Internal toothing: k = (Measurement gap number)				
Base tangent length (no backlash) (mm)	[Wk]	27.940	27.940	0.000
Actual base tangent length ('span') (mm)	[Wk.e/i]	27.874/27.836	27.874/27.836	0.000/0.000
Diameter of contact point (mm)	[dMWk.m]	73.879	73.879	0.000
Theoretical diameter of ball/pin (mm)	[dm]	3.502	3.502	3.358
Eff. Diameter of ball/pin (mm)	[DMeff]	3.500	3.500	3.500
Theor. dim. centre to ball (mm)	[MrK]	39.451	39.451	-108.495
Actual dimension centre to ball (mm)	[MrK.e/i]	39.370/39.324	39.370/39.324	-108.620/-108.686
Diameter of contact point (mm)	[dMMr.m]	73.845	73.845	-222.084
Diametral measurement over two balls without clearance (mm)	[MdK]	78.901	78.901	-216.990
Actual dimension over balls (mm)	[MdK.e/i]	78.740/78.647	78.740/78.647	-217.241/-217.372
Actual dimension over rolls (mm)	[MdR.e/i]	78.740/78.647	78.740/78.647	0.000/0.000
Actual dimensions over 3 rolls (mm)	[Md3R.e/i]	0.000/0.000	0.000/0.000	0.000/0.000
Tooth thickness (chordal) in pitch diameter (mm)	['sn]	3.478	3.478	2.129

(mm)	['sn.e/i]	3.408/3.368	3.408/3.368
2.034/1.984			
Reference chordal height from da.m (mm)	[ha]	2.463	2.463
0.602			
Tooth thickness (Arc) (mm)	[sn]	3.479	3.479
2.129			
(mm)	[sn.e/i]	3.409/3.369	3.409/3.369
2.034/1.984			

Backlash free center distance (mm)	[aControl.e/i]	73.821/73.718	-74.207/-74.319
Backlash free center distance, allowances (mm)			
	[jta]	-0.179/-0.282	-0.207/-0.319
Centre distance allowances (mm)	[Aa.e/i]	0.015/-0.015	0.015/-0.015
Circumferential backlash from Aa (mm)	[jt_Aa.e/i]	0.012/-0.012	0.012/-0.012
Radial clearance (mm)	[jr]	0.297/0.164	0.334/0.192
Circumferential backlash (transverse section) (mm)			
	[jt]	0.238/0.132	0.274/0.157
Normal backlash (mm)	[jn]	0.221/0.122	0.254/0.146

Entire torsional angle (°) [j.tSys] 0.1890/0.1214
(j.tSys: Torsional angle of planet carrier for blocked shaft)

7. GEAR ACCURACY

		------- Gear 1	---------- Gear 2	---------- Gear 3 ---
According ISO 1328:				
Accuracy grade	[Q-ISO1328]	6	6	
6				
Single pitch deviation (µm)	[fpt]	7.50	7.50	
8.50				
Base circle pitch deviation (µm)	[fpb]	7.00	7.00	
8.00				
Cumulative circular pitch deviation over k/8 pitches (µm)				
	[Fpk/8]	12.00	12.00	
16.00				
Profile form deviation (µm)	[ffa]	6.50	6.50	
7.50				
Profile slope deviation (µm)	[fHa]	5.50	5.50	
6.00				
Total profile deviation (µm)	[Fa]	8.50	8.50	
10.00				
Helix form deviation (µm)	[ffb]	10.00	10.00	
10.00				
Helix slope deviation (µm)	[fHb]	10.00	10.00	
10.00				
Total helix deviation (µm)	[Fb]	14.00	14.00	
15.00				
Total cumulative pitch deviation (µm)	[Fp]	26.00	26.00	
35.00				
Concentricity deviation (µm)	[Fr]	21.00	21.00	
28.00				
Total radial composite deviation (µm)	[Fi"]	31.00	31.00	
37.00				
Radial tooth-to-tooth composite deviation (µm)				
	[fi"]	9.50	9.50	
9.50				
Total tangential composite deviation (µm)				
	[Fi']	37.00	37.00	
47.00				
Tangential tooth-to-tooth composite deviation (µm)				
	[fi']	11.00	11.00	
12.00				

Tolerance for alignment of axes (recommendation acc. ISO/TR 10064, Quality 6)

Maximum value for deviation error of axis (µm)			
	[fSigbet]	12.92	12.92
Maximum value for inclination error of axes (µm)			
	[fSigdel]	25.85	25.85

Indications for the manufacturing by wire cutting:				
Deviation from theoretical tooth trace (µm)	[WireErr]	187.4	187.4	
62.5				
Permissible deviation (µm)	[Fb/2]	7.0	7.0	
7.5				

9. DETERMINATION OF TOOTHFORM

Data for the tooth form calculation :
Data not available.

6/7

REMARKS:
- Specifications with [.e/i] imply: Maximum [e] and Minimal value [i] with
  consideration of all tolerances
  Specifications with [.m] imply: Mean value within tolerance
- For the backlash tolerance, the center distance tolerances and the tooth thickness
deviation are taken into account. Shown is the maximal and the minimal backlash corresponding
 the largest resp. the smallest allowances
 The calculation is done for the Operating pitch circle..
- Calculation of Zbet according Corrigendum 1 ISO6336-2(2008) with Zbet = 1/(COS(beta)^0.5)

End report lines: 398

D.2. Loads and Kinematics

KISSsoft - Release 03-2011L
LND-7330757468@CS

File
Name : redut epicic 1
Changed by : pedromarques on: 15.07.2013 at: 11:25:43

Calculation of path of contact under load
Mesh gear 1 - gear 2 (Right Tooth Flank)

Partial load for calculation		100.00	%
Center distance	[a]	74.00	mm
Single pitch deviation	[fpt]	0.00	µm
Coefficient of friction	[µ]	0.05	
Torque	[T1]	83.33	Nm

		min	max	Delta	µ	sigma
Transmission error	(µm)	-95.6012	-95.3482	0.2530	-95.4384	0.0840
Stiffness curve	(N/mm/µm)	26.3759	28.8448	2.4690	28.0087	0.8460
Line load	(N/mm)	1.4265	90.6337	89.2071	35.9703	7.6417
Torque Gear 1	(Nm)	83.3218	83.4098	0.0879	83.3326	0.0106
Torque Gear 2	(Nm)	82.6921	82.8133	0.1212	82.7427	0.0353
Loss power	(W/mm)	0.0004	1.7188	1.7184	0.3631	0.2485
Flash temperature	(°)	43.8550	53.2886	9.4337	46.2968	1.6030
Lubricating film	(µm)	0.4787	0.9582	0.4795	0.6170	0.0353
Hertzian stress	(N/mm²)		719.8666		434.4645	

Transverse contact ratio under load	[Epsa']	1.60
Overlap ratio under load	[Epsb']	1.08
Total contact ratio under load	[Epsg']	2.68

KHbeta Calculation
Gear 1
Point in polar co-ordinates:
R = 37.000 mm , phi = 0.000 °
Displacement calculated in direction 112.071 °

	y	phi1.t	f1.t	f1.b	f1.tot	f1.C
1	-20.0000 mm	0.0000°	-0.0000 mm	0.0000 mm	0.0000 mm	0.0000 mm
2	-18.0000 mm	0.0001°	-0.0001 mm	0.0000 mm	-0.0001 mm	0.0000 mm
3	-16.0000 mm	0.0002°	-0.0001 mm	0.0000 mm	-0.0001 mm	0.0000 mm
4	-14.0000 mm	0.0003°	-0.0002 mm	0.0000 mm	-0.0002 mm	0.0000 mm
5	-12.0000 mm	0.0005°	-0.0003 mm	0.0000 mm	-0.0003 mm	0.0000 mm
6	-10.0000 mm	0.0006°	-0.0003 mm	0.0000 mm	-0.0003 mm	0.0000 mm
7	-8.0000 mm	0.0006°	-0.0004 mm	0.0000 mm	-0.0004 mm	0.0000 mm
8	-6.0000 mm	0.0007°	-0.0004 mm	0.0000 mm	-0.0004 mm	0.0000 mm
9	-4.0000 mm	0.0008°	-0.0005 mm	0.0000 mm	-0.0005 mm	0.0000 mm
10	-2.0000 mm	0.0009°	-0.0005 mm	0.0000 mm	-0.0005 mm	0.0000 mm
11	0.0000 mm	0.0010°	-0.0006 mm	0.0000 mm	-0.0006 mm	0.0000 mm
12	2.0000 mm	0.0010°	-0.0006 mm	0.0000 mm	-0.0006 mm	0.0000 mm
13	4.0000 mm	0.0011°	-0.0006 mm	0.0000 mm	-0.0006 mm	0.0000 mm
14	6.0000 mm	0.0011°	-0.0007 mm	0.0000 mm	-0.0007 mm	0.0000 mm
15	8.0000 mm	0.0012°	-0.0007 mm	0.0000 mm	-0.0007 mm	0.0000 mm
16	10.0000 mm	0.0012°	-0.0007 mm	0.0000 mm	-0.0007 mm	0.0000 mm
17	12.0000 mm	0.0012°	-0.0007 mm	0.0000 mm	-0.0007 mm	0.0000 mm
18	14.0000 mm	0.0013°	-0.0007 mm	0.0000 mm	-0.0007 mm	0.0000 mm
19	16.0000 mm	0.0013°	-0.0008 mm	0.0000 mm	-0.0008 mm	0.0000 mm
20	18.0000 mm	0.0013°	-0.0008 mm	0.0000 mm	-0.0008 mm	0.0000 mm
21	20.0000 mm	0.0013°	-0.0008 mm	0.0000 mm	-0.0008 mm	0.0000 mm

Gear 2
Point in polar co-ordinates:
R = 37.000 mm , phi = 180.000 °
Displacement calculated in direction 112.071 °

	y	phi2.t	f2.t	f2.b	f2.tot	f2.C
1	-20.0000 mm	0.0000°	0.0000 mm	0.0000 mm	0.0000 mm	0.0000 mm
2	-18.0000 mm	0.0000°	0.0000 mm	0.0000 mm	0.0000 mm	0.0000 mm
3	-16.0000 mm	0.0000°	0.0000 mm	0.0000 mm	0.0000 mm	0.0000 mm
4	-14.0000 mm	0.0000°	0.0000 mm	0.0000 mm	0.0000 mm	0.0000 mm
5	-12.0000 mm	0.0000°	0.0000 mm	0.0000 mm	0.0000 mm	0.0000 mm
6	-10.0000 mm	0.0000°	0.0000 mm	0.0000 mm	0.0000 mm	0.0000 mm
7	-8.0000 mm	0.0000°	0.0000 mm	0.0000 mm	0.0000 mm	0.0000 mm
8	-6.0000 mm	0.0000°	0.0000 mm	0.0000 mm	0.0000 mm	0.0000 mm
9	-4.0000 mm	0.0000°	0.0000 mm	0.0000 mm	0.0000 mm	0.0000 mm
10	-2.0000 mm	0.0000°	0.0000 mm	0.0000 mm	0.0000 mm	0.0000 mm
11	0.0000 mm	0.0000°	0.0000 mm	0.0000 mm	0.0000 mm	0.0000 mm
12	2.0000 mm	0.0000°	0.0000 mm	0.0000 mm	0.0000 mm	0.0000 mm
13	4.0000 mm	0.0000°	0.0000 mm	0.0000 mm	0.0000 mm	0.0000 mm
14	6.0000 mm	0.0000°	0.0000 mm	0.0000 mm	0.0000 mm	0.0000 mm
15	8.0000 mm	0.0000°	0.0000 mm	0.0000 mm	0.0000 mm	0.0000 mm

16	10.0000 mm	0.0000°	0.0000 mm	0.0000 mm	0.0000 mm	0.0000 mm
17	12.0000 mm	0.0000°	0.0000 mm	0.0000 mm	0.0000 mm	0.0000 mm
18	14.0000 mm	0.0000°	0.0000 mm	0.0000 mm	0.0000 mm	0.0000 mm
19	16.0000 mm	0.0000°	0.0000 mm	0.0000 mm	0.0000 mm	0.0000 mm
20	18.0000 mm	0.0000°	0.0000 mm	0.0000 mm	0.0000 mm	0.0000 mm
21	20.0000 mm	0.0000°	0.0000 mm	0.0000 mm	0.0000 mm	0.0000 mm

Explanations:
y : Width
phi's : Static torsion
fat : Displacement due to torsion
fib : Displacement due to bending
f.tot : Total displacement (f.b+f.t)
f.C : Change due to tooth trace modification

Load distribution
Contact stiffness = 10.810 N/mm/µm

	y	g	w
1.	-20.0000 mm	4.9158 µm	53.1422 N/mm
2.	-18.0000 mm	4.9893 µm	53.9364 N/mm
3.	-16.0000 mm	5.0591 µm	54.6910 N/mm
4.	-14.0000 mm	5.1252 µm	55.4058 N/mm
5.	-12.0000 mm	5.1877 µm	56.0809 N/mm
6.	-10.0000 mm	5.2465 µm	56.7163 N/mm
7.	-8.0000 mm	5.3016 µm	57.3120 N/mm
8.	-6.0000 mm	5.3530 µm	57.8679 N/mm
9.	-4.0000 mm	5.4007 µm	58.3842 N/mm
10.	-2.0000 mm	5.4448 µm	58.8607 N/mm
11.	0.0000 mm	5.4852 µm	59.2976 N/mm
12.	2.0000 mm	5.5220 µm	59.6947 N/mm
13.	4.0000 mm	5.5550 µm	60.0521 N/mm
14.	6.0000 mm	5.5844 µm	60.3698 N/mm
15.	8.0000 mm	5.6101 µm	60.6478 N/mm
16.	10.0000 mm	5.6322 µm	60.8860 N/mm
17.	12.0000 mm	5.6505 µm	61.0846 N/mm
18.	14.0000 mm	5.6652 µm	61.2435 N/mm
19.	16.0000 mm	5.6763 µm	61.3626 N/mm
20.	18.0000 mm	5.6836 µm	61.4420 N/mm
21.	20.0000 mm	5.6873 µm	61.4817 N/mm

Explanations:
g : Flank overlap
w : Line load

wmax = 61.482 N/mm, wm = 58.570 N/mm
wm = (Ft/b)/cos(a_wt)
KHb = wmax/wm = 1.050 (Calculation according to ISO 6336-1, Appendix E)
Notice: The influence of the exceeding tooth width is not taken into account in the calculation of KHbeta.

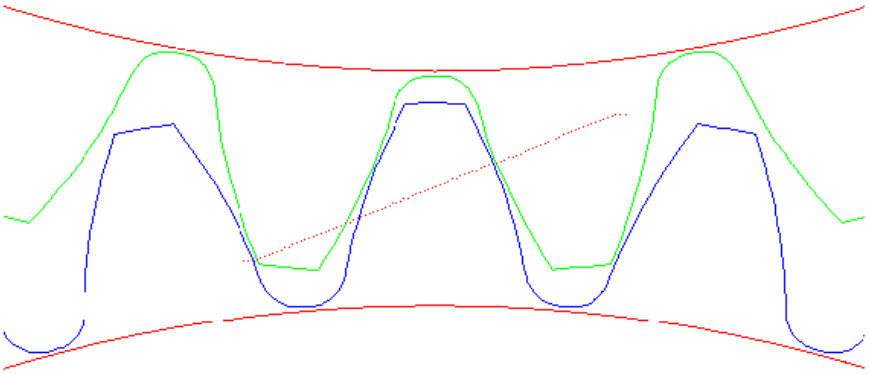

Figure: Path of contact

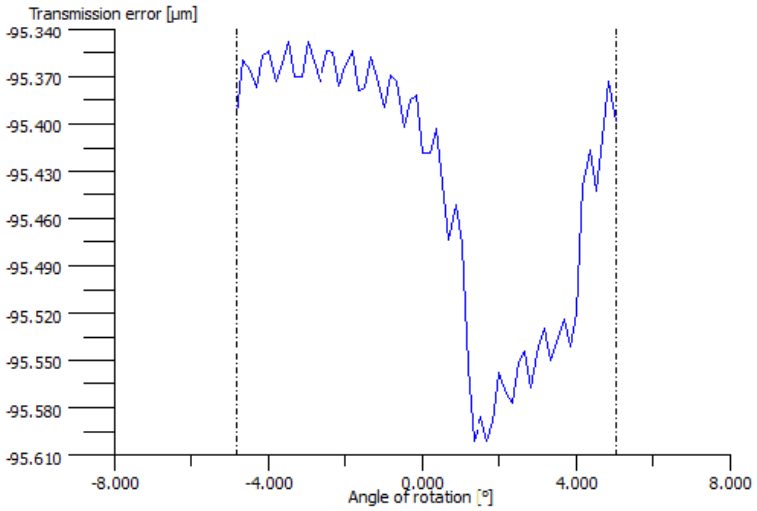

wt = 100 %, a = 74 mm, fpt = 0 µm, µ = 0.05

Figure: Transmission error

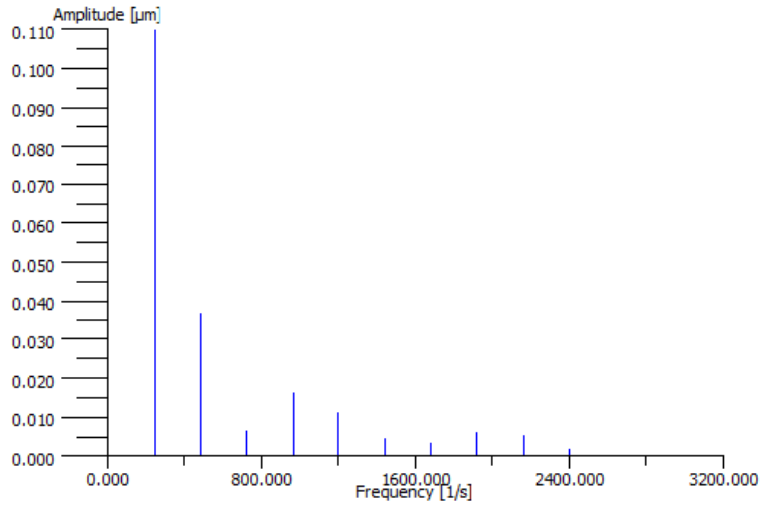

1st Harmonic frequency [1/s] : 240

Harmonics	Amplitude [µm]
1.	0.1095460537
2.	0.03655827928
3.	0.006558506975
4.	0.01630136907
5.	0.01111404186
6.	0.004260043617
7.	0.003436081212
8.	0.005913702267
9.	0.005352477706
10.	0.001888394782

Figure: FFT of transmission error

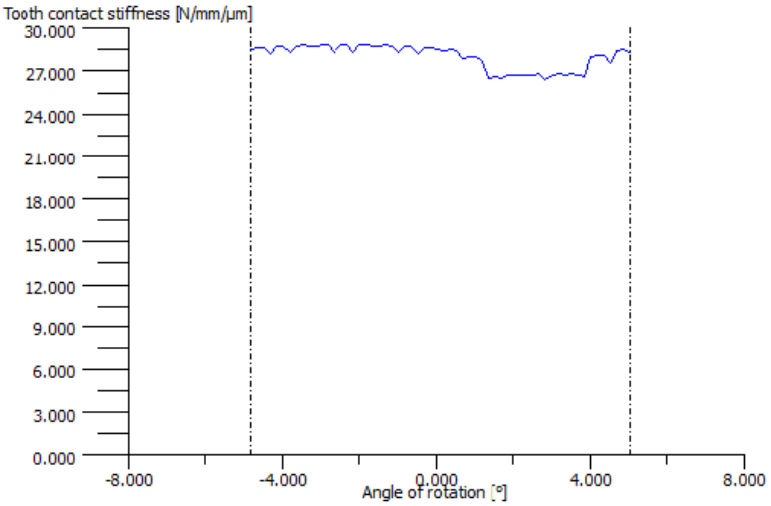

wt = 100 %, a = 74 mm, fpt = 0 µm, µ = 0.05

Figure: Stiffness curve

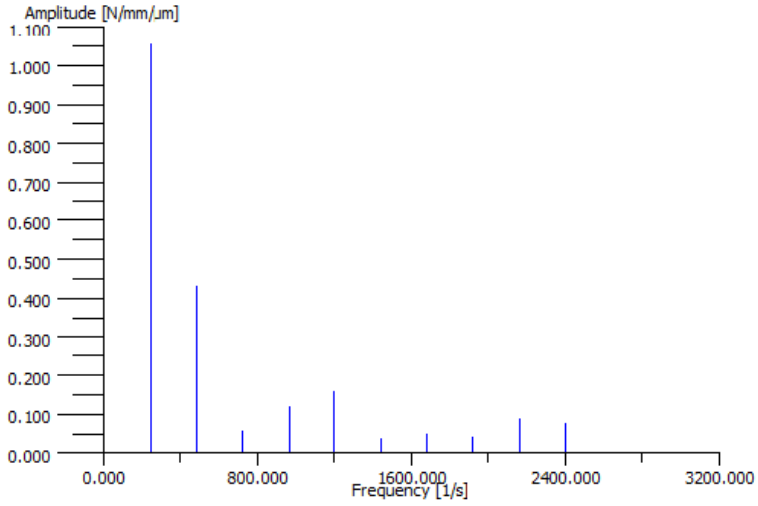

1st Harmonic frequency [1/s] : 240

Harmonics	Amplitude [N/mm/µm]
1.	1.053785754
2.	0.4293904842
3.	0.0543280418
4.	0.1186966194
5.	0.1590661247
6.	0.03700094199
7.	0.04839622616

5/19

8. 0.04012240967
9. 0.08810735514
10. 0.07518318797

Figure: FFT of contact stiffness

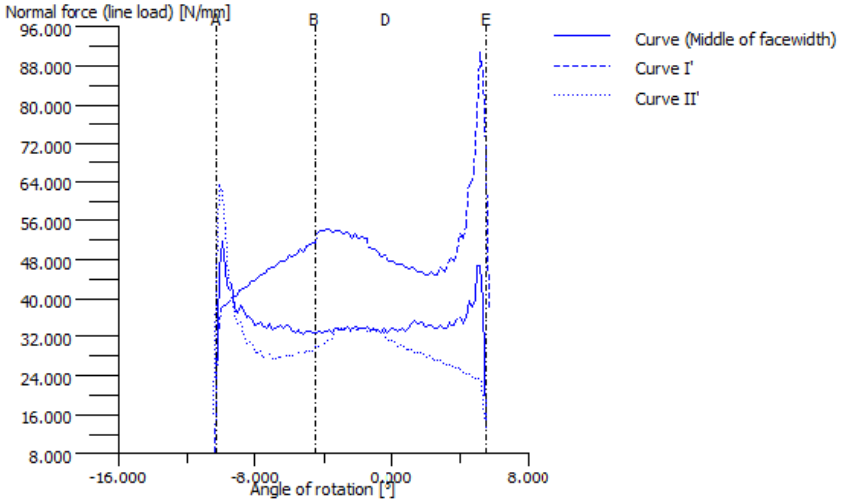

wt = 100 %, a = 74 mm, fpt = 0 µm, µ = 0.05

Figure: Normal force curve (Line load)

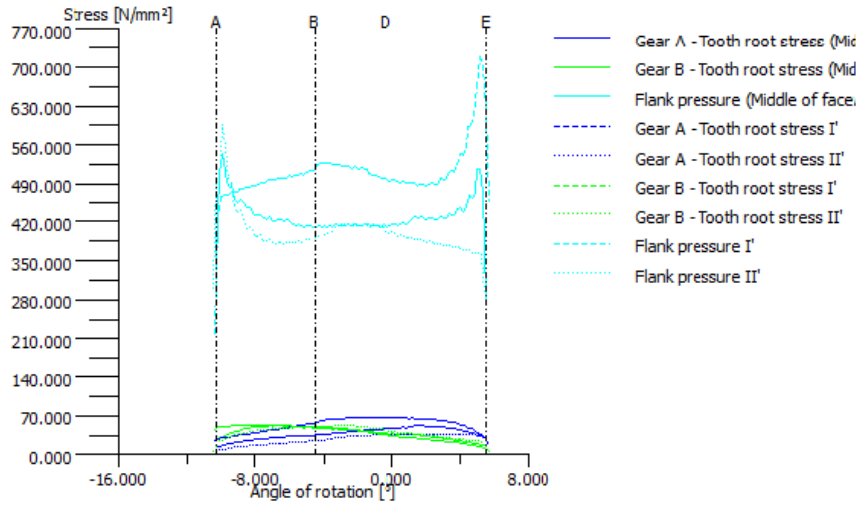

wt = 100 %, a = 74 mm, fpt = 0 µm, µ = 0.05

6/19

Figure: Stress curve

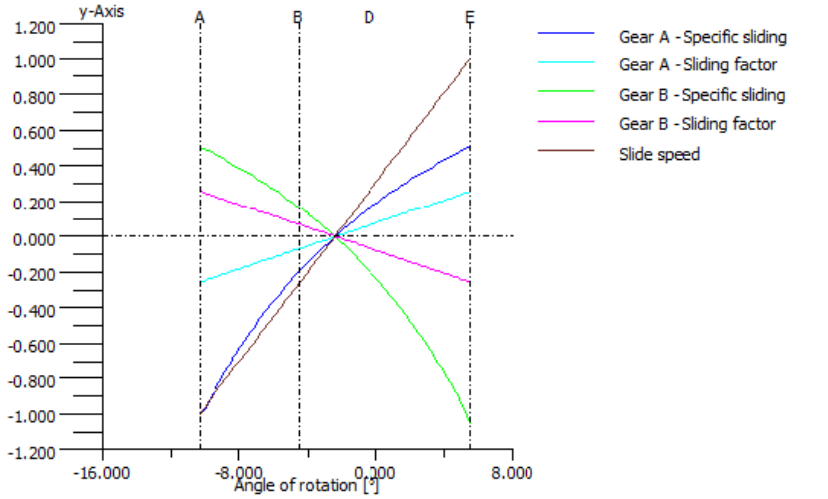

wt = 100 %, a = 74 mm, fpt = 0 µm, µ = 0.05
vg: 1.0 = 0.397 m/s

Figure: Kinematics

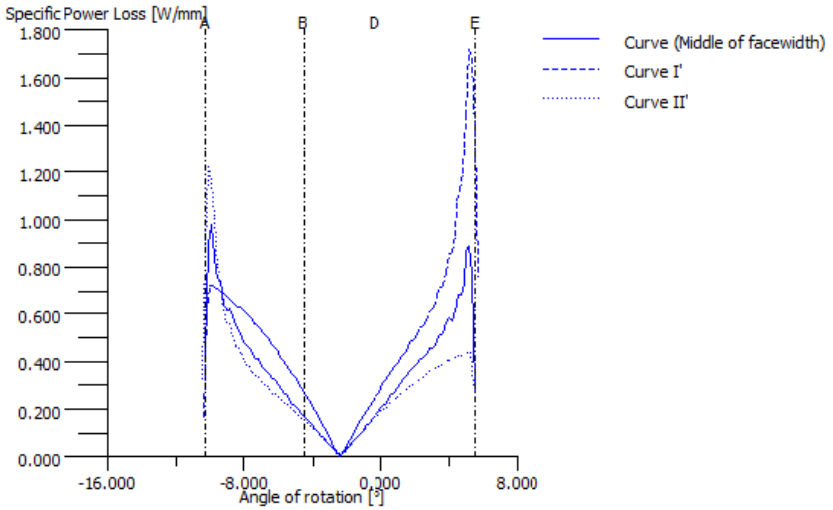

wt = 100 %, a = 74 mm, fpt = 0 µm, µ = 0.05
Displaying power losses per mm facewidth

7/19

Figure: Loss power

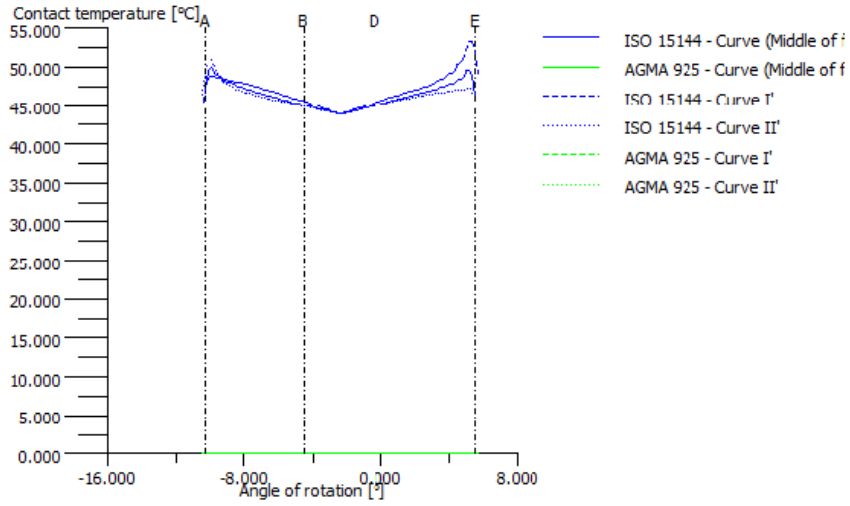

wt = 100 %, a = 74 mm, fpt = 0 µm, µ = 0.06396193238
theOil = 42.5 °C, theM = 43.9 °C, etaM = 220.40 mPa*s

Figure: Flash temperature (ISO TR 15144)

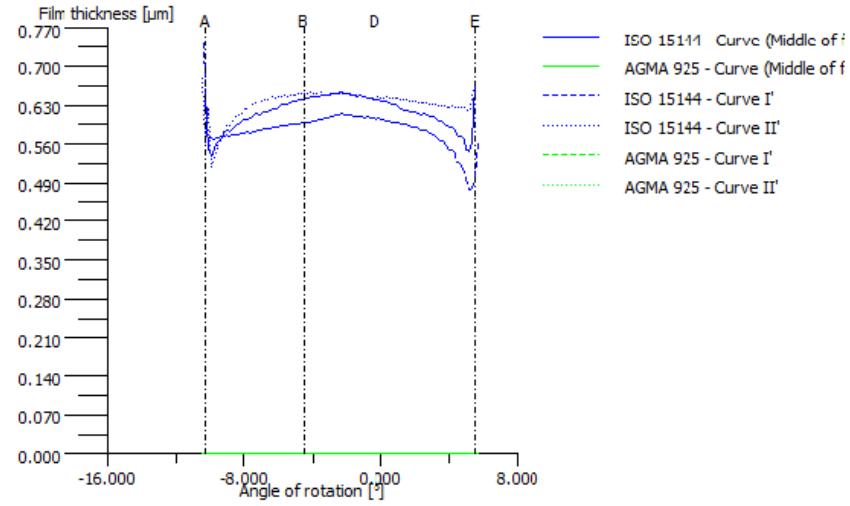

wt = 100 %, a = 74 mm, fpt = 0 µm, µ = 0.06396193238
theOil = 42.5 °C, theM = 43.9 °C, etaM = 220.40 mPa*s
hmin(ISO) = 0.479 µm, Ra = 0.600 µm

Figure: Lubricating film (ISO TR 15144)

Calculation of path of contact under load
Mesh gear 2 - gear 3 (Left Tooth Flank)

Partial load for calculation		100.00	%
Center distance	[a]	-74.00	mm
Single pitch deviation	[fpt]	0.00	µm
Coefficient of friction	[µ]	0.05	
Torque	[T1]	83.33	Nm

		min	max	Delta	µ	sigma
Transmission error	(µm)	-109.8788	-109.7155	0.1633	-109.7503	0.0434
Stiffness curve	(N/mm/µm)	32.9453	36.0210	3.0757	35.3151	0.6525
Line load	(N/mm)	0.4247	69.0395	68.6148	31.9708	5.4167
Torque Gear 2	(Nm)	83.2568	83.4010	0.1442	83.3322	0.0190
Torque Gear 3	(Nm)	-249.5341	-249.1153	0.4189	-249.3400	0.0544
Loss power	(W/mm)	0.0000	0.3419	0.3419	0.0892	0.0575
Flash temperature	(°)	42.9750	44.3609	1.3859	43.3237	0.2417
Lubricating film	(µm)	0.5088	1.9692	1.4604	0.8737	0.2047
Hertzian stress	(N/mm²)		420.8079		242.3298	

Transverse contact ratio under load	[Epsa']	1.80
Overlap ratio under load	[Epsb']	1.15
Total contact ratio under load	[Epsg']	2.95

KHbeta Calculation
Gear 1
Point in polar co-ordinates:
R = 37.000 mm , phi = 0.000 °
Displacement calculated in direction 112.071 °

	y	phi2.t	f2.t	f2.b	f2.tot	f2.C
1	-20.0000 mm	0.0000°	0.0000 mm	0.0000 mm	0.0000 mm	0.0000 mm
2	-18.0000 mm	0.0000°	0.0000 mm	0.0000 mm	0.0000 mm	0.0000 mm
3	-16.0000 mm	0.0000°	0.0000 mm	0.0000 mm	0.0000 mm	0.0000 mm
4	-14.0000 mm	0.0000°	0.0000 mm	0.0000 mm	0.0000 mm	0.0000 mm
5	-12.0000 mm	0.0000°	0.0000 mm	0.0000 mm	0.0000 mm	0.0000 mm
6	-10.0000 mm	0.0000°	0.0000 mm	0.0000 mm	0.0000 mm	0.0000 mm
7	-8.0000 mm	0.0000°	0.0000 mm	0.0000 mm	0.0000 mm	0.0000 mm
8	-6.0000 mm	0.0000°	0.0000 mm	0.0000 mm	0.0000 mm	0.0000 mm
9	-4.0000 mm	0.0000°	0.0000 mm	0.0000 mm	0.0000 mm	0.0000 mm
10	-2.0000 mm	0.0000°	0.0000 mm	0.0000 mm	0.0000 mm	0.0000 mm
11	0.0000 mm	0.0000°	0.0000 mm	0.0000 mm	0.0000 mm	0.0000 mm
12	2.0000 mm	0.0000°	0.0000 mm	0.0000 mm	0.0000 mm	0.0000 mm
13	4.0000 mm	0.0000°	0.0000 mm	0.0000 mm	0.0000 mm	0.0000 mm
14	6.0000 mm	0.0000°	0.0000 mm	0.0000 mm	0.0000 mm	0.0000 mm
15	8.0000 mm	0.0000°	0.0000 mm	0.0000 mm	0.0000 mm	0.0000 mm
16	10.0000 mm	0.0000°	0.0000 mm	0.0000 mm	0.0000 mm	0.0000 mm
17	12.0000 mm	0.0000°	0.0000 mm	0.0000 mm	0.0000 mm	0.0000 mm
18	14.0000 mm	0.0000°	0.0000 mm	0.0000 mm	0.0000 mm	0.0000 mm
19	16.0000 mm	0.0000°	0.0000 mm	0.0000 mm	0.0000 mm	0.0000 mm
20	18.0000 mm	0.0000°	0.0000 mm	0.0000 mm	0.0000 mm	0.0000 mm
21	20.0000 mm	0.0000°	0.0000 mm	0.0000 mm	0.0000 mm	0.0000 mm

Gear 2
Point in polar co-ordinates:
R = -111.000 mm , phi = 0.000 °
Displacement calculated in direction 112.071 °

	y	phi3.t	f3.t	f3.b	f3.tot	f3.C
1	-20.0000 mm	0.0000°	0.0000 mm	0.0000 mm	0.0000 mm	0.0000 mm
2	-18.0000 mm	-0.0000°	0.0000 mm	0.0000 mm	0.0000 mm	0.0000 mm
3	-16.0000 mm	-0.0000°	0.0000 mm	0.0000 mm	0.0000 mm	0.0000 mm
4	-14.0000 mm	-0.0000°	0.0000 mm	0.0000 mm	0.0000 mm	0.0000 mm
5	-12.0000 mm	-0.0000°	0.0000 mm	0.0000 mm	0.0000 mm	0.0000 mm
6	-10.0000 mm	-0.0000°	0.0000 mm	0.0000 mm	0.0000 mm	0.0000 mm
7	-8.0000 mm	-0.0000°	0.0000 mm	0.0000 mm	0.0000 mm	0.0000 mm
8	-6.0000 mm	-0.0000°	0.0000 mm	0.0000 mm	0.0000 mm	0.0000 mm
9	-4.0000 mm	-0.0000°	0.0001 mm	0.0000 mm	0.0001 mm	0.0000 mm
10	-2.0000 mm	-0.0000°	0.0001 mm	0.0000 mm	0.0001 mm	0.0000 mm
11	0.0000 mm	-0.0000°	0.0001 mm	0.0000 mm	0.0001 mm	0.0000 mm
12	2.0000 mm	-0.0000°	0.0001 mm	0.0000 mm	0.0001 mm	0.0000 mm
13	4.0000 mm	-0.0000°	0.0001 mm	0.0000 mm	0.0001 mm	0.0000 mm
14	6.0000 mm	-0.0000°	0.0001 mm	0.0000 mm	0.0001 mm	0.0000 mm

15	8.0000 mm	-0.0000°	0.0001 mm	0.0000 mm	0.0001 mm	0.0000 mm
16	10.0000 mm	-0.0000°	0.0001 mm	0.0000 mm	0.0001 mm	0.0000 mm
17	12.0000 mm	-0.0000°	0.0001 mm	0.0000 mm	0.0001 mm	0.0000 mm
18	14.0000 mm	-0.0000°	0.0001 mm	0.0000 mm	0.0001 mm	0.0000 mm
19	16.0000 mm	-0.0000°	0.0001 mm	0.0000 mm	0.0001 mm	0.0000 mm
20	18.0000 mm	-0.0000°	0.0001 mm	0.0000 mm	0.0001 mm	0.0000 mm
21	20.0000 mm	-0.0000°	0.0001 mm	0.0000 mm	0.0001 mm	0.0000 mm

Explanations:
y : Width
phi's : Static torsion
fat : Displacement due to torsion
fib : Displacement due to bending
f.tot : Total displacement (f.b+f.t)
f.C : Change due to tooth trace modification

Load distribution
Contact stiffness = 12.253 N/mm/µm

	y	g	w
1.	-20.0000 mm	4.7243 µm	57.8860 N/mm
2.	-18.0000 mm	4.7325 µm	57.9860 N/mm
3.	-16.0000 mm	4.7402 µm	58.0811 N/mm
4.	-14.0000 mm	4.7476 µm	58.1711 N/mm
5.	-12.0000 mm	4.7545 µm	58.2561 N/mm
6.	-10.0000 mm	4.7610 µm	58.3361 N/mm
7.	-8.0000 mm	4.7672 µm	58.4111 N/mm
8.	-6.0000 mm	4.7729 µm	58.4812 N/mm
9.	-4.0000 mm	4.7782 µm	58.5462 N/mm
10.	-2.0000 mm	4.7831 µm	58.6062 N/mm
11.	0.0000 mm	4.7876 µm	58.6612 N/mm
12.	2.0000 mm	4.7917 µm	58.7112 N/mm
13.	4.0000 mm	4.7953 µm	58.7562 N/mm
14.	6.0000 mm	4.7986 µm	58.7962 N/mm
15.	8.0000 mm	4.8015 µm	58.8312 N/mm
16.	10.0000 mm	4.8039 µm	58.8612 N/mm
17.	12.0000 mm	4.8059 µm	58.8862 N/mm
18.	14.0000 mm	4.8076 µm	58.9063 N/mm
19.	16.0000 mm	4.8088 µm	58.9213 N/mm
20.	18.0000 mm	4.8096 µm	58.9313 N/mm
21.	20.0000 mm	4.8100 µm	58.9363 N/mm

Explanations:
g : Flank overlap
w : Line load

wmax = 58.936 N/mm, wm = 58.570 N/mm
wm = (Ft/b)/cos(a_wt)
KHb = wmax/wm = 1.006 (Calculation according to ISO 6336-1, Appendix E)
Notice: The influence of the exceeding tooth width is not taken into account in the calculation of KHbeta.

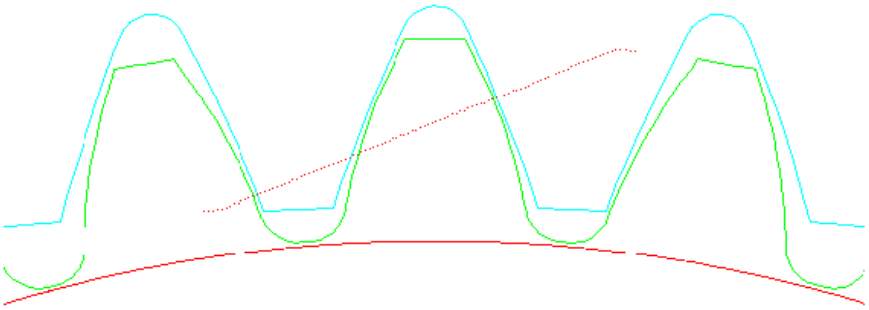

Figure: Path of contact

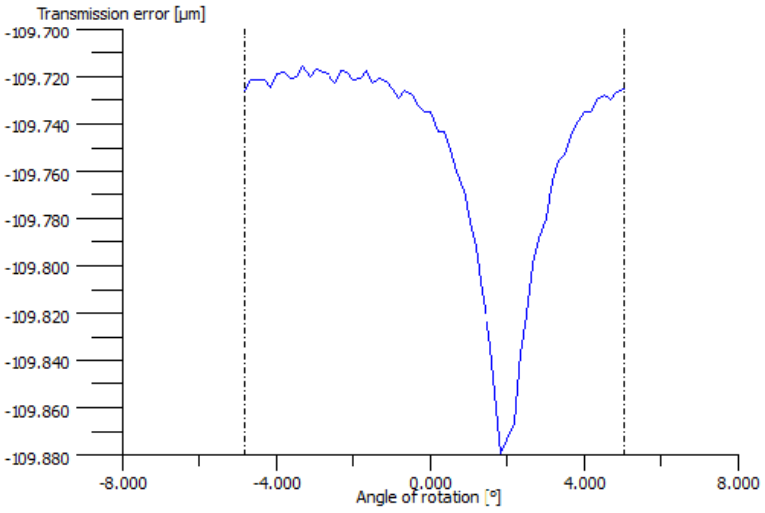

wt = 100 %, a = -74 mm, fpt = 0 µm, µ = 0.05

Figure: Transmission error

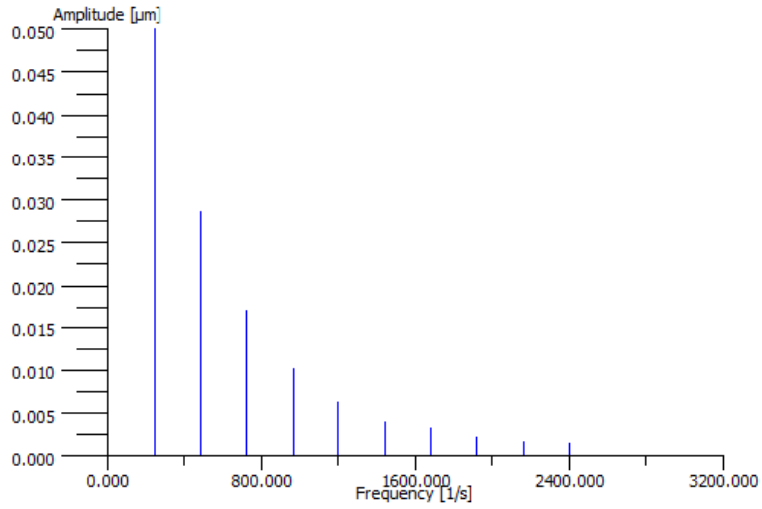

1st Harmonic frequency [1/s] : 240

Harmonics	Amplitude [µm]
1.	0.04996308559
2.	0.02854768433
3.	0.01702788816
4.	0.01021983624
5.	0.006204456236
6.	0.004005115857
7.	0.00333372945
8.	0.002233901218
9.	0.001585446914
10.	0.001463987767

Figure: FFT of transmission error

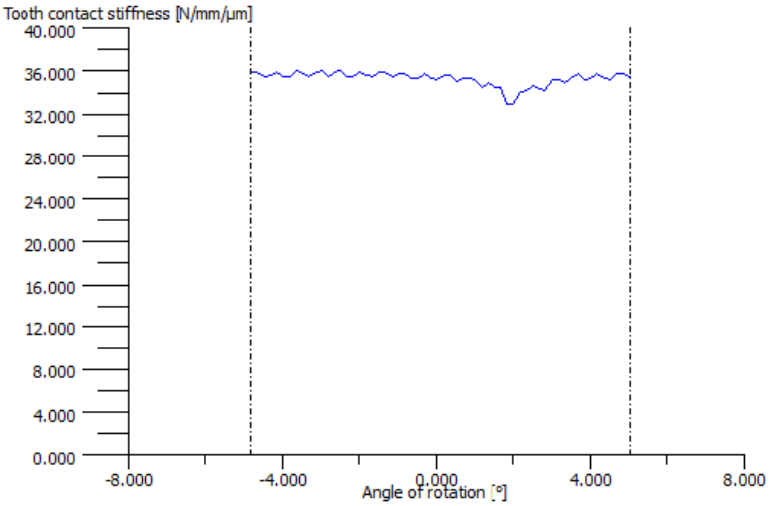

wt = 100 %, a = -74 mm, fpt = 0 µm, µ = 0.05

Figure: Stiffness curve

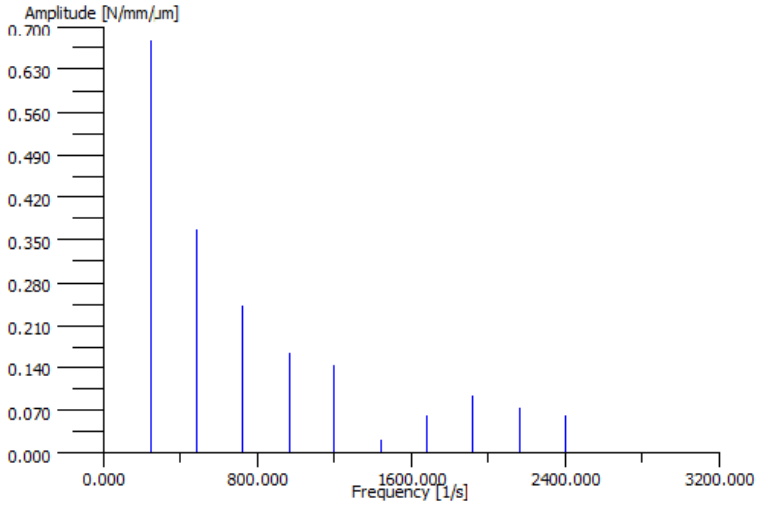

1st Harmonic frequency [1/s] : 240

Harmonics	Amplitude [N/mm/µm]
1.	0.6762787909
2.	0.3657684415
3.	0.2404671301
4.	0.1614084893
5.	0.1418131998
6.	0.01969689689
7.	0.06037681442

13/19

8. 0.09289960784
9. 0.07380626645
10. 0.05956621154

Figure: FFT of contact stiffness

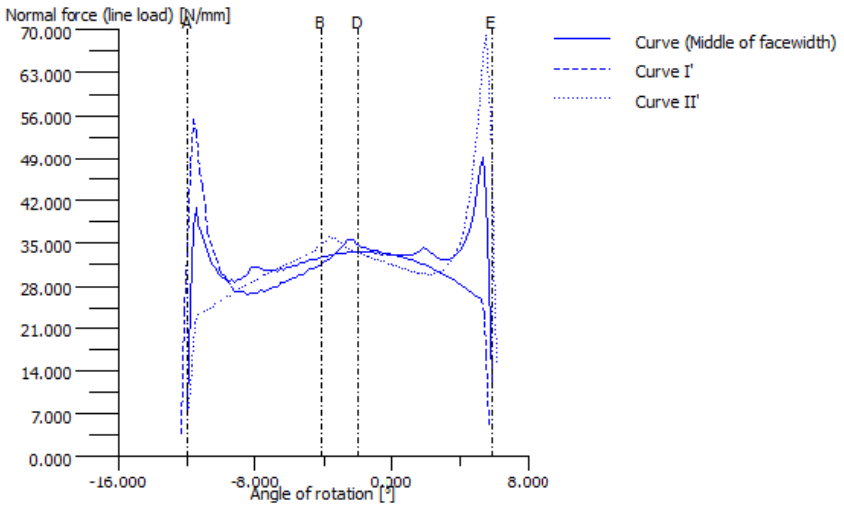

wt = 100 %, a = -74 mm, fpt = 0 µm, µ = 0.05

Figure: Normal force curve (Line load)

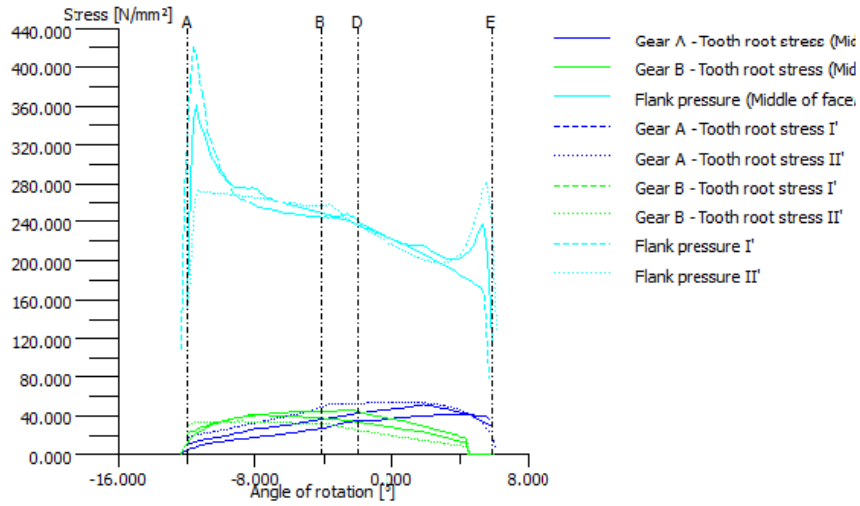

wt = 100 %, a = -74 mm, fpt = 0 µm, µ = 0.05

Figure: Stress curve

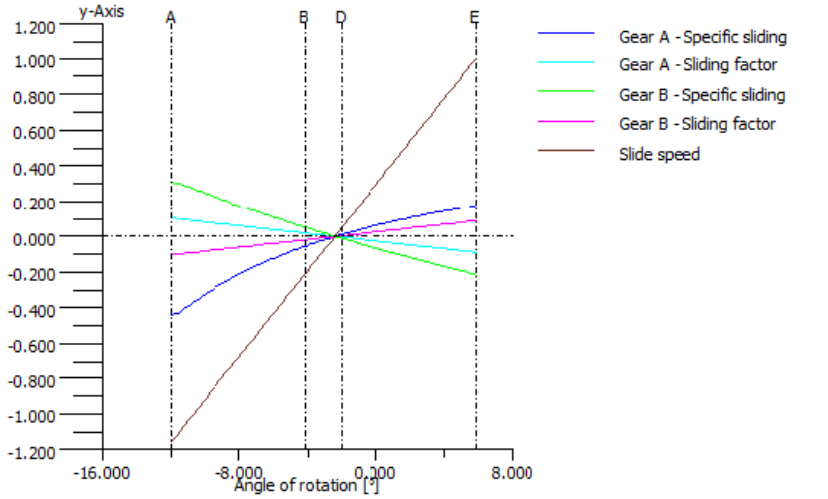

wt = 100 %, a = -74 mm, fpt = 0 µm, µ = 0.05
vg: 1.0 = 0.104 m/s

Figure: Kinematics

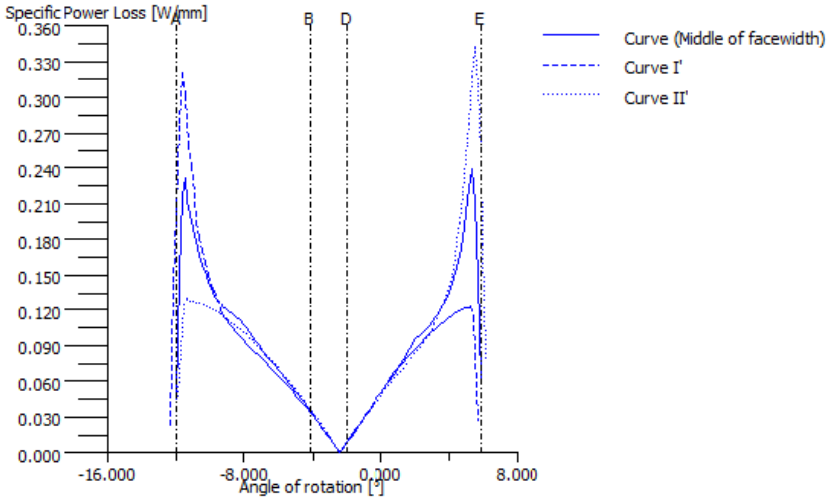

wt = 100 %, a = -74 mm, fpt = 0 µm, µ = 0.05
Displaying power losses per mm facewidth

15/19

Figure: Loss power

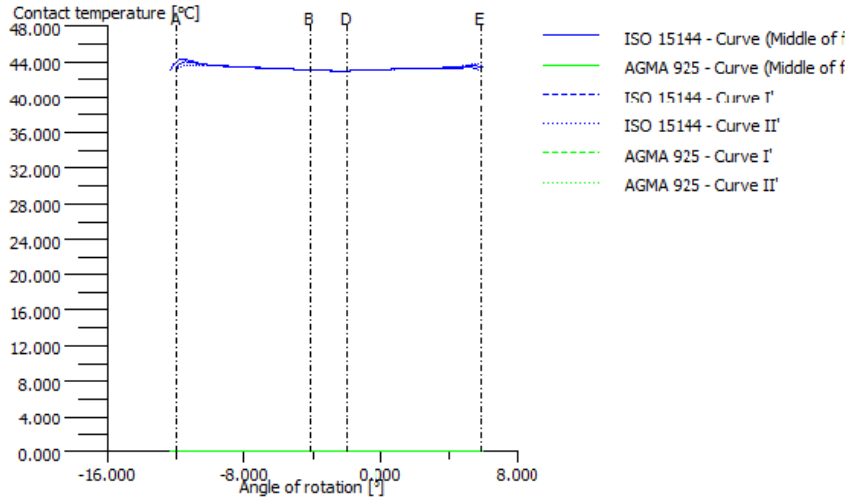

wt = 100 %, a = -74 mm, fpt = 0 µm, µ = 0.03901368843
theOil = 42.5 °C, theM = 43.0 °C, etaM = 232.82 mPa*s

Figure: Flash temperature (ISO TR 15144)

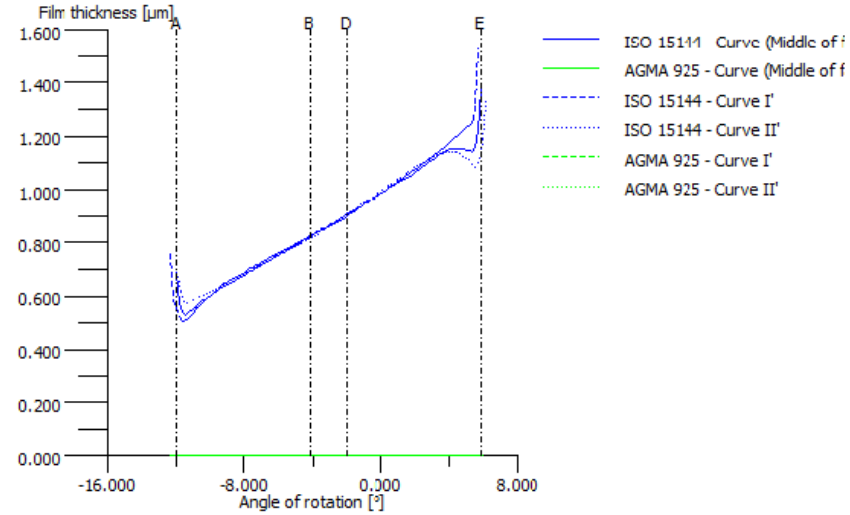

wt = 100 %, a = -74 mm, fpt = 0 µm, µ = 0.03901368843
theOil = 42.5 °C, theM = 43.0 °C, etaM = 232.82 mPa*s
hmin(ISO) = 0.509 µm, Ra = 0.600 µm

Figure: Lubricating film (ISO TR 15144)

Calculation of path of contact under load

		min	max	Delta	μ	sigma
Transmission error of planet stage	(Nm)	-39.7950	-38.5731	1.2219	-39.0386	0.4257
Planet stage stiffness	(Nm/°/mm)	4101.9885	4286.2231	184.2346	4205.6936	
49.6059						

Angular shifting of planet meshing, relative to operating pitch points C
Planet 1, meshing with sun: -0°, meshing with rim: -5°
Planet 2, meshing with sun: 3.48768e-005°, meshing with rim: -4.99997°
Planet 3, meshing with sun: -3.48768e-005°, meshing with rim: -5.00004°

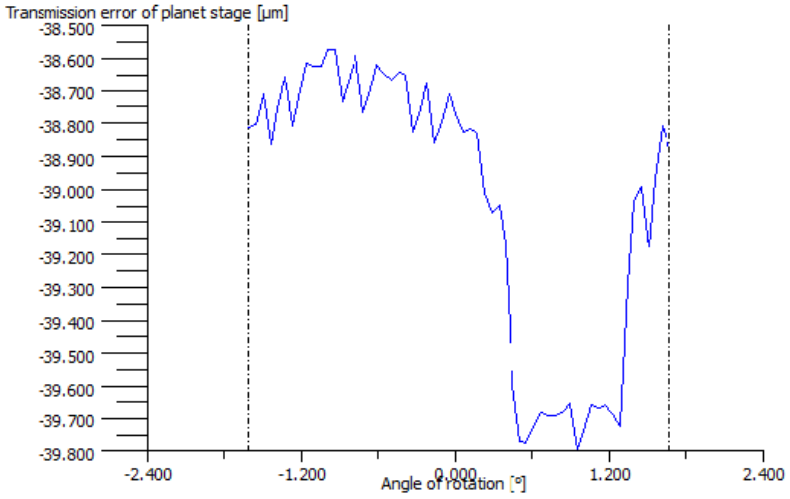

wt = 100 %, a = 74 mm,
fpt1 = 0 µm, fpt2 = 0 µm,
µ1 = 0.05, µ2 = 0.05

Figure: Transmission error of planet stage

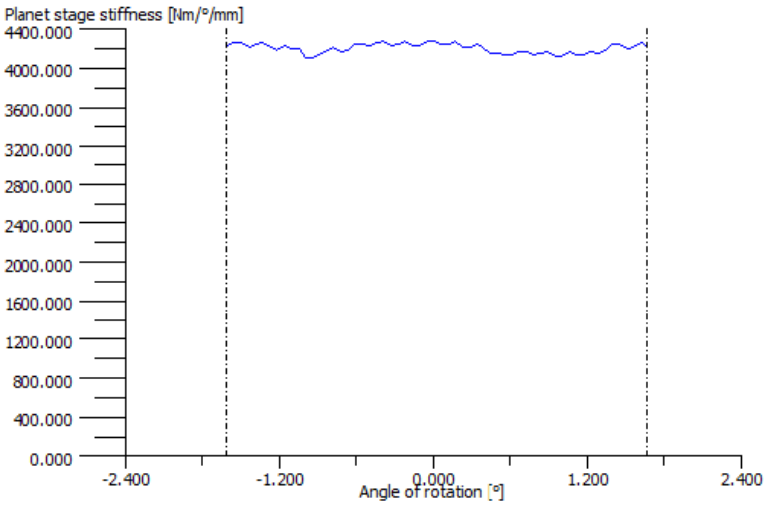

wt = 100 %, a = 74 mm,
fpt1 = 0 µm, fpt2 = 0 µm,
µ1 = 0.05, µ2 = 0.05

Figure: Stiffness curve of planet stage

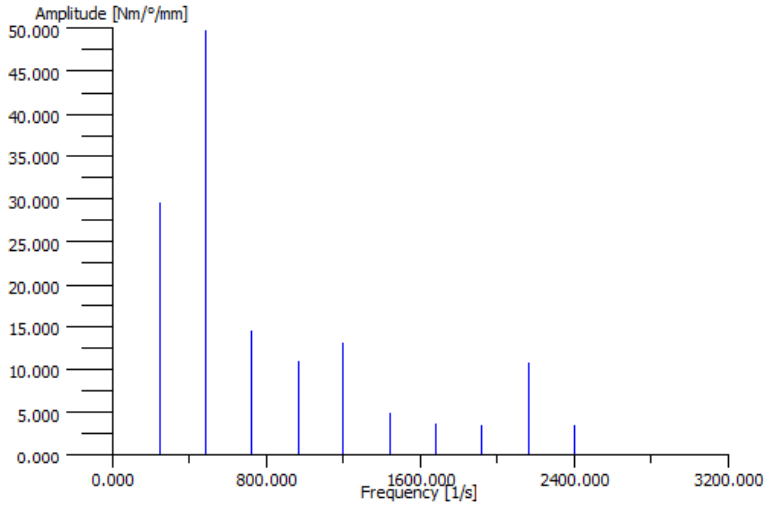

1st Harmonic frequency [1/s] : 240

Harmonics	Amplitude [Nm/°/mm]
1.	29.50128263
2.	49.61112476
3.	14.35648769
4.	10.85576379
5.	12.99485593

18/19

6. 4.855477549
7. 3.699621602
8. 3.433905514
9. 10.70139291
10. 3.465599321

Figure: FFT of stiffness curve planet stage

End report lines: 309